Studies on Metal Hydride Based Hydrogen Storage and Purification Systems

A thesis submitted in partial fulfillment of the requirements for the degree of

Doctoral of Philosophy

by

Alok Kumar
(176151007)

School of Energy Science and Engineering
Indian Institute of Technology Guwahati
Guwahati-781039, Assam, India

August 2022

School of Energy Science and Engineering
Indian Institute of Technology Guwahati
Guwahati-781039, Assam, India

THESIS CERTIFICATE

This is to certify that the work contained in the thesis entitled **Studies on Metal Hydride Based Hydrogen Storage and Purification System** by **Alok Kumar (Reg. No 176151007)**, a student of the School of Energy Science and Engineering, Indian Institute of Technology Guwahati, for the award of the degree of **Doctor of Philosophy** has been carried out under my supervision and that this work has not been submitted elsewhere for any degree.

Dr. P. Muthukumar
Professor,
Department of Mechanical Engineering
Indian Institute of Technology Guwahati
Guwahati-781039, Assam, India.

Dedicated to my

Parents

Mrs. Kiran Devi & Mr. Girish Kumar

and

Wife

Mrs. Rashmi Kumari

ACKNOWLEDGEMENT

First and foremost, I will express my deep and sincere gratitude to my supervisor Prof. P. Muthukumar, Department of Mechanical Engineering, Indian Institute of Technology Guwahati, for his continuous guidance and support during my PhD research work. I thank him for his sincere advice, encouragement, motivation and excellence guidance, which enabled me to stand motivated and overcome difficulties during my research work. His caring nature, fatherly behaviour and easily approachable nature helped me in expressing different problems and approach towards the research work. His prompt nature always helped in quick correction and revision for all of my manuscripts. I look forward to be associated with him and further developing our relationship.

I would like to thank Department of Science and Tecnology (DST), Ministry of New and Renewable Energy (MNRE), Govt. of India and NTPC Netra for funding and supporting various projects.

I am thankful to my doctoral committee members, Prof. Amaresh Dalal (Department of Mechanical Engineering), Prof. Chandan Das (Department of Chemical Engg.) and Dr. Pankaj Kalita (School of Energy Science and Engineering) for their valuable suggestions and encouragement during the period of my research work. I will express my sincere thanks to Prof. V. S Moholkar (Ex HOS), Prof. Kaustubha Mohanty (Ex. HOS) and Prof. Vaibhav V Goud, HOS for providing necessary facilities for conducting smooth research. I would also take this opportunity to thank former and present HOD of Mechanical Engineering, Prof. S. K. Dwivedy and Prof. K. S. R. Krishna Murthy for alloying to use the departmental labs for experiments.

I express my heartfelt thanks to all the faculty members and staff of SESE for their cooperation during my PhD tenure. I express my sincere thanks to Mr. Dhiren Huzuri, Technical Superintendent, SESE, for providing initial help in learning and analysing gas sample using Gas Chromatography. I heartily thanks to Mr. Nip Borah, Sr. Technical Superintendent, Department of Mechanical Engineering for his cooperation and help in facilitating equipment's and tools for conducting experiments.

I express my deepest and sincere thanks to my senior Dr. R Nithin Narmada, Mr. J. Sunku Prasad, P. Vivek Selvan, and team mates Mr. Sayantan Jana, Mr. Abhishek Parida, Mr. Subham Parasar and Mr. K. Malleswararao for their sincere help and support in conduction experiments and discussing technical things. I will also thank all my labmates, Mr. M. Arun Kumar, Dr. Gurpreet Sing Sodhi, Dr. Vigneshwaran, Mr. G Sureandhar, Dr. C.R Rao, Dr. L.K Kaushik Dr. Mrinal Bhowmik, Dr. D.V.N. Lakshmi, Mr. C. Aswin Karthik, Mr. Tat Suraj Arun, Ms. Sunita Deb, Ms. Pratibha Maurya, Ms. Juri Sonowal, Ms. Nayanita Kalita and Ms. Akshini More for their cooperation and help.

I express my deepest thanks goes to my family members and bow my head to express sincere gratitude to the Almighty God for giving me strength, health and the spirit to conduct and complete my research work.

Alok Kumar

ABSTRACT

The world is witnessing an inevitable shift of energy dependency from fossil fuels to cleaner energy sources like wind, solar, hydrogen, etc. The governments from all over the world have realized that for limiting the global rise in temperature to 1.5 °C, hydrogen has to be given a reasonable/sizable share in meeting global energy demand by mid of 20th century. Hydrogen can be produced through several means using renewable energy sources and can be stored either in solid, liquid or gaseous state. Though, compressed and liquefied hydrogen storages are well-established technologies in the commercial sector, however, due to the leakage risk, boil-off losses and explosive nature, world is exploring a safer way of hydrogen storage i.e. absorption/adsorption based solid-state hydrogen storage technology. Although hydrogen can be produced from various extraction processes, such as through decomposition of fossil fuels, electrolysis of water, thermolysis of water, biomass conversion, etc., it is not always in the pure form. Metal hydride (MH)- hydrogen system can be a suitable solution for safe hydrogen storage and easy purification technology.

Considering these issues, in the present study, thermodynamic screening of MH alloys was performed on the basis of PCI of MH alloys, to filter suitable alloys for efficient working of metal hydride based hydrogen purification system MHHPS. From thermodynamic alloy screening, $LaNi_{4.7}Al_{0.3}$, $LaNi_5$ and $La_{0.9}Ce_{0.1}Ni_5$ were found suitable for hydrogen purification application and have been considered for the present studies. In order to check feasibility of metal hydride (MH) for hydrogen storage and purification application, parametric investigation on $LaNi_{4.7}Al_{0.3}$, $LaNi_5$ and $La_{0.9}Ce_{0.1}Ni_5$ based small scale reactor were performed by varying different set of experimental parameters like hydrogen supply pressure (2 – 20 bar), absorption temperature (20 – 30 °C), and desorption temperature (10 – 90 °C) at fixed flow rate of 'heat transfer fluid (HTF)' at 4 lpm for small scale system. All the small scale reactors were identical in design and were filled with 1.2 kg of $LaNi_{4.7}Al_{0.3}$, $LaNi_5$ and $La_{0.9}Ce_{0.1}Ni_5$ each. For small scale studies, the experiments were carried out using 6 ECT reactor configuration. However, the effect of HTF flow rate was studied in the large scale reactor with 99 ECT, wherein the reactor was filled with 40 kg $LaNi_{4.7}Al_{0.3}$ and flow rate was varied from 10 lpm to 30 lpm. The results show that, all the selected alloys were suitable for hydrogen storage and purification application.

The reactor design in the present study aims at getting evenly distributed embedded cooling tubes and maintain a near equal bed thickness at all the locations of the metal hydride bed, wherein a porous filter is centrally placed in a cylinder, with a varying number of cooling tubes placed around the filter. A two dimensional numerical model has been solved using COMSOL Multiphysics 4.3a. Transient heat and mass transfer phenomenon occurring in hydride bed during absorption, pressure gradient between supply condition and hydride bed, flow and diffusion of hydrogen through bed, removal of heat from hydride bed by HTF with emphasis on convective boundary condition, and resultant axial variation of HTF were considered in this study.

The design for reactor was finalized after comparing numerical results of three different reactors. The configuration of the three reactors were obtained by fixing the alloy volume and the length of the reactor in each case as similar. The configuration was also established by keeping the reactor fabrication simple by single layer cooling tube stacking. The shell diameter and thickness were taken as per ASTM standard. The numerical model was validated with the experimental results carried out in the fabricated MH reactor of 6 ECT. The geometry as well as the thermophysical properties were defined as per alloy and reactor used in the experiments, so as to simulate this experimental investigation.

According to the result obtained, it was observed that, with increase in the pressure gradient from 10 to 30 bar, the rate of absorption increases rigorously and the fastest absorption was observed for 30 bar supply pressure. This was because of the increase in the pressure gradient for the higher pressure range. This pressure gradient acts as driving force for the absorption and increases the rate of absorption for its higher value. On comparison among all three reactor configuration, for all the cases, 6 ECT configuration showed better reaction kinetics than the other two reactor configuration i.e. 9 ECT and 5 ECT. This was because of the minimum bed thickness in case of the 6 ECT reactor. However, for 9 ECT reactor, the bed thickness between the tubes was minimum, but at the same time there was comparatively thicker bed in the radial direction. This led to slower heat dissipation from the outer periphery of the MH bed, which finally showers down the reaction kinetics. The sequence of reaction kinetics was in the order 6 ECT > 9 ECT > 5 ECT reactor. For the better analysis of the numerical results, the temperature and the rate of absorption contours were plotted for supply pressure of 10, 20 and 30 bar and time interval of 250 s. The rate of heat removal was faster for the 6 ECT reactor, as compared to other two configurations. Because of

faster heat removal, the rate of absorption in the 6 ECT reactor is also faster. Hence 6 ECT reactor was finalized for small scale system study. Adopting same design methodology 99 ECT reactor, having 50 kg alloy capacity, was fabricated for large scale application.

The optimum operating conditions for the 99 ECT reactor filled with 40 kg $LaNi_{4.7}Al_{0.3}$ was obtained through parametric studies. The activation was carried out by successive absorption and desorption processes. In the third absorption cycle, MHHSS had absorbed 552.356 g of hydrogen to reach a maximum storage capacity of 1.4 wt% at 40 bar pressure and 30 °C temperature. The testing of MHHSS was carried out by varying H_2 supply pressure, absorption and desorption temperatures and heat transfer fluid (HTF) flow rate. It was observed that the supply pressure has significant effect on absorption rate, and the optimum supply pressure was observed in the range of 10-15 bar. Similarly, during the desorption cycle, optimum desorption temperature was found in the range of 80-90 °C. The optimum flow velocity for HTF was observed in the range of 20-30 lpm.

Similarly, parametric studies for optimizing the operational parameters of the coupled reactor in multi-stage MHHPS were performed using small scale (6 ECT) reactors. For efficient system operation, the suggested absorption temperature is in the range of 20 °C to 30 °C with supply pressure 5 bar to 20 bar, while the flushing and desorption are suggested in the ranges of 15 °C to 20 °C and 70 °C to 90 °C, respectively.

Further, for TCD (thermal conductivity detector) analysis, an optimum method was developed for GC (gas chromatography), wherein column flow is fixed at 6 mL/min and oven temperature was raised from 60 °C to 150 °C. The system was calibrated with standard gas sample. The poisoning effect of various gaseous impurities (mainly CH_4, CO_2, CO, N_2, Ar) in the single and multi-stage MHHPS has been investigated by varying the impurity level from 10% to 50% by weight in H_2 gas mixture and by performing cyclic test with 10% impurity level. The system includes a reactor configured with embedded cooling tubes, centrally located SS316 sintered porous filter, an identical three bed space, each filled with 1.2 kg $La_{0.9}Ce_{0.1}Ni_5$, $LaNi_5$ and $LaNi_{4.7}Al_{0.3}$ alloy, a cold and hot fluid supply line with a fluid pump, and gas valves.

According to the results, the system delivered 99.9995% pure hydrogen for 10% to 20% impure gas mixture in a single stage. While, for higher impurity level, the purity level of desorbed

hydrogen was in the range of 95% to 99.9% for single stage operation. However, for higher impurity, the multistage operation is capable to deliver pure hydrogen (99.9995%). According to the cyclic study, the reaction kinetics of the reactor bed got affected significantly.

CO showed significant poisoning effect in the La-Ni based AB_5 alloys. Methanation was dominant when CO interacted with hydrogen and alloy simultaneously. Therefore, it is advised to use CO free impure gas sample, wherever MH based hydrogen purification technologies are used. However, presence of less CO content (1-2%) may not affect the working of such system. Maintaining desorption temperature above 100 °C could also be possible solution for such impurities, wherein the moisture generated during methanation can be removed in each desorption cycle. Apart from CO and O_2 as impurity should not be used in such systems, as it oxidises the MH reactor. The poisoning effect of gases are in the order $Ar<N_2<CH_4<CO_2<CO$. Moreover, it is not suggested to use CO above 0.5-1%. Further, for large scale hydrogen storage and purification, 99 ECT reactor was filled with 40 kg $LaNi_{4.7}Al_{0.3}$, having hydrogen storage and purification capacity of over 6000 l, in a single stage.

Bed regeneration was possible for all the three alloys. It was observed that within one regeneration cycle (evacuation followed by absorption of pure hydrogen), the MH bed was completely regenerated for N_2 and Ar and Impurity. However, it took two regeneration cycle to reactivate alloy bed, which got poisoned from CH_4 and CO_2. For poisoning from CO, the regeneration time was maximum, as it took 3 regeneration cycle to reactivate the alloy bed. The purification ability of the alloys was in order $LaNi_{7.4}Al_{0.3}$ > $LaNi_5$ > $La_{0.9}Ce_{0.1}Ni_5$. Because of its operating temperature range in between 20-90 °C, the system can be coupled with solar/waste heat recovery system for its operation. The system is very simple in operation and cost effective.

NOMENCLATURE

C_a	Reaction rate	1/s
C_p	Specific heat	J/kgK
Cp_s	Specific heat of alloy	J/kgK
E_a	Activation Energy	J/mol H_2
H	Enthalpy of hydride formation	J/mol
K	Permeability	m^2
k_e	Effective thermal conductivity of alloy	W/mK
k_g	Effective thermal conductivity of gas	W/mK
M_g	Molar mass of hydrogen	g/mol
M_a	Molecular weight of alloy	g/mol
n	Number of moles of hydrogen	mol
P	Pressure	bar
Po	Reference pressure	bar
Q	Heat Transfer	J
R	Universal gas constant	J/mol K
S	Entropy of hydride formation	J/molK
t	Time	s
T	Temperature	°C
u	Velocity	m/s
V	Volume	m^3

Greek Symbols

β	Hysteresis factor	
φ, φ_o	Slope factor	
μ	Dynamic viscosity	Kg/ms
ρ	Density	Kg/m^3
ε	Porosity	
υ	Kinematic viscosity	m^2/s
λ	Thermal conductivity	W/mK

Subscripts

a	Absorption
d	Desorption
e	Effective
eq	Equibrium
end	End of reaction
f	HTF
g	Gas
in	Inlet
out	Outlet
0	Ambient
s	Supply presure
si	Initial sate
ss	Saturated state

Abbreviations

GC	Gas chromatography
HTF	Heat transfer fluid
MH	Metal hydride
MHHSS	Metal hydride based hydrogen storage system
MHHPS	Metal hydride based hydrogen purification system
MSMHHPS	Multistage metal hydride hydrogen purification system
MHHC	Metal hydride based hydrogen compressor
MHCHS	Metal hydride based heating and cooling system
MHHFC	Metal hydride coupled with hydrogen fuel cell
MHTESS	Metal hydride based thermal energy storage system
PCI	Pressure concentration isotherm
TCD	Thermal conductivity detector

TABLE OF CONTENT

LIST OF FIGURES

LIST OF TABLES

CHAPTER 1 INTRODUCTION

1.1 World Energy Scenario

With population growth and increase in global energy consumption, particularly in sectors such as residential, transportation, health, industries, etc., the energy demand of the world is increasing at a very high rate (Arto et al., 2016; Mesarić and Krajcar, 2015; Wiedenhofer et al., 2013). During the past one-decade worldwide net energy consumption has been almost doubled. Since 18th century, the major energy consumption for chemical industries, thermal power plants, automobile sector, etc., were obtained from traditional energy sources such as, biomass, coal, fossil fuel, etc. This led to the rise of CO_2 concentration in the environment, that caused global warming. The global primary energy consumption from various energy sources is depicted in **Fig. 1.1**, wherein it can be observed that, before the 20th century, the primary energy sources were biomass, coal and fossil fuels.

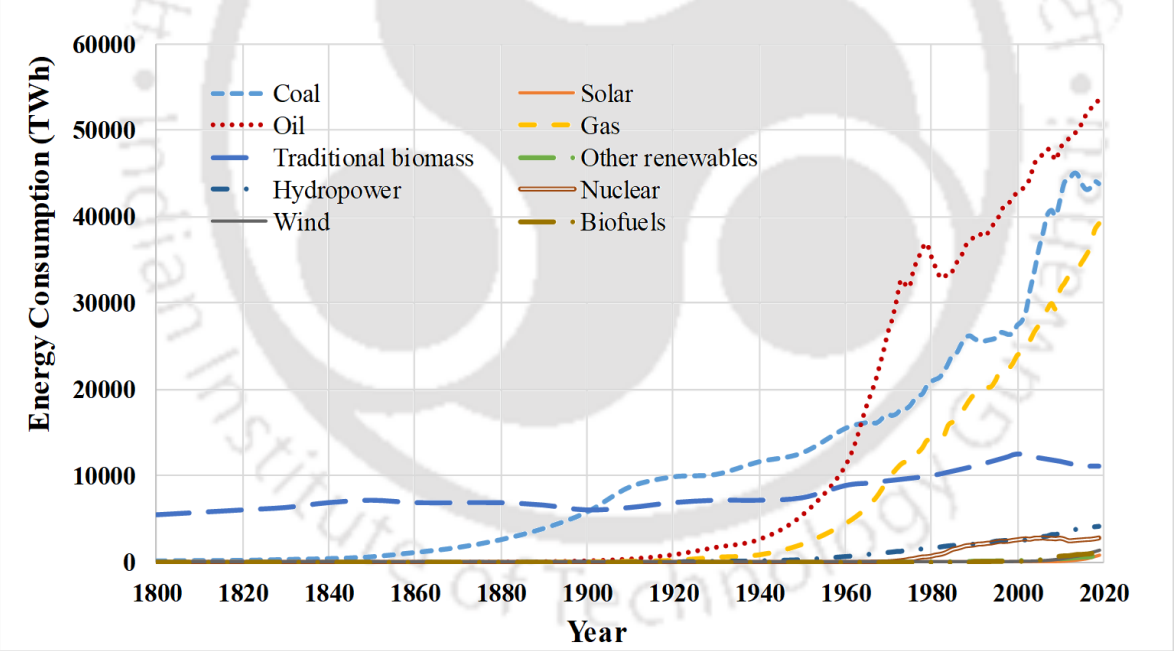

Fig. 1.1 Global primary energy consumption (Smil, 2017)

In the late 19th century and early 20th century, the world realised the alarming situation of the global temperature rise, and started making attempts to use the green energy technology to fulfil the primary energy demand (**Fig. 1.1**). It was realised that the renewable energy sources can be a suitable alternative, and the world witnessed a parallel shift towards the renewable energy

utilisation technology, as a future energy alternative (Jacobson, 2009; Smil, 2017). Plenty of renewable energy resources like solar energy, wind energy, tidal energy, etc., are available unlimited. Still, due to their intermittent availability, it becomes difficult to rely on them as continuous energy sources. However, by deploying different renewable energy conversion technology and coupling it with suitable energy storage technology can bring an immense change in the efficient utilization of renewable sources by storing it in different forms during their availability and utilizing it whenever it is required (Gregory and Rogner, 1998).

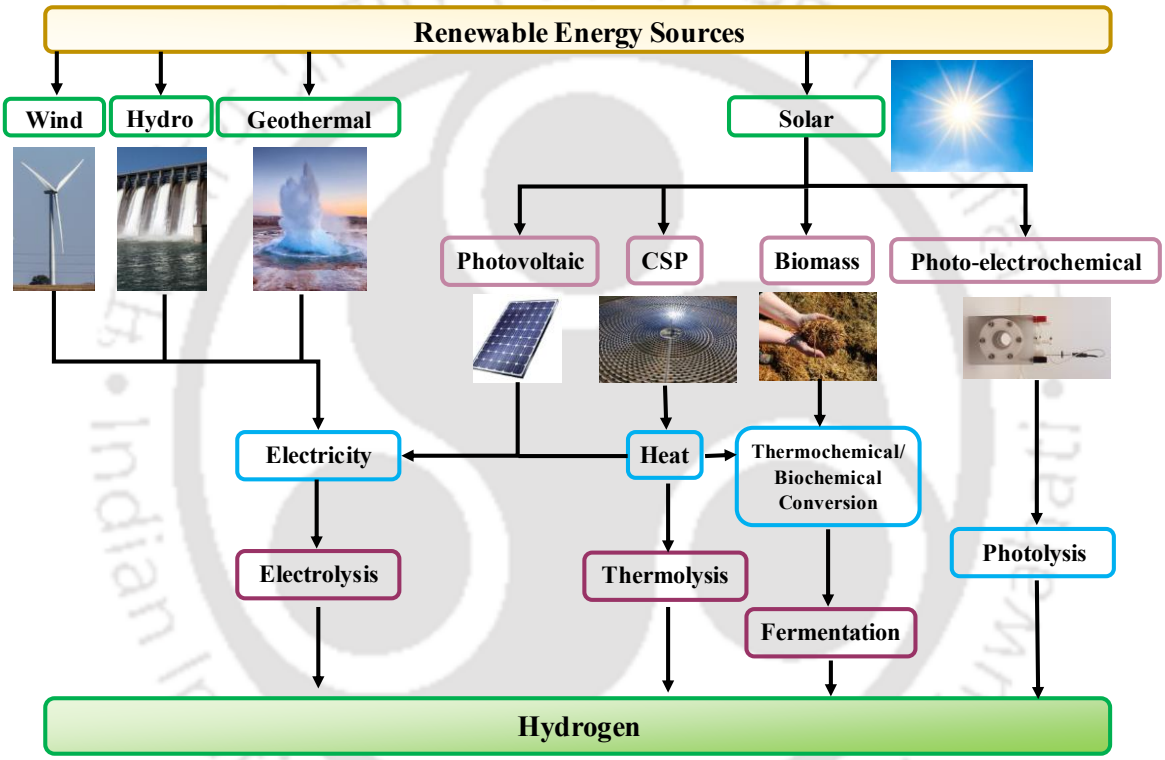

Fig. 1.2 Schematic of the various renewable sources linked to hydrogen energy

Hydrogen is the third most abundant element present on earth which can be extracted through electrolysis, fossil fuels decomposition, thermochemical/photochemical processes, bio photolysis, PV electrolysis, thrombolysis of water, dark fermentation, photo catalysis, etc. (Acar and Dincer, 2019; López Ortiz et al., 2016).

As depicted in **Fig. 1.2**, hydrogen can be produced through all natural sources of energy. It can be produced through electrolysis of water, wherein the water molecule (H_2O) can be broken into

hydrogen and oxygen molecule, where oxygen can be rejected to the atmosphere and hydrogen can be stored. One of the attractive property of hydrogen, which separates it from other conventional fuels and makes it an excellent fuel/energy carrier, is its high gravimetric energy density (calorific value per unit weight) (Abe et al., 2019). The energy density in hydrogen as compared to other available energy sources is presented in **Fig. 1.3**. Hydrogen is an excellent alternative for all other conventional energy sources and it is capable of replacing these conventional energy sources with better conversion efficiencies. Because of its high calorific value (120 MJ/kg) and zero pollution characteristic, it can be a best substitute to all other conventional fuels like fossil fuels, biomass, etc. as shown in **Fig. 1.4** (Jain, 2009)**.**

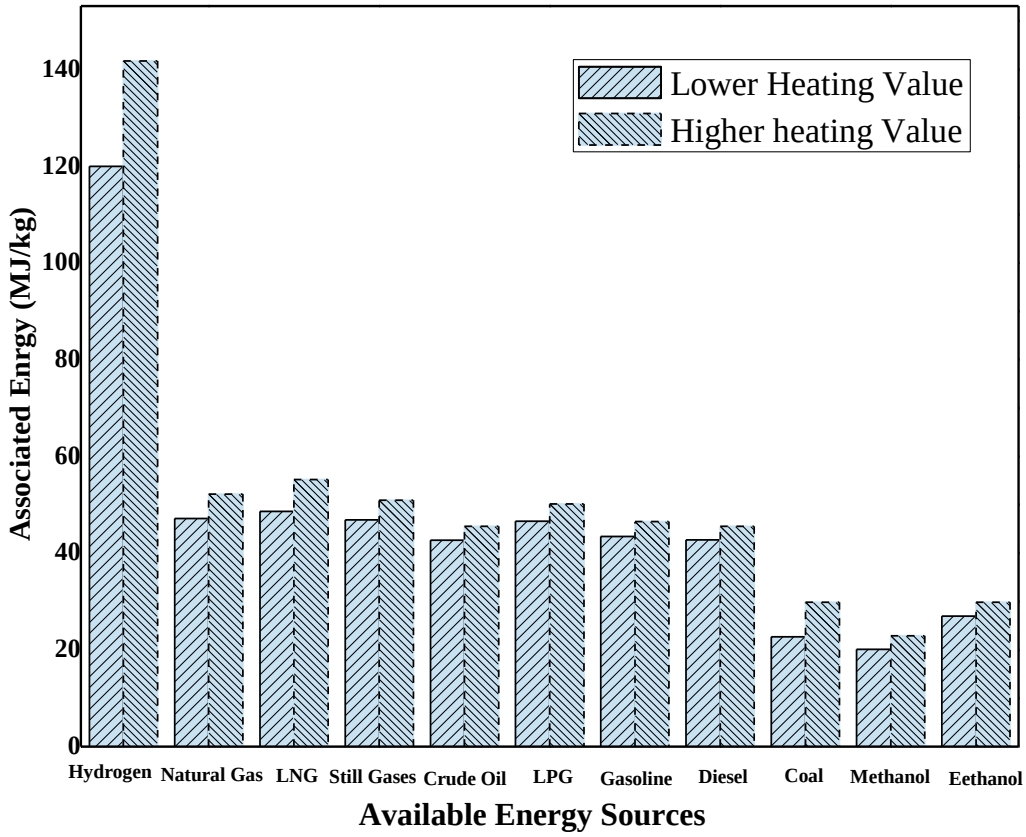

Fig. 1.3 Comparison of energy associated with different available energy sources

Though hydrogen is most abundantly available element on the earth (hydrocarbons, water, etc.), but its availability in free state is very limited. Like any other commodity, hydrogen also needs to be produced, stored and transported for end user application (Abdalla et al., 2018). Hydrogen can be an excellent replacement as next generation fuel with zero pollution and high calorific value,

however, its storage is still challenging, because of its very low density (~0.082 kg/m^3 at STP) and high flammability (Abe et al., 2019). The conventional way of storing hydrogen in compressed form is always having risk of leakage and explosion (Moradi and Groth, 2019; Zuttel, 2003; Züttel, 2004).

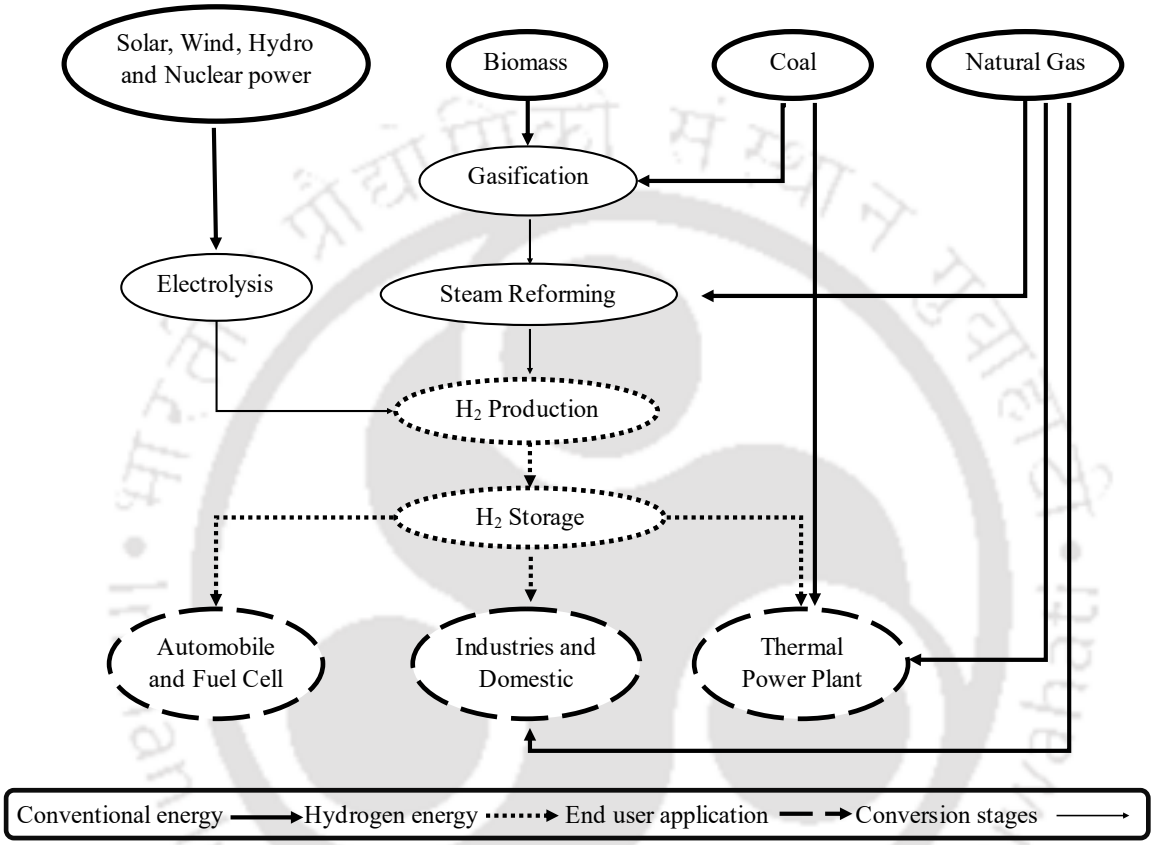

Fig. 1.4 Linkage between hydrogen and other energy system

1.2 Hydrogen Economy and Future Prospective

Among one of the most suitable substitute for conventional fuels/energy carrier, hydrogen finds its spot, right at the top, due to eco-friendly characteristics and high calorific value (120 MJ/kg) (Acar and Dincer, 2019; Moradi and Groth, 2019). Though the availability of hydrogen in a free state is very limited, however, it is most easily and abundantly available element in the environment, as it is available in the form of compounds like hydrocarbons, water, etc. Hence, it cannot be directly used like other commodities; rather, it needs to be produced from various sources (**Fig. 1.2**), stored (compressed form, cryo-compressed form, solid-state, etc.) and

transported for end-user application (Abdalla et al., 2018). **Fig. 1.5** presents the schematic view of hydrogen economy, wherein hydrogen can be produced from several energy sources, but its storage and transportation is always challenging.

Hydrogen as a suitable option for future energy carrier, can be produced using natural energy sources like wind, solar, hydro, etc., through electrolysis of water, when the electricity produced is in excess than the demand (**Fig. 1.2**). Further, the hydrogen produced through these sources can be stored in the MH reactor, or can be compressed up to 450 bar and stored in gas cylinders. During the unavailability of natural energy sources like sun, wind, etc., the stored hydrogen can be sent to a hydrogen-fuel cell, wherein the electricity can be produced to cope with energy demand. A part of hydrogen can also be mixed with the biofuels to improve its calorific value, which can be used in automobiles, or it can be directly used in fuel cell operated cars/vehicles.

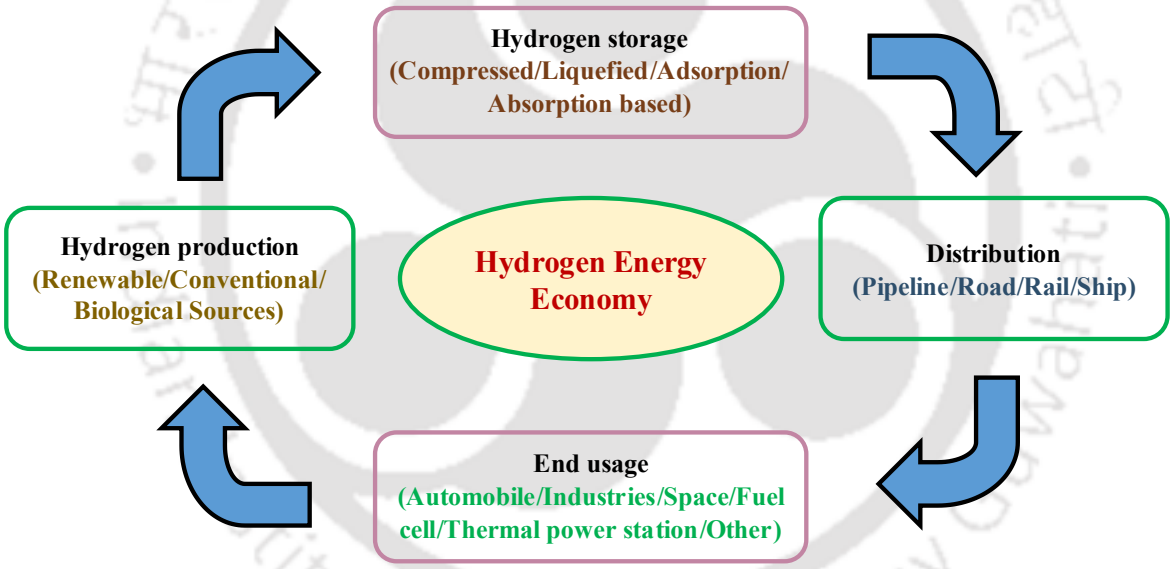

Fig. 1.5 Schematic view of Hydrogen Energy Economy

1.3 Challenges in Hydrogen Storage

As depicted in **Fig. 1.6**, hydrogen can be stored in various ways. Despite unique characteristics like high calorific value, excellent energy carrier and ecofriendly nature, hydrogen has some practical limitations also. Due to high inflammability and low density (~0.082 kg/m^3 at STP), its storage becomes a challenging task. The compressed form of hydrogen storage is having a risk of explosion and leakage (Abdalla et al., 2018; Moradi and Groth, 2019).

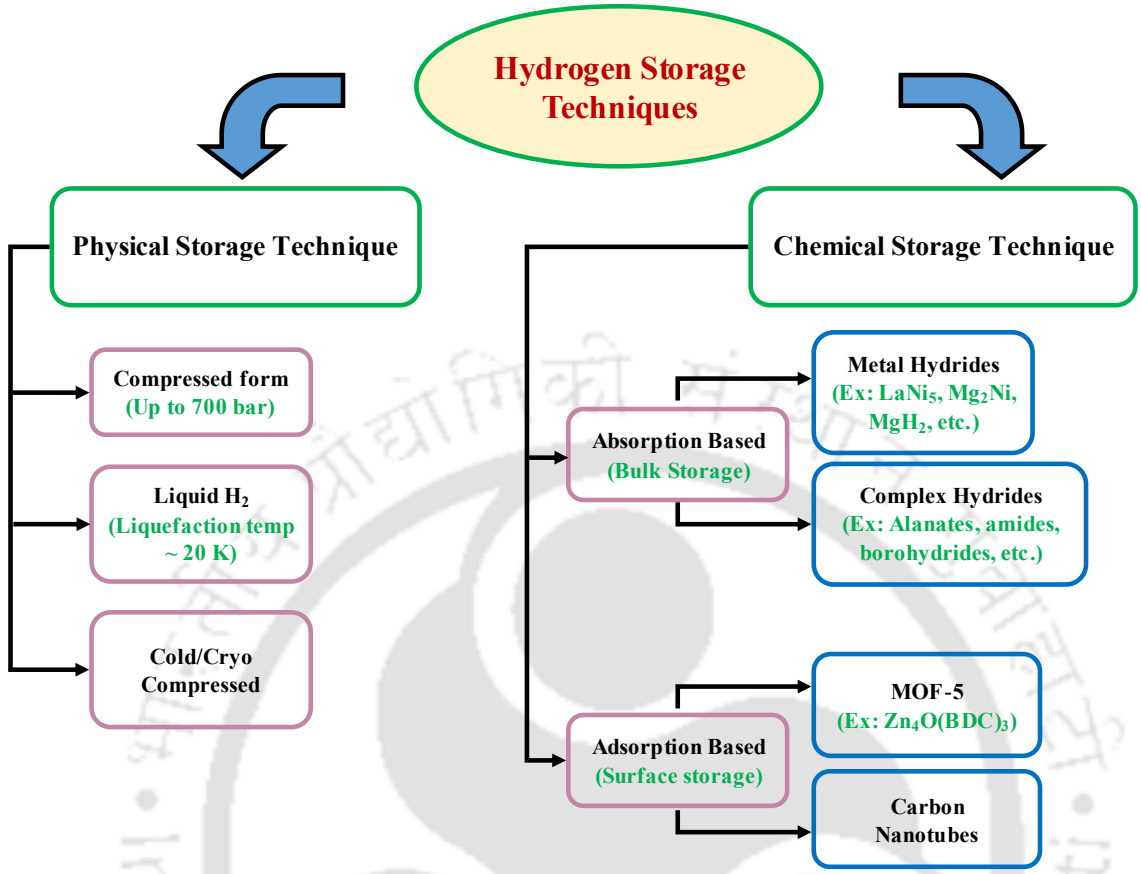

Fig. 1.6 Various hydrogen storage techniques

Apart from compressed hydrogen storage, several other options are being explored by researchers; some of the options and issues related to the hydrogen storage techniques are as follows:

- **Low-pressure storage:** Under this technique, low-pressure hydrogen (5-20 bar) is stored in underground cavities, or it can be stored in overground gasholders, which requires a large ground area. As hydrogen is highly inflammable (even 4% by volume in the air is inflammable), there is always a risk of explosion.
- **High-pressure storage:** Commercial compressed hydrogen cylinders are available, wherein the hydrogen is stored in its compressed gas state under pressure cylinders, which can hold pressure up to 700 bar. However, because of very high pressure, there is always a risk of explosion or leakage. Moreover, the energy required to compress the hydrogen to a higher pressure demands huge compression work in the form of electrical/mechanical input. Also, the tubes and fittings used for the hydrogen gas circuit are very expensive.

- **Storage in the form of liquid hydrogen:** Hydrogen can also be cryogenically stored in the form of liquid at ~21 K and 1 bar. However, maintaining such a low temperature is very difficult and expensive too, so there will be a continuous boil-off losses in the cryogenic hydrogen storage system to the surrounding because of the large temperature difference.
- **Solid-state hydrogen storage:** It mainly comprises of two categories i.e., adsorption storage (MOF, CNT, MWCNT, etc.) and absorption storage (Metal hydrides, complex hydrides, etc.). In adsorption, hydrogen is stored in the microscopic pores and within the CNT structures, but in absorption, it is a bulk phenomenon wherein hydrogen chemically reacts with intermetallic alloys and gets absorbed in the metal lattice to form MH (Muthukumar et al., 2018). When it comes to reliability, efficiency and safety, solid-state hydrogen storage technology is the best suited option.

1.4 Solid-State Hydrogen Storage

Solid-state hydrogen storage technology is gaining immense attention from scientific community day-by-day as it is a safest and reliable way to store hydrogen at desirable operating conditions for different applications. Due to sweeping shift of energy generation towards renewables, hydrogen has evolved as an energy carrier for wide range of applications including automobile, industries, domestic, fuel cell, etc. (Bossel and Eliasson, 2002). The solid-state hydrogen storage techniques are broadly classified into two categories:

a) Absorption based: It is bulk phenomenon, where the hydrogen atoms get absorbed into metal lattice to form metal hydride.
b) Adsorption based: It is surface phenomenon, where the hydrogen atoms are trapped in the pores, surfaces and cracks of the adsorbent materials.

Fig. 1.7 presents the details of different solid-state hydrogen storage techniques. However, as the present thesis mainly focuses on the absorption based solid state hydrogen storage systems and purification and hence, the discussion will be limited to absorption based hydrogen storage materials and its interaction with hydrogen.

1.4.1 Intermetallic Alloys

In order to use the metals as reversible hydrides, it is required to combine a strong hydride forming elements **A** with a weak hydriding element **B** to form alloys (especially intermetallic compounds)

to get the desired thermodynamic properties. Due to exothermic/endothermic reaction during hydriding/dehydriding process, it has an added advantage of serving several thermal applications (M. Lototskyy et al., 2015), like cooling system (Muthukumar et al., 2016; Satheesh et al., 2009), heat pump (Muthukumar and Satheesh, 2013; Satheesh and Muthukumar, 2010), heat transformer (Satya Sekhar and Muthukumar, 2013), hydrogen compressors (Muthukumar et al., 2012a, 2005), etc. (Lynch, 1991).

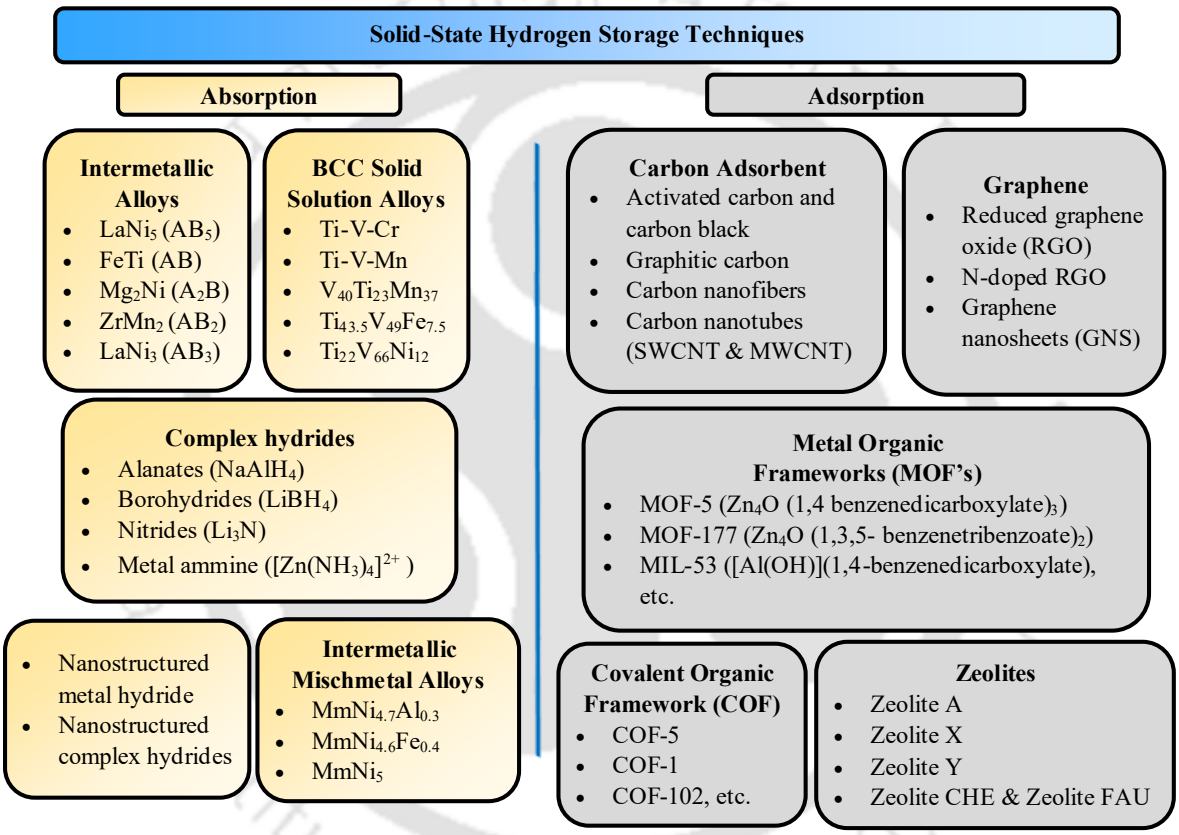

Fig. 1.7 Solid state hydrogen storage techniques

1.5 Thermodynamics of MH Formation

Metal hydrides are reversible chemical compounds formed when metal reacts with hydrogen at certain temperature and pressure called absorption process, which is an exothermic reaction generating enormous amount of heat. Similarly, when heat is imparted to the metal hydride at certain temperature, the hydrogen gets liberated from the metal lattice by an endothermic reaction

called desorption process. The Pressure - Composition - Isotherm (PCI) relates the hydriding and dehydriding reaction of bed with the equilibrium bed pressure, bed temperature and hydrogen concentration. The actual PCI characteristics and van't Hoff plot for the single-plateau metal hydride alloys is shown in **Fig. 1.8**. The PCI consists of three distinct phases which are α - phase, (α+β) - phase and β - phase. The α - phase is the solid solution phase in which initial concentration of hydrogen dissociate into individual atoms and diffuse into the metal lattice and is represented by a steep increase in pressure at constant temperature. Similarly, upon reaching final concentration, all metal atoms form chemical bonds with hydrogen leading to β – phase and completes formation of metal hydride. Any further addition of hydrogen causes a steep increase in pressure as it remains in gaseous state. In the intermediate transition region, named as (α + β) – phase, the conversion of α to β phase occurs gradually with increase in concentration at constant temperature and equilibrium pressure, ideally denoted by a flat plateau.

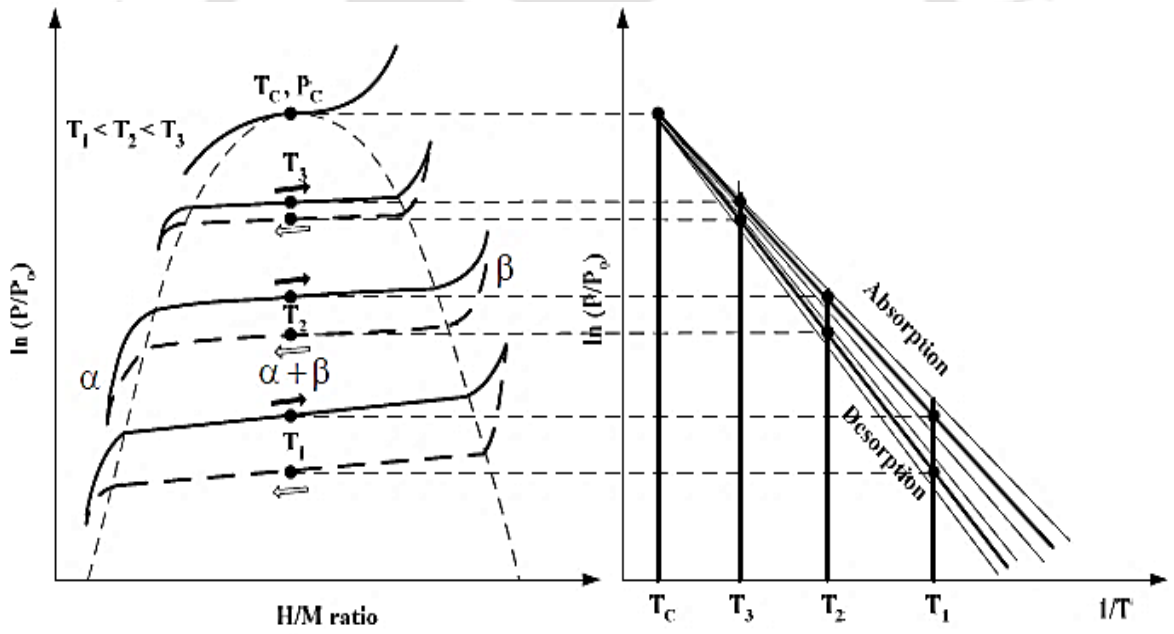

Fig. 1.8 Schematic representation of PCI characteristics and van't Hoff plot for some MH.

However, in actual case this transition region has a slight slope causing an increase in pressure. Enhancement of this region is the primary focus of research for all the MH based applications as it ensures transfer of hydrogen at near constant operating conditions. The length of this region represents the amount of hydrogen that can be stored reversibly with small pressure variation.

Hence, the MH with wide plateau region at requisite operating condition is advantageous. Beyond critical temperature T_c, plateau region disappears and α – phase converts into β – phase directly. From the van't Hoff plot, negative slope and the intercept denotes the enthalpy (ΔH) and entropy (ΔS) of reaction, respectively.

The absorption and the desorption processes of metal hydrides can be represented by the following equations:

General equation,

$$Metal + H_2 \leftrightarrow Metal\,hydride + Heat \tag{1.1}$$

In chemical reaction form,

$$M + \frac{x}{2} H_2 \rightarrow MH_x \quad (\alpha - phase) \tag{1.2}$$

$$MH_x + \frac{y-x}{2} H_2 \rightarrow MH_y \quad (\beta - phase) \tag{1.3}$$

Because of interaction of hydrogen atom with different intermetallic alloys of different crystalline structure, their physical and chemical properties vary. This variation in the properties of intermetallic alloys results in the wide range of structure, variation in reaction kinetics and hydrogen storage capacity (Ao et al., 2013; Chen and Zhu, 2008; Crivello et al., 2016; Mohammedi et al., 2015; Principi et al., 2009). The sequence of steps involved in hydriding and dehydriding processes are given by (Martin et al., 1996). The five steps of absorption process in sequence are as follows:

i. Physisorption of hydrogen molecules on the metal surface
ii. Dissociation of hydrogen molecules
iii. Penetration of hydrogen atoms from the surface into the bulk of the metal
iv. Diffusion of hydrogen atoms through the hydride layer, involving interstitial and/or vacancy mechanism
v. Hydride formation at metal hydride interface by nucleation and growth.

1.6 Scope of Metal Hydride based Hydrogen Storage System (MHHSS)

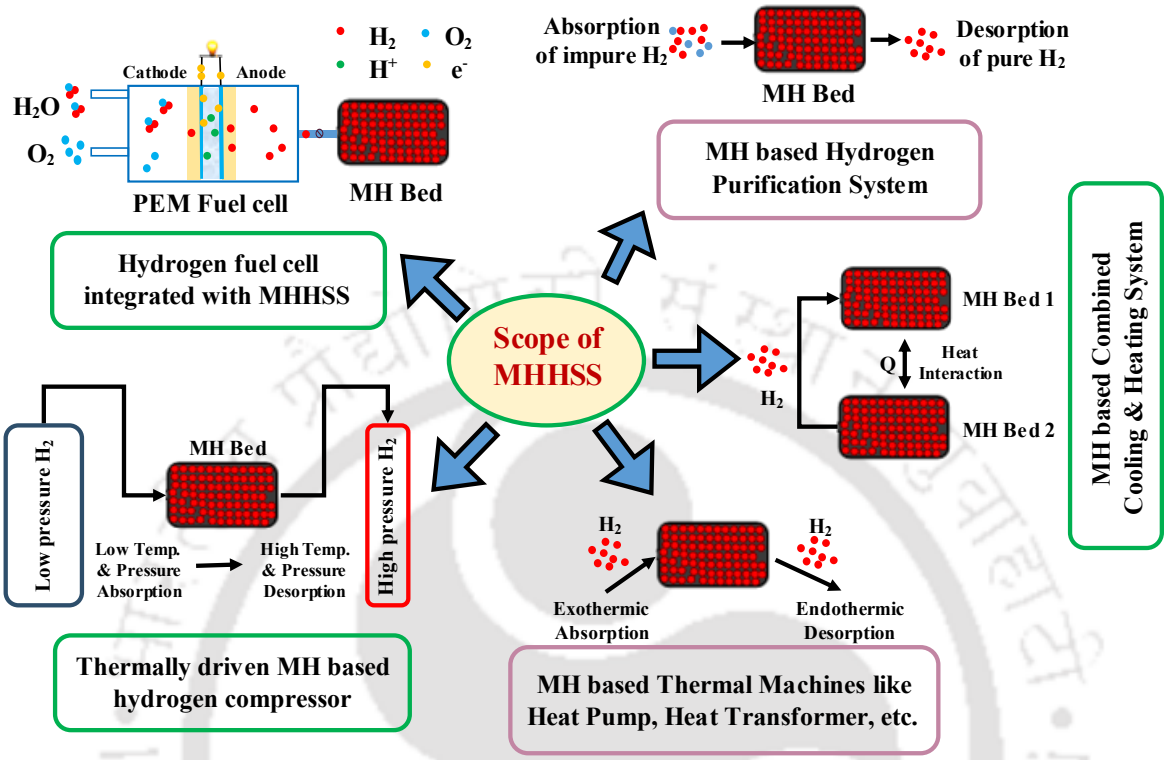

Fig. 1.9 Different possible applications of MH-Hydrogen system

As discussed earlier, the exothermic/endothermic characteristics during absorption/desorption process in the metal hydride-hydrogen systems act as an added advantage of using such systems as a thermal machine (Muthukumar et al., 2018). As depicted in the **Fig. 1.9**, MH-hydrogen systems can be used in a wide range of applications, that too in the form of green and clean in operation. Some of these applications are discussed in this section.

1.6.1 Metal hydride based hydrogen purification system (MHHPS)

The intermetallic alloys have a strong affinity towards hydrogen. While interacting with the gaseous mixture (hydrogen with other gases) during absorption process, it absorbs only hydrogen and forms metal hydride, while the other gases remain in the void space. The absorption process in MHHPS is followed by flushing, wherein the unabsorbed gases present in void spaces are flushed out of the MH reactor to ensure the presence of pure hydrogen within the reactor. Further, the desorption process is carried at high temperature, in order to obtain pure hydrogen. Several successful MHHPS has been studied and implemented practically to separate hydrogen gas from

an impure gas mixture (Chen et al., 2014; Dunikov et al., 2012; Schweppe et al., 1997; Zhang et al., 2012).

The material selection for hydrogen purification application should be on the basis of the following alloy characteristics:

- The equilibrium pressure of alloy at ambient temperature should be a little less than atmospheric pressure i.e., 1 bar. This enables the alloy to absorb hydrogen at low temperature and pressure, and ensures negligible hydrogen loss during the flushing process. Moreover, it increases the net amount of hydrogen recovered.
- The equilibrium pressure of alloy at higher temperature (> 60 °C) should be more than 2 bar to ensures the reversibility of hydrogen absorbed during the absorption process and reduced hydrogen loss.

1.6.2 Metal hydride based hydrogen compressor (MHHC)

Whenever it comes to compressed hydrogen storage, compressing hydrogen to a higher pressure is always a key challenge. The conventional mechanical compressors used in such an application consume a lot of high grade energy input in the form of electricity. Even the working of mechanical compressors involves several moving machine parts, that gets wear and tear over a period of time, which finally adds to the maintenance cost of the system.

MHHC is a thermally driven machine that does not consist of any internal moving parts, ensuring its maintenance-free performance. Moreover, it requires waste/solar heat input (anything above 70 °C, depending upon alloy), which cuts off the electrical requirement for running the system and makes its operational cost negligible (Muthukumar et al., 2012a, 2005; Odysseos et al., 2013). The material selection for MHHC should be on the basis of the following alloy characteristics:

- The alloy should be capable of absorbing hydrogen at low temperature (near ambient) and low pressure (5-10 bar), or the MH alloy can be selected according to the delivery pressure of hydrogen from its production unit.
- The desorption temperature should be selected according to the availability of waste heat temperature or on the basis of required delivery pressure. However, for higher delivery pressure, multi-stage compression is suggested wherein two or more different MH reactors are arranged in series, according to their PCT characteristics.

1.6.3 Metal hydride based Cooling and Heating System (MHCHS)

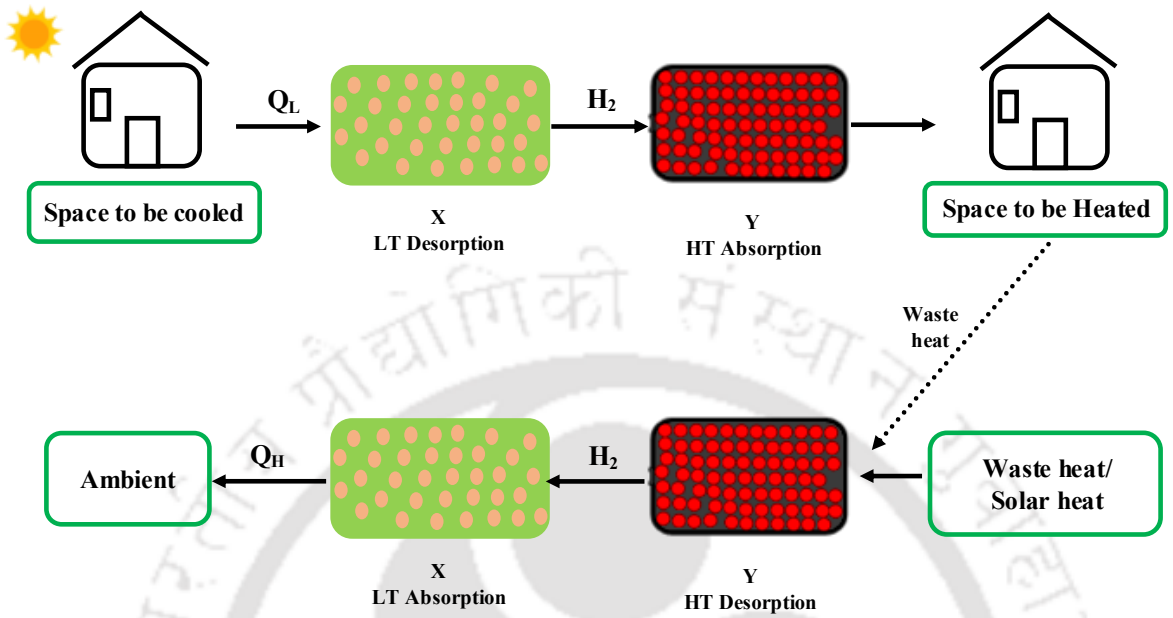

Fig. 1.10 Binary MH reactor coupled to produce heating/cooling effect

The exothermic/endothermic characteristics, during the absorption/desorption process in the MH bed, enables MH-hydrogen system to provide additional cooling/heating effect during hydrogen storage/extraction. A simple working of coupled low and high temperature reactor, to produce heating and cooling effect is depicted in the **Fig. 1.10**. Two reactors X and Y respectively filled with low temperature (LT) and high temperature (HT) intermetallic alloy with two operating pressure i.e. low pressure (LP) and high pressure (HP) are coupled. Initially, both X and Y reactors are kept at ambient temperature, wherein reactor X is in fully absorbed state. By using heat Q_L (from space to be cooled), reactor X desorbs and discharges hydrogen to the reactor Y at high pressure, which facilitates reactor Y to absorb the hydrogen. As absorption is exothermic in nature, the reactor Y produces heating effect during absorption process. The same phenomenon is observed in the reverse half cycle.

1.6.4 Metal hydride reactor coupled with hydrogen fuel cell (MHHFC)

Hydrogen fuel cell is an excellent alternative for producing power using hydrogen and oxygen without affecting the environment. MH reactor coupled with fuel cell provides pure hydrogen at a constant rate to the fuel cell stacks for continuous power generation. Moreover, the endothermic

characteristics of the desorbing MH reactor act as an additional advantage of removing excess heat of the fuel cell stack, which ensures efficient working of the fuel cell.

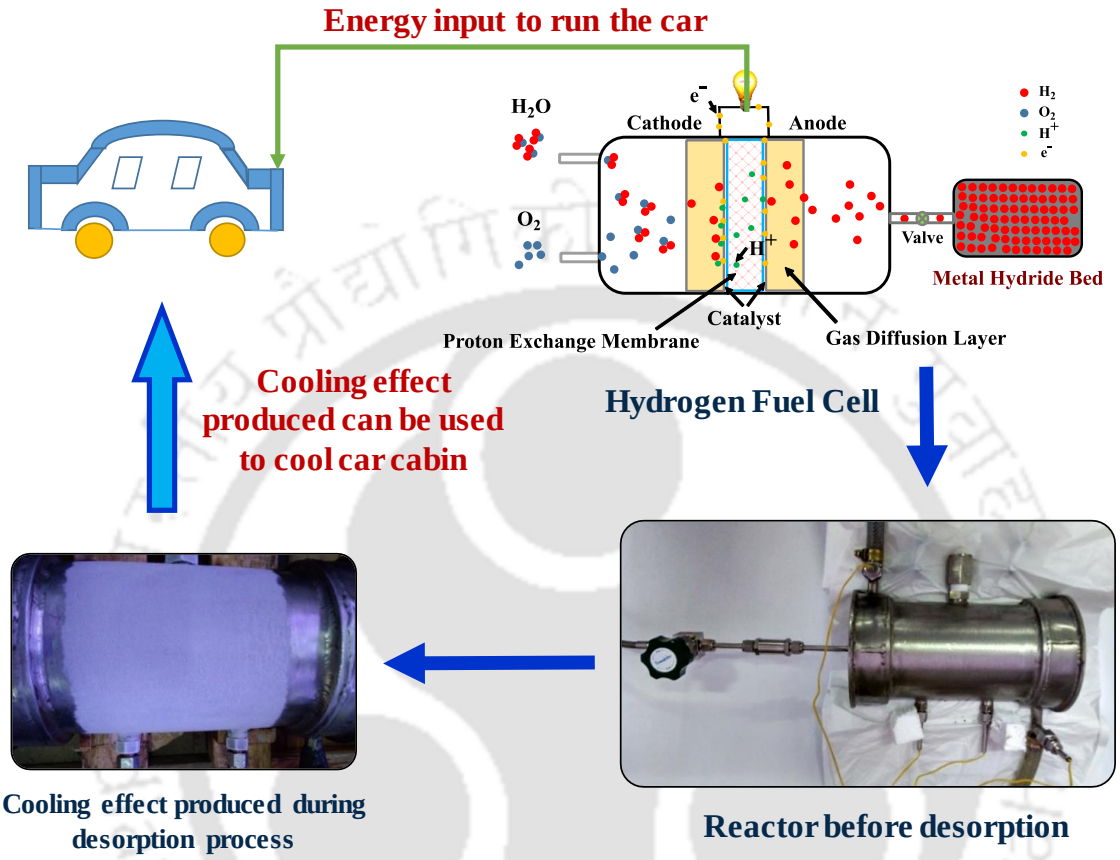

Fig. 1.11 Schematic of MHHFC for automobile application

The MH-fuel cell technologies can also be used for automobile application, wherein the fuel cell helps to power the automobile by extracting hydrogen for the MH reactor. Simultaneously, the cooling effect produced in the MH reactor can be utilized to cool the cabin space of the automobile (Davids et al., 2019; M. V. Lototskyy et al., 2015a). The schematic of MHHFC for automobile application is depicted in **Fig. 1.11,** wherein, MH reactor supplies hydrogen to power a fuel-cell operated car and simultaneously produce cooling effect due to endothermic desorption, which can be used to cool cabin space.

1.6.5 Metal hydride based thermal energy storage system (MHTESS)

Another appealing concept is to utilize a metal hydride-hydrogen system in thermochemical energy storage applications, considering its wide range of operating temperatures, high energy

density, exergetic efficiency, and environmentally friendly nature. Two MH beds are coupled to each other in this process, wherein the high temperature metal hydride (HTMH) bed desorbs hydrogen to the low temperature metal hydride (LTMH) bed by absorbing thermal energy from the external source (solar/waste heat). This process is called charging. When thermal energy needs to be released from HTMH bed, hydrogen from LTMH bed is supplied to the HTMH bed. Since, absorption is exothermic in nature, thermal energy stored in HTMH can be utilized. This process is called discharging. The charging/discharging processes of the coupled-reactor systems are controlled thermally by controlling the pressure using heat input in the reactors (Sunku Prasad et al., 2019).

1.7 Types of Metal Hydrides

In order to use the metals as reversible hydrides, it is required to combine a strong hydride forming elements **A** with a weak hydriding elements **B** to form alloys (especially intermetallic compounds) to get the desired thermodynamic properties. According to the study carried out by Sandrock [6], the following different types of intermetallic compounds are developed in the past few decades.

1.7.1 Titanium based hydrides (AB type)

Among all hydride forming alloys, titanium based alloys are the most attractive to scientific community due to their low molecular weight and high hydrogen storage capacity (up to 1.9 wt.%) (Ćirić et al., 2012). On reaction with hydrogen, Ti forms monohydrides and dihydrides, which exhibits BCC structure and shows two plateaus indicating formation of two (mono and di) distinct hydrides at room temperature. Normally, the desorption temperature of titanium hydrides is well above 600 °C, which can be brought down near to ambient conditions by alloying titanium with transition group elements, like Fe, Co, Cr, Ni, V, etc. According to Sastri et al., (1998), out of all transition elements Ti-Fe alloy is most suitable for hydrogen storage applications, but the activation of Ti-Fe alloy is always challenging, as it requires high temperature and Ti is highly sensitive towards gaseous impurities like oxygen.

1.7.2 Zirconium based hydrides (AB_2 type)

AB_2 alloys are mainly Zirconium (Zr) and Titanium (Ti) based alloys, where Zr/Ti (A) forms alloys with transition metals (B) like Mn, V, Cr, Fe, Co, etc. According to Sandrock, (1999), AB_2 alloys are known as potential material for hydrogen storage because of their ease in activation,

large hydrogen storage capacity and fast reaction kinetics. Shaltiel et al., (1977) studied the hydrogenation characteristics of various Zirconium-based alloys such as ZrV_2, $ZrCr_2$, $ZrMn_2$, $ZrFe_2$, and $ZrCo_2$. Most of these alloys could absorb large quantities of hydrogen but plateau pressures at room temperature of these compounds are very low (like 0.007 bar at 50 ºC for $ZrMn_2$) inhibiting them from using in practical applications. Moreover, because of the presence of transition metals in AB_2 alloys, it gets contaminated very easily with the impurity present in the hydrogen (Principi et al., 2009). However, AB_2 type (laves phase) alloys are mainly composed of rare earth metals and nonmagnetic metals, which are simpler compounds with lesser contamination tendency as compared to the transition metals (Lu et al., 2001).

1.7.3 Magnesium based hydrides (A_2B type)

Generally, A_2B alloys are the combination of alkali earth metal (A) and transition metal (B) (Kabutomori and Ohnishi), for example, Mg_2Ni is the most commonly known A_2B alloy. Though pure Mg has an outstanding hydrogen storage capacity (~7.6 wt.%), but still, it's very high desorption temperature due to very strong and stable bonding between Mg-H atoms in MgH_2, limits its scope in several practical applications (J. Li et al., 2018; Mohtadi and Orimo, 2016; Shao et al., 2012). However, its stability can be diluted by alloying it with different metals like, transition metals (Co, Ni, Cu, Fe, Sc, Y, Ag), rare earth metals (La, Ce) and non-transition metals (Al, Li, etc.), to make it suitable for practical applications (Bogdanović and Spliethoff, 1987; Floriano et al., 2016; Zhou et al., 2019). The two most common and reversible Mg based A_2B type hydrogen storage alloys are Mg_2Ni and Mg_2Fe. Mg_2Ni has very high hydrogen storage capacity (~3.6 wt.%) but the major problem with such alloy is its high desorption temperature. Mg_2Ni reacts with hydrogen to form Mg_2NiH_4 at 300 °C and 2 MPa (Han et al., 2001; Zhu et al., 2011). The reaction kinetics of Mg_2Ni MH is further tailored through partial replacement of Ni or Mg with metals like Cu, Pd, Zn, Mn, Cr and rare earth metals (Zhu et al., 2013).

1.7.4 AB_3/A_2B_7 type of metal hydride

The most promising characteristics of AB_3 and A_2B_7 (similar structure as AB_3) alloys that attracts scientific community are its easy activation with good hydrogenation/dehydrogenation properties under moderate temperature & pressure, and low cost with reasonably large hydrogen storage capacities (Yan et al., 2017). AB_3 alloys have several applications like used as negative electrode in Ni-MH batteries, hydrogen storage for fuel cell and several other applications (Liu et al., 2016).

AB_3 alloys exhibits faster reaction kinetics in most of the cases if the heat transfer dominates the response time of AB_3 alloy particles. But still, the alloy substitution in both A and B elements of such alloys, greatly influences their combined heat & mass transfer characteristics, hysteresis, plateau slope and hydrogen storage capacity (Chen et al., 2000).

1.7.5 Rare earth based hydrides (AB_5 based)

AB_5 alloys are mostly composed of rare earth metals (La, Pr, Ce, Nd, Er, etc.) and d-block metals (Ni, Mn, Fe, Mo, Co etc) (Young and Nei, 2013). On interaction with hydrogen, AB_5 alloys forms AB_5H_6 metal hydride with $CaCu_5$ structure (hexagonal), having better cyclic stabilities, high reversibility, low equilibrium pressure, fast absorption/desorption kinetics, resistance to impurities and low hysteresis. However, due to the limitations of hexagonal $CaCu_5$ structure, the hydrogen storage capacity of such alloys are lower (well within 1.5 wt.%) as compared to other intermetallic alloys like, AB_2, AB_3, Mg based alloys, etc (Pan et al., 2003). $LaNi_5$ is the most commonly used AB_5 alloy which gravimetric hydrogen storage capacity is 1.49 wt.% with desorption plateau pressure of 1.8 bar at 25°C with almost flat plateau slope (Van Mal et al., 1974). Because of its reversibility at room temperature and pressure, $LaNi_5$ alloys is used in wide range of engineering applications like heat pump, heat transformers, fuel cell, refrigerator, etc. However, to achieve desired absorption/desorption conditions for a particular application, La and Ni in $LaNi_5$ are partially substituted with several elements like Pr, Ce, Gd, Sm, etc. for partial La substitution and Fe, Al, Cu, Mn, Co, etc. for partial Ni substitution (Mi et al., 2019; Souza and Ticianelli, 2003; Van Mal et al., 1974). In past four decades, hybridization of material properties for AB_5 alloys by substitution techniques in order to modify its absorption/desorption characteristics for particular engineering applications have been a prime interest for the researchers of hydrogen community.

1.7.6 Mischmetal based hydrides

Even though $LaNi_5$ based alloys possess favorable hydrogen storage characteristics, La based alloy is very expensive. One possible method of avoiding the high price of lanthanum is to replace it with mischmetal (Mm) which is much cheaper than Lanthanum. Mischmetal is a mixture of rare earth metals (La-32 to 35 wt%, Ce-48 to 50 wt%, Nd-13 to 14 wt%, Pr- 4 to5 wt% and other rare earth metals 1.5 wt%) obtained directly by the reduction of oxide ore (Sastri et al., 1998). However,

the composition of these elements varies from batch to batch. Therefore, the equilibrium pressure may vary from one sample to another.

1.7.7 BCC solid solution alloys

Solid solution alloys formed by dissolving one or more hydrogen absorbing metallic elements, in which one act as a primary element (solvent) and all other act as minor element (solute). Unlike the intermetallic compounds, solid solution alloys need not be in stoichiometric composition and can dissolve solute in random stoichiometry within a solvent (Sandrock G (Sandrock, 1999) and Broom D (Broom, 2011); thermodynamic data is given by Fukai Y (Fukai, 2005)). BCC solid solution alloys have better hydrogen storage capacity than AB_5 intermetallic compounds. They have low working temperature and pressure than magnesium hydrides. BCC structure has more voids for hydrogenation as compared with FCC structure, providing more space for hydrogen. The well-known BCC solid solutions are Ti-V-Cr and Ti-V-Mn systems. BCC solid solution attracted more attention in 1998 when Iba and Akiba (Akiba and Iba, 1998; Iba and Akiba, 1997) introduced the Laves phases related Ti-V BCC solid solutions which can have reversible hydrogen capacity near to 2.4 wt.%. The hydrogen capacity of BCC solid solutions can reach nearly twice the gravimetric hydrogen capacity of AB_5 intermetallics.

1.8 Summary and Organization of Thesis

Considering the growing energy demand and global warming issues, the world is shifting towards renewable energy sources, which are clean and eco-friendly in nature. Hydrogen as an excellent energy carrier, fuel and eco-friendly nature becomes first priority as a prominent replacement of all conventional energy sources. However, its storage is always a challenging task, but the rigorous research in the field of metal hydride – hydrogen technology, has brought it forward as one of the efficient technology to satisfy the future energy demand. As hydrogen can be produced from renewable energy sources like solar, wind, etc., coupling of MH-hydrogen system with wind/solar/hydro energy can cope up to serve the growing world energy demand and can help in controlling the rise in global warming. The increase in utility of such systems will bring down the initial cost of the system. These systems can be installed from small to larger scale, that will help to fulfil localized energy demand, which will finally lead to energy sustainability. Hence, such systems can be the efficient future energy support for the global community. Moreover, the

exothermic/endothermic characteristics of the MH-hydrogen systems during absorption/desorption process spread its applicability to a wide range such as hydrogen compression, cooling, heating, hydrogen purification, thermal energy storage, heat pump, heat transformer, fuel cell, etc. One of the most prominent characteristics of metal hydrides is its alloy tailoring feature. A wide range of MH alloys can be synthesized according to the desired PCT characteristics targeting suitable applications. To design and implement such MH based thermal machines, prior thermodynamic analysis is needed, which has been briefed. This thesis is organised in 7 chapters, and a brief description of each chapters are discussed below:

Chapter 1 starts with a brief description on the present energy scenario and importance of hydrogen energy economy in fighting global warming issues. It briefs different hydrogen storage techniques, their advantages and disadvantages. A brief description on MH based hydrogen storage systems and its related engineering applications like heating and cooling, thermal energy storage, hydrogen purification, hydrogen compression, etc., has been included in this chapter. It also repots thermodynamic of MH formation and briefs different category of MH alloys available for hydrogen storage.

Chapter 2 is focused on state of art of literatures related to metal hydrides and its engineering applications, mainly hydrogen storage and purification. The chapter presents the basic requirement of alloy selection for a particular application such as hydrogen purification. The discussion on importance of reactor design for enhanced heat and mass transfer characteristics of MH bed have been focused. The chapter summarises almost all studies in the literature related to hydrogen purification using MHHPS. At end of the chapter, literature closure and objectives of the present work is briefed.

Chapter 3 is dedicated to the design and fabrication of reactor for hydrogen storage and purification application. The results and discussion on the outcome from the COMSOL based numeric models for optimised reactor design is discussed. The details of the reactor configuration, and fabrication of small and large scale reactors are discussed in this chapter. The finalization of hydrogen purification alloys for the present study is also part of this chapter.

Chapter 4 is focused on the details of experimental setup developed for the hydrogen purification studies. Description of methods for TCD analysis using gas chromatography is also part of this

chapter. Complete description on experimental details of sample preparation, hydrogen purification in single and multistage hydrogen purification system is included in this chapter.

Chapter 5 is dedicated on reactor activation and parametric studies on the reactors for hydrogen purification. The parametric studies on large scale reactor (99 ECT with 40 kg alloy) and small scale reactor (6 ECT with 1.2 kg alloy) for obtaining optimum operating conditions for hydrogen purification is presented in this chapter.

Chapter 6 is dedicated to experimental studies on single and multistage metal hydride based purification systems. In this chapter results and discussion in the effect of different gaseous impurities on the MHHPS is reported. The regeneration of MH reactors after poisoning is discussed in details with different impurities. The cyclic study and purification characteristics of single and multistage hydrogen purification is also depicted in this chapter. The TCD analysis of the gas samples of absorption, desorption and flushing is depicted in this chapter.

Chapter 7 summarises the conclusions obtained from the different studies conducted as per objectives of the present thesis. It also reports the limitations and future scope of MHHPS.

CHAPTER 2 STATE OF ART

2.1 Introduction

As discussed in the previous chapter, the world energy economy is shifting towards the hydrogen energy economy, which mainly comprise of four stages, i.e. hydrogen production (López Ortiz et al., 2016), hydrogen storage and packaging (Schlapbach and Züttel, 2001), distribution and end user utilization acknowledging safety concerns (Ogden, 1999). As hydrogen is one of the most abundant element present in the nature, it can be obtained through several well established extraction processes, such as through decomposition of fossil fuels, electrolysis of water, thermolysis of water, biomass conversion, forming, gasification, dark fermentation, PV electrolysis, bio photolysis, etc (Dincer and Acar, 2014; Gao et al., 2018; Nahar et al., 2017; Sengodan et al., 2018).

Hydrogen is utilised in different applications/devices such as hydrogen fuel cell, food and chemical industries, automobile industries, weather balloon, synthesis of chemical compounds, space sector, etc (Belz, 2016; El-Eskandarany et al., 2020; Kadier et al., 2016; Köhler et al., 2010; Petrecca and Decarli, 2008). In most of the applications, there is a requirement of highly pure grade hydrogen. For example, the performance of generators in the thermal power plants are directly affected by the purity level of hydrogen (Allen B. Wright, Tucson, AZ (US); Eddy J. Peters, Tucson, 2002). However, hydrogen obtained through most of the hydrogen producing techniques are not 100% pure (Grashoff et al., 1983). Hence, it becomes essential to purify hydrogen for end user application. Several well stablished hydrogen purification techniques used to purify/separate hydrogen from gas mixtures of different impurities level are membrane diffusion, pressure swing adsorption, cryogenic separation, catalytic purification, metal hydride baseD purification, etc., (Bhuiya et al., 2015; Chen et al., 2014; Grashoff et al., 1983; Ngene et al., 2017). In comparison to different purification techniques, metal hydride based hydrogen purification technique is the simplest technique to purify hydrogen through thermally driven steps, as shown in **Fig. 2.1**, wherein, the purification process is accomplished in three simple steps, i.e. absorption, flushing and desorption (Muthukumar et al., 2018). During absorption, impure gas mixture is supplied to the metal hydride (MH) bed which is maintained at low temperature through regular circulation of heat transfer fluid (HTF) through the HTF line in the bed, and because of high affinity of MH alloy towards hydrogen, it absorbs hydrogen and the other gaseous impurities remains in the void space.

Absorption is followed by flushing, wherein, the bed is maintained at low temperature and the impure gases in the void space is released to the atmosphere. In the last stage i.e. desorption, the temperature of MH bed is raised up to the desorption temperature through circulation of high temperature HTF, and pure hydrogen is obtained as an end product.

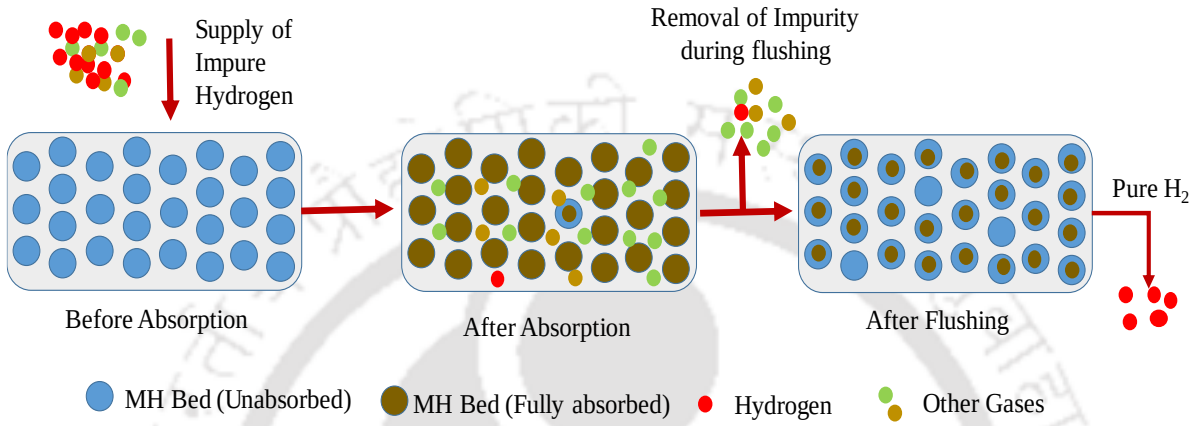

Fig. 2.1 Schematic of metal hydride based hydrogen purification system (MHHPS)

Considering the importance and future prospective of the MHHPS and their application in various sectors, the global status of such systems is reported in the present chapter. The chapter is drafted in a way that, it will help scientific community to get an overview of future scope in this field and attract hydrogen community to carry out exhaustive research to cope up the challenges related to MHHPS.

2.2 MH Alloy Selection

Selection of MH alloy plays a significant role in executing the targeted application successfully and efficiently (Sun et al., 1992). Alloy tailoring is one of the significant characteristics of MH alloy, because of which a wide verity and class of alloys have been explored targeting several thermal applications (Mohtadi and Orimo, 2016; Muthukumar et al., 2018). Some of the alloys like MgH_2, complex metal hydrides, etc., have very high hydrogen storage capacity (~7.5 wt%), but due to their high stability and high desorption temperatures, these are not suitable for MHHPS (Ngene et al., 2017; Xie et al., 2020). However, some metal hydride from AB_5, A_2B and AB_2 type are suitable for hydrogen purification application. Depending on the PCT characteristics of the

alloys, suitable alloy for hydrogen purification application should have following thermos-physical properties (Payá et al., 2009):

- Low absorption temperature and pressure (near ambient)
- Flat plateau
- High hydrogen storage capacity
- Fast reaction kinetics
- Hysteresis
- Anti-poisoning characteristics
- Easy availability and low cost

The state of a MH-hydrogen system is determined using van't Hoff equations given by (Nishizaki et al., 1983a). The equation relates equilibrium pressure of bed (P_{eq}) to the bed temperature (T), reaction enthalpy (ΔH) and formation entropy (ΔS), where 'c' represents hydrogen concentration at any given time 't' and 'c_{fin}' is final concentration, 'P_0' is the reference pressure i.e. ambient pressure in most case and 'φ_s', 'φ_o' and 'β' are plateau slope factor, slope constant and hysteresis factor, respectively.

$$\frac{P_{eq}}{p_o} = exp\left[\frac{\Delta S}{R_u} - \frac{\Delta H}{R_u T} + (\varphi_s \pm \varphi_o) \times tan\left(\pi\left(\frac{c}{c_{fin}} - \frac{1}{2}\right)\right) \pm \frac{\beta}{2}\right] \quad 2.1$$

(Voskuilen et al., 2014) reported a comprehensive approach for MH alloy selection targeting different thermal applications of MH-hydrogen system. They developed a robust thermodynamic equilibrium model using 300 different hydrides from the literature. The thermodynamic model is presented based on different thermos-physical properties and their absorption/desorption reaction expression using MATLAB toolbox.

2.3 Heat and Mass Transfer Characteristics in the MH Bed

The MH reactors are designed on the principle of optimization of combined heat and mass transfer characteristics of the MH bed. The rate of hydrogen absorption/desorption to/from the MH bed is governed by the heat and mass transfer characteristics of the MH bed and its reaction kinetics. Faster reaction kinetics is one of the most important and essential attributes of MH alloys. The reaction kinetics of the hydride bed is strongly influenced by the rate at which the heat can be removed/supplied from/to the reaction bed. As the thermal conductivity of MH alloys is very less

and therefore, it becomes very essential to optimize bed thickness in such a manner, that it could facilitate effective transfer of excess heat from the bed, in order to boost its absorption/desorption kinetics (Kallweit and Hahne, 2019; Zhao et al., 2020). Metal hydride reactor is an engineered vessel with sufficient mechanistic strength, that allows the MH alloy to remain packed in the form of MH bed, and facilitate the hydrogen transfer to/from the MH bed and assists the smooth flow of HTF through the bed to accomplish hydriding/dehyriding process. The effective thermal conductivity of metal hydrides is affected by several factors such as phase of the metal hydride, properties of interstitial gases, alloy structure, inter granular contact, alloy doping, etc.

Ram Gopal and Srinivasa Murthy, (1993) reported that, for faster reaction kinetics, bed should be designed with small bed thickness, which promotes faster rate of heat transfer. The reaction kinetics near the convective boundary is rapid as the rate of heat transfer is high. Therefore, the reactor design plays a major role in the absorption/desorption performance of the MH reactors.

Jemni and Nasrallah, (1995a, 1995b) have established a 2-D mathematical model for predicting the heat and mass transfer characteristics within the hydride bed and they found that the increase in effective thermal conductivity of solid accelerates the reaction kinetics. Aldas et al., (2002) have observed that the formation of hydride is faster near the cooled boundary walls and slower in the core region of the bed. At any absorption temperature, absorption rate can be increased with supply pressure, as increase in the supply pressure will lead to increase in the pressure gradient between the equilibrium pressure of the MH bed and the supply pressure. This increase in the pressure gradient acts as driving force for the faster rate of absorption.

Askri et al., (2009) studied the reaction kinetics with different reactor designs of cylindrical tanks with fins for better heat transfer and observed that the optimization resulted in 80% improvement of the storage time over the un-optimized case. The high rates of heat transfer trigger the reaction kinetics and leads to reduction in hydrogen absorption and desorption cycle time. Flueckiger et al., (2010) characterized $Ti_{1.1}CrMn$ based MH based by conducting experiments at very high pressure i.e. 253 bar and 275 bar. They observed that the effective thermal conductivity of bed reduces because of smaller particle size associated with reactive conditions. It was also observed that at very high pressure, there was a significant increase in thermal conductivity, i.e. 0.3 to 0.7 W/mK for activated alloy. Smith and Fisher, (2012) studied the effect of particle shape, size and packing

on heat transfer in MH's. The study shows that with increase in bed density, the thermal conductivity of bed increases. Matsushita et al., (2014) also studied the effect of bed packing on thermal conductivity. This study shows that effective thermal conductivity of the MH bed is maximum for lower bed porosity and vise-versa.

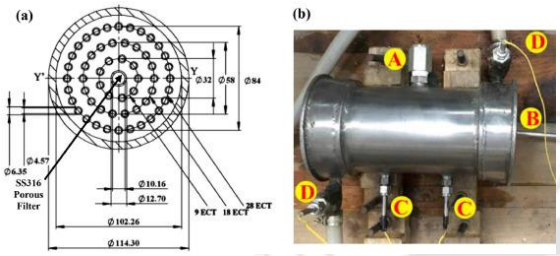

(Nithin Narmada Raju et al., 2019)

Reactor with ECT

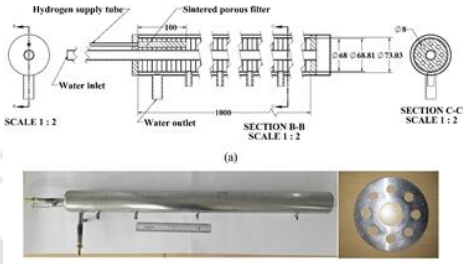

(Sunku prasad and Muthukumar, 2022)

Annular Reactor with Fin

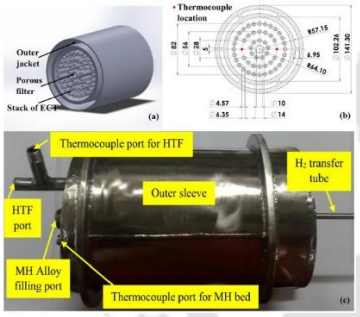

(Jana et al., 2022)

Reactor with ECT and OCJ

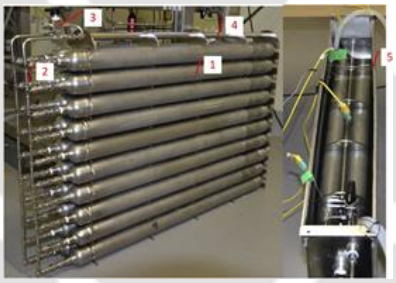

(Lototskyy et al., 2016)

Integrated Tubular Reactor

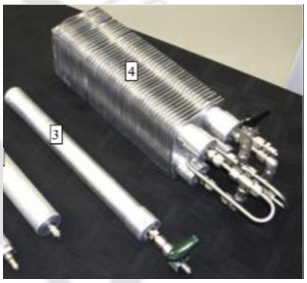

(M. V. Lototskyy et al., 2015b)

Tubular Reactor with Fin

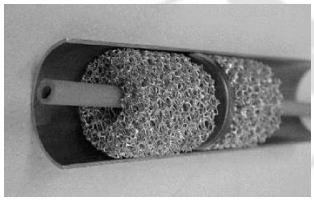

(Klein and Groll, 2002)

Reactor with Metal Foam

(Magnetto et al., 2006)

Ring Manifold Reactor

(Linder et al., 2010)

Capillary Tube Reactor

Fig. 2.2 Different reactor configuration studied by researchers

Anbarasu et al., (2014) have presented the reaction kinetics for different supply pressures (10-35 bar) and effective thermal conductivity of hydride bed (0.2-2.5 W/mK), and observed that either

by increasing supply pressure or effective thermal conductivity of the bed, the reaction kinetics of MH formation is accelerated.

A several systematic detailed reviews have been reported to cover different aspect of reactor design, such as reactor strength, hydrogen transfer, bed packing, etc (Yang et al., 2010). Similarly, Shafiee and McCay, (2016) and Afzal et al.,(2017) reported different reactor configuration and fin design, imparted to MH-hydrogen system for its efficient working. Some of the fabricated and tested reactor configurations are depicted in **Fig. 2.2**

2.4 Developmental Status of MHHPS

Metal hydrides are well known for their excellent absorption characteristics for hydrogen due to their admirable affinity towards hydrogen (Tarasov et al., 2020). Making use of this significant characteristics, a wide range of research has been carried out to study the hydrogen purification characteristics of metal hydride-hydrogen systems. Separation of hydrogen (using MH) from the raw gas mixture originating from different sources has been tested and reported by many researchers all around the world. The major findings in this field is reported in this section.

2.4.1 Effect of alloy tailoring and impurities on MHHPS

According to Chen et al., (2014), when intermetallic alloys are exposed to a mixture of gases, it absorbs only hydrogen and the other gases remains in the void space or interacts with the alloy surface to form resistive blanket for hydride formation. The continuous interaction of the impure gases deteriorates the reaction kinetics within the MH bed and decreases hydrogen storage capacity of the MH bed.

Au et al., (1996) in 1996, reported the use of metal hydride in recovering, storing, purifying and transporting hydrogen from an industrial purge gas of an ammonia plant. They used four reactor system, cumulatively filled with 1600 kg of $MlNi_{5-x}Al_x$ for storing, transporting and purifying 200 Nm^3 of hydrogen from a purged gas carrying 45-50 % of hydrogen along with NH_3, N_2, CH_4 and Ar as impurity contents. The purity level of hydrogen obtained was 99.999%, which took nearly 4 h to separate hydrogen from pre-treated purged gas. The hydrogen recovery was above 70%, with added advantage of saving power consumption up to 97%, which finally adds to nearly 60% reduction in hydrogen price.

Schweppe et al., (1997) reported poisoning effect of O_2, CO_2, H_2S, CO or N_2 gases in $LaNi_5$ system used for hydrogen storage application. They used Sieverts apparatus, which was attached with a diffusion pump, to perform experimental studies related to reactor activation, absorption and alloy poisoning. It was observed that, presence of N_2 in the void space of the reactor, does not affect the rate of hydrogen absorption at all, while for the other gases prefilled gases, the initial rate of reaction reduces by a factor of 2 to 10 times. However, O_2 critically damages the absorption characteristics of the alloy by forming an oxide layer on the surface of $LaNi_5$ alloy.

Oztek, (2005) tested Mg_2Ni, VTiNi and $LaNi_5$, as a separation platform to separate hydrogen and helium from a mixture of hydrogen and helium. Considering the reversible characteristics of $LaNi_5$ on interaction with the mixture, it was considered as suitable alloy for hydrogen separation. Lin et al., (2007) explored $LmNi_{4.8}Al_{0.2}$ alloy from AB_5 group of alloys, and studied its anti-poisoning characteristics for hydrogen storage application. The alloy was activated in the presence of pure hydrogen, and then they were exposed to CO and H_2S, each 1000 ppm as impurity with pure hydrogen. The poisoning effect of CO was more dominating as compared to H_2S. However, the poisoned alloy was regenerated/reactivated after one pure hydrogen absorption cycle at high pressure. Dunikov et al., (2012) reported the effect of nitrogen (N_2) impurity on the absorption kinetics of the MH bed, which constitutes of AB_5 alloy. They investigated four reactor system, wherein, two of each were filled with $Mm_{0.8}La_{0.2}Ni_{4.1}Fe_{0.8}Al_{0.1}$ and $LaFe_{0.1}Mn_{0.3}Ni_{4.8}$ alloys. Despite of non-poisoning characteristics of the N_2, even it's little (3.25%) presence as impurity in the hydrogen sample, reduces the absorption kinetics very significantly.

Wan et al., (2014) reported the effect of CO on the hydrogenation/dehydrogenation characteristics of $LaNi_{4.7}Al_{0.3}$ alloy. When fully activated sample were exposed to impure hydrogen with 300 ppm CO content at 30 °C, the bed was completely poisoned and was unable to absorb hydrogen further, after 3 absorption/desorption cycle. However, upon heating the MH bed to a temperature near 80 °C, it regained its absorption characteristics. Hanada et al., (2015) reported a comparative study to study the poisoning effect of CO_2 on different AB_5 alloys, i.e. $LaNi_5$, $LaCo_5$, $CaNi_5$ and $MmNi_{4.025}Co_{0.4}Mn_{0.275}Al_{0.3}$. According to their study, the magnitude of poisoning effect varies in the order $CaNi_5 < LaNi_5 << MmNi_{4.025}Co_{0.4}Mn_{0.275}Al_{0.3} < LaCo_5$. The results were obtained after comparing absorption characteristics of all four alloys exposed to CO_2 environment.

Hydrogen generation through biological process have been focused area of research in past few decades. However, the bio-hydrogen produced from biological processes are not pure and it always contain some by-product along with hydrogen. Use of metal hydrides for bio hydrogen storage and purification has been proven as an efficient technology in past two decades (Akhlaghi and Najafpour-Darzi, 2020; Kazakov et al., 2016; Singh and Wahid, 2015). However, depending upon the impurity content of the other gases in impure hydrogen sample, purification process may be accomplished in single or multiple purification stages.

Dunikov et al., (2016) used two stage MHHPS, wherein they used $La_{0.9}Ce_{0.1}Ni_5$ as low-pressure/first stage purification alloy and $LaNi_{4.8}Mn_{0.3}Fe_{0.1}$ as high pressure/second stage alloy. One kg of both the alloys were filled in two reactor system coupled together. Impurity content in the inlet sample were in the range of 40-60%, with an operating purification capacity of 110 st,L/h. The amount of hydrogen recovers was 94% and the pure hydrogen obtained was used to run a PEM fuel cell with maximum load of 200 W. Kazakov et al., (2020) used two alloy based MHHPS to separate hydrogen from biogas mixture with high CO_2 concentration. They used $LaNi_{4.4}Fe_{0.3}Al_{0.3}$ and $LaNi_{4.6}Mn_{0.2}Al_{0.2}$ alloys in their hydrogen purification study. The alloy showed reversible characteristics of 1.1 wt.%. However, even in single purification stage, hydrogen can be efficiently separated from even a lean hydrogen mixture sample, but in such cases, the bed poisoning is very frequent which leads to frequent bed regeneration. Dunikov and Blinov, (2020, 2019a, 2019b) reported hydrogen separation from a lean hydrogen-methane mixture wherein hydrogen content was only 5-15%. The used $LaNi_{4.8}Mn_{0.3}Fe_{0.1}$ alloy for hydrogen separation, wherein impure sample was injected at 9.5 bar. The hydrogen recovery was ~75%.

Zhang et al., (2012) studied the poisoning effect of O_2 and N_2 on $Zr_{0.9}Ti_{0.1}V_2$ hydrogen storage alloy as an alternative of AB_5 MH alloys, wherein AB_2 alloys were tested and reported as significant alloy for hydrogen storage and purification applications. Initially the annealed sample of $Zr_{0.9}Ti_{0.1}V_2$ was exposed to O_2 and N_2 for 30 s, 60 s and 180 s respectively at ambient temperature and further they were regenerated. It was observed that, hydrogen storage capacity of oxygen poisoned sample was nearly nil, however the nitrogen poisoned sample reobtains the hydrogen absorption capacity with a capacity of 2.85 H/A (hydrogen to alloy molar ratio). Moreover, the regeneration temperature of the O_2-poisoned alloy was nearly 100 K higher than normal activation temperature. They also used ion etching process to find the thickness of

passivated surface layer. It was observed that the O_2-poisoned sample had ~58 nm passivated surface layer, while the un-poisoned sample had ~36 nm.

Hanada et al., (2017) reported the effect of CO_2 impurity on the absorption kinetics of Ti-Zr-Mn-Cr based AB_2 alloy. They investigated $Ti_{0.515}Zr_{0.485}Cr_{0.8}$ and $Ti_{0.515}Zr_{0.485}Mn_{1.2}M_{0.1}$ (M=Ni, Co or Fe) alloy on the basis of their affinity towards hydrogen, before and after its exposure to CO_2. According to the study, $Ti_{0.515}Zr_{0.485}Mn_{1.2}Fe_{0.1}$ has highest tolerance towards CO_2 impurity followed by Co substitution, while the other Ni decreases the CO_2 poisoning tolerance of the alloy. The order of poisoning tolerance was AB_2-Ni < AB_2 < AB_2-Co < AB_2-Fe (AB_2= $Ti_{0.515}Zr_{0.485}Cr_{0.8}$).

2.4.2 Effect of additives and surface modification on MHHPS

Lototsky et al., (2011) studied surface modification of AB_5 type of MH alloy through electroless deposition of Pd in N_2H_4/NaH_2PO_2 based plating bath, to improve storage and purification performance. The absorption rate was improved around 100 times as compared to the conventional material. Highly efficient purification was observed for the modified alloy mass when tested using hydrogen mixture sample containing CO_2 and CO. The surface modification resulted in preventing the poisoning effect of the bed material and during desorption highly pure hydrogen was obtained.

Fleming et al., (2001) studied the effect of heat transfer on hydrogen separation process by conducting experiments using a helical shell and tube type heat exchanger, wherein Pd/k bed was used as separation medium. For improving the hydrogen separation rate, metallic foam was also introduced as bed component. Addition of metallic foam in the Pd/k bed optimized the cyclic time and hence enhanced the rate of pure hydrogen separation from the stream of mixture gases. Among different metal foams used in the experiment, copper metal foam showed better results.

Miura et al., (2013, 2012) reported that the integration of aluminum foam with metal alloy makes the system more effective for hydrogen purification, but the volumetric capacity of the hydride reactor reduces slightly. The investigation also says that, the presence of carbon monoxide in mixed gases causes adverse influence on MH purification system, for which CO selective adsorbent with MH intermediate buffer method has been taken into consideration.

Wang et al., (1995) studied the effect of fluorination treatment on $LaNi_{4.7}Al_{0.3}$ and found that pure hydrogen obtained after fluorination was 99.9999% pure. Along with poisoning properties, few

other properties are to be improved as well for effective purification and favourable life of MH bed. MH bed should be pulverization resistance and should have good thermal conductivity. Sohn and Emami, (2011) reported the dehydrogenation rate optimization of milled MH samples doped with TiH (TiH_2 in -MgH_2) and found around 107-118 kJ/mol drop in the activation energy of combined alloy. 99.9% pure hydrogen was delivered at rate of 1.6 g H_2/s for 80 kW fuel cell.

Modibane et al., (2013) reported the poisoning tolerance of MH alloy by surface modification of AB_5 type alloy. Effective surface modification was achieved by fluorination followed by electroless deposition of Pd. Desorption sample was 92-95% pure hydrogen. It was found that $Ta_{77}Nb_{23}$ is suitable for membrane formation because of its mechanical properties and production ease. Shaijumon et al., (2005) reported the effect of carbon nanotubes along with multiwall MH nanotubes on hydrogen purification. Reaction kinetics were improved by addition of carbon nanotubes. Highly pure hydrogen was delivered during the desorption process (Nearly 99.9 %). Some of the MH alloys, that can be suitable for hydrogen purification application is listed in **Table 2.1**.

Table 2.1 Some commonly used metal hydrides for H_2 purification and their properties (Dehouche et al., 2005; Huston and Sandrock, 1980; Sandrock, 1999; Sheppard et al., 2016)

Metal alloy	H_2 (wt %)	Plateau slope $\Delta \ln (P_{abs})/\Delta(H/M)$	Hysteresis $\ln(P_{abs}/P_{des})$	Minimum mass of alloy (kg) for 100 kg of H_2 storage	Equilibrium pressure of MH at 25 ^oC (bar)
$LaNi_{4.25}Al_{0.75}$	1.13	2.7	0.23	8849.56	0.024
Mg_2Ni	1.15	0.43	-	8695.65	-
$CaNi_5$	1.2	0.19	0.16	8303.79	0.5
$MmNi_{4.5}Al_{0.5}$	1.2	0.36	0.11	83333.33	3.8
$Fe_{0.8}Ni_{0.2}Ti$	1.21	0.36[a]	0.05	8264.46	0.91
$MmNi_{4.7}Al_{0.3}$	1.2152	0.4356	0.533	8229.1	3.45
$MmNi_{3.5}Co_{0.7}Al_{0.8}$	1.24	1.2	0.2	8064.52	0.11
$LaNi_{4.7}Al_{0.3}$	1.27	0.32	0.05	7874.02	0.44
$LaNi_{4.8}Sn_{0.2}$	1.2894	0.4469	0.2822	7755.54	0.46

$LmNi_{4.9}Sn_{0.1}$	1.2985	0.2594	0.4999	7701.19	1.33
$TiFe_{0.8}Ni_{0.2}$	1.3	0.36	0.05	7664.56	0.1
$MNi_{4.5}Al_{0.5}$	1.36	0.48	0.11	7352.94	4.25
$CaNi_5$	1.39	0.19	0.16	7194.24	0.55
$LaNi_{4.8}Sn_{0.2}$	1.4	0.22	0.19	7142.86	0.5
$LaNi_{4.7}Al_{0.3}$	1.4	0.48	0.05	6917.72	0.42
$ZrFe_{1.5}Cr_{0.5}$	1.5	1.26	0.34	6666.67	4.0
$LaNi_5$	1.5	0.13	0.13	6666.7	1.8
$Ca_{0.7}M_{0.3}Ni_5$	1.60	3.27	0.10	6250	4.2
FeTi	1.75	0.00[b]	0.64	5714.286	10.0
$ZrMn_2$	1.77	0.74	0.99	5649.72	0.001
$Fe_{0.9}Mn_{0.1}Ti$	1.79	0.65[c]	0.62	5586.59	8.7
TiFe	1.86	0	0.64	5376.34	4.1
$TiMn_{1.5}$	1.86	0.57	0.93	5376.34	8.4
$CaNi_5$ (M)	1.87	0.19	0.16	5347.59	0.5
$Ti_{0.98}Zr_{0.02}V_{0.43}$ $Fe_{0.09}Cr_{0.05}Mn_{1.5}$	1.9	1.1	-	5263.16	11
$TiFe_{0.9}Mn_{0.1}$	1.9	0.92	0.62	5263.67	2.6
$TiMn_{1.5}$	1.9	0.57	0.93	5354.43	8.4
$Ti_{0.98}Zr_{0.02}V_{0.48}$- $Fe_{0.09}Cr_{0.05}Mn_{1.5}$	1.9	1.1	-	5243.67	11
Mg	2.04	0.17[d]	-	4901.96	-
$TiMn_{1.4}V_{0.62}$	2.15	1.4	-	4651.16	3.6
$NaAlH_4$ Na_3AlH_6	3.7	Negligible	Negligible	2670.89	0.7
$(V_{0.9}Ti_{0.1})_{0.95}Fe_{0.05}$	3.7	0.45	0.8	2693.04	0.5
V	3.8	0.15	0.2-07	2613.92	2.1
Mg_2Cu	3.84	0.02[e]	-	2604.167	-
The measurement was obtained at [a]70 °C, [b]30 °C, [c]40 °C, [d]324 °C and [e]298 °C respectively.					

2.4.3 Patents on MHHPS

Peterson and Dimartino, (1987) patented a MH based hydrogen purification system, wherein the system comprises of Fe, Ti, Ni, Ca, Mn, Mg and rare earth based multiple reactor bed and was used in separation of pure hydrogen from mixture of gases composed of O_2, N_2, CO, CO_2, H_2O, and CH_4 in six stages. The product received at outlet of 4^{th} stage of purification process showed 97% concentration wise pure hydrogen. Carrea; and Warrick, (2000) developed a Ti-V-Fe-Zr based hydrogen purification system. The system was developed to remove the impurities like CO_2, N_2 and O_2 at temperature below 350 °C. After getter sage 99.9 % pure hydrogen was gained. Further purification level is improved to 99.999 % by cryogenic separation. Carrea and Warrick, (2001) tested the same system with Ti-V-Fe-Zr alloy for lower level of impurity (of order < 1ppb or less) but with moisture. In first stage of purification, around 10 ppb of methane was found in the mixture. In second methane was separated to achieve 99.999% purity level of H_2

Golben, (2003) developed Pt-Pd,-Ru based hydrogen purification, compression and storage system. Though the study does not disclose the exact configuration of the MH alloy used, but according to the reported results the used of novel metal in MH alloy prevented the poisoning of MH bed from steam, O_2, CO_2 and CO gases and improved the hydrogen purification and storage performance. The system purified hydrogen gas up to 99.99% and improves compressor efficiency. Golbe, (2010) developed a hydrogen purification system based on complex hydrides for fuel cell and hydrogen compression application. They used catalytic convertor in the beginning of the system to convert CO to CH_4 and then sent to the purification reactor. Because of using complex metal hydrides, the operating temperature of the system was high (~300 °C) and the reversibility of the purification bed was poor.

Tessier et al., (2018) developed a Mg based hydrogen purification system. The system was mainly used to separate hydrogen from a methane-hydrogen mixture. Due to use of Mg based metal hydride, the operating temperature of the system was very high (~350 °C).

Tough a clear state of art on MH-Hydrogen system and developed MHHPS is discussed in this chapter, still hydrogen community is involved in rigorous research to make these alloys more promising for commercial usage. The worldwide developmental status of intermetallic alloys and results on different compositions and doping is reported in Table 2.2.

Table 2.2 Developmental status of Metal Hydride-Hydrogen Systems

Citation **Institute/Organization** **Country/Place** **Year**	**Alloy Details** **Operating Conditions**	**Research Approach**	**Key findings**
Sunku prasad and Muthukumar, (2021) IIT Guwahati India 2021	$LaNi_5$ 9 kg T_{abs}: 15 °C to 30 °C P_{abs}: 10 bar to 30 bar T_{des}: 40 °C to 70 °C	• To study absorption/desorption characteristics of annular finned reactor under various conditions. • Comparison of annular reactor performance with other reactor configurations	• Significant improvement in the absorption and desorption performance (about 56% and 44% respectively for absorption and desorption) was observed as compared to the embedded cooling tube with outer cooling jacket reactor configuration. • A low HTF flow rate (2.5 lpm) is sufficient for smooth absorption/desorption.
Afzal et al., (2021) IIT Bombay India 2021	$La_{0.9}Ce_{0.1}Ni_5$ 47.5 kg T_{abs}: 25 °C to 40 °C T_{des}: 25 °C - 60 °C	• To study heat transfer enhancement characteristics of honeycomb based MH reactor configuration. • To check the feasibility of MH reactor for fuel cell application.	• Improvement in the hydrogenation characteristics was around 20% for each pressure rise of 5 bar. • The reactor can meet the hydrogen supply condition of a 2 kW fuel cell.
Karmakar et al., (2020) IIT Bombay India 2021	$LaNi_5$ 10 kg P_{abs}: 10-30 bar T_{abs}: 5 °C – 30 °C T_{des}: 50 °C - 80 °C HTF flow rate: 20 lpm	• To study effect of varying different parameters like absorption temperature, hydrogen supply pressure and desorption temperature on the absorption/desorption characteristics of MH reactor filled with 10 kg $LaNi_5$ alloy.	• Maximum reversible hydrogen storage capacity of 1.13 wt.% was obtained. • The alloy is capable of taking hydrogen even at low supply pressure i.e. 10 bar, however, with increase in hydrogen supply pressure, the reaction kinetics increases. • Suitable desorption temperature is above 70 °C.
Jenne et al., (2020) IIT Guwahati India 2020	$La_{0.9}Ce_{0.1}Ni_5$ Alloy mass: 1.4 kg T_{abs}: 10 – 20 °C T_{des}: 70 – 90 °C P_{abs}: 10-30 bar P_{des}: 1 bar HTF flow rate: 5 lpm	• To study hydriding / dehidriding characteristics of $La_{0.9}Ce_{0.1}Ni_5$ by varying bed temperature and hydrogen supply pressure at fixed HTF flow rate of 5 lpm. • To study cyclic performance of the MH bed for 50 cycles.	• The alloy requires high desorption temperature (preferably above 70 °C) for efficient desorption. • Increase in supply pressure significantly affects amount pf hydrogen absorbed. Nearly 45% increase in storage capacity was observed for pressure rise from 10 to 30 bar. • After 50 cycle, the absorption capacity of alloy dropped to 15.52 g from 19.1 g at 40 bar.

Chen et al., (2019) Harbin Institute of Technology China 2019	$Ti_{33}V_{37}Mn_{30-x}Ce_x$ (x = 0, 0.2, 0.4 & 0.6) T_{abs} = 293K & T_{des} = 423 K P_{abs} = 3 MPa & P_{des} = 0.1 MPa	• To study the effect of Ce substitution for Mn on hydrogenation/dehydrogenation properties of $Ti_{33}V_{37}Mn_{30}$ BCC solid solution alloy. • To study the change in structural morphology of the material. • To obtain composition with optimum reversible hydrogen storage capacity.	• The reversible hydrogen storage capacity reached 2.25 wt.% for $Ti_{33}V_{37}Mn_{29.4}Ce_{0.6}$. • The desorption capacity varied with temperature and observed to be 1.98, 2.02 and 2.25 wt% respectively for 363 K, 393 K and 423 K desorption temperatures. • On Ce substitution, there was increase in the abundance of BCC phase, while a decrease in C14 Laves phase was observed.
Dixit and Huot, (2019) University of Quebec at Trois-Rivieres Canada 2019	$Ti_xV_{70-x}Cr_{30}$ (x = 10, 20, 30, 40, 50) added with 4 wt.% of 7Zr+10Ni	• To study effect of Zr-Ni addition and varying Ti proportion on the reaction kinetics, crystal structure and morphology of the alloy.	• During hydrogenation, the crystal structure changes from BCC phase to FCC phase for x = 20, 30 & 40. • Hydrogen storage capacity increased with increase in the Ti content of the alloy. • For x = 50, maximum hydrogen absorption was observed i.e. 3.6 wt% and minimum of 1 wt.% for x =10.
Davids et al., (2019) University of Western Cape South Africa 2019	Ti based AB_2 Alloy (A=Ti+Zr; B= Fe+Mn+Cr+Ni+V) Alloy mass = 6 kg P_{abs} = 15-40 bar; P_{des} = 1 bar HTF flow rate: 2 m/s T_{des} = 15-25 °C	• To investigate performance of MHHSS for light fuel cell vehicular applications. • To study the effect of internal and external fins on hydrogen discharge rate.	• Hydrogen Charged = 80 g • For alloy loaded, specific power varied from 41.7 W/kg (250 W) to 166.7 W/kg (1000 W), with the discharge ratio dropping from 42.6% to 11%, respectively.
Balcerzak, (2019) Poznan University of Technology Poland 2019	$Ti_{0.5}V_{1.5-x}Mn_x$ (x = 0, 0.1, 0.2, 0.3) P_{abs}: 0.1 MPa to 60 MPa Tabs: 303 K	• The effect of Mn content on the hydrogenation properties of nano-crystalline Ti-V-Mn based alloys were investigated. • To observe the stability of BCC phase with higher Mn content.	• Initial hydrogen storage capacity of $Ti_{0.5}V_{1.4}Mn_{0.1}$ alloy was observed as 3.07 wt.% at room temperature which decreased further because of less cyclic stabile of alloy. • The chemical changes due to Mn content increased the reversibility of alloy, and $Ti_{0.5}V_{1.2}Mn_{0.3}$ was observed as most reversible alloy, though the hydrogen storage capacity was little less as compared to the other compositions.

Majid et al., (2019) Meiji University Japan 2019	Mg-graphite, Mg-$TiFe_{0.8}Mn_{0.2}$-Fe, Mg-$TiFe_{0.8}Mn_{0.2}$-graphite, Mg-Fe-graphite and Mg-$TiFe_{0.8}Mn_{0.2}$-Fegraphite T_{des}= 200 C P_{des} = 2.5-2.6 MPa	• To improve the hydrogen desorption properties of MgH_2, substitution of several composites with $TiFe_{0.8}Mn_{0.2}$, graphite, and Fe was investigated.	• Dehydrogenation peak temperatures was decreased to 90, 160 and 165 °C for Mg-$TiFe_{0.8}Mn_{0.2}$-graphite, Mg-Fe-graphite, and Mg-$TiFe_{0.8}Mn_{0.2}$-Fe-graphite composites, respectively.
Raju et al., (2019) IIT Guwahati India 2019	$LaNi_{4.7}Al_{0.3}$ 4 kg P_{abs}=5-20 bar, T_{abs}=20-40 °C, T_{des}=70-90 °C	• Parametric study was carried out to obtain optimum absorption and desorption condition • 55 Embedded cooling tube reactor of SS316 material was used for study	• Material was capable of absorbing hydrogen as even lower pressure. • Desorption was significant only at higher temperature range of 80-90 °C
.Zhang et al., (2019) Hangzhou Dianzi University, China 2019	La_2Mg_{17} 10 mg P_{abs}= 4 MPa & P_{des}=0.1 MPa	• Effect of surface doping using magnetron sputtering of La_2Mg_{17} alloy using yttrium-based coating on hydrogen storage properties was studied. • The surface condition of doped alloy during absorption/desorption process was also carried out using SEM, XRD and XPS analysis.	• Maximum hydrogen storage capacity of 4.1 wt.% was achieved. • For reversible cycle, suitable desorption condition was observed as 0.1 MPa desorption pressure and 673 K desorption temperature.
Shang et al., (2019) Central Iron and Steel Research Institute, Beijing, China 2019	TiFe $Ti_{1.1}Fe_{0.8}Mn_{0.2}$ 1 g Cylindrical Reactor Temperature range: 313-353K P_{abs}= 3 MPa	• Effect of adding over-stoichiometrical Ti with TiFe and partially substituting Fe with Mn on hydrogen storage performance.	• Due to partial substitution of Fe with Mn, average grain size decreases (from 26.0 nm to 16.5 nm), which increases overall reaction kinetics and hydrogen storage capacity. • A slight lift in the dehydrogenation enthalpy was also observed i.e. 13.36 kJ/mol H_2 to 23.63 kJ/mol H_2 • Effect of adding Ti was not very significant, while partial substitution of Fe with Mn significantly affected activation temperature, which dropped from 573 K to 423 K.
Łodziana et al., (2019)	$LaNi_{4.75}M_{0.25}$	• To study sorption characteristics of AB_5 type MH alloy.	• $LaNi_{4.7}Ag_{0.25}$ and $LaNi_{4.75}Pb_{0.25}$ were most stable and favorable alloys for hydrogen storage.

Polish Academy of Sciences, Krakow, Poland 2019	(M: Ag, Al, Au, B, Bi, Ca, Cd, Cu, Cr, Fe, Ga, Ge, In, Ir, K, Mg, Mn, Mo, Nb, Pb, Pd, Pt, Rh, Ru, Sb, Sn, Ti, V, W, Y, Zn, Zr) Sample size: 700-900 mg	• To study thermodynamic stability of different alloy configurations. • To study surface segregation properties of different alloy compositions.	• $LaNi_{4.75}Bi_{0.25}$, $LaNi_{4.75}Fe_{0.25}$ and $LaNi_{4.75}Si_{0.25}$ were not suitable for hydrogen storage.
Yao et al., (2018) Zhejiang University China 2018	$Ti_{1.02}Cr_{1.1}Mn_{0.3}Fe_{0.6}$ T_{abs}= Room temp P_{abs}=34-43 MPa	• To study effect of rare earth doping (RE=La, Ce, Ho) on performance of $Ti_{1.02}Cr_{1.1}Mn_{0.3}Fe_{0.6}$ based hydrogen storage system	• $Ti_{1.02}Cr_{1.1}Mn_{0.3}Fe_{0.6}La_{0.03}$ alloy showed the best overall properties and was fully activated at room temperature. • Its hydrogen storage capacity was up to 1.715 wt.% and the dissociation enthalpy was 16.63 kJ/mol H_2 with a desorption plateau slope of 0.098.
Y. Li et al., (2018) Central Iron and Steel Research Institute China 2018	$Mg_{68}Ti_9Ni_{23}$ $Mg_{85}Ni_{15}$-0.2 wt.% Ti T_{des} = 520-630K P_{abs} = 0.01-1 MPa	• To study the absorption and desorption properties MgNi-Ti and MgTiNi alloys using PCT measurement.	• The $Mg_{85}Ni_{15}$-0.2 wt.% Ti alloy had a reversible hydrogen storage capacity of 5.22 wt.% at 653 K • The enthalpies, obtained by PCI data, of hydrogenation for these two alloys were estimated to be about 5 kJ/mol lower than MgH_2.
Chen et al., (2018) Harbin Institute of Technology China 2018	$Ti_{23}V_{40}Mn_{37}$ alloy $Ti_{23-x}Hf_xV_{40}Mn_{37}$ (x = 0, 2 and 4)	• To study effect of hafnium (Hf) substitution for Ti in $Ti_{23}V_{40}Mn_{37}$ on the hydrogen storage capacity and cyclic stability.	• The hydrogen desorption capacity of Hf substituted alloys was improved significantly, and it reached the value of 1.88 wt.% at 293 K when the composition is $Ti_{19}Hf_4V_{40}Mn_{37}$.
Kamble et al., (2018) University of Quebec at Trois-Rivieres Canada 2018	Zr, Ni and Zr_7Ni_{10} doped 52Ti-12V-36Cr Dopant amount: 4 wt% Zr_7Ni_{10}, 4 wt% Zr, 2.2 wt% Zr and 4 wt% Ni	• To study the effect on hydrogenation properties of Zr, Ni and Zr_7Ni_{10} doped 52Ti-12V-36Cr BCC alloy. • To study the change in crystal structure of the doped alloy.	• Addition of Zr and/or Ni reduced the hydrogenation time of the alloy. • Addition of 4 wt.% Zr_7Ni_{10} showed low hydrogenation time and high hydrogen storage capacity of 3.76 wt.%
Chen et al., (2018) Harbin Institute of Technology China 2018	$V_{35}Ti_xMn_{65-x}$ (x = 20, 25, 30, 35 and 40)	• To investigate the effect of varying Ti/Mn ratio in Ti-V-Mn alloy on the hydrogen storage properties. • To study the variation in the crystal structure of the different composition alloys.	• No significant change was observed in the basic crystal structure of the alloy and all alloys was observed to inherit BCC phase and C14 Laves phase. • The alloys with higher Ti/Mn ratio was observed to have higher stability.

			• $V_{35}Ti_{35}Mn_{30}$ had maximum hydrogen storage capacity of 3.35 wt.% at 293 K.
Patel et al., (2018) University of Quebec at Trois-Rivieres Canada 2018	TiFe with X wt% Zr (X = 4, 8)	• To study effect of annealing on the hydrogenation and microstructural properties of TiFe alloys doped with Zr. • To study the effect on rate of hydrogenation of the doped alloys.	• There was significant drop in the hydrogen storage capacity of annealed alloy. (~1.5 wt.% for as-cast to 1.05 wt.% annealed TiFe + 8 wt% Zr) • Drastic reduction in reaction kinetics was observed for annealed alloy. • Annealing is not suitable for Zr substitution in TiFe alloys.
Leng et al., (2017) Shanghai University China 2017	$TiFe_{0.9}Mn_{0.1}Ce_x$ (x = 0, 0.02, 0.04, 0.06) Pabs= 4 MPa Tabs = 353 K	• To study hydrogen storage characteristics of Ce substituted $TiFe_{0.9}Mn_{0.1}$. • To study the cyclic stability of doped alloys.	• Substitution of very small amount of Ce, significantly improved the activation kinetics of alloy. • There was no much change in the hydrogen storage capacity of different compositions, there was very slight drop in the hydrogen storage property of alloys i.e from 1.74 wt.% for $TiFe_{0.9}Mn_{0.1}$ to 1.7 wt.% for $TiFe_{0.9}Mn_{0.1}Ce_{0.6}$. • The alloys were possessing improved cyclic stability.
Liu et al., (2017) Beihang University China 2017	$(Ti_{0.85}Zr_{0.15})_{1.05}Mn_{1.2}Cr_{0.6}V_{0.1}M_{0.1}$ (M=Ni, Fe, Cu) Pabs = 4 MPa Tabs = 273 K to 318 K Tdes = 273 K to 318 K	• To study the hydrogen absorption characteristics of $(Ti_{0.85}Zr_{0.15})_{1.05}Mn_{1.2}Cr_{0.6}V_{0.1}M_{0.1}$ alloys produced from arc melting techniques.	• Alloys were activated in single absorption cycle at room temperature and 4 MPa hydrogen supply pressure. • The increase in the hydrogenation capacity for M substitution was observed in the order Ni<Fe<Cu • The maximum reversible hydrogen storage capacity was 1.81 wt.% at 273 K for M=Cu.
Cao et al., (2016) South China University of Technology 2016	Zr-Fe-V alloys with different compositions of Zr, Fe and V T_{des} Range: -30 °C to 80 °C	• To study hydrogen storage characteristics of Zr-Fe-V based BCC alloys. • To study the change in C14 BCC phase by substitution Al in Place of Fe. • To find PCI of different compositions.	• Among different compositions, $(Zr_{0.7}Ti_{0.3})_{1.04}Fe_{1.8}V_{0.2}$ alloy showed reversible hydrogen storage capacity of 1.51 wt.% at 11.2 bar and 0 °C absorption conditions with best overall properties. • Same composition has hydrogen storage capacity of 1.95 wt.% at 35 MPa.

Casini et al., (2016) Federal Institute of Education, Science and Technology of Rondonia Brazil 2016	$La_{0.7}Mg_{0.3}Al_{0.3}Mn_{0.4}Sn_{0.5-x}Cu_xNi_{3.8}$ alloys (where X = 0.0, 0.1, 0.2, 0.3, and 0.5)	• To study effect of Cu for Sn substitution on hydrogen storage characteristics and crystal structure of Cobalt free AB_5 alloys • To determine PCI of different compositions.	• The hydrogen storage capacity increased with increase in the Cu content. • $La_{0.7}Mg_{0.3}Al_{0.3}Mn_{0.4}Cu_{0.5}Ni_{3.8}$ showed maximum hydrogen storage capacity of 1.32 wt.%
Lototskyy et al., (2015a) University of Western Cape South Africa 2015	AB_2 Type MH with different compositions (A = Ti + Zr; B = Fe + Mn + Cr + Ni; Ti:Fe = 1:1; Ti:Zr = 0.55:0.45) Pressure: 1 – 100 bar Operating temperature : 0 to 60 °C	• To study the performance of MH based hydrogen storage system coupled with fuel cell. • To study the hydrogen discharge rate by using fins of different material in the reactor.	• Reversible hydrogen storage capacity for different compositions was observed between 1.2 to 1.6 wt.%. • By adding fins of high thermal conductive materials (Copper & Aluminum) results in significant improvement of hydrogen discharge rate.
Anbarasu et al., (2014; 2014b) Indian Institute of Technology Guwahati India 2014	$LmNi_{4.91}Sn_{0.15}$ 2.75 kg P_{abs}: 10 – 35 bar; P_{des} = 1 bar T_{abs}: 20–30 °C; T_{des}: 30-60 °C HTF flow rate: 2.2 – 30 lpm	• To obtain optimum absorption/desorption conditions of $LmNi_{4.91}Sn_{0.15}$ alloy with different reactor configuration (36 & 60 embedded cooling tube) • To study the effect of temperature, pressure and HTF flow rate on absorption/desorption conditions.	• Maximum hydrogen storage capacity of 1.18 wt.% was observed for both rector configurations. • The absorption time was 47% faster in 60 ECT reactor as compared to 36 ECT • The desorption time was 46.7 % faster in 60 ECT reactor as compared to 36 ECT
Sekhar et al., (2013) Indian Institute of Technology Guwahati India 2013	Mg + 30% $MmNi_5$ T_{abs}: 120-150 °C; T_{des}: 300-350 °C P_{abs}: 10 – 30 bar And $MmNi_{4.08}Co_{0.2}Mn_{0.62}Al_{0.1}$ T_{abs}: 30 – 180 °C; T_{des}: 40-60 °C P_{abs}: 10-30 bar	• To study optimum absorption/desorption characteristics of both $MmNi_{4.08}Co_{0.2}Mn_{0.62}Al_{0.1}$ and Mg + 30% $MmNi_5$ alloys. • To study reaction kinetics and reversible hydrogen storage capacity of alloys	• Hydrogen storage capacity of Mg + 30% $MmNi_5$ at 20 bar and 150 °C was observed as 2.5 wt.% while for $MmNi_{4.08}Co_{0.2}Mn_{0.62}Al_{0.1}$ at 30 bar and 30 °C was observed as 1.2 wt.% • With increase in supply pressure the hydrogen absorption capacity of both the alloys were increased. • Desorption rate was faster at higher temperatures for both the alloys

2.5 Literature Closure

On the basis of literature, it can be easy observed that, the research in the field of metal hydride based hydrogen storage and its related engineering applications is gaining huge attention day by day all over the world. Hydrogen being an energy carrier and alternative to the conventional energy sources, it's very essential for the scientific community to make it available cheaper and safer on the user end. Hence, a great effort from the research community and industries is being put to bring it from laboratory scale to commercial line. Form the literatures, the present status of metal hydride based hydrogen storage and purification systems can be summarized as following:

- Alloy selection is very important aspect of MHHSS because of wide band of alloys available with wide range of absorption/desorption characteristics, to be used for different applications. Several researchers worked on improving/finding the PCI characteristics of different MH alloy.
- Significantly, a large analytical studies reported the hydriding/dehydriding characteristics of MH based hydrogen storage system by varying different parameters like hydrogen supply pressure, absorption temperature, desorption temperature and HTF flow rate. As the properties of different MH alloys are significantly different, hence it is essential to find the optimum working condition of each alloy as per the target application.
- Several researchers worked on the different reactor design for MHHSS for obtaining optimized absorption/desorption results. These designs include capsule reactor model, embedded cooling tube model, capillary tube bundle model, reactor with helical coil heat exchanger, reactor with internal and external fins, tube bundle model etc. The main objective of testing several reactor designs is to optimize bed thickness and improve the cycle time.
- In order to improve the thermal conductivity of MH bed, several researchers used metal wire mesh, graphite flacks, Pellets, etc., as bed ingredient. By using these ingredients in bed, there is significant improvement in the thermal conductivity of bed, but at the same time hydrogen storage capacity of bed decreases due to the 10-20% bed volume being occupied by such ingredients.
- Apart from hydrogen storage, the metal hydrides are promising solution for the

purification system because of their remarkable properties like selective hydrogen absorption from gaseous mixtures, reversibility of interaction with hydrogen, mild operating conditions and compactness. Several researchers working in this field achieved hydrogen purification level up to 99.999% at very low cost as compared to several conventional purification techniques like pressure swing adsorption and cryogenic methods.

- The major challenges in a metal hydride based hydrogen purification (MHHP) system includes poisoning of the metal hydrides by other contaminants present in hydrogen and secondly issues associated with continuous purification system.

Though a lot of work are reported in the field of metal hydride based hydrogen storage and purification system in the literature, but most of them are analytical or offering solution to particular gas composition (single or binary impurities). Even the impurity level reported are in the lower range i.e <10% in most of the cases. Very few works in this field have discussed about regeneration of MH alloy after poisoning. This is the motivation of present work and the objectives are framed accordingly.

2.6 Objectives

The following objectives are framed for the present work.

- Thermodynamic screening of MH alloy for MH based hydrogen storage and purification system.
- Design and fabrication of MH reactor suitable for hydrogen storage and purification.
- To develop experimental test facility for studying single and multi-stage MH based hydrogen storage and purification system (MHHSPS).
- To develop method for analyzing gas composition using TCD (Thermal Conductivity Detector) in gas chromatograph (GC).
- To study the absorption and desorption characteristics of small and large-scale metal hydride based hydrogen storage and purification system under different operating conditions.
- Testing the performance of hydrogen purification systems at different impurity levels with gases like N_2, CH_4, CO, and CO_2.

- To study poisoning and regeneration characteristics of selected MH alloy against different impurities like N_2, CH_4, CO, Ar and CO_2, through cyclic study of absorption/desorption characteristics in MHHSPS
- To test the performance of multistage hydrogen purification system for higher impurity level of gases like N_2, CH_4, CO, CO_2, Ar etc.

2.7 Summary

The present chapter summarises the feasibility of metal hydrides for hydrogen purification application and the work carried out in this field. It also briefs the basic criteria of the alloy selection for the metal hydride based hydrogen purification system. As the reaction kinetics within the reactor is largely affected by the reactor design, a brief on reactor design and heat transfer augmentation techniques are also summarised in the present chapter.

CHAPTER 3 DESIGN AND FABRICATION OF REACTOR

3.1 Introduction

From the previous chapter, it was observed that the Embedded Cooling Tube (ECT) based metal hydride reactor designs, are more efficient in heat transfer and reaction kinetics. However, the cooling tube arrangement should be optimised as per reactor size and application. Therefore, the reactor design in the present study aims at getting evenly distributed embedded cooling tubes and maintain a near equal bed thickness at all the locations of the metal hydride bed, wherein a porous filter is centrally placed in a cylinder, with a varying number of cooling tubes placed around the filter. A two dimensional numerical model has been solved using COMSOL Multiphysics 4.3a. Transient heat and mass transfer phenomenon occurring in hydride bed during absorption, pressure gradient between supply condition and hydride bed, flow and diffusion of hydrogen through bed, removal of heat from hydride bed by HTF with emphasis on convective boundary condition, and resultant axial variation of HTF were considered in this study.

3.2 Assumptions

The process of simplifying the actual physical problem to a set of equations incorporating proper assumptions without affecting the actual physics is the first step of any numerical study. The assumptions considered for the present study are following:

- Hydrogen is an ideal gas.
- MH bed (the solid phase) is isotropic in nature and has uniform porosity.
- Adiabatic reactor walls and filter.
- The effect of radiative heat transfer is negligible (low temperature alloy).
- Local thermal equilibrium between the MH bed and gas is valid.
- Thermal conductivity and specific heat capacity of chosen alloy are independent of pressure, temperature and concentration of hydrogen.

Simulations are performed in COMSOL Multiphysics 4.3a to analyse and compare the effect of geometrical configuration on the temperature distributions of hydride bed and HTF as well as hydrogen diffusion during absorption.

3.3 Equations

For solving numerical simulations, following equations and boundary conditions were used.

3.3.1 van't Hoff equation

The equilibrium pressure (***P_{eq}***) of the MH bed during the absorption/desorption process, is calculated using van't Hoff equation given by (Nishizaki et al., 1983b),

$$\frac{P_{eq}}{P_0} = \exp\left[\frac{\Delta H}{R_u T} - \frac{\Delta S}{R_u} + (\varphi_s \pm \varphi_o) \times \tan\left(\pi\left(\frac{c}{c_f} - \frac{1}{2}\right)\right) \pm \frac{\varphi}{2}\right] \qquad 3.1$$

where '+' sign refers to absorption process, '**-**' sign refers to desorption process. **P_o** denotes ambient pressure, '**φ_s**' is slope factor, '**φ_o'** is slope constant and '**φ'** is hysteresis factor. Fraction of hydrogen absorbed/desorbed, '**c**' is defined as the ratio of the number of hydrogen atoms absorbed/desorbed to the number of metal atoms per mole of alloy, while '**c_f'** denotes final fraction.

3.3.2 Rate of reaction

The rate of mass of hydrogen absorbed by the metal hydride, '***ζ_a***' per unit time and per unit volume is given by (Mayer et al., 1987). Wherein, '***C_a***' is absorption rate coefficient, '***E_a***' is activation energy of absorption reaction, '***P_g'*** is supply pressure, '***P_{eq}***' is equilibrium pressure in absorbing bed, '***ρ_{ss}***' is density of hydride bed at saturation state while '***ρ_t***' is density of hydride bed at any given time '***t***'.

$$\zeta_a = C_a \exp\left(-\frac{E_a}{R_u T}\right) \ln\left(\frac{P_g}{P_{eq}}\right)(\rho_{ss} - \rho_t) \qquad 3.2$$

The rate of mass of hydrogen desorbed by the metal hydride, '***ζ_d***' per unit time and per unit volume is given by.

$$\zeta_d = C_d \exp\left(-\frac{E_d}{R_u T}\right)\left(\frac{P_{eq} - P_g}{P_{eq}}\right)(\rho_t - \rho_o) \qquad 3.3$$

Wherein, '***C_d***' is desorption rate coefficient, '***E_d***' is activation energy of desorption reaction, '***P_{eq}***' is equilibrium pressure in desorbing bed, while '***P_d***' is desorption pressure and '***ρ_o'*** is initial density of hydride bed.

3.3.3 Mass balance

During absorption, the bed acts as a sink for the hydrogen. Considering the sink term as rate of mass of hydrogen absorbed per unit volume, the hydrogen mass balance equation is formulated as: (Muthukumar et al., 2012b). Wherein, '$\boldsymbol{\rho_g}$' denotes the density of hydrogen gas within the bed, '$\boldsymbol{u}$' is the velocity vector and '$\boldsymbol{\varepsilon}$' represents porosity.

$$\varepsilon \frac{\partial \rho_g}{\partial t} + \nabla.(\rho_g \vec{u}) = -\zeta_a \qquad 3.4$$

For solid phase where amount of hydrogen absorbed is source term, mass balance equation is considered as:

$$(1-\varepsilon)\frac{\partial \rho_t}{\partial t} = \zeta_a \qquad 3.5$$

During desorption, the bed acts as a source for the hydrogen. Hence, the hydrogen mass balance equation can be formulated as:

$$\varepsilon \frac{\partial \rho_g}{\partial t} + \nabla.(\rho_g \vec{u}) = \zeta_d \qquad 3.6$$

Similarly, for solid phase, mass balance equation is given as:

$$(1-\varepsilon)\frac{\partial \rho_t}{\partial t} = -\zeta_d \qquad 3.7$$

The density of hydrogen gas inside bed, '$\boldsymbol{\rho_g}$' is obtained from ideal gas equation. where '$\boldsymbol{P_g}$' is the gas pressure and '$\boldsymbol{T}$' is the temperature within MH bed while '$\boldsymbol{M_g}$' is the molecular weight of gaseous hydrogen and '$\boldsymbol{R_u}$' is the universal gas constant.

$$\rho_g = \frac{P_g M_g}{R_u T} \qquad 3.8$$

3.3.4 Darcy's Law

Velocity of hydrogen flow inside MH bed (u) is modelled considering pressure gradient using Darcy's Law as given by:

$$\vec{u} = -\left(\frac{K}{\mu_g}\right)\nabla P \qquad 3.9$$

where '$\boldsymbol{K}$' is the permeability of the MH bed and '$\boldsymbol{\mu_g}$' is the dynamic viscosity of hydrogen gas.

3.3.5 Energy equation for MH bed

Assuming thermal equilibrium between the metal hydride bed and hydrogen gas, combined energy equation is considered, as given by (Muthukumar et al., 2012b),

$$(\rho C_p)_e \frac{\partial T}{\partial t} + (\rho_g C_{pg})(\vec{u}.\nabla T) = k_e \nabla^2 T + Q \qquad 3.10$$

where, '$\boldsymbol{k_e}$' is effective thermal conductivity of metal hydride bed, while '$\boldsymbol{Q}$' is the heat source/sink term, respectively.

The heat source '$\boldsymbol{Q_a}$' and heat sink term '$\boldsymbol{Q_d}$' are respectively considered as:

$$Q_a = \zeta_a \left(\frac{\Delta H}{M_g}\right) \qquad 3.11$$

$$Q_d = \zeta_d \left(\frac{\Delta H}{M_g}\right) \qquad 3.12$$

In the energy balance equation, effective heat capacity '$\boldsymbol{(\rho C_p)_e}$' of MH bed is given by:

$$(\rho C_p)_e = \varepsilon(\rho C_p)_g + (1-\varepsilon)(\rho C_p)_s \qquad 3.13$$

where '$\boldsymbol{(\rho c_p)_g}$' denotes heat capacity of gas phase, while '$\boldsymbol{(\rho c_p)_s}$' represents heat capacity of solid phase. Similarly, the effective thermal conductivity is obtained as

$$k_e = \varepsilon k_g + (1-\varepsilon)k_s \quad (3.14)$$

3.3.6 Hydrogen storage capacity of MH bed

Number of moles of hydrogen absorbed/desorbed is given by (Muthukumar et al., 2012b):

$$n_g = \frac{m_s N_s (c_{end} - c_{ini})}{2M_s} \quad (3.15)$$

where 'm_s' denotes mass and 'M_s' denotes molecular weight of MH alloy, respectively. The term 'N_s' denotes the number of metal atoms per mole of alloy. The mass of hydrogen absorbed/desorbed (m_g) is given by:

$$m_g = n_g M_g \quad (3.16)$$

Amount of hydrogen absorbed (in wt.%) is given by:

$$wt.\% = \frac{m_g}{m_a} = \frac{N_s M_g (c_{end} - c_{ini})}{2M_s} \times 100 \quad (3.17)$$

3.3.7 Initial boundary conditions

Initially (t = 0), the hydride bed temperature, gas phase temperature and HTF temperature, hydride equilibrium pressure and hydride density are assumed to be constant and uniform throughout the reactor.

$$\rho_t = \rho_0 \quad (3.18)$$

$$T = T_0 \quad (3.19)$$

$$P_g = P_0 \quad (3.20)$$

The outer boundary of the metal hydride reactor is assumed to be adiabatic throughout the process (t > 0):

$$\left.\frac{\partial T}{\partial r}\right|_{r=R_o} = 0 \qquad 3.21$$

The porous filter is adiabatic in nature while the pressure along filter is uniform throughout the process (t > 0). During absorption, along the wall of porous tube:

$$P_s = P_g\big|_{r=r_{op}} \qquad 3.22$$

$$\left.\frac{\partial T}{\partial r}\right|_{r=r_{op}} = 0 \qquad 3.23$$

Similarly, during desorption:

$$P_d = P_g\big|_{r=r_{op}} \qquad 3.24$$

$$\left.\frac{\partial T}{\partial r}\right|_{r=r_{op}} = 0 \qquad 3.25$$

The HTF flows through the ECT, inside the bed, and convective boundary condition at each cooling tube interface is given by, where r_{ot} is the outer radius of the ECT.

$$-k_e \frac{\partial T}{\partial r}\left(r_{ot}\right) = h(T - T_f) \qquad 3.26$$

The required constants, thermophysical properties of $LaNi_5$ and hydrogen are listed in Table 3.1.

Table: 3.1 Thermophysical properties of $LaNi_5$

Properties	**Symbol**	**Unit**	**Value**
Ambient Temperature	T_o	°C	25
HTF Temp	T_{cool}	°C	25
Density of Intermetallic Alloy	ρ_o	kg/m^3	8400
Density of Intermetallic Alloy (α-phase)	ρ_{si}	kg/m^3	8406
Density of Intermetallic Alloy (β-phase)	ρ_{ss}	kg/m^3	8515
Reaction Rate	C_a	1/s	59.187
Activation Energy	E_a	J/mol	-21170
Enthalpy of Hydride Formation	H	J/mol	-29879
Entropy of Hydride Formation	S	J/mol K	-111.74
Initial Concentration	C_o	-	0
Concentration at	C_{ini}	-	0.05
Concentration at	C_{end}	-	0.99
Molar mass of Hydrogen	M_g	g/mol	2.016
Universal Gas Constant	R	J/mol K	8.314
Hydrogen Supply Pressure	P_s	bar	10, 20, 30
Specific heat of gas	Cp_g	J/kg K	14283
Specific heat of Alloy	Cp_s	J/kg K	419
Density of Gas	ρ_g	kg/m^3	0.0838
Effective Thermal Conductivity of Alloy	k_e	W/m K	1.32
Thermal Conductivity of Hydrogen	k_g	W/m K	0.18
Molecular Weight of Alloy	M_a	g/mol	432.5

The tube arrangement and the reactor details of the fabricated reactor is depicted in **Fig. 3.1.**

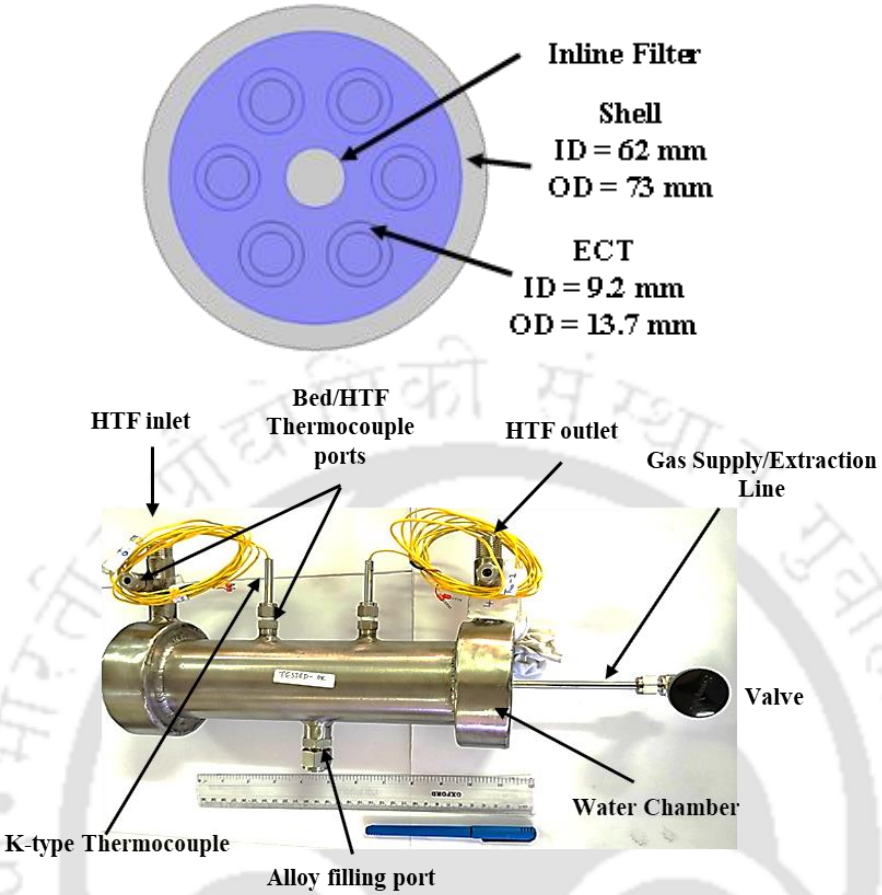

Fig. 3.1 2D schematic of ECT arrangement and pictorial view of the fabricated reactor

3.4 Validation of Numerical Model

The numerical model was validated with the experimental results carried out in the fabricated MH reactor of 6 ECT. The geometry as well as the thermophysical properties were defined as per alloy and reactor used in the experiments, so as to simulate this experimental investigation. The pictorial view of the reactor and the schematic of thermocouple placement is depicted in **Fig. 3.2**.

Upon comparison, a good coherence was observed between the numerically predicted results and the reported experimental data. The comparative analysis of the variation in the bed temperature of the experimental outcomes with the numerical findings are shown in **Fig. 3.3**. The deviation from the experimental results were in the range of 0.2-3% (in initial stage of the reaction) to 5-12% (towards the end of reaction) for supply pressures of 30 bar. The possible reasons of the deviation could be because of the estimation of exact thermocouple position within the MH bed. This approximation may have uncertainty of ±1 mm. Moreover, according to the assumption, the

reactor wall is adiabatic in nature, however practically there will be some heat loss from the reactor wall during the absorption/desorption process. This finally add up to the uncertainty in the obtained result. The uncertainty in estimation of thermo-physical properties of the alloys also adds up in the deviation of the results. However, the deviation is in the permissible range (less than 15%). So, the model can be further considered for the comparative analysis of the MH reactors of different configurations.

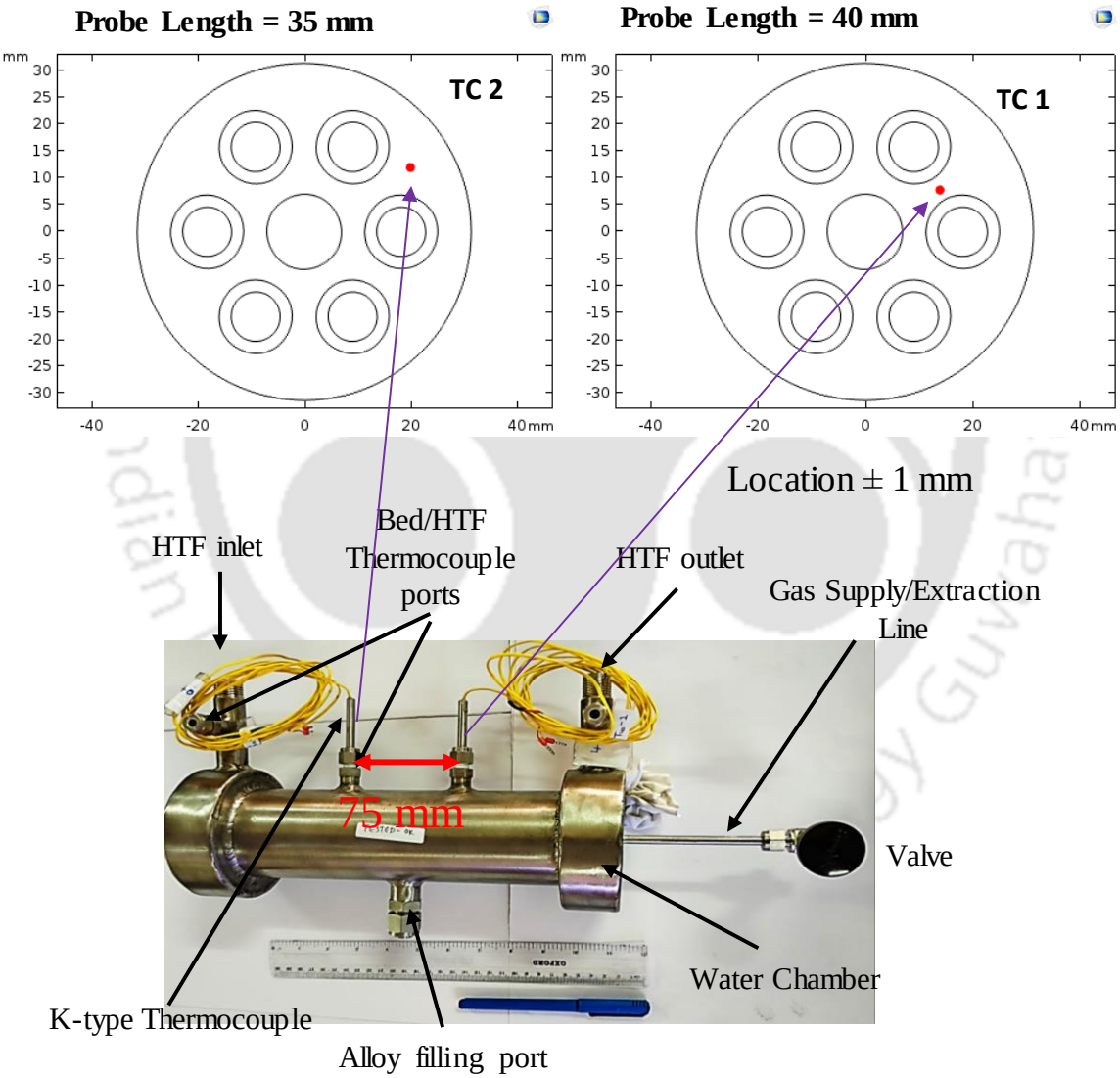

Fig. 3.2 Pictorial view of the fabricated reactor and thermocouple position within the reactor.

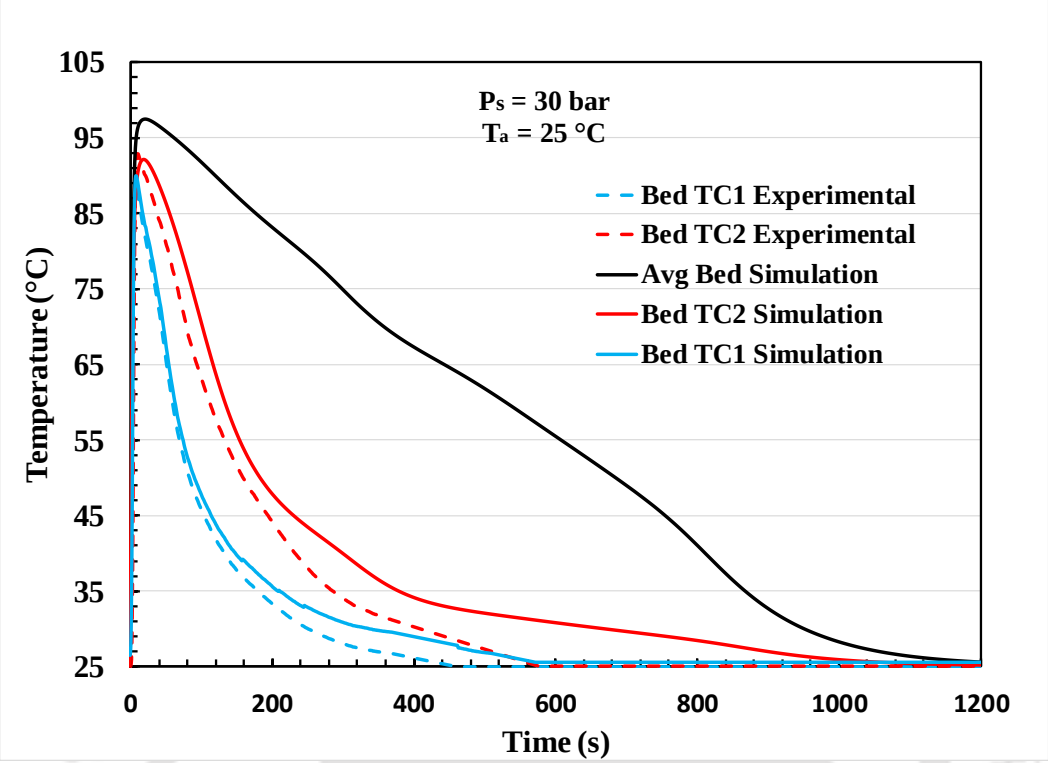

Fig. 3.3 Validation of numerical model with the experimental results

3.5 Numerical Analysis and Results

Considering the requirement of rigorous purification study to analyse the MH bed behavior for different gaseous impurities and impurity levels, prototype reactors with 6 ECT have been designed and fabricated. The purpose of fabricating small reactor is to perform exhaustive purification tests on shortlisted MH alloy with different impure samples of hydrogen mixed with gases like CO, CO_2, N_2, CH_4, O_2, etc. Considering the partial pressure of different gasses, making a large size samples, for bigger reactors was very difficult. Hence smaller reactor configurations for around 1.5 kg alloy capacity were numerically studied. The details of the reactor configuration are mentioned in **Table 3.2**

Table 3.2 Specification for numerical investigation for different reactor configuration

Specifications	Configuration 1	Configuration 2	Configuration 3
Shell diameter	OD = 73 mm ID = 62.8 mm	OD = 73 mm ID = 62.8 mm	OD = 73 mm ID = 62.8 mm

Reactor length	225 mm	225 mm	225 mm
No. of ECT	9	6	5
ECT diameter	ID = 6.84 mm OD = 10.3 mm	ID = 9.2 mm OD = 13.7 mm	ID = 9.2 mm OD = 13.7 mm
Alloy Density	8400 kg/m^3	8400 kg/m^3	8400 kg/m^3
Available alloy volume	0.000493 m^3	0.000471 m^3	0.000498 m^3
Bed porosity	0.5	0.5	0.5
Alloy capacity	1.65 kg	1.6 kg	1.65 kg
Alloy filled	1.2 kg	1.2 kg	1.2 kg
HTF flow rate	4 lpm	4 lpm	4 lpm
HTF velocity	0.20 m/s	0.17 m/s	0.20 m/s
Heat transfer coefficient (h)	936 W/m^2K	811 W/m^2K	868 W/m^2K
Image	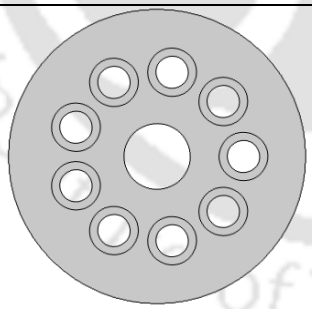	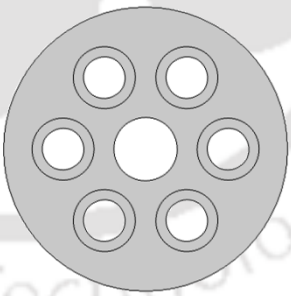	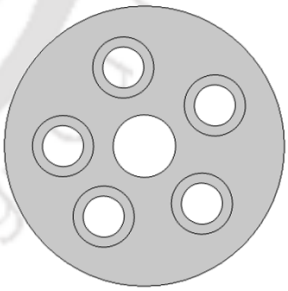

The configuration of the three reactors were obtained by fixing the alloy volume and the length of the reactor in each case as similar. The configuration was also established by keeping the reactor fabrication simple by single layer cooling tube stacking. The shell diameter and thickness were taken as per ASTM standard. The ASTM table for standard seamless tube sizing is depicted in

Fig. 3.4. Since, the commercial cylinder used for the experiments has maximum pressure of 150 bar, the tube sizes were selected accordingly.

ALLOWABLE WORKING PRESSURE AT TEMPERATURE

Temperature (°C):				50	100	150	200	250	300	325	350	375	400	425	450	475	500	525	550	575	600	625	650	675	700
Design Strength (MPa):				138	138	138	133	125	119	117	114	112	111	110	108	107	106	106	103	95	81	65	50	39	30
Size			Sch	WT	Allowable Working Pressure (MPa)																				
DN	NPS	mm	No	(mm)																					
10	⅜	17.15	10S	1.65	25.4	25.4	25.4	24.5	23.0	21.9	21.5	21.0	20.6	20.4	20.2	19.9	19.7	19.5	19.5	18.9	17.5	14.9	11.9	9.2	7.2	5.5
		17.15	40S	2.31	36.9	36.9	36.9	35.5	33.4	31.8	31.3	30.5	29.9	29.7	29.4	28.9	28.6	28.3	28.3	27.5	25.4	21.6	17.4	13.4	10.4	8.0
		17.15	80S	3.20	53.9	53.9	53.9	51.9	48.8	46.4	45.7	44.5	43.7	43.3	42.9	42.1	41.8	41.4	41.4	40.2	37.1	31.6	25.4	19.5	15.2	11.7
15	½	21.34	5S	1.65	20.0	20.0	20.0	19.3	18.1	17.3	17.0	16.5	16.3	16.1	16.0	15.7	15.5	15.4	15.4	14.9	13.8	11.8	9.4	7.3	5.7	4.4
		21.34	10S	2.11	26.1	26.1	26.1	25.2	23.7	22.5	22.2	21.6	21.2	21.0	20.8	20.5	20.3	20.1	20.1	19.5	18.0	15.3	12.3	9.5	7.4	5.7
		21.34	40S	2.77	35.4	35.4	35.4	34.1	32.0	30.5	30.0	29.2	28.7	28.4	28.2	27.7	27.4	27.2	27.2	26.4	24.3	20.8	16.7	12.8	10.0	7.7
		21.34	80S	3.73	49.8	49.8	49.8	48.0	45.1	43.0	42.2	41.2	40.4	40.1	39.7	39.0	38.6	38.3	38.3	37.2	34.3	29.2	23.5	18.1	14.1	10.8
20	¾	26.67	5S	1.65	15.8	15.8	15.8	15.2	14.3	13.6	13.4	13.0	12.8	12.7	12.6	12.4	12.2	12.1	12.1	11.8	10.9	9.3	7.4	5.7	4.5	3.4
		26.67	10S	2.11	20.5	20.5	20.5	19.8	18.6	17.7	17.4	17.0	16.7	16.5	16.4	16.1	15.9	15.8	15.8	15.3	14.1	12.0	9.7	7.4	5.8	4.5
		26.67	40S	2.87	28.7	28.7	28.7	27.7	26.0	24.7	24.3	23.7	23.3	23.1	22.9	22.5	22.2	22.0	22.0	21.4	19.8	16.8	13.5	10.4	8.1	6.2
		26.67	80S	3.91	40.6	40.6	40.6	39.1	36.8	35.0	34.4	33.6	33.0	32.7	32.4	31.8	31.5	31.2	31.2	30.3	28.0	23.8	19.1	14.7	11.5	8.8
25	1	33.40	5S	1.65	12.5	12.5	12.5	12.0	11.3	10.8	10.6	10.3	10.1	10.0	9.9	9.8	9.7	9.6	9.6	9.3	8.6	7.3	5.9	4.5	3.5	2.7
		33.40	10S	2.77	21.6	21.6	21.6	20.8	19.6	18.6	18.3	17.8	17.5	17.4	17.2	16.9	16.7	16.6	16.6	16.1	14.9	12.7	10.2	7.8	6.1	4.7
		33.40	40S	3.38	26.8	26.8	26.8	25.8	24.3	23.1	22.7	22.2	21.8	21.6	21.4	21.0	20.8	20.6	20.6	20.0	18.5	15.7	12.6	9.7	7.6	5.8
		33.40	80S	4.55	37.4	37.4	37.4	36.0	33.8	32.2	31.7	30.9	30.3	30.0	29.8	29.2	29.0	28.7	28.7	27.9	25.7	21.9	17.6	13.5	10.6	8.1
32	1¼	42.16	5S	1.65	9.8	9.8	9.8	9.4	8.9	8.4	8.3	8.1	7.9	7.9	7.8	7.7	7.6	7.5	7.5	7.3	6.7	5.7	4.6	3.5	2.8	2.1
		42.16	10S	2.77	16.8	16.8	16.8	16.2	15.2	14.5	14.3	13.9	13.7	13.5	13.4	13.2	13.1	12.9	12.9	12.6	11.6	9.9	7.9	6.1	4.8	3.7
		42.16	40S	3.56	22.0	22.0	22.0	21.2	19.9	19.0	18.7	18.2	17.9	17.7	17.6	17.2	17.1	16.9	16.9	16.4	15.2	12.9	10.4	8.0	6.2	4.8
		42.16	80S	4.85	30.9	30.9	30.9	29.8	28.0	26.6	26.2	25.5	25.1	24.8	24.6	24.2	24.0	23.7	23.7	23.1	21.3	18.1	14.6	11.2	8.7	6.7
40	1½	48.26	5S	1.65	8.5	8.5	8.5	8.2	7.7	7.3	7.2	7.0	6.9	6.8	6.8	6.7	6.6	6.5	6.5	6.4	5.9	5.0	4.0	3.1	2.4	1.9
		48.26	10S	2.77	14.6	14.6	14.6	14.1	13.2	12.6	12.4	12.1	11.8	11.7	11.6	11.4	11.3	11.2	11.2	10.9	10.0	8.6	6.9	5.3	4.1	3.2
		48.26	40S	3.68	19.7	19.7	19.7	19.0	17.9	17.0	16.7	16.3	16.0	15.9	15.7	15.4	15.3	15.2	15.2	14.7	13.6	11.6	9.3	7.1	5.6	4.3
		48.26	80S	5.08	28.0	28.0	28.0	27.0	25.4	24.1	23.7	23.1	22.7	22.5	22.3	21.9	21.7	21.5	21.5	20.9	19.3	16.4	13.2	10.1	7.9	6.1
50	2	60.33	5S	1.65	6.8	6.8	6.8	6.5	6.1	5.8	5.7	5.6	5.5	5.4	5.4	5.3	5.2	5.2	5.2	5.1	4.7	4.0	3.2	2.5	1.9	1.5
		60.33	10S	2.77	11.6	11.6	11.6	11.1	10.5	10.0	9.8	9.5	9.4	9.3	9.2	9.0	9.0	8.9	8.9	8.6	8.0	6.8	5.4	4.2	3.3	2.5
		60.33	40S	3.91	16.6	16.6	16.6	16.0	15.0	14.3	14.1	13.7	13.5	13.3	13.2	13.0	12.9	12.7	12.7	12.4	11.4	9.7	7.8	6.0	4.7	3.6
		60.33	80S	5.54	24.1	24.1	24.1	23.2	21.8	20.8	20.4	19.9	19.6	19.4	19.2	18.9	18.7	18.5	18.5	18.0	16.6	14.2	11.4	8.7	6.8	5.2
65	2½	73.03	5S	2.11	7.2	7.2	7.2	6.9	6.5	6.2	6.1	5.9	5.8	5.8	5.7	5.6	5.6	5.5	5.5	5.3	4.9	4.2	3.4	2.6	2.0	1.6
		73.03	10S	3.05	10.5	10.5	10.5	10.1	9.5	9.0	8.9	8.6	8.5	8.4	8.3	8.2	8.1	8.0	8.0	7.8	7.2	6.1	4.9	3.8	3.0	2.3
		73.03	40S	5.16	18.2	18.2	18.2	17.5	16.5	15.7	15.4	15.0	14.8	14.6	14.5	14.2	14.1	14.0	14.0	13.6	12.5	10.7	8.6	6.6	5.1	4.0
		73.03	80S	7.01	25.3	25.3	25.3	24.4	22.9	21.8	21.5	20.9	20.5	20.4	20.2	19.8	19.6	19.4	19.4	18.9	17.4	14.9	11.9	9.2	7.2	5.5

NOMINAL PIPE SIZE	OD	SCHEDULE DESIGNATIONS			WALL THICKNESS		WEIGHT		ID	
INCH MM	INCH MM	ASME			INCH	MM	LBS/ FOOT	KG/ METER	INCH	MM
1/8	0.405	10		10S	0.049	1.24	0.19	0.28	0.307	7.82
6	10.3	STD	40	40S	0.068	1.73	0.24	0.37	0.269	6.84
		XS	80	80S	0.095	2.41	0.31	0.47	0.215	5.84
1/4	0.540	10		10S	0.065	1.65	0.33	0.48	0.410	10.40
8	13.7	STD	40	40S	0.088	2.24	0.43	0.63	0.364	9.22
		XS	80	80S	0.119	3.02	0.54	0.80	0.302	7.66
3/8	0.675	10		10S	0.065	1.65	0.42	0.63	0.545	13.80
10	17.1	STD	40	40S	0.091	2.31	0.57	0.84	0.493	12.48
		XS	80	80S	0.126	3.20	0.74	1.10	0.423	10.70

Shell Size

ECT Sizes

Fig. 3.4 Table for SS GRADE TP316 PIPES - ASTM A 312, Seamless SS 316 Tubes

All the three possible reactor configurations were simulated under different supply pressure of 10, 20 and 30 bar. The result obtained for the bed temperature variation and the amount of hydrogen absorbed with respect to time is depicted in **Fig. 3.5**. The reason for plotting all the numerical results in the same plot is to give a clear picture of the comparative study. According to the result obtained, it was observed that, with increase in the pressure gradient from 10 to 30 bar, the rate of absorption increases rigorously and the fastest absorption was observed for 30 bar supply pressure. This was because of the increase in the pressure gradient for the higher pressure range. This

pressure gradient acts as driving force for the absorption and increases the rate of absorption for its higher value.

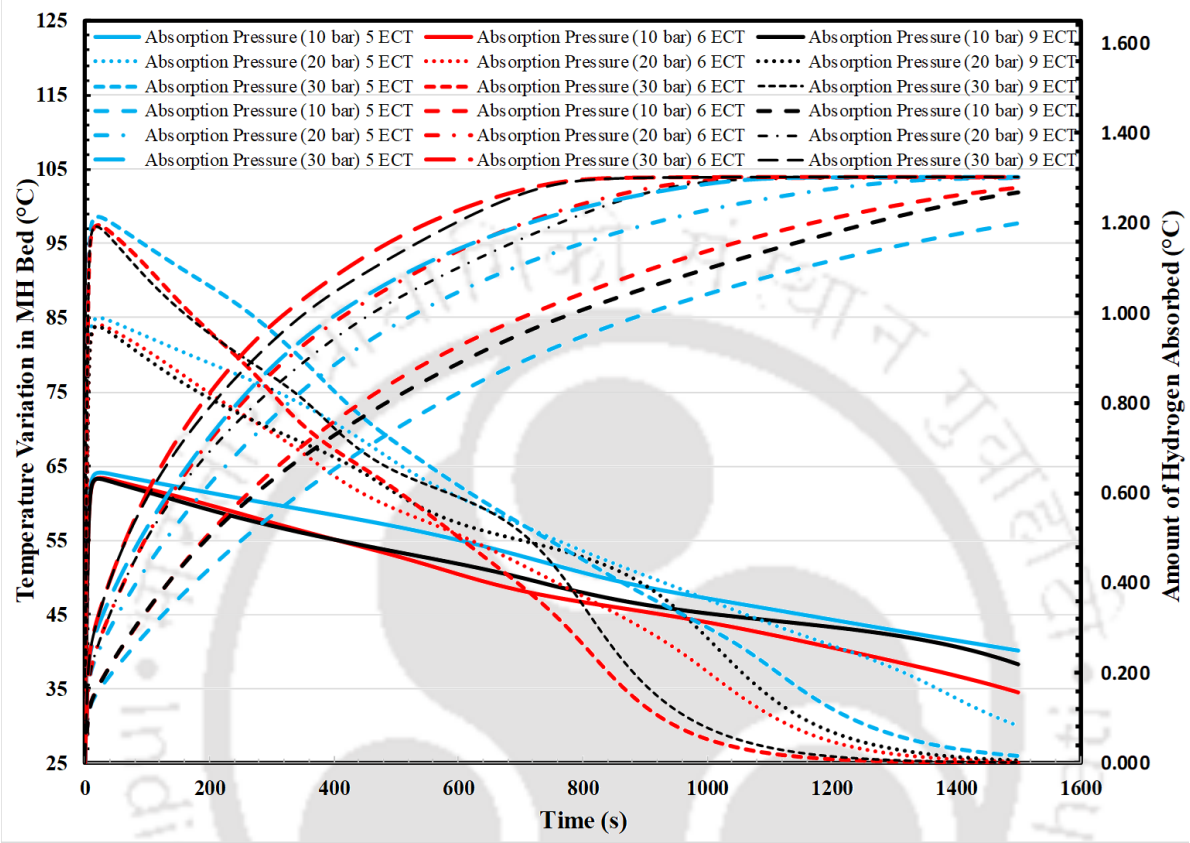

Fig. 3.5 Representation of bed temperature variation (Y-1 axis) and amount of hydrogen absorbed (Y-2 axis) from the numerical investigation.

It was also observed that for 30 bar supply pressure, the peak bed temperature was maximum for all the three reactor configurations. This is because of the faster rate of absorption at the elevated pressure, there is excess heat generation within the MH bed. However, if it is compared among all three reactor configuration, for all the cases, 6 ECT configuration showed better reaction kinetics than the other two reactor configuration i.e. 9 ECT and 5 ECT. This was because of the minimum bed thickness in case of the 6 ECT reactor. However, for 9 ECT reactor, the bed thickness between the tubes was minimum, but at the same time there was comparatively thicker bed in the radial direction. This led to slower heat dissipation from the outer periphery of the MH bed, which finally showers down the reaction kinetics. The sequence of reaction kinetics was in the order 6 ECT > 9 ECT > 5 ECT reactor.

Table 3.3 Temperature contours for different reactor configuration at P_s = 10 bar

Time (s)	5 ECT	6 ECT	9 ECT
250	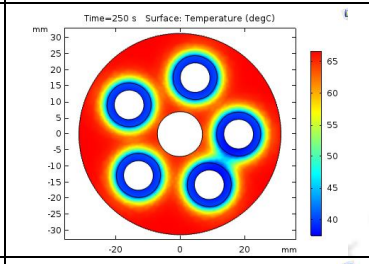	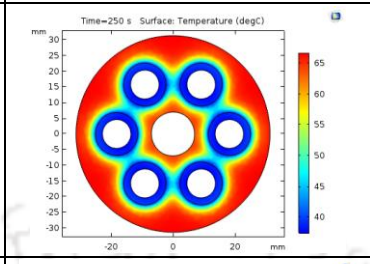	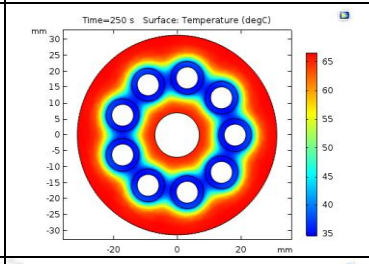
500	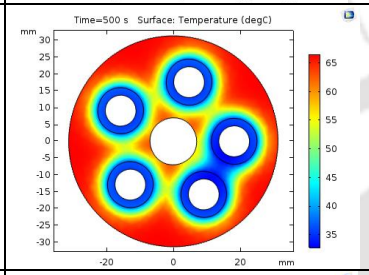	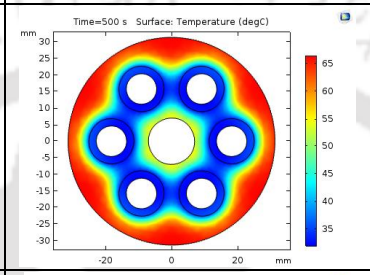	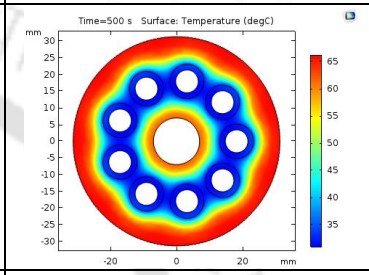
750	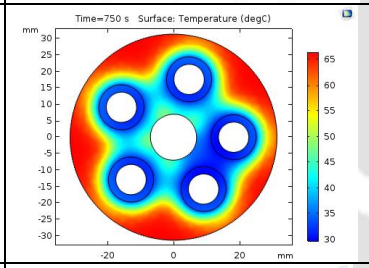	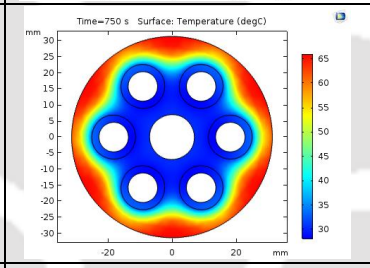	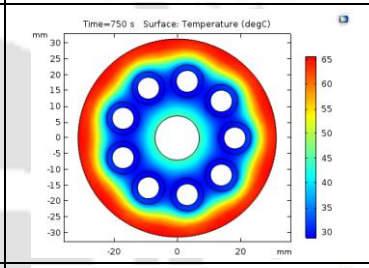
1000	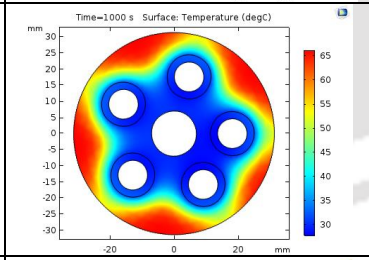	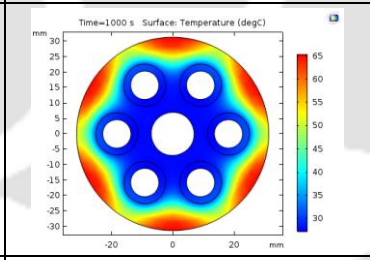	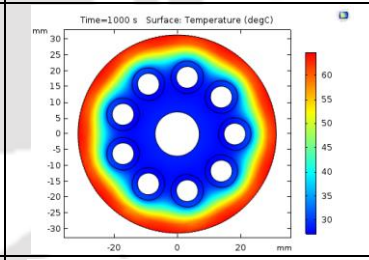
1250	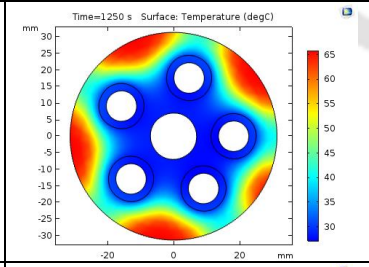	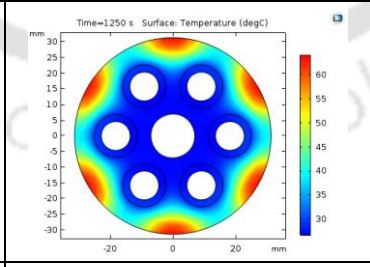	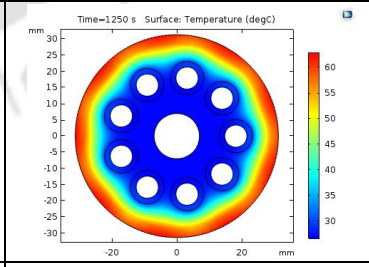
1500	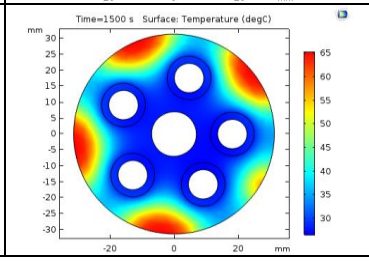	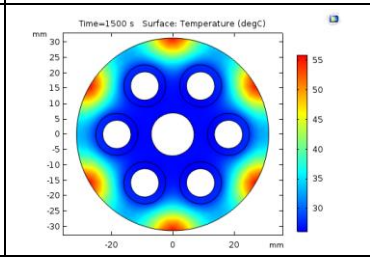	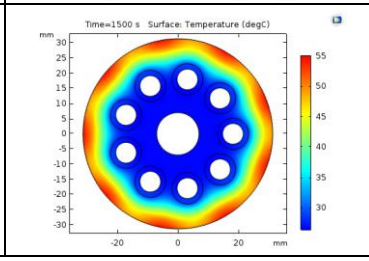

Table 3.4 Rate of absorption contours for different reactor configuration at P_s = 10 bar

Time (s)	5 ECT	6 ECT	9 ECT
250	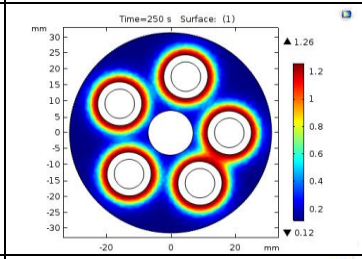	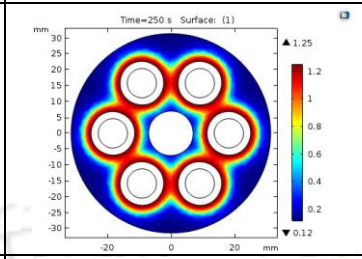	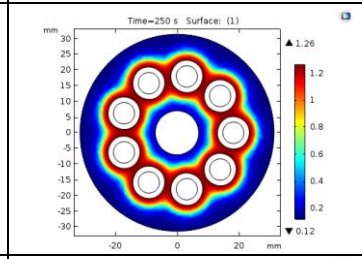
500	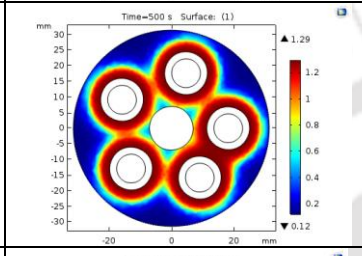	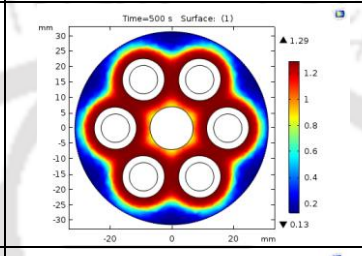	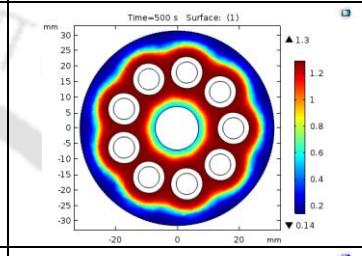
750	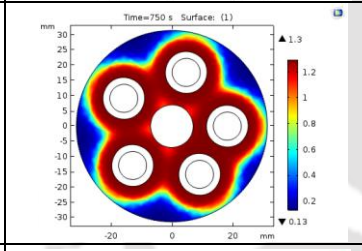	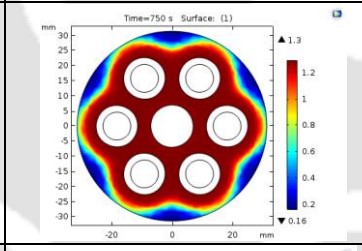	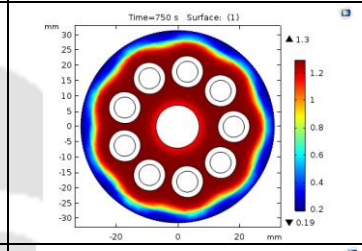
1000	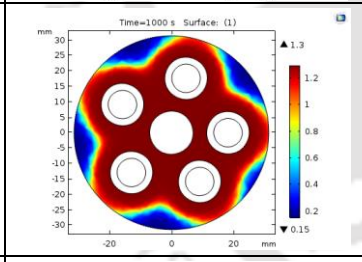	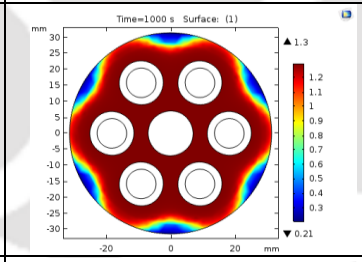	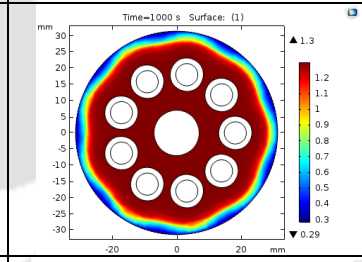
1250	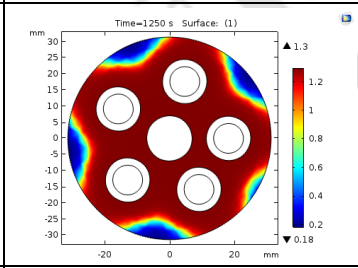	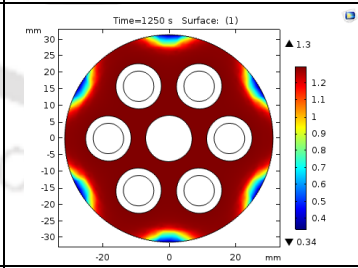	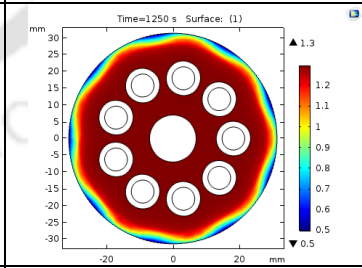
1500	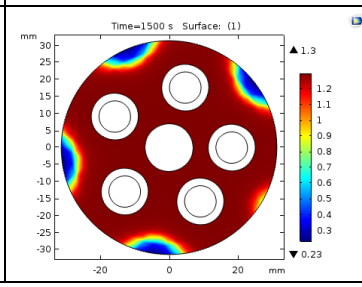	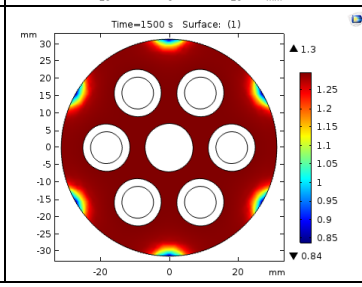	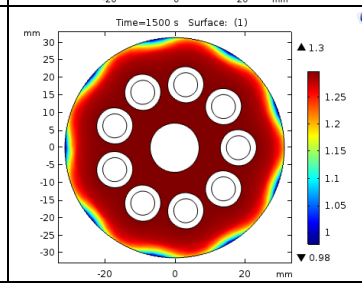

Table 3.5 Temperature contours for different reactor configuration at P_s = 20 bar

Time (s)	5 ECT	6 ECT	9 ECT
250	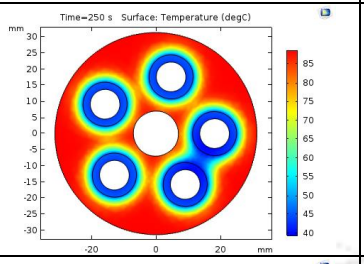	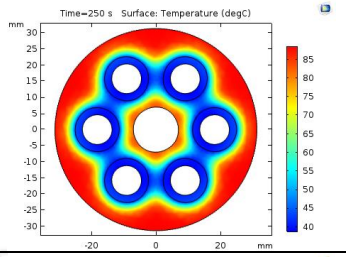	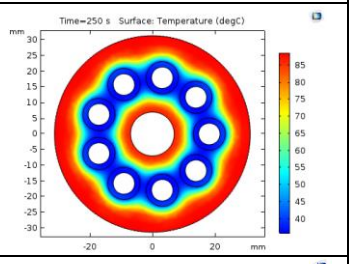
500	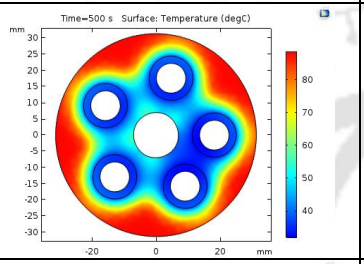	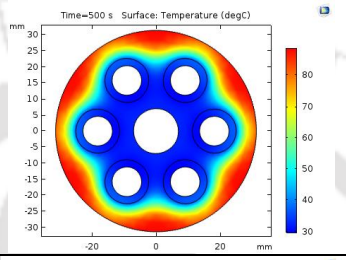	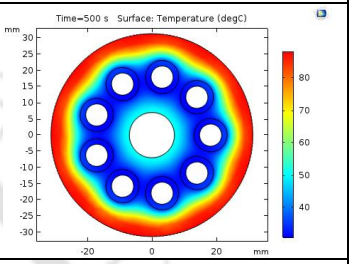
750	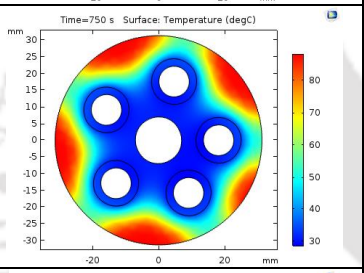	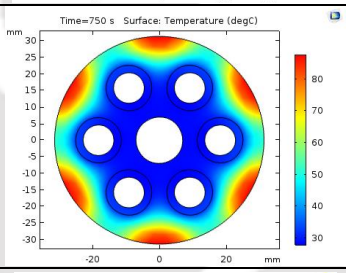	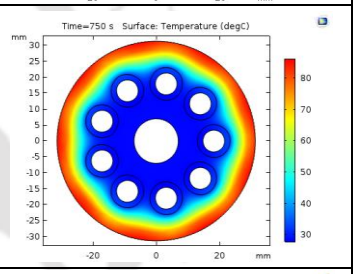
1000	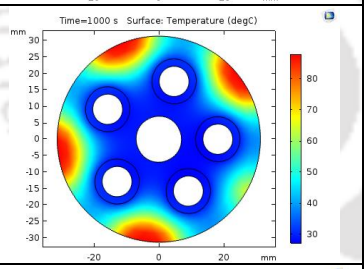	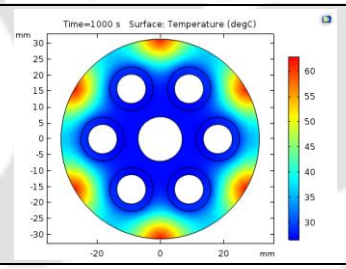	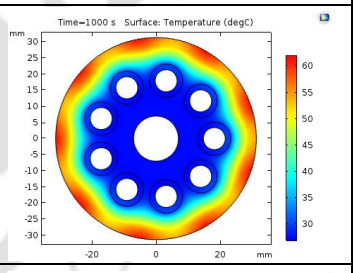
1250	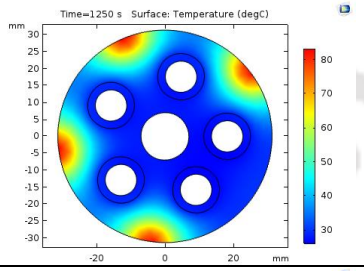	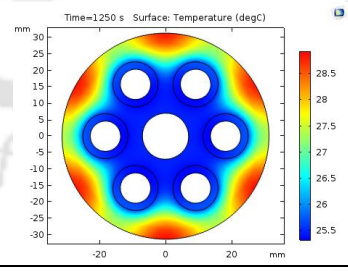	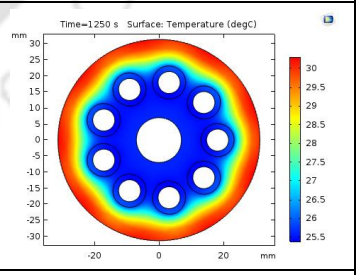
1500	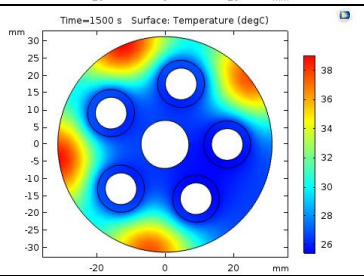	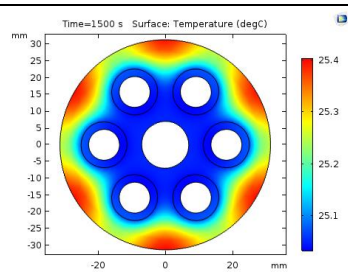	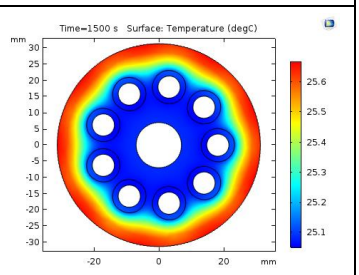

Table 3.6 Rate of absorption contours for different reactor configuration at P_s = 30 bar

Time (s)	5 ECT	6 ECT	9 ECT
250	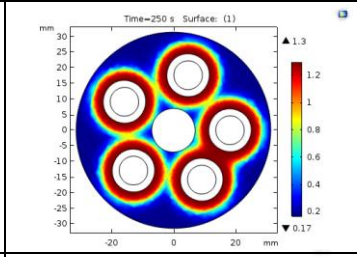	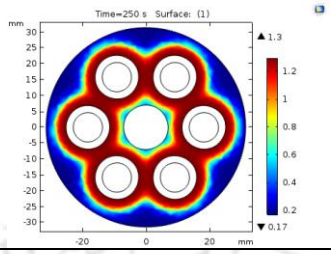	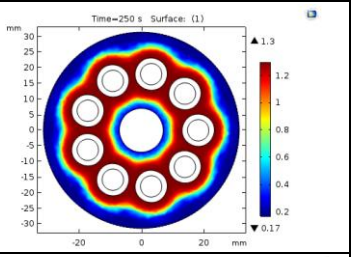
500	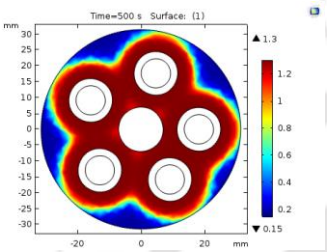	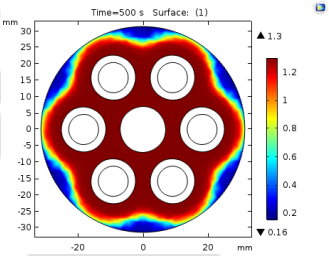	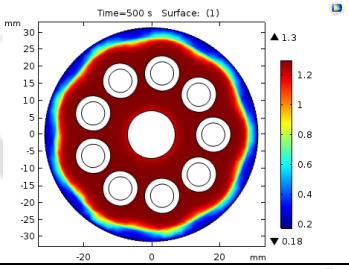
750	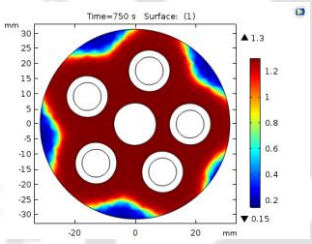	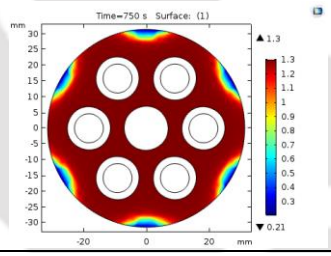	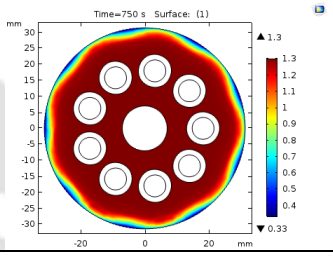
1000	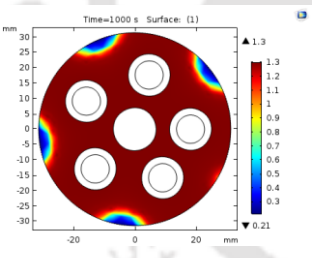	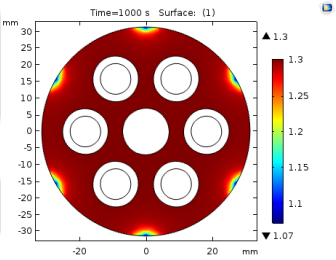	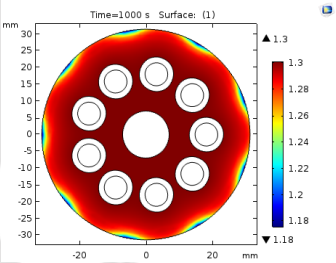
1250	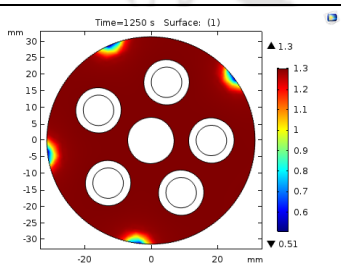	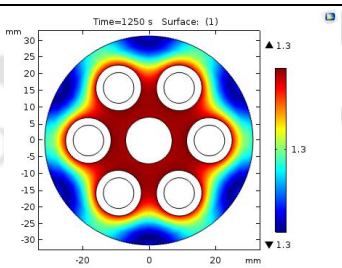	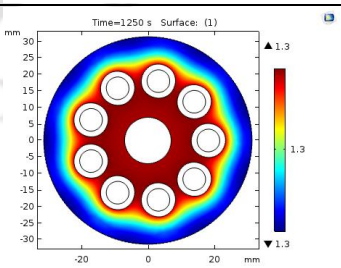
1500	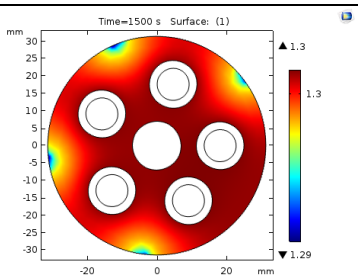	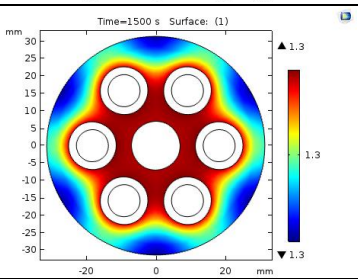	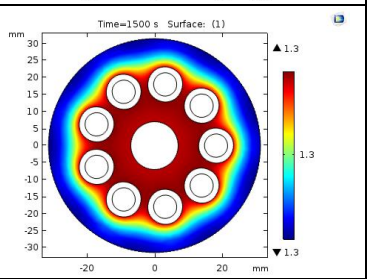

Table 3.7 Temperature contours for different reactor configuration at P_s = 30 bar

Time (s)	5 ECT	6 ECT	9 ECT
250	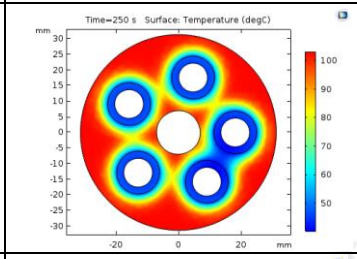	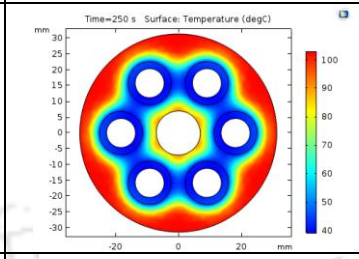	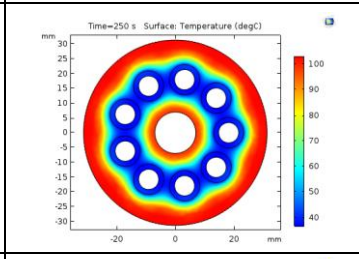
500	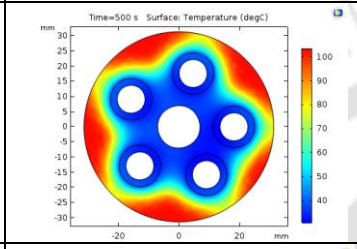	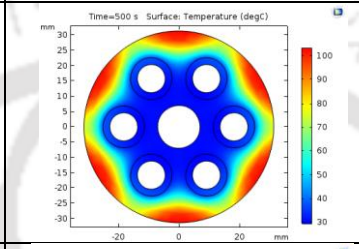	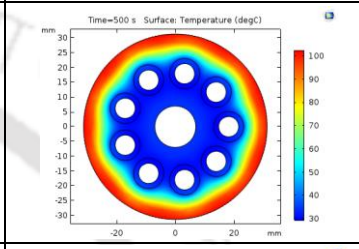
750	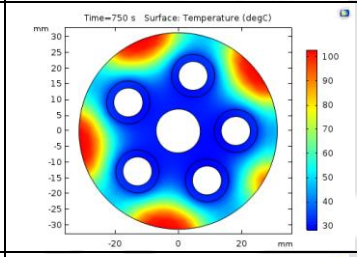	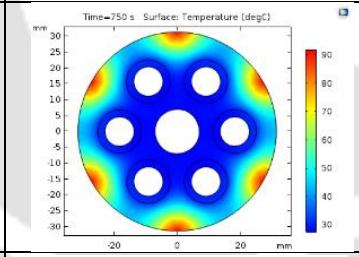	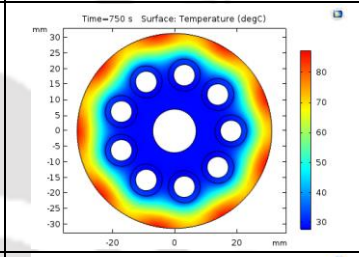
1000	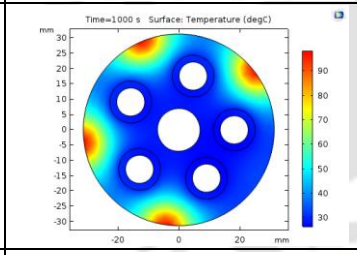	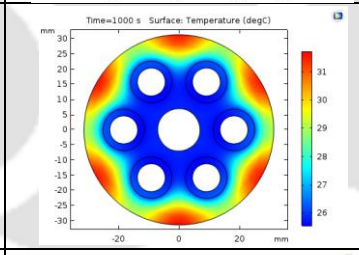	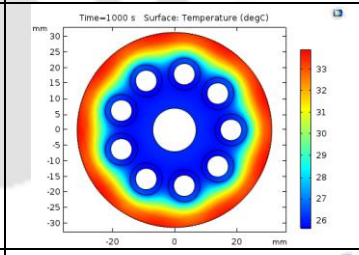
1250	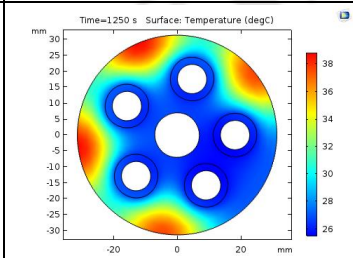	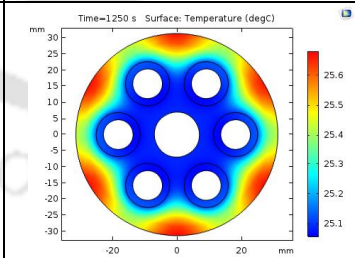	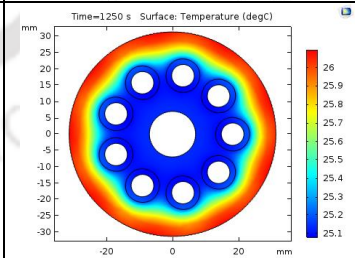
1500	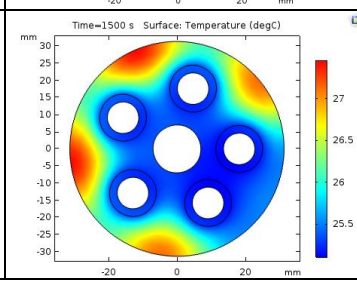	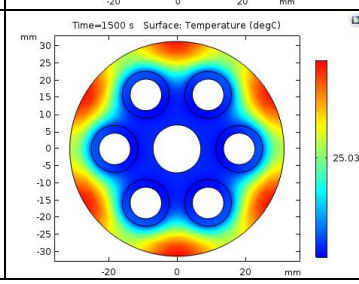	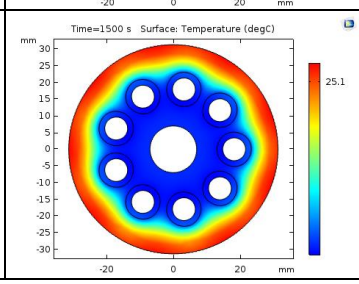

Table 3.8 Rate of absorption contours for different reactor configuration at P_s = 30 bar

Time (s)	5 ECT	6 ECT	9 ECT
250	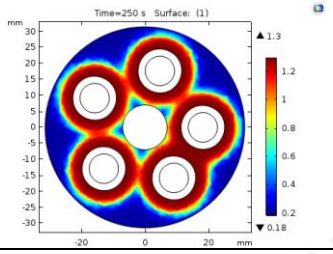	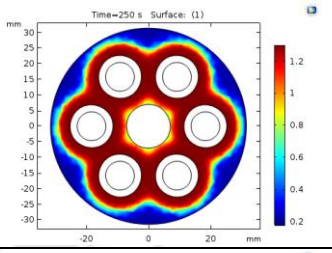	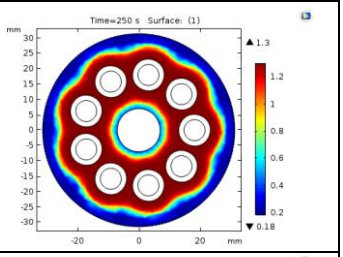
500	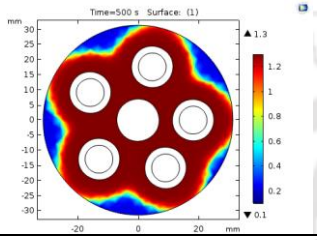	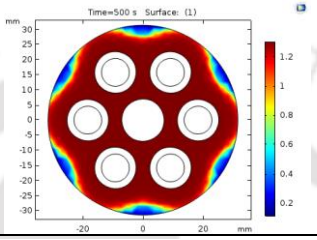	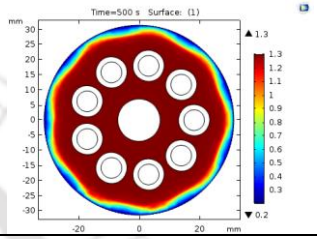
750	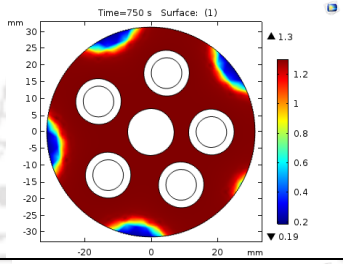	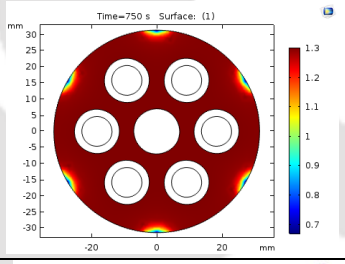	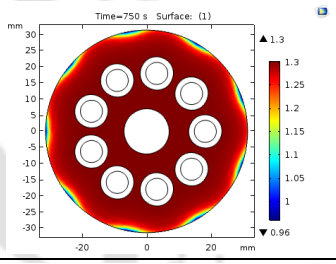
1000	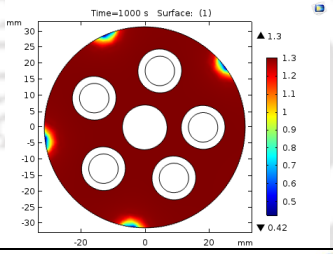	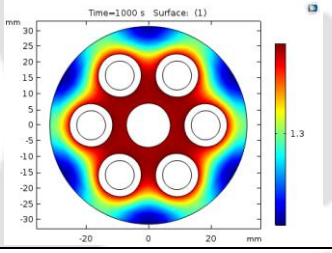	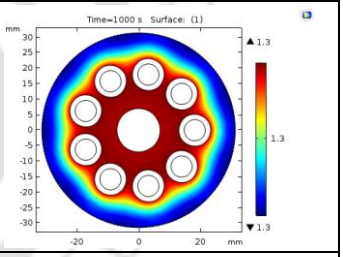
1250	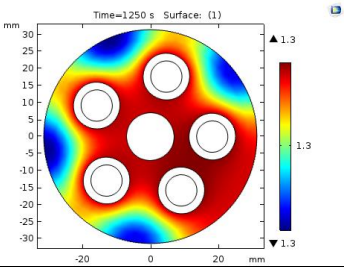	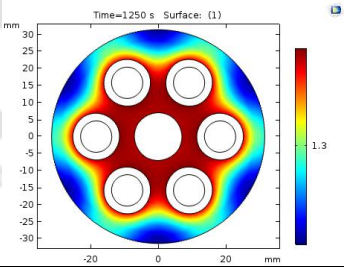	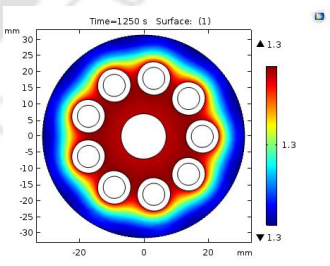
1500	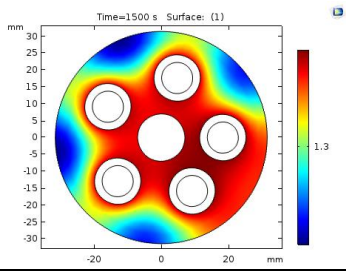	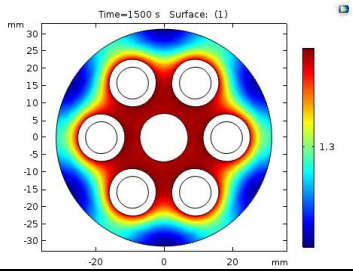	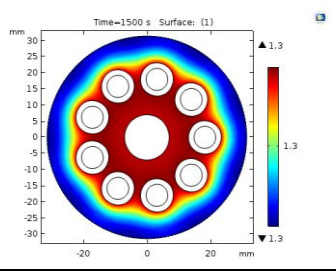

For the better analysis of the numerical results, the temperature and the rate of absorption contours were plotted for supply pressure of 10, 20 and 30 bar and time interval of 250 s. As depicted in **Table 3.3**, for 10 bar supply pressure, the rate of heat removal was faster for the 6 ECT reactor, as compared to other two configurations. Because of faster heat removal, the rate of absorption in the 6 ECT reactor is also faster, which can be depicted in **Table 3.4**. However, in case of 5 ECT reactor, the bed thickness is more as compared with other configuration, which restricts the effect of heat excess heat removal from the remote area (away from cooling tube) of the bed. This leads to the accumulation of excess heat generated during the absorption process. This excess heat affects the absorption kinetics of the system. Similarly, for ECT reactor, the bed thickness in radial direction is more as compared to 5ECT and 6ECT, which leads to delay in the heat removal from the surface of the reactor, which finally delayed the reaction kinetics.

Likewise, 10 bar supply pressure, similar pattern of the results is observed for 20 and 30 bar. The temperature and rate of absorption contours for the 20 bar supply pressure is depicted in **Table 3.5** and **Table 3.6** respectively. Similarly, contours for the 30 bar supply pressure is depicted in **Table 3.7** and **Table 3.8** respectively. In all the cases, the configuration which performed better is reactor with 6 ECT, which is followed by 9 ECT and 5 ECT configuration.

3.6 Reactor Fabrication and Testing

Considering negligible hydrogen diffusion through the reactors during idle condition, SS 316 was choosen as material for the reactor fabrication. Steel tubes come in standard sizes viz. 5S, 10S, 40S, 80S. Their dimensions and pressure rating are presented in **Fig. 3.4**. Based on the required safe operating pressure of up to 140 bar, the dimensions of the outer casing of the reactor was chosen. Considering single stage stacking and simple design, tube of 40 schedule with 73 mm outer dia and 7 mm thickness was selected for shell configuration. The embedded cooling tubes were arranged in a single stacks surrounded by SS316 sintered porous tube of 2 µm tube size.

3.6.1 Fabrication and alloy filling in 6 ECT Reactor (Small Scale Reactor)

Considering the feasibility of impure sample preparation for rigorous cyclic purification test, prototype reactors of 6 ECT was designed and fabricated. The schematic view of the reactor with dimensional details is presented in **Fig. 3.6** and **Fig. 3.7.**

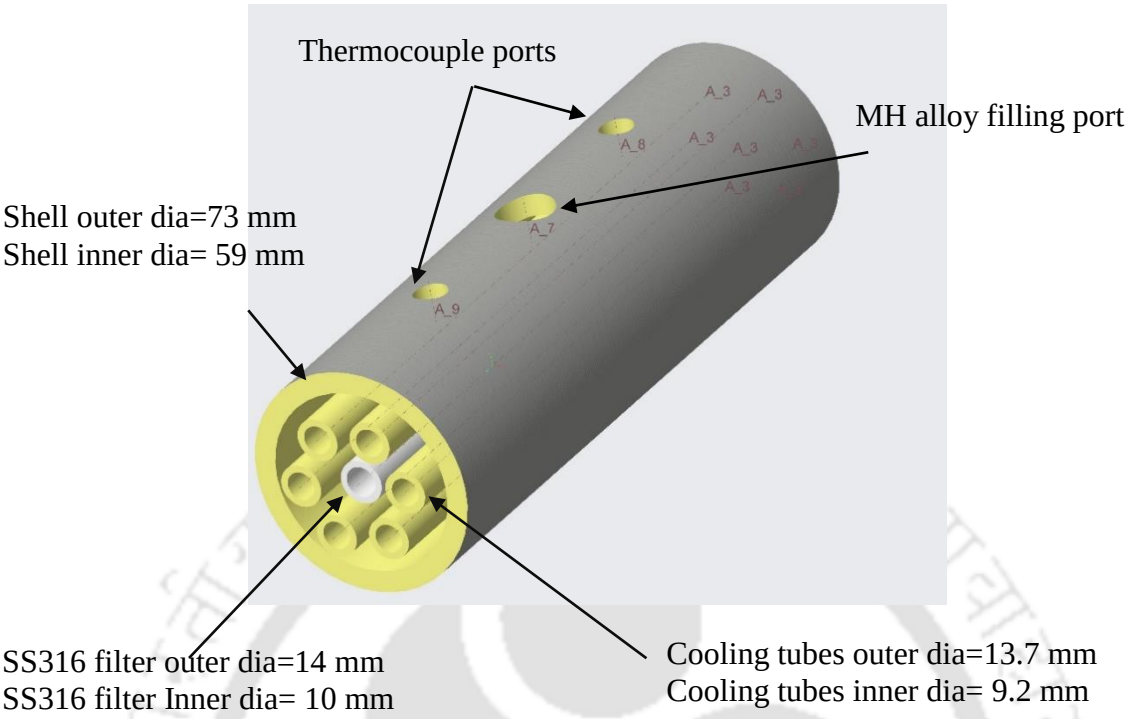

Fig. 3.6 Schematic view of cooling tubes and inline filter position of the MH reactor

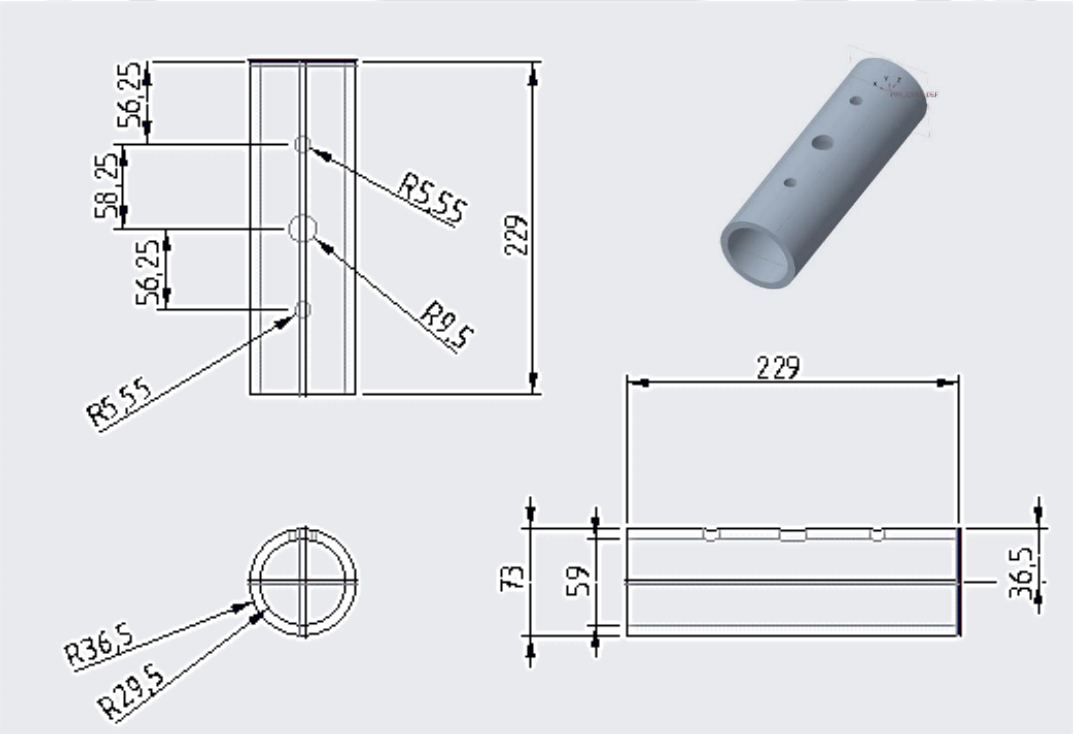

Fig. 3.7 Dimensional details of the 6 ECT MH Reactor. (All dimensions are in mm)

The material used for fabrication of 6 ECT MH reactor was SS316 grade alloy steel. Swagelok fittings of required dimensions were used as thermocouple ports and alloy filling ports. All the parts were welded using "Tungsten Inert Gas (TIG)" welding. The steps involved in the fabrication of reactor is presented in **Fig. 3.8**. Inline SS316 sintered filter of 2 μm pore size is welded to ensure uniform distribution of hydrogen to/from MH bed through the hydrogen supply tube. The total raw material used to fabricate 4 number of 6 ECT reactor is shown in **Table 3.9**.

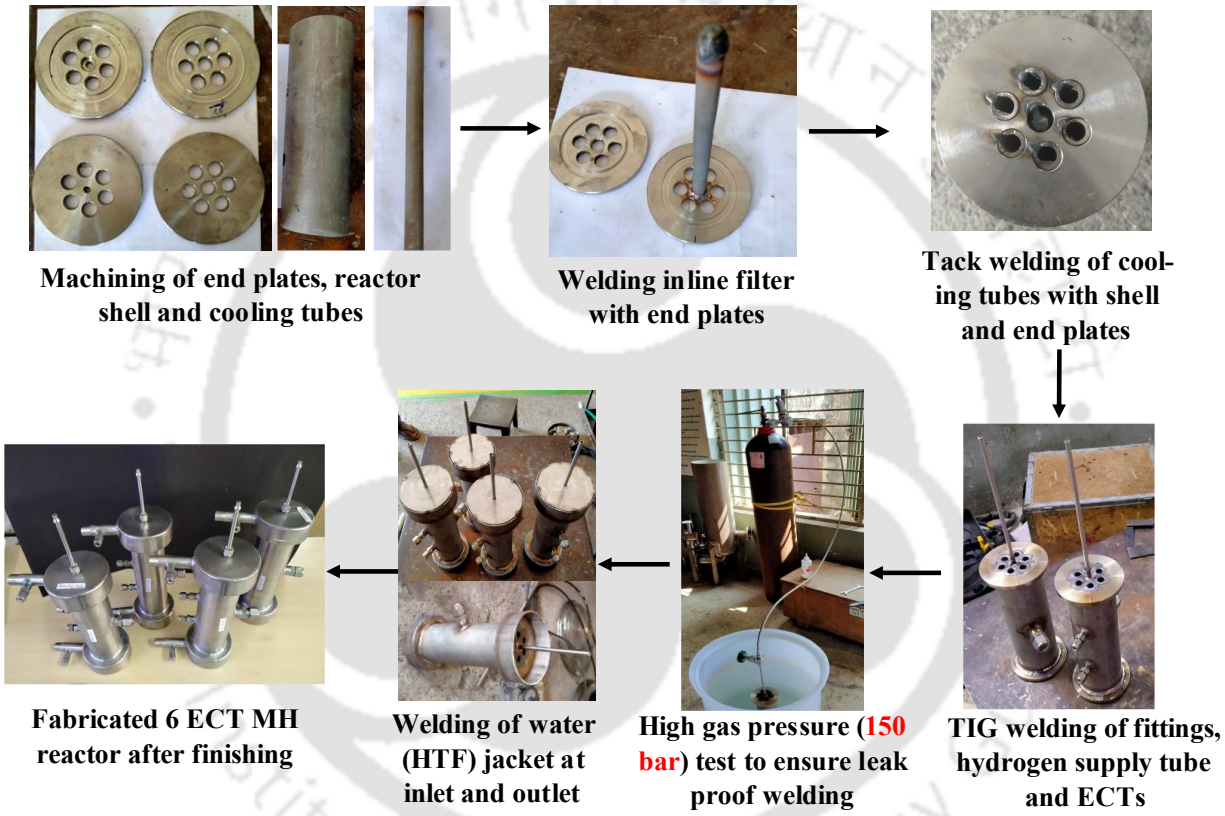

Fig. 3.8 Sequence of steps involved in the reactor fabrication

The fabrication of the reactor was carried out at Shakunth Aqua Products, a Chennai based fabrication company. For fabrication of the reactor, initially the raw material was procured and machined using CNC. Suitable groove of 2 mm depth was provided in the end plates to ensure proper and leak proof weld joint. Further, the SS sintered porous filter was welded with the end plate followed by stacking of ECT with tack welding. After tacking of the ECT, shell was placed and welded with end plated from both side. At the end the ECT's were welded from the outside

and the Swagelok fitting for the alloy filling port and weld connectors for the thermocouple were also welded. Once the reactor configuration was welded, it was tested with argon gas at 140 bar pressure. After ensuring the no leak in the reactors, the HTF jacket at both the ends were welded.

Table 3.9 Raw material procured for fabricating 4 number of 6 ECT reactor

S. No.	Part Name	Dimension	Quantity (Each Reactor)	Total Quantity (4 Reactors)
1.	Shell (SS 316)	Seamless Tube 73 mm OD 59 mm ID	239 mm	1 m
2.	Cooling Tube (SS 316)	Seamless Tube 13.7 mm OD 9.2 mm ID	1.5 m	6 m
3.	Hydrogen tube (SS 316)	Seamless Tube 6.35 mm OD 4.57 mm ID	250 mm	1 m
4.	Reactor Back & Reactor Front	SS 316 Circular disk 101.6 mm dia 7 mm thickness	2 No.	8 No.
5.	Water Jacket Disk	SS 316 Circular disk 101.6 mm dia 3 mm thickness	2 No	8 No.
6.	Water Jacket Tube	SS 316 tube 107.6 mm OD 101.6 mm ID	2 No. of 40mm length each	350 mm
7	SS 316 Porous Filter	14 mm OD 10 mm ID	250 mm	1 m
8	Swagelok fittings	For thermocouples and filling port	SS316 weld connector ¼ inch 4 number and 1 number ½ inch in each reactor	Weld connector ¼ inch 16 number & ½ inch 4 number

For detailed purification study, fabricated reactors were filled with 1.2 kg of and $La_{0.9}Ce_{0.1}Ni_5$, $LaNi_5$ and $LaNi_{4.7}Al_{0.3}$ alloy in each for multi-stage purification study. Before filling the alloy, the raectors were pressurised with H_2 gas at 100 bar and was left for 24 hour, to ensure leak proof arrangement. Further, K-type thrtmocouple with probe length of 40 mm and 30 mm were calibrated and attched with the bed theromocouple slot in the reactor, each located at 75 mm from

adjacent ends of the reactor.. The filled reactors with thermocouple attachement is presented in **Fig. 3.9**.

Fig. 3.9 Pictorial view of reactors filled with 1.2 kg of $La_{0.9}Ce_{0.1}Ni_5$ $LaNi_5$ and $LaNi_{4.7}Al_{0.3}$

3.6.2 Fabrication and alloy filling in 99 ECT Reactor (Large Scale Reactor)

According to the design methodology adopted by (Raju et al., 2019), MH reactor with 99 ECT was fabricated using SS316 material. The pictorial view of the fabricated reactor is shown in Fig. 3.10 and the tube arrangements with dimensional details are given in **Table 3.10**. The embedded cooling tubes used for circulating HTF during absorption/desorption process was made of SS316 material with 6.35 mm outer diameter and 4.57 mm inner diameter. Cooling tubes were aligned straight with the help of a supporting SS316 disk at centre while they were welded on both ends to SS316 circular plates of 10 mm thickness. These end plates are termed as flange plates. On the outside end of these end flange plates, cylindrical chambers of SS 316 with 2 mm thickness were welded and they act us HTF collection chambers at inlet and outlet.

As shown in **Fig. 3.10a**, inline SS316 sintered filter of 2 μm pore size and 14 mm outer diameter was introduced at centre for uniform supply/collection of hydrogen in/from MH bed during absorption/desorption process and also to prevent the carry-over of MH powder by H_2 gas during

desorption. Suitable fittings were provided for integrating thermocouples in the reactor bed and at heat transfer fluid inlet/outlet. The reactor was designed and tested to withstand the pressure up to 140 bar.

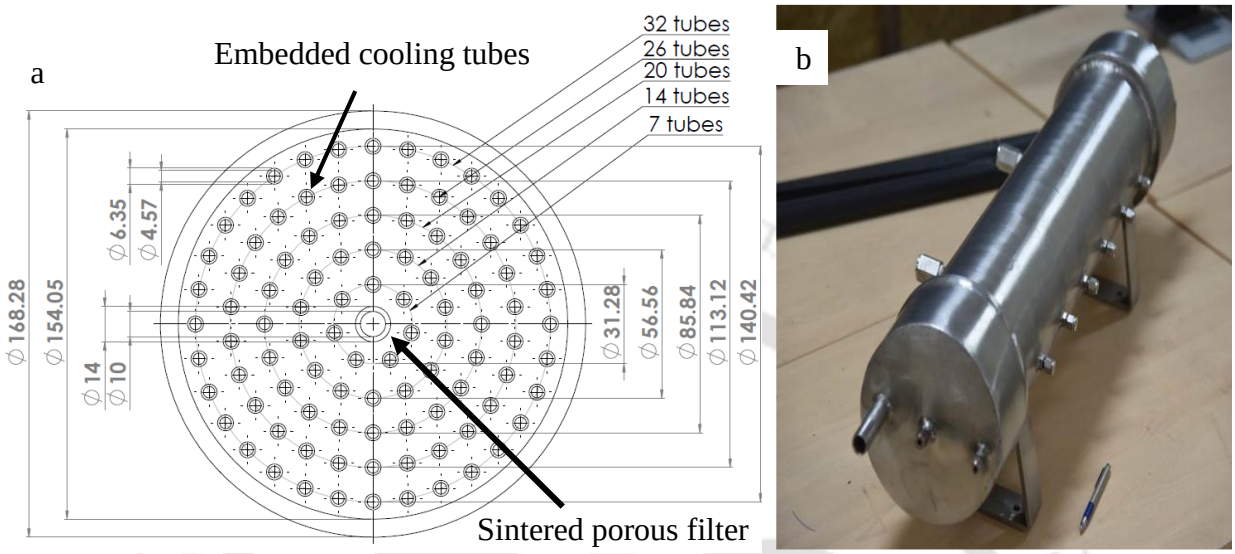

Fig. 3.10 (a) Pictorial view of Embedded cooling tube arrangements and (b) fabricated reactor.

Table 3.10 Dimensional details of 99 Embedded cooling tube MH Reactor.

Outer Diameter (mm)	Inner Diameter (mm)	Radial location of cooling tubes from the center (mm)	Number of cooling tubes in radial location	Total number of cooling tubes	Reactor Length (mm)	Mass of Reactor (kg)	Mass of alloy (kg)
168.28	154.04	15.64	7	99	700	31.96	40
		28.28	14				
		42.92	20				
		56.56	26				
		70.21	32				

Fig. 3.11 shows the pictorial view of activated MH reactor integrated with components like secondary inline filter, K-type thermocouples, HTF tube fitting, etc. The 700 mm long reactor bed was provided with the provision of connecting 6 thermocouples at equidistance from each other. Two alloy filling ports of 1inch diameter were provided for smooth filling of the alloy and to ensure, even distribution of alloy throughout the reactor. A secondary inline filter was provided at

both the reactor ends, to ensure the enactment of alloy within the reactor, if the primary filter goes through any failure.

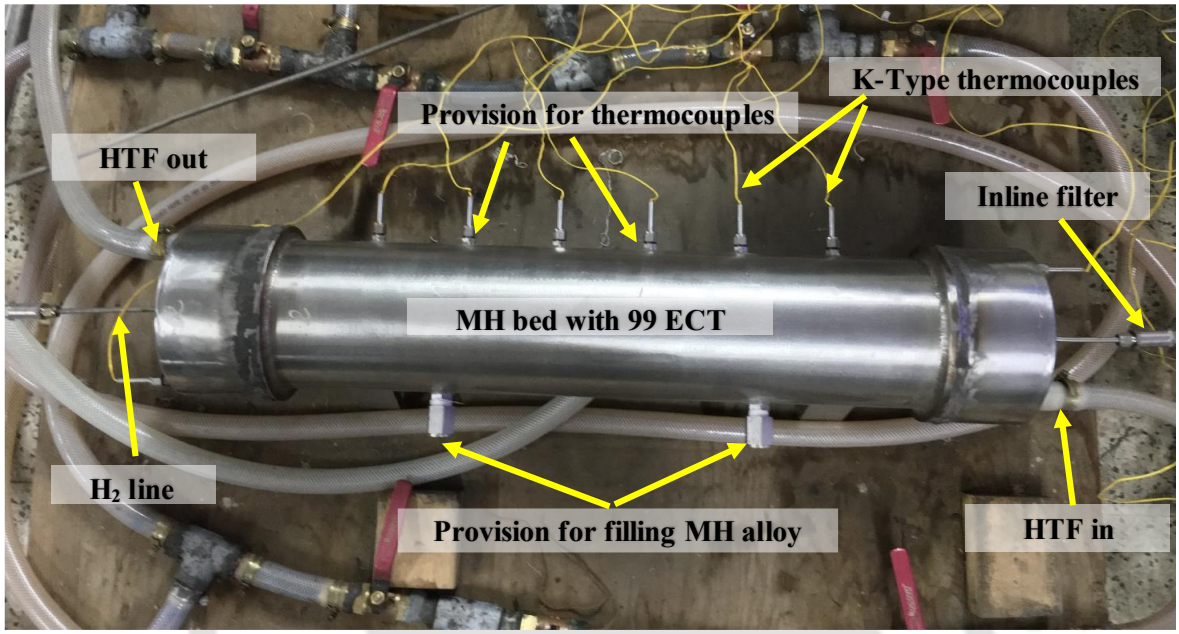

Fig. 3.11 Pictorial view of activated metal hydride reactor

3.7 Alloy Selection

In order to counter a specific application, selection of suitable MH alloy is very essential [6]. Considering the hydrogen storage and purification application, few suitable alloys have been shortlisted on the basis of their PCI characteristics.

3.7.1 Selection of $LaNi_{4.7}Al_{0.3}$

As depicted in **Fig. 3.12**, the PCI of $LaNi_{4.7}Al_{0.3}$ shows nearly flat plateau. Following observations can be drawn from the PCI curve of $LaNi_{4.7}Al_{0.3}$**.**

- For low absorption temperature (20 °C to 30 °C), the alloys can easily absorb hydrogen at even low pressure (1 bar to 2 bar).
- The stability of alloy at ambient conditions makes it suitable for hydrogen purification application.
- Considering its higher desorption temperature (> 70 °C), the alloy can easily be flushed at ambient conditions for removal of impure gases.

Considering all the observations made from PCI curve, the alloy is very much suitable for hydrogen storage and purification applications.

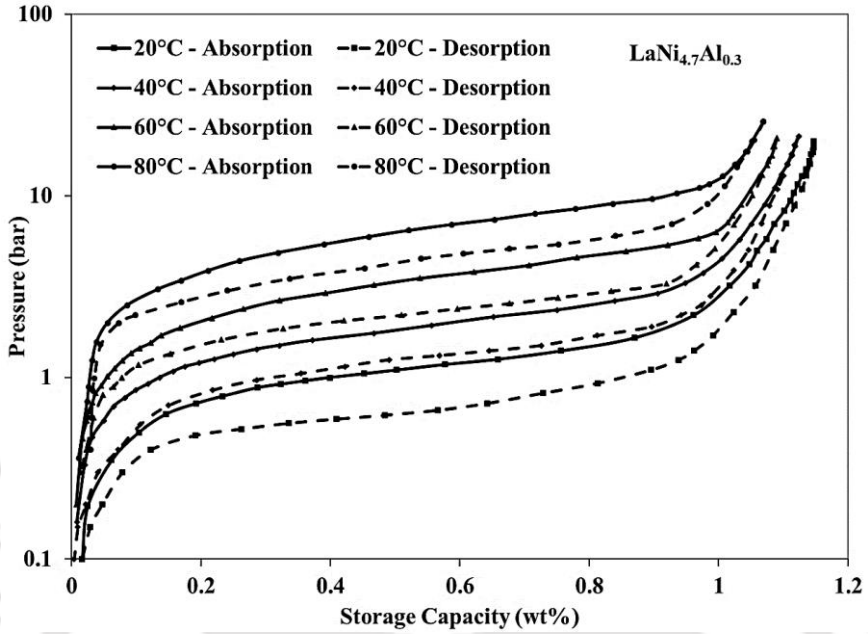

Fig 3.12 PCI of $LaNi_{4.7}Al_{0.3}$

3.7.2 Selection of $La_{0.9}Ce_{0.1}Ni_5$

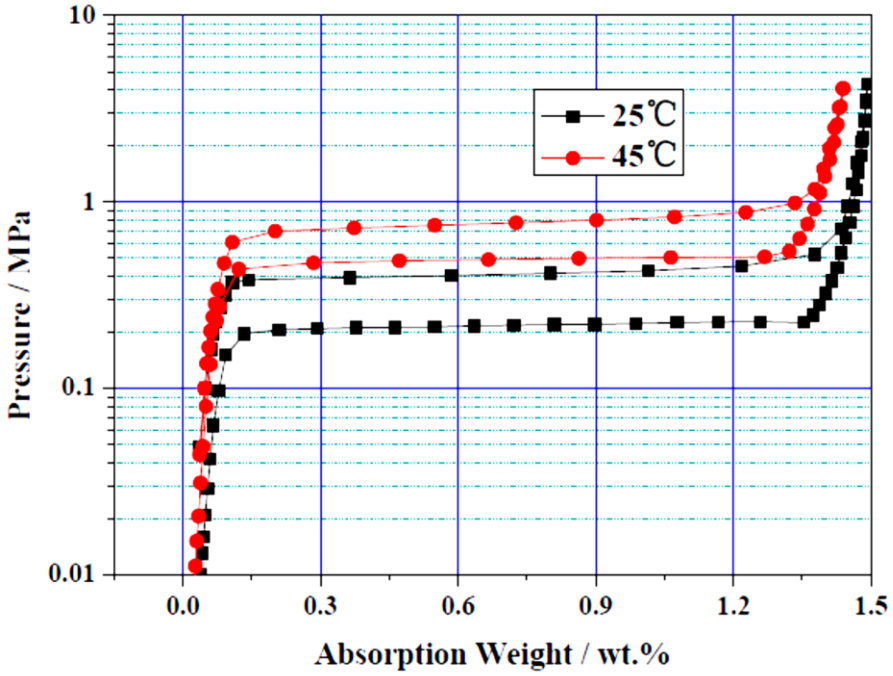

Fig. 3.13 PCI of $La_{0.9}Ce_{0.1}Ni_5$

The PCI curve of $La_{0.9}Ce_{0.1}Ni_5$ is shown in **Fig. 3.13**. Following observations can be made from the PCI curve of $La_{0.9}Ce_{0.1}Ni_5$:

- The flat plateau of the PCI curve ensures the reversibility of the alloy for a particular absorption/desorption conditions.
- Significant hysteresis between the absorption-desorption curve, makes it suitable for hydrogen purification application.
- As the equilibrium pressure of alloy is above atmospheric pressure (for 25 °C temperature), it is difficult for the alloy to flush it at ambient conditions, as it can lead to hydrogen loss. However, bringing down the bed temperature during flushing can be a better option.

Considering the mentioned reasons, $La_{0.9}Ce_{0.1}Ni_5$ alloy can be used for hydrogen storage and purification. Though, the flushing temperature has to be low (~15 °C), however, the alloy can be used in the first stage of MH based multi stage purification system, as it can be desorbed at desirable high pressure at temperature above 60 °C, which will enable enhanced absorption in $LaNi_{4.7}Al_{0.3}$.

3.7.3 Selection of $LaNi_5$

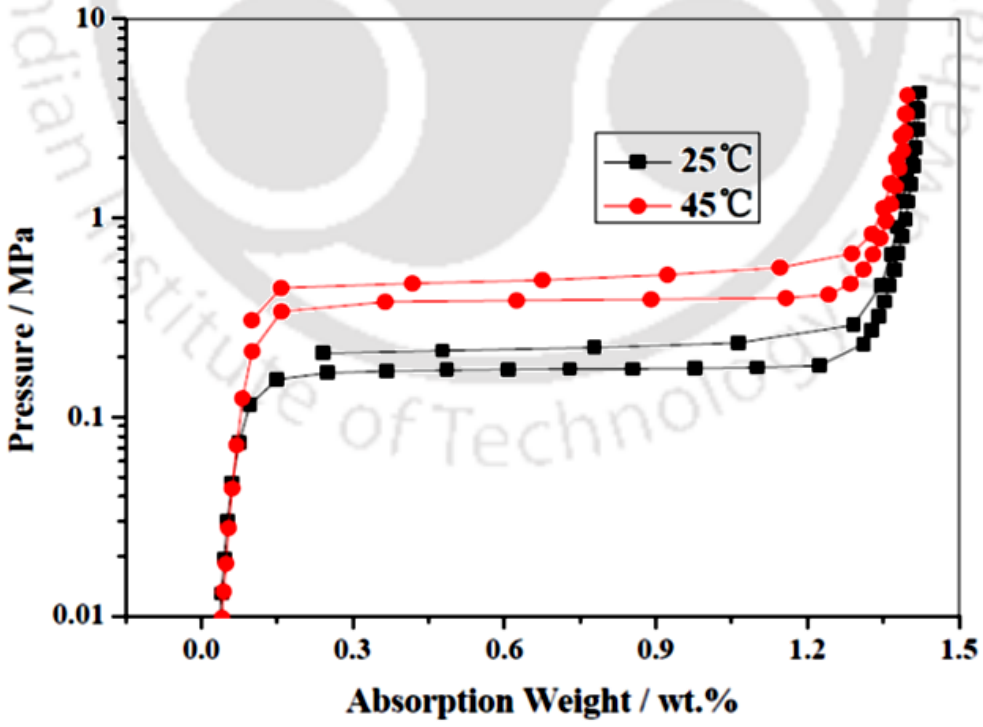

Fig. 3.14 PCI of $LaNi_5$

Considering the PCI of $LaNi_5$ as depicted in **Fig. 3.14**, following observations are made:

- The alloy is suitable for MH based hydrogen purification system, as its equilibrium pressure near ambient temperature is near to ambient pressure. Because of relatively less equilibrium pressure at room temperature, there will be less hydrogen loss during the flushing process, as the pressure gradient will drive the spontaneous desorption of the system.
- The efficient desorption pressure of the alloy is well above 50 °C; this will facilitate hydrogen recovery by using waste heat of 50 °C to 70 °C magnitude.

Considering all the observations made from PCI curve, the alloy is very much suitable for hydrogen storage and purification applications.

3.8 Summary

The present chapter reports the details of the numerical model developed for the fabrication of the MH reactor and the comparison between the different reactor configurations. The design methodology and the equations considered for the numerical simulation along with the result obtained is also discussed in the chapter. The chapter also reports the criterial of tube selection for the different reactor configuration. The fabrication procedure and the configuration of the small (6 ECT) and large scale (99 ECT) reactors are also reported in the present chapter. Based on PCI characteristics of three different alloys, $LaNi_{4.7}Al_{0.3,}$ $LaNi_5$ and $La_{0.9}Ce_{0.1}Ni_5$ are found suitable for hydrogen storage and purification application. Further, confirmation for the suitability in purification application is made through parametric studies of the alloys, which is discussed in the next chapter

CHAPTER 4 SETUP FOR EXPERIMENTAL INVESTIGATION

The experimental setup was developed to carry out detailed parametric and purification studies on the single and multi-stage MHHPS, wherein the impure sample preparation, absorption of impure mixture, flushing, desorption and sample collection for gas chromatography were carried out using a single gas circuit of specific configuration, as depicted in **Fig. 4.1**.

4.1 Experimental Setup for Single Reactor/Single Stage Experiments

An experimental facility was developed to conduct experimental studies on the metal hydride based hydrogen storage and purification system (MHHSPS). The experimental test setup constitutes of Coriolis mass flow meter (CFM), data acquisition system (DAQ), high and low temperature recirculating baths, heat transfer fluid (HTF) flow meter, vacuum pump, gas chromatography, gas cylinders, high pressure gas circuit with valves and fittings and HTF circuit. The experimental setup was fabricated in such a way that, it can be used for preparing impure sample, collecting samples for TCD (thermal conductivity detector) analysis in gas chromatography, and performing experiments to test working of MHHPS. The schematic of experimental test facility is depicted in **Fig. 4.1**. Initially the impure gas sample was prepared wherein the respective gas was transferred from the pure gas cylinders to the sample cylinder through the gas circuit, and the gases were mixed in particular weight (gram) ratio. For example, in order to prepare the gas mixture of particular composition, initially the gas circuit and the sample cylinder was evacuated using a vacuum pump. Further, the valves V_1 and V_2 were kept open and CO_2 was sent to a sample cylinder by opening CO_2 cylinder, and valve V_7 of the sample cylinder. The amount of gas transferred was measured by CFM. Once the required amount of gas was transferred to the sample cylinder, respective valves were closed and the circuit was re-evacuated. The same process was repeated for the other gases, and the absorption mixture of particular composition was prepared in the sample cylinder. The pictorial view of the experimental setup is depicted in **Fig. 4.2**.

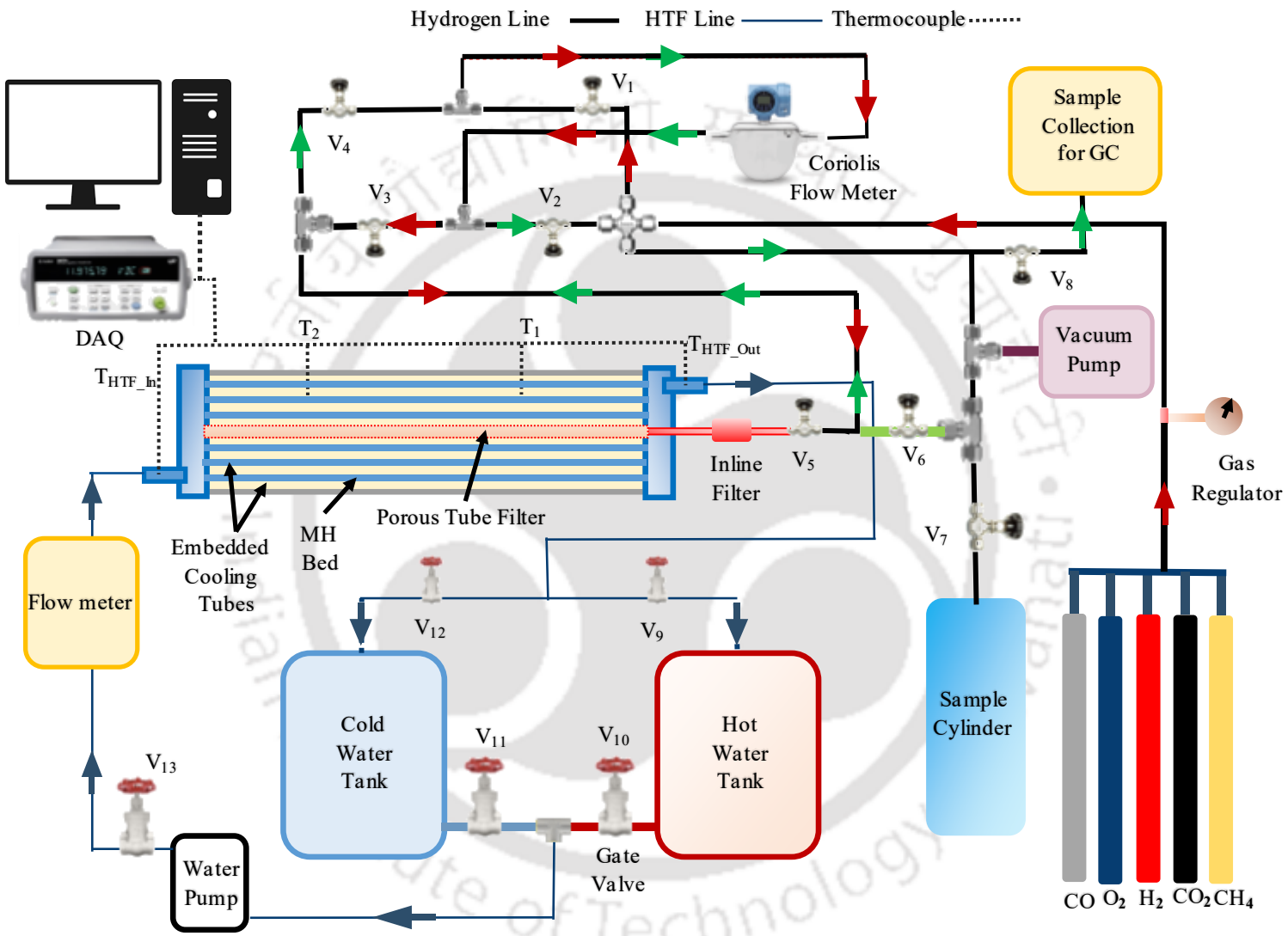

Fig. 4.1 Schematic of Experimental Test Setup for MHHPS

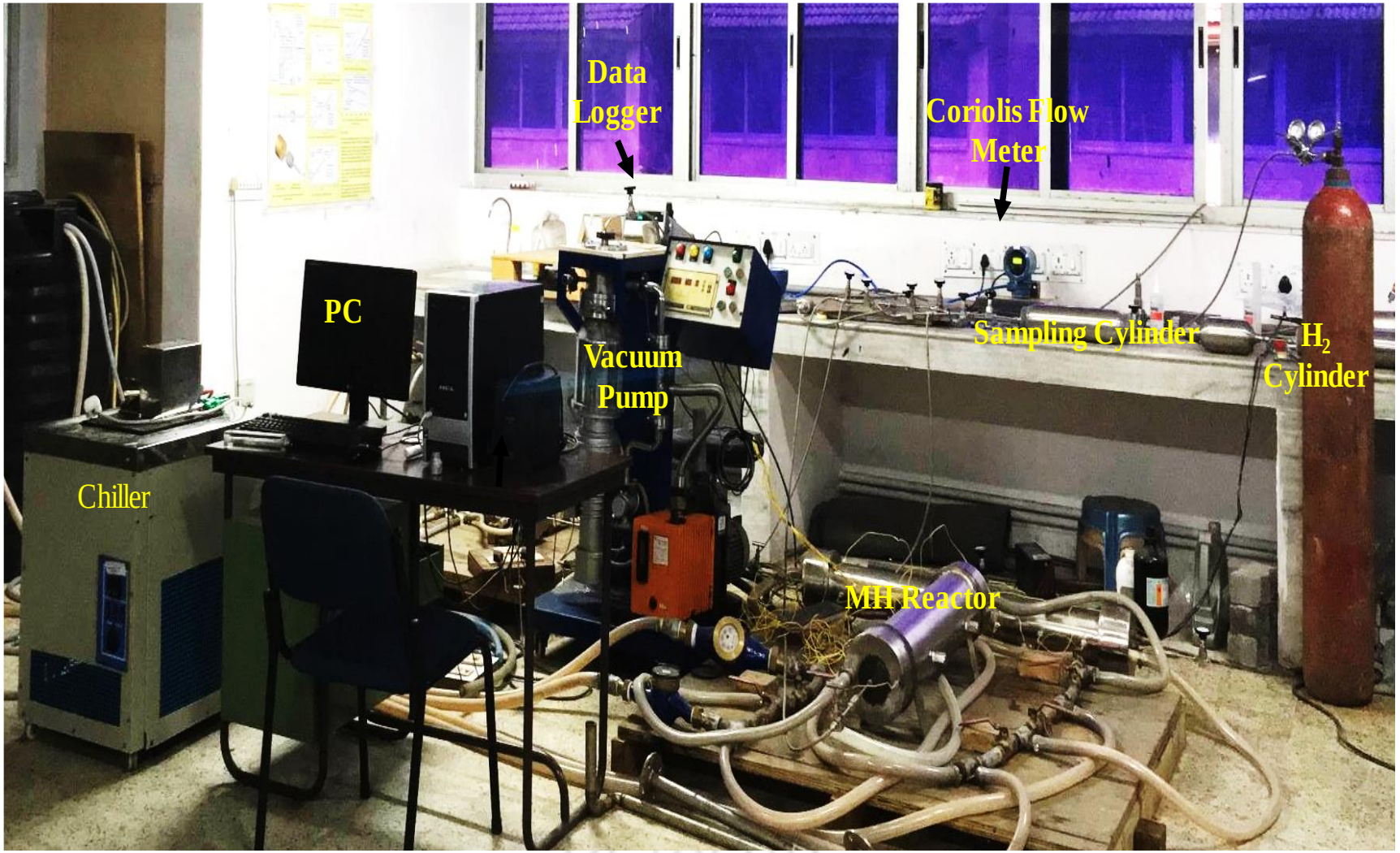

Fig. 4.2 Schematic of Experimental Test Setup for MHHPS

Further, the MH reactor was prepared for absorption, wherein the bed was maintained at low temperature (20 °C) through continuous recirculation of cold HTF (water). The recirculation of water through the reactor was facilitated by the continuous operation of the cold recirculating bath, wherein the valves V_{11}, V_{12} and V_{13} were kept in open position. Once the MH bed reaches, desired absorption temperature, impure hydrogen from the sample cylinder was supplied to the reactor through the Coriolis mass flow meter (to record amount of gas transferred to the reactor), by positioning valves V_7, V_1, V_3 and V_5 in open condition. The pressure of the gas was set using the pressure regulator attached with the sample cylinder. The variation in the temperature of the HTF and the MH bed were recorded using K-type thermocouples attached with the DAQ and computer.

Once the absorption was complete, the bed was further brought down to the lower temperature, i.e 15 °C and prepared for flushing. During the flushing process, the impure gases from the void space of the reactor was removed by keeping valve V_5, V_2 and V_4 open, and the gas was collected for Thermal Conductivity Detector (TCD) analysis in the gas chromatography through valve V_8.

Further, the MH reactor was prepared for desorption, wherein the reactor was brought to an elevated temperature (90 °C), through the continuous recirculation of HTF from high temperature recirculating bath. During this process, V_9, V_{10} and V_{13} were kept open and the high temperature recirculating bath was maintained at 90 °C. Ensuring the equilibrium condition for the MH bed and HTF, valves V_5, V_2 and V_4 were opened and the reactor was desorbed to open atmosphere. The absorption, desorption and flushing samples were collected for TCD analysis in gas chromatograph.

4.2 Experimental Setup for Multi-Stage MHHPS Studies

As discussed in the previous chapter, three identical MH reactors with 6 ECT was fabricated and each were filled with 1.2 kg $La_{0.9}Ce_{0.1}Ni_5$ (R1), $LaNi_5$ (R2) and $LaNi_{4.7}Al_{0.3}$ (R3) in the shell side of each reactor, and were placed in first, second and third purification stages, respectively. Water was used as HTF, which flows through the tube side to facilitate heat transfer in the MH bed. A complete one cycle of the experiment was carried out in three steps i.e. absorption of impure mixture, flushing of void gases and desorption of absorbed hydrogen. The impure mixture consists of hydrogen and other gas (CO_2, CO, N_2, Ar, CH_4, etc). During absorption, the MH bed is maintained at room temperature (25-30 °C) and the impure hydrogen gas mixture was supplied to the reactor through gas

circuit from the impure sample cylinder at required pressure using gas pressure regulator. The schematic of the experimental setup is depicted in **Fig. 4.3**. As the MH alloy has high affinity to hydrogen gas, it starts absorbing the hydrogen from the gas mixture to form solid solution, whereas the impure gas remains in the void space. As absorption is an exothermic process, a constant supply of HTF at room temperature is maintained through the reactor bed, in order to remove the evolved heat from the bed to facilitate faster absorption. These impure gases are removed from the reactor by flushing the reactor at low temperature (preferably 15-20 °C). After which, the MH bed is raised to a higher temperature (70-90 °C) by circulating HTF through the reactor bed using high temperature bath. As soon as the bed attains the requisite temperature, the outlet valve is opened to collect pure hydrogen. For higher level of impurity, the system is operated in multi stage. The pictorial view of the test setup developed at IIT Guwahati is depicted in **Fig. 4.4** and **Fig 4.5**.

As discussed in the previous paragraph, each cycle of the purification experiment is divided into three stages i.e. absorption, flushing and desorption. The detailed discussion on the procedure adopted for each stages in the purification study for musty-stage system are as follows:

4.2.1 Absorption of Impure Mixture

Initially, stage 1 reactor (R1) was utilized for the absorption process. The MH alloy bed is maintained at room temperature (20-30 °C) using constant supply of HTF through the HTF line and ECT, by keeping valves V_w1, V_w2, V_w11 and V_w14 in open position and pump in a running mode, to ensure recirculation of cold fluid though R1. Further, the impure hydrogen gas mixture was supplied from the source to the reactor through gas circuit keeping valveS V_g1, V_g4 and V_g5 in open position at a specific supply pressure of about 10-15 bar. The impure gas mixture gets distributed uniformly in the reactor bed through the sintered porous filter. As the R1 containing $La_{0.9}Ce_{0.1}Ni_5$, which has high affinity to hydrogen gas, it starts absorbing the hydrogen from the gas mixture to form $La_{0.9}Ce_{0.1}Ni_5$-H_6 compound. However, the other gases are unabsorbed and remain in the void space of the reactor. As absorption is an exothermic process, a constant supply of HTF at room temperature was maintained through the reactor length, in order to remove the excess heat from the powder bed. This ensures faster absorption rate. Higher supply pressure (10-25 bar) also leads to the faster rate of absorption because of higher pressure gradient between the equilibrium pressure of MH bed at absorption temperature and supply condition.

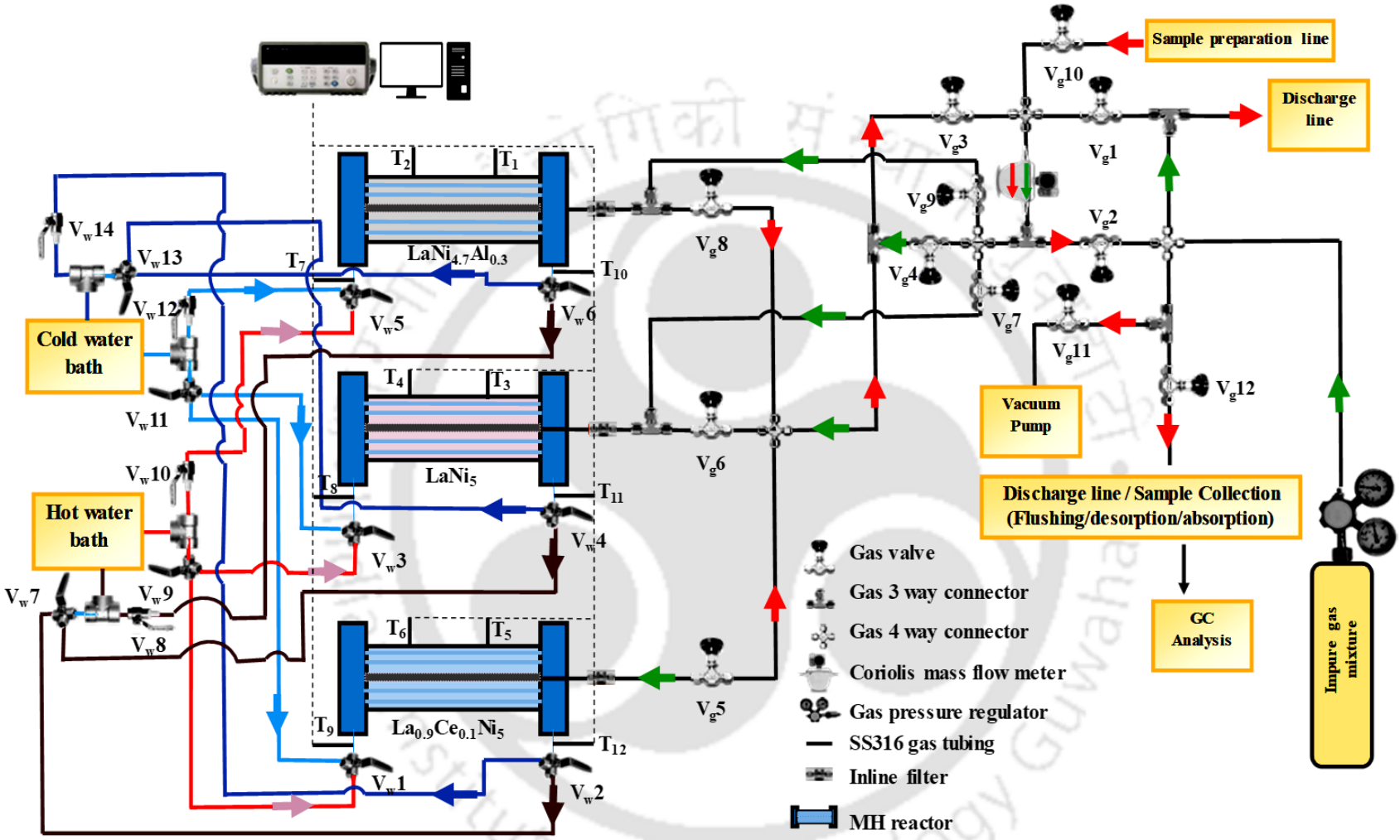

Fig. 4.3 Schematic view of 3-Stage MHHPS experimental setup

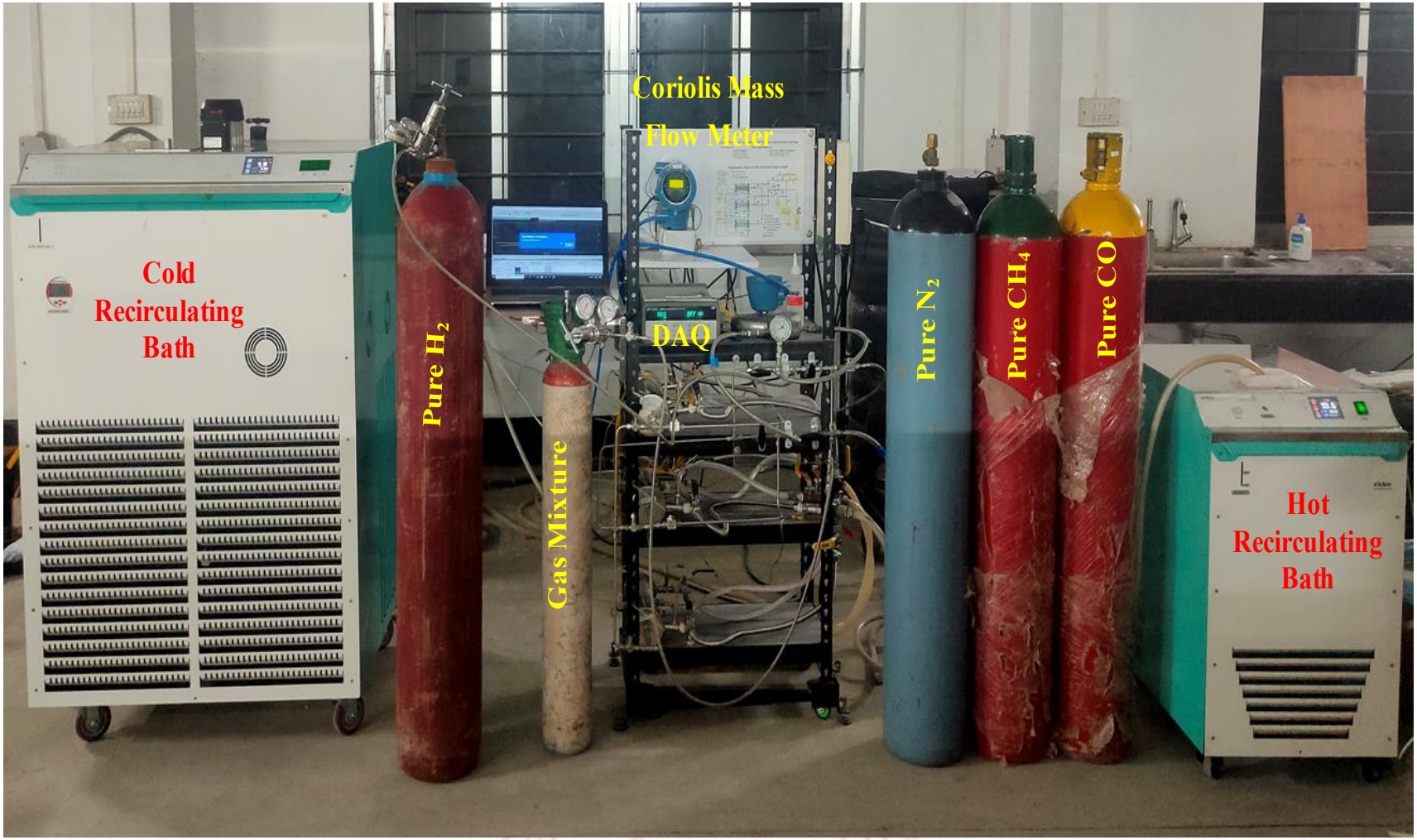

Fig. 4.4 Pictorial view of the 3-stage MHHPS

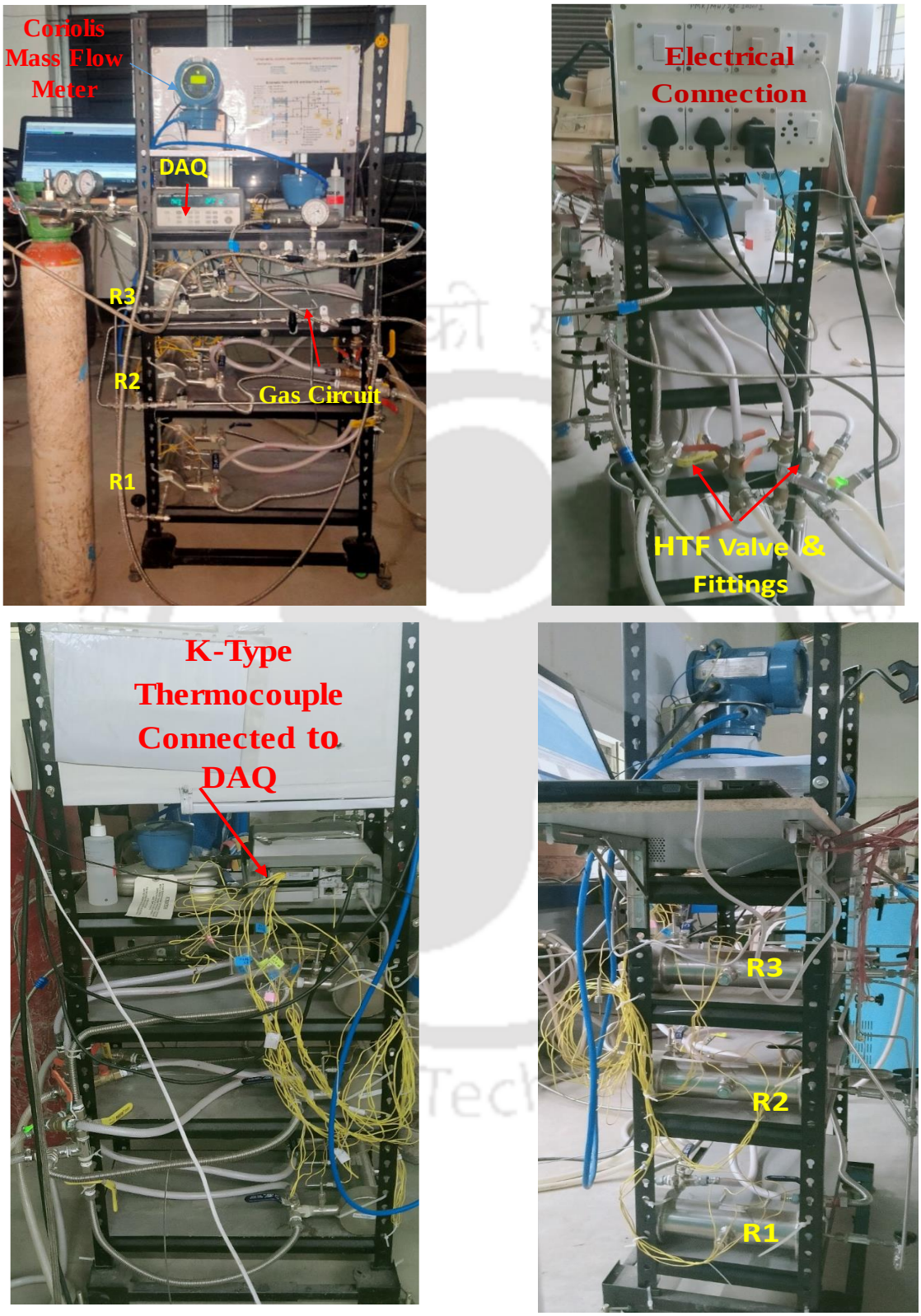

Fig. 4.5 Setup structure from (a) Front view, (b) right side view, (c) back side view & (d) left side view

4.2.2 Flushing of Void Gases

After completion of absorption process, the impure gases remain in the void space of the alloy bed are removed from the reactor by flushing the reactor at low temperature. During flushing, the reactor R1 is maintained at room temperature (15-20 °C), keeping HTF valve arrangements same as absorption, while the gas circuit is set to desorption mode, by keeping valves V_g5, V_g3 and V_g2 in open to atmosphere, or exposed to vacuum pressure using vacuum pump. In few second, the impure gases present in the void space are flushed out to the atmosphere through a flushing line. After completion of flushing, all the gas circuit valves are closed, and the reactor is prepared for desorption process.

4.2.3 Desorption of the Absorbed Hydrogen

In order to prepare MH bed for desorption, R1 was connected to high temperature recirculating bath, wherein, HTF at 70 °C to 90 °C was supplied to the reactor bed. A thermal equilibrium between the bed and HTF is ensured before the start of desorption. For the high temperature HTF circulation, valves V_w1, V_w2, V_w7 and V_w9 are kept in open position with the pump in running mode. Because of endothermic nature, the desorption reaction utilizes the available input heat from HTF to desorb the stored hydrogen. As soon as the bed achieves the required temperature, the desorption valves are opened as per single or multistage operational requirement. If the impurity content in the gas mixture is in the range of 5-20%, the purified hydrogen can be collected directly after single stage. In this case, valves V_g5, V_g3 and V_g2 can be operated and can be collected in the collection chamber or can be directly utilized for fuel cell application.

However, if the impurity content is more than 20%, the hydrogen gas from reactor R1 can be sent to reactor R2 ($LaNi_5$). During this process, R2 being the absorbing reactor, shall be connected to the cold fluid line by keeping valves V_w3, V_w4, V_w11 and V_w13 in open position to facilitate continuous circulation of cold HTF within bed R2, and simultaneously bed R1 is maintained at higher temperature, same as in desorption phase 1. Once the reactors R1 and R2 attain their respective bed temperature, the gas valves V_g5, V_g3 and V_g7 should be opened to allow the transfer of gas from R1 to R2 through the Coriolis mass flow meter. Once, the transfer is completed, R2 is further cooled to the flushing temperature (15-20 °C), wherein the gas valves V_g6, V_g3 and V_g2 are opened to flush out void gases.

Further, the bed temperature of the reactor R2 can be raised up to temperature (80-90 °C) through continuous circulation of HTF from the hot water bath, setting valves V_w3, V_w4, V_w7 and V_w9 in open position. Once the MH bed attains the required desorption temperature, gas valves V_g6, V_g3 and V_g2 should be opened, to allow pure hydrogen flow outside the reactor and can be collected for further utilization.

For obtaining ultra-pure hydrogen (99.9995% purity), instead of going with desorption of R2, the hydrogen can be diverted from R2 to R3. For this, R2 should be supplied with high temperature HTF (80-90 °C) and R3 should be supplied with low temperature HTF (20-30 °C) by setting HTF valves in respective positions. Once both the bed attains respective temperature, gas valves V_g6, V_g3 and V_g9 are opened to allow flow of hydrogen from R2 to R3. Further, the reactor R3 is flushed at 20-25 °C in the similar way as R1 and R2. During flushing of R3 gas valves, V_g8, V_g3 and V_g2 are opened and cold HTF is recirculated through HTF valve V_w5, V_w6, V_w12 and V_w14. The ultra-pure hydrogen can be obtained by desorbing reactor R3. For that, the reactor R3 is raised to 90-95 °C by recirculating high temperature HTF, keeping valves V_w5, V_w6, V_w10 and V_w9 in open. Once the bed attains required desorption temperature, the gas valve V_g8, V_g3 and V_g2 are opened to collect ultra-pure hydrogen.

During various steps of hydrogen separation, the temperature of MH bed and HTF are measured using K-type thermocouples, that are connected to a data acquisition system (DAQ). During all stages of the separation cycle, the system is operated in a closed loop to isolate it from atmospheric contaminants. The hydrogen transfer to/from the reactor were recorded using the Coriolis mass flow meter and the cold and hot HTF were circulated using low and high temperature recirculating baths. After certain number of purification cycles, the bed poisoning was witnessed. Therefore, the MH bed needs to be regenerated time to time (depending upon impurity level).

4.2.4 Regeneration of the Alloy Bed

Depending upon the impurity contents, the bed can be poisoned/degenerate after considerable number of absorption/desorption cycles (number of cycle totally depends on the amount of impurity and type of impurity). However, the bed can be regenerated by reactivation process, wherein the MH reactor is evacuated at high temperature (90-95 °C) using vacuum pump. During the regeneration of alloy bed, the respective reactor is supplied with the high temperature HTF (90-95 °C), and parallel, the vacuum pump is operated by achieving the vacuum pressure of 10^{-2}

to 10^{-1} mbar. Once the bed achieves set vacuum pressure, all the valves are closed and the reactor is cooled down and the absorption process is repeated with pure hydrogen. During the regeneration absorption process, pure hydrogen is supplied at higher pressure (20-30 bar). Once the absorption is completed, MH bed is again raised to higher temperature (90-95 °C) and the evacuation process is repeated followed by absorption. This absorption-desorption-evacuation is repeated till the bed gets regenerated. It takes 2-3 cycle for complete regeneration of be. However, if the poisoning is very significant, it may take even more number of absorption/desertion cycles. The optimum operating conditions for each stage of the MSMHHSS based upon rigorous experimental studies is reported in **Table 4.1**.

Table 4.1 Operating parameters for MSMHHSS

Operating Cycle	Optimum Operating Range			
	Parameter	R1 ($La_{0.9}Ce_{0.1}Ni_5$)	R2 ($LaNi_5$)	R3 ($LaNi_{4.7}Al_{0.3}$)
Absorption Half Cycle	Absorption Temperature	20 – 25 °C	20 – 30 °C	20 – 35 °C
	H_2 Supply Pressure	10 – 20 bar	10 to 15 bar	5 to 10 bar
Flushing	Flushing Temperature	10 – 20 °C	15 – 20 °C	20 – 25 °C
	Flushing Pressure	Ambient	Ambient	Ambient
Desorption Half Cycle	Desorption Temperature	80 – 90 °C	85 – 90 °C	90 – 95 °C
Regeneration Cycle	Evacuation Temperature	90 – 95 °C	90 – 95 °C	95 - 105 °C
	Evacuation Pressure	10^{-2}-1 mbar	10^{-2}-1 mbar	10^{-2}-1 mbar
	Absorption Temperature	20 – 25 °C	20 – 30 °C	25 – 35 °C
	H_2 Supply Pressure	25 – 35 bar	25 to 30 bar	20 o 25 bar

The core of the system discussed above does not have any mechanically moving components within it. It works mainly on the thermal input, which can be obtained from the waste heat recovery system or solar thermal heat input. The lifecycle of the reactor bed is significantly good, and it can be regenerated over time as per requirement. The system is capable of delivering 99.90-99.9995% pure hydrogen in a single or multi stage operation (depending on impurity content) for an input hydrogen mixture having a purity level up to 50%. However, it is capable of separating hydrogen from a gas mixture with even 90% impurity. But at the same time, for that high impurity content, the cyclic life of the metal hydride bed will largely affected.

The present system can be used for several engineering applications. Some non-limiting examples of the engineering applications where the hydrogen separation system can be added to, include fuel cells, process industries, generator coil cooling, petrochemical industries, for purifying hydrogen generated through biological and chemical means etc.

4.3 Gas Chromatography

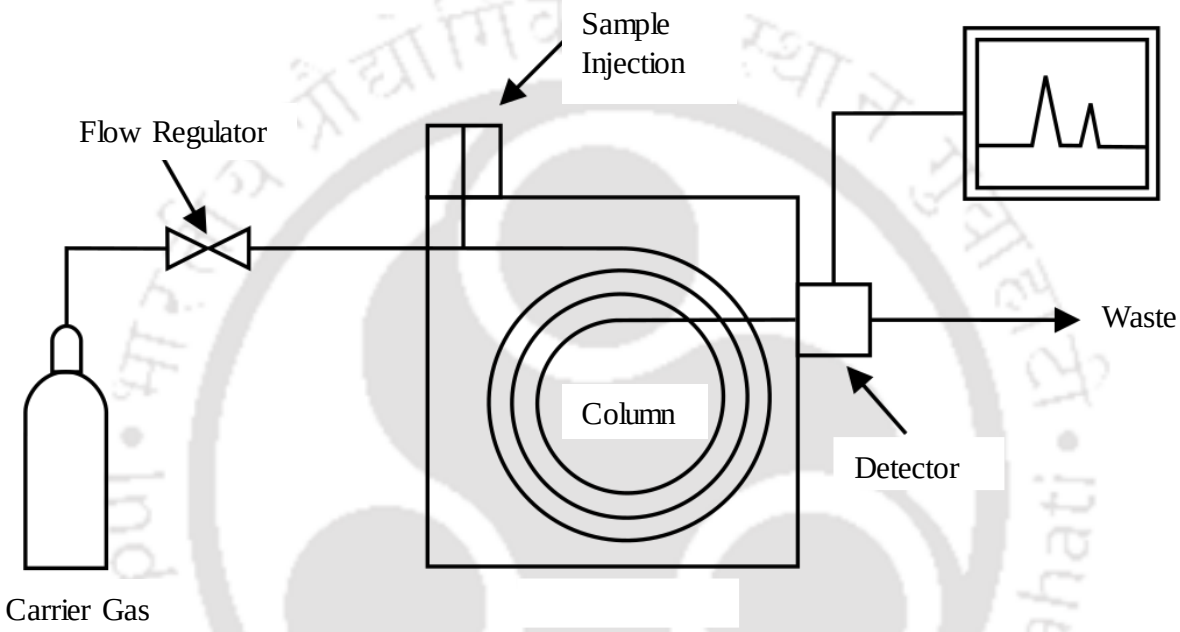

Fig. 4.6 Schematic of Gas Chromatograph

An instrument used for chemical analysis of a gas composition through separation is known is a gas chromatograph. As depicted in **Fig. 4.6**, a gas chromatograph mainly comprises of a column (packed/capillary) to facilitate gas passes at different rate on the basis of their chemical composition, physical properties and interactive nature with the column lining (stationary phase). The gas is electronically detected at the exit near the detector which is generally kept at higher temperature as compared to column. The main function of the stationary phase in the column is to separate different components, causing each one to exit the column at a different time. Other parameters that can be used to alter the order or time of retention are the carrier gas flow rate, column length and the temperature.

4.3.1 Development of TCD method for the present study

The sample detection (retention time) in the TCD mainly depends upon carrier gas flow rate, oven temperature and column length. As depicted in **Fig. 4.7**, with increase in the oven temperature, the peak size increases. This phenomenon is due to the higher sensitivity of filament at higher temperature as gas passes through it. However, the cycle life of the filament decreases at higher temperature. Similarly, with increase in the carrier flow rate, peak separation decreases significantly, this is because of the faster transport of gases through the column, with the carrier gas. However, for efficient peak separation, lower flow rate is preferred, but at the same time sample running time increases.

Considering all these issues, the method parameter for the present study was set as:

- Column flow: 6 mL/min
- Oven temperature 60 °C (Sequentially raised to 150 °C)
- Detector temperature: 250 °C.
- Total run time: 20 min.

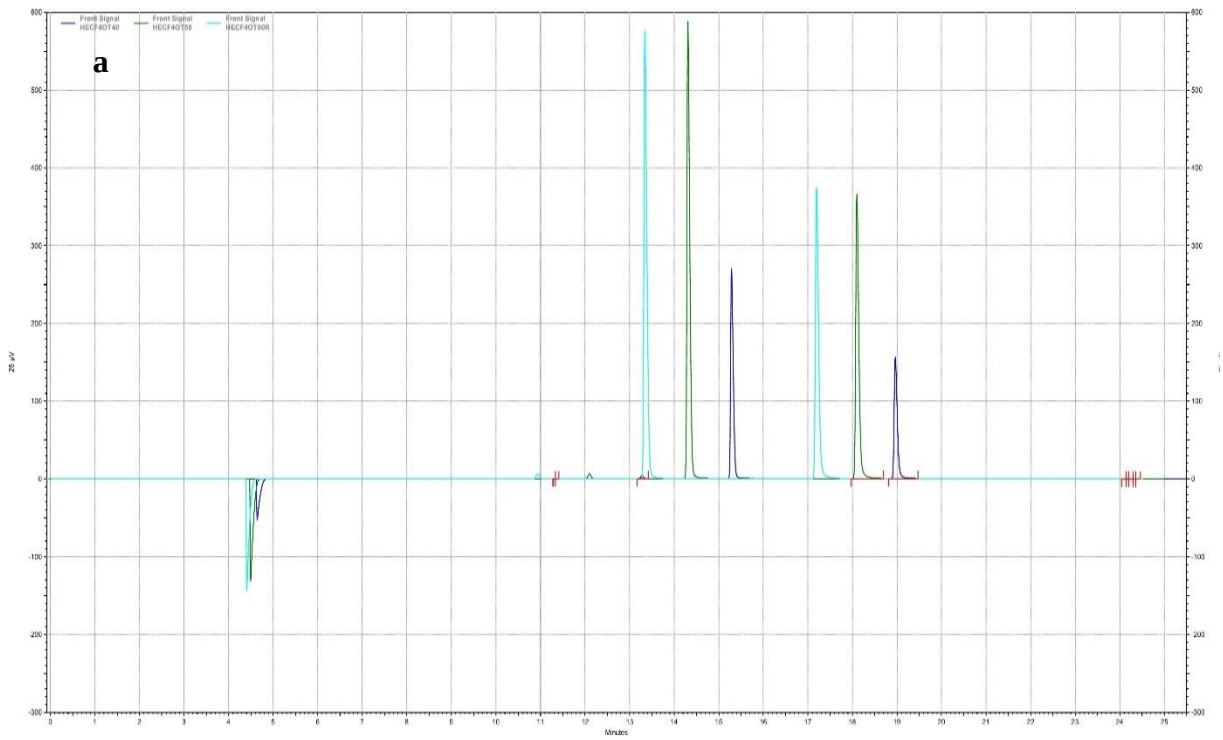

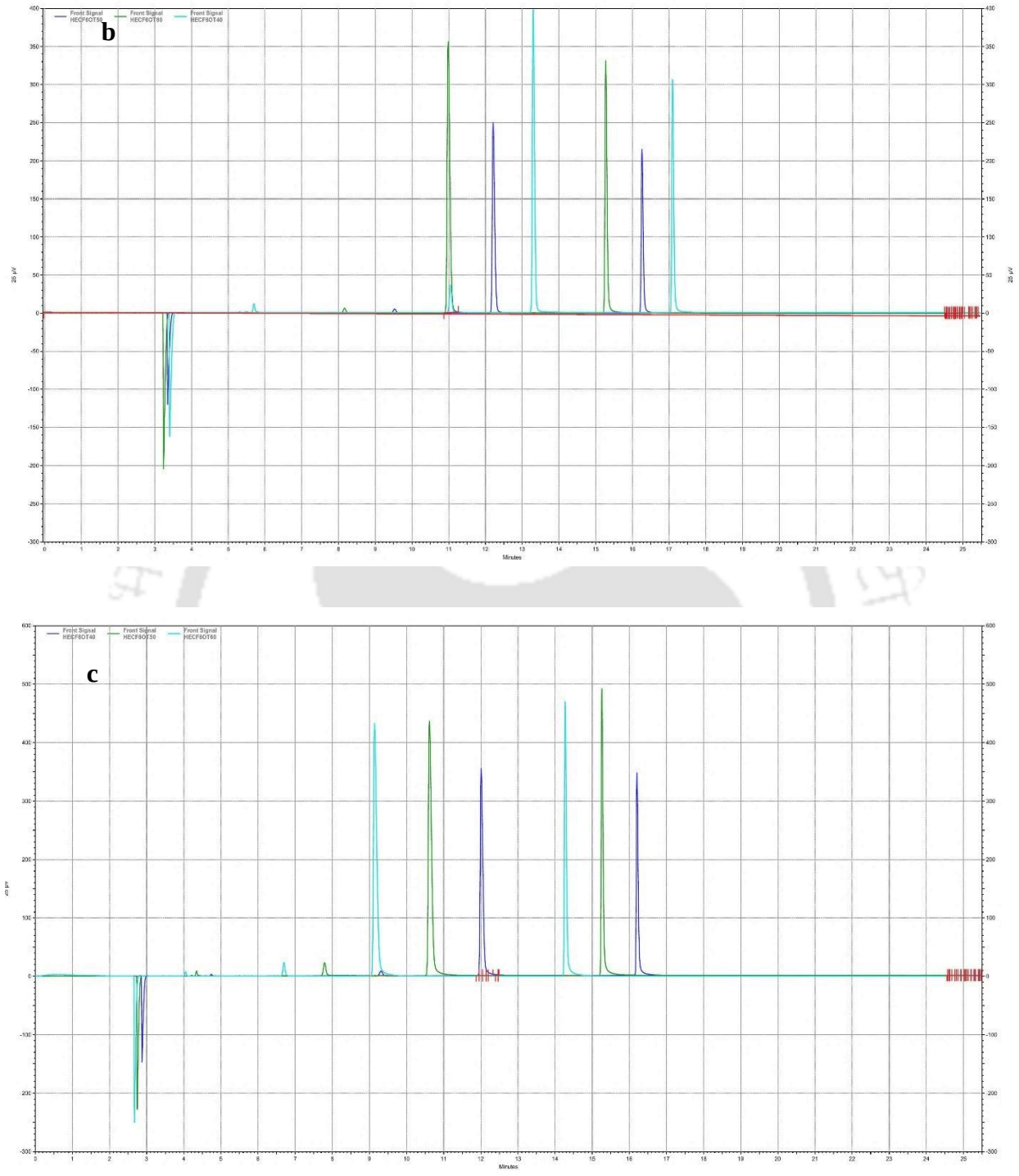

Fig 4.7 Peak retention time variation with varying **(a)** column flow 4 mL/min, **(b)** column flow 6 mL/min and **(c)** column flow 8 mL/min, for oven temperature 40 °C, 50 °C & 60 °C in each case. Gas sequence is hydrogen, methane and carbon monoxide.

4.3.2 Calibration with standard gas sample

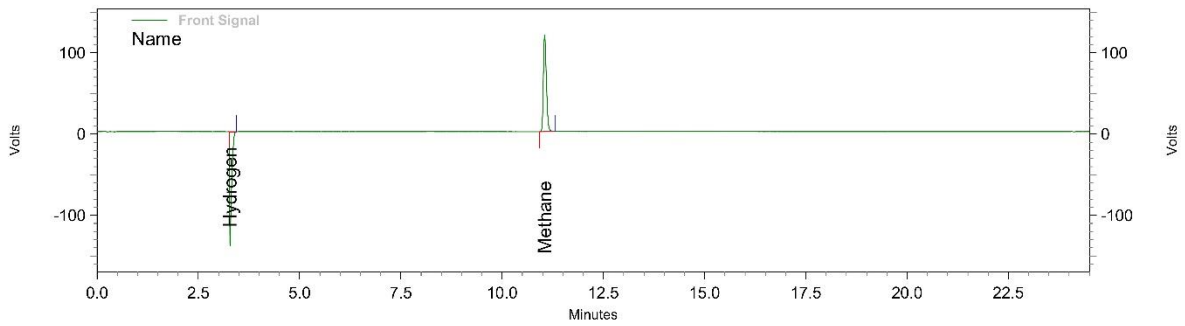

Front Signal Results

Pk #	*Name*	*Retention Time*	*Area*	*Concentration*
1	Hydrogen	3.280	3472259	**90.000**
2	Methane	11.050	4684173	**10.000**

Fig. 4.8 Standard calibration report for gas mixture with 90% H_2 and 10% CH_4 by weight**.**

Thermal conductivity detector (TCD) was used to analyze the gas composition at each stage of the purification cycle. During the absorption, flushing and desorption process, the gas samples are collected for its analysis using gas chromatograph (GC). The TCD analysis is carried out using AGILENT 8890 GC, wherein "CP Molsieve 5A" column is used for analysis. During TCD analysis, column flow is kept as 6 mL/min and oven temperature is systematically raised from 60 °C to 150 °C. The detector temperature is set at 250 °C with helium as carrier gas. Additionally, the system is calibrated with gas sample of known composition, to compare the result using single level calibration. The report of a sample calibration of gas mixture with 90% hydrogen and 10% methane by weight is depicted in **Fig. 4.8**. The negative peak detected after 3 min represents hydrogen, while the positive peak detected near 11th minute represents methane gas

4.4 Summary

The present chapter explains about the details of experimental setup for both single and multistage metal hydride based hydrogen purification system. It summarises details of all the equipment's used in the setup and its purpose. The detailed experimental circuit also explains the flow of HTF and gas within the system during the absorption, flushing and desorption process. The chapter also explains the method developed for the gas chromatography analysis, to detect the purity level of the hydrogen in the gas samples at different stage of the experiments.

CHAPTER 5 REACTORS ACTIVATION AND PARAMETRIC STUDIES

In the previous chapter, the fabrication of experimental setup and the reactors are discussed. The results related to the reactor activation and the parametric studies is discussed in this chapter. The manufacturing process of the intermetallic alloys for hydrogen storage involves melting, spray atomization and ball milling. While going through these processes, a resistive oxide layers are formed on the surface of the alloy particles. The process of removing the resistive layer for easy absorption of hydrogen in the intermetallic alloys is known as activation process.

5.1 Activation Procedure

The reactor activation is carried at higher hydrogen supply pressure (P_s) and lower/room temperature. The activation pressure and temperature is decided on the basis of PCT characteristics of a particular intermetallic alloy. For example, if the equilibrium pressure of any intermetallic alloy is in the range of 1 bar to 10 bar at 25 °C, the supply pressure for its activation may be considered between 30 bar to 50 bar at 25 °C. Higher the pressure gradient, lesser will be the number of activation cycle. Before activation, the filled reactor is tested with argon gas at 80-150 bar (depending upon reactor design and application it can be even more), to ensure no gas leakage from the fittings and MH reactor. Further, the reactor bed is raised to higher temperature (80-90 °C) and it is evacuated down to 10^{-1}-10^{-2} mbar using vacuum pump, to ensure the removal of trapped moisture and atmospheric gases from the void space. After evacuation, the reactor was cooled down to corresponding absorption temperature and hydrogen is supplied at higher pressure. This process is repeated till the activation gets completed. Before commencing the activation process, the entire system including reactor and the circuits is tested for any leakages using argon gas at 80-150 bar pressure and followed by vacuum down to 10^{-3} mbar.

5.1.1 Activation of 6 ECT Reactor filled with 1.2 kg $La_{0.9}Ce_{0.1}Ni_5$

The reactor activation was carried at hydrogen supply pressure (**P_s**) of 30 bar and 25 °C absorption temperature (**T_a**). Before activation, the filled reactor was tested with argon gas at 80 bar, to ensure no gas leakage from the fittings, tube circuit and MH reactor. Further, the reactor bed was raised to 90 °C and was evacuated down to 0.02 mbar using a vacuum pump, to ensure the removal of trapped moisture and atmospheric gases from the void space. After evacuation, the reactor was cooled to 25 °C through the HTF circulation from cold bath and hydrogen was supplied at 30 bar.

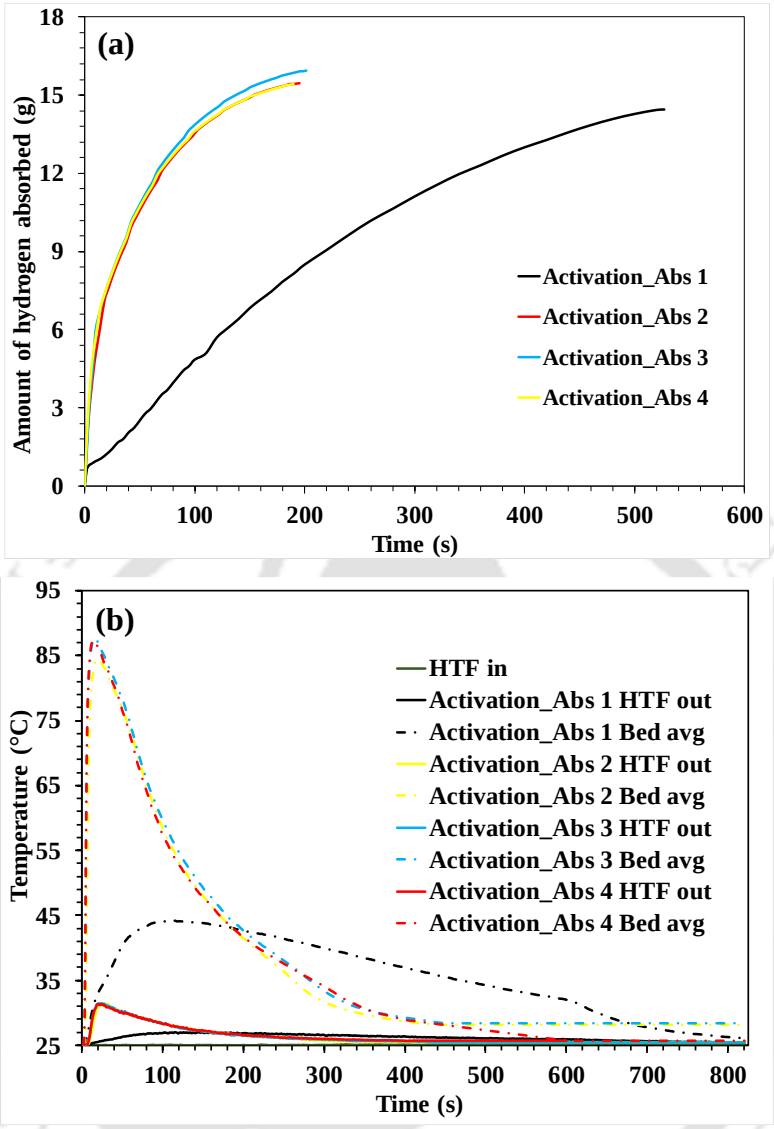

Fig 5.1 (a) Amount of hydrogen absorbed during each activation cycle, and **(b)** the average bed and HTF temperature variation for respective activation cycle for $La_{0.9}Ce_{0.1}Ni_5$

As shown in **Fig. 5.1a**, in the first activation cycle, 14.4501 g hydrogen was absorbed in 527 s, while peak bed temperature recorded was around 44 °C (**Fig. 5.1b**). Considering slow reaction kinetics in the first activation cycle, reactor was again evacuated by raising the temperature to 90 °C. Further, the activation cycle was repeated 3 times to ensure complete activation of the MH bed, where in amount of hydrogen absorbed was recorded as 15.4484 g, 15.8293 g & 15.5207 g respectively in 2^{nd}, 3^{rd} & 4^{th} activation cycle, with absorption time of 190 to 200 s. The repeatability in the amount of hydrogen absorbed and bed temperature variation during 2^{nd}, 3^{rd} & 4^{th} activation

cycle are presented in **Fig. 5.1**, which confirms the successful activation of the MH reactor with 1.2 kg of $La_{0.9}Ce_{0.1}Ni_5$, having storage capacity of 1.32 wt.%.

5.1.2 Activation of 6 ECT Reactor filled with 1.2 kg $LaNi_5$

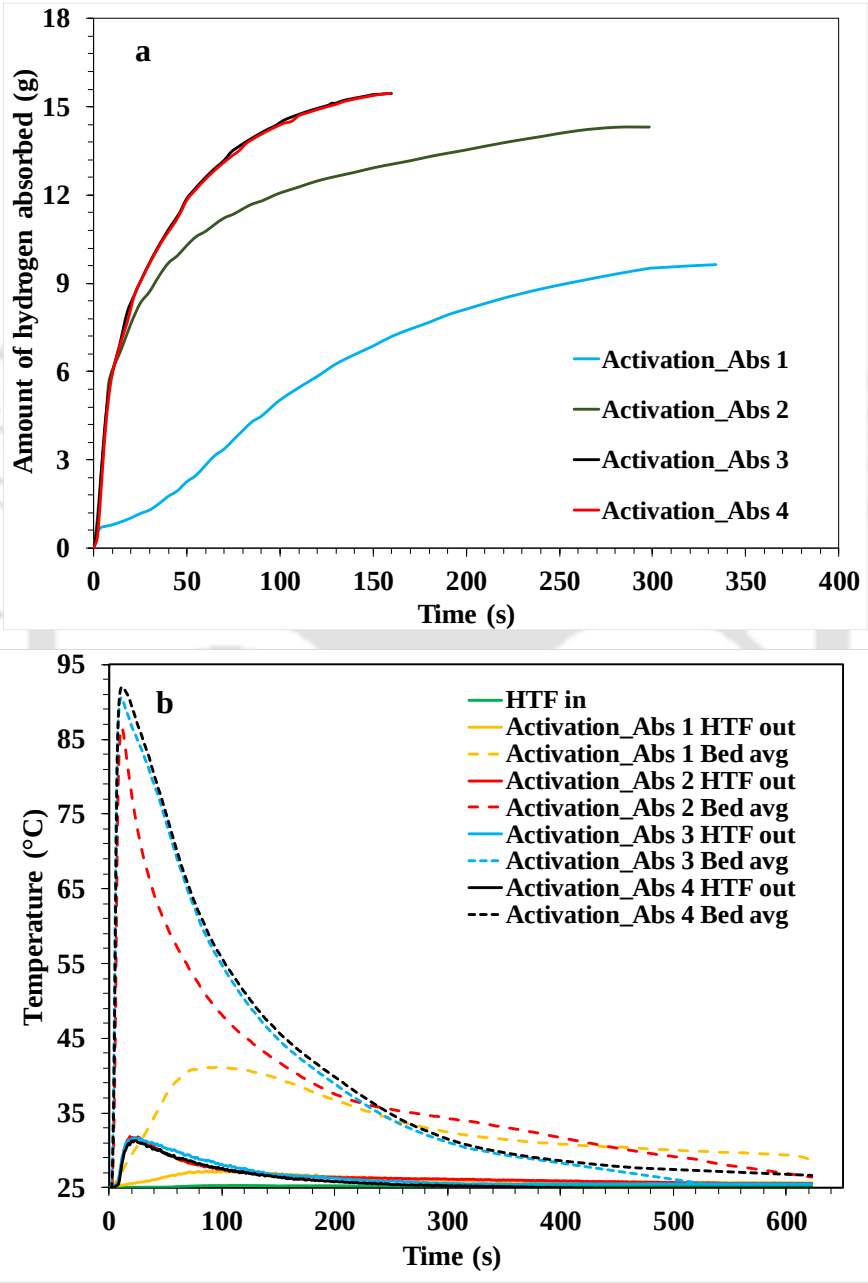

Fig. 5.2 (a) Amount of hydrogen absorbed during each activation cycle, and **(b)** the average bed and HTF temperature variation for respective activation cycle for $LaNi_5$

Like previous, the reactor activation was carried at hydrogen supply pressure (**P_s**) of 30 bar and 25 °C absorption temperature (**T_a**). Before activation, the reactor was tested for no leak condition of reactor, fittings and gas circuit with argon gas at 80 bar. Further, the reactor bed was raised to 90 °C and was evacuated down to 0.02 mbar using vacuum pump, to ensure the removal of trapped moisture and atmospheric gases from the void space of the reactor. After evacuation, the reactor was cooled to 25 °C through HTF circulation from cold bath and hydrogen was supplied at 30 bar. In the first activation cycle, 9.6336 g hydrogen was absorbed in 334 s (**Fig. 5.2a**), while peak bed temperature recorded was around 29 °C **(Fig. 5.2b**). Considering slow reaction kinetics in the first activation cycle, reactor was again evacuated at 90 °C. Further, the activation cycle was repeated 3 times to ensure complete activation of the MH bed, where in amount of hydrogen absorbed was recorded as 14.3242 g, 15.4672 g & 15.4633 g respectively in 2^{nd}, 3^{rd} & 4^{th} activation cycle, with absorption time of 298 s, 160 s & 160 s respectively. The repeatability in the amount of hydrogen absorbed and bed temperature variation during 2^{nd}, 3^{rd} & 4^{th} activation cycle presented in **Fig. 5.2**, depicts the successful activation of the MH reactor with 1.2 kg of $LaNi_5$, having storage capacity of 1.3 wt.%.

5.1.3 Activation of 6 ECT Reactor filled with 1.2 kg $LaNi_{0.7}Al_{0.3}$

Like previous, the reactor activation was carried at hydrogen supply pressure (**P_s**) of 30 bar and 25 °C absorption temperature (**T_a**). In the first activation cycle, 0.6495 g hydrogen was absorbed in 4 s (**Fig. 5.3a**), while peak bed temperature recorded was around 26 °C (**Fig. 5.3b**). Considering slow reaction kinetics in the first activation cycle, reactor was again evacuated at 90 °C. Further, the activation cycle was repeated 3 times to ensure complete activation of the MH bed, where in amount of hydrogen absorbed was recorded as 13.2013 g, 15.8205 g & 16.0232 g respectively in 2^{nd}, 3^{rd} & 4^{th} activation cycle, with absorption time of 305 s, 130 s & 128 s respectively. The repeatability in the amount of hydrogen absorbed and bed temperature variation during 2^{nd}, 3^{rd} & 4^{th} activation cycle presented in **Fig. 5.3**, depicts the successful activation of the MH reactor with 1.2 kg of $LaNi_{4.7}Al_{0.3}$, having storage capacity of 1.35 wt.%.

As it can be observed from the activation temperature plot of all the three reactors, the peak bed temperature attained during absorption are in the order $La_{0.9}Ce_{0.1}Ni_5$ > $LaNi_5$ > $LaNi_{4.7}Al_{0.3}$. This was because of the equilibrium bed temperature of alloy at ambient condition are in reverse sequence. Due to which there is increase in pressure gradient, and finally results in faster absorption with higher peak temperature.

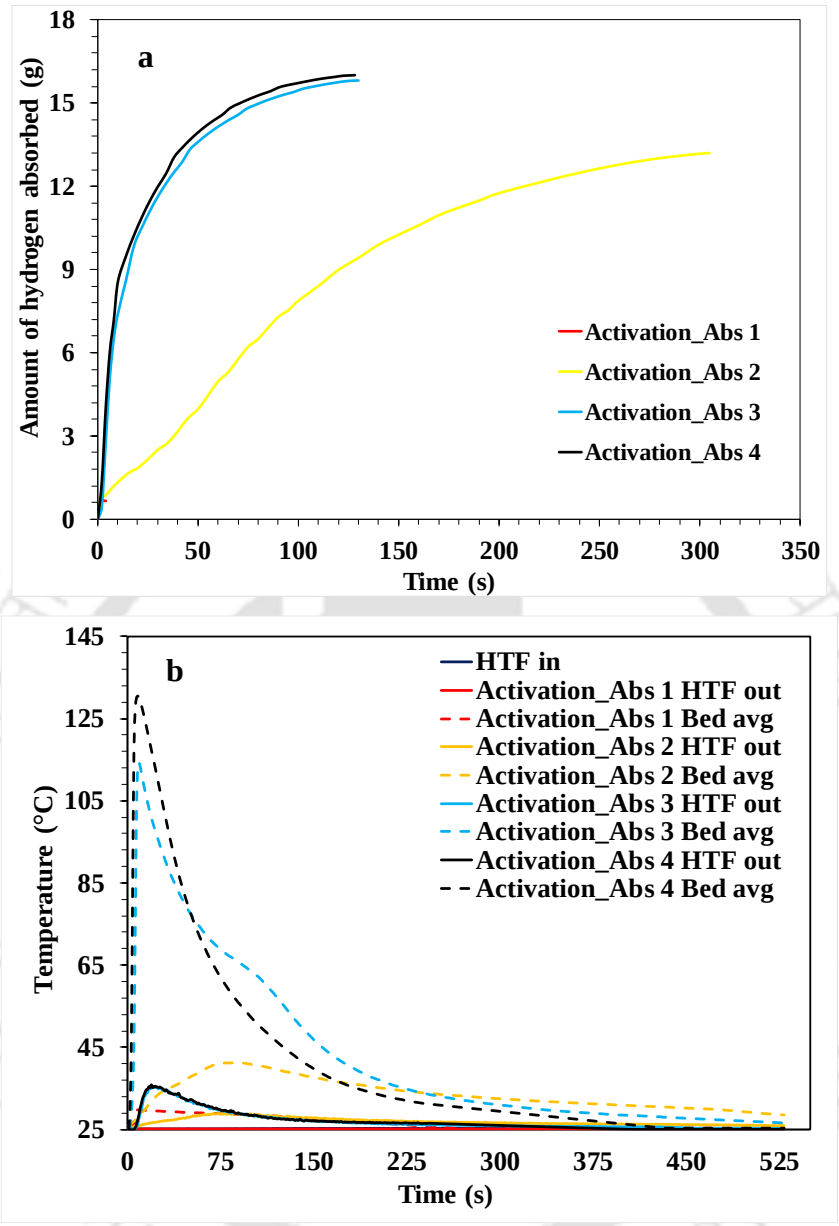

Fig. 5.3 (a) Amount of hydrogen absorbed during each activation cycle, and (b) the average bed and HTF temperature variation for respective activation cycle for $LaNi_{4.7}Al_{0.3}$

5.1.4 Activation of 99 ECT Reactor filled with 40 kg $LaNi_{0.7}Al_{0.3}$

After ensuring zero leakage, the entire system was evacuated down to 10^{-3} mbar and then flushed with hydrogen gas at 25 bar pressure. Activation procedure was initiated by evacuating system while maintaining the bed at 80 °C. After complete evacuation, hydrogen was supplied at 40 bar maintaining at 25 °C. On first attempt, 108.215 g of hydrogen was absorbed. This amounts to 0.27

wt% of storage capacity. Then, the bed was evacuated down to 10^{-3} mbar at 60 °C. This cyclic process was repeated until the MH reached its maximum storage capacity.

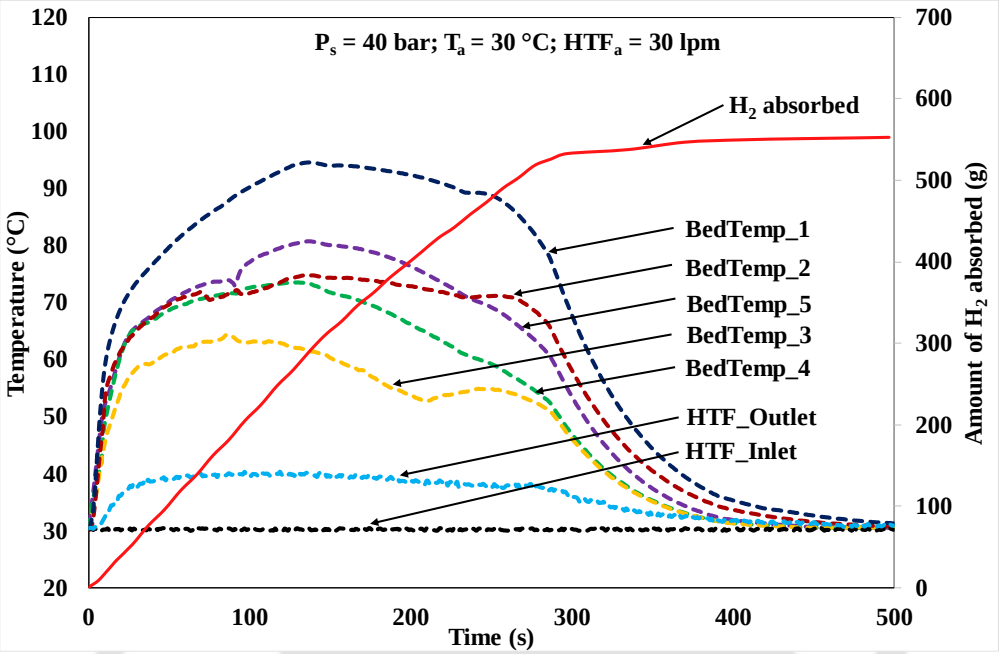

Fig. 5.4 Amount of H_2 absorbed and variation of temperatures during final activation cycle

The temperature variation of MH bed and HTF that were obtained during third activation cycle alongside the amount of hydrogen absorbed during this cycle are depicted in **Fig. 5.4**. In this cycle, at supply pressure of 40 bar, MHHSS absorbed 552.356 g of hydrogen amounting to a maximum storage capacity of nearly 1.4 wt%. Increase in bed temperature was rapid signifying faster absorption kinetics wherein the region nearer to HTF outlet (BedTemp_1) attained a maximum temperature of 95 °C within 140 s corroborating rapid reaction. In about 300 s, the reaction was stabilizing as corroborated by the rate of hydriding while the temperature gain of HTF was quite uniform during this period as well.

5.2 Parametric Study

The purification process in a MH-Hydrogen system comprises of three steps, i.e., absorption, flushing and desorption. It is very essential to obtain suitable operating conditions for these three processes. In order to obtain suitable operating condition of supply pressure (**P_s**) & absorption temperature (Ta) for absorption, also suitable flushing temperature to avoid hydrogen losses during

flushing and desorption temperature (T_d) for efficient desorption, in MHHPS, absorption and desorption studies were performed at different conditions with pure hydrogen.

5.2.1 Parametric Study of 6 ECT Reactor filled with 1.2 kg $La_{0.9}Ce_{0.1}Ni_5$

For observing the absorption behaviour of the MHHPS, parametric study was performed by varying P_s from 2 bar to 20 bar keeping the absorption temperature (T_a) at 25 °C. The parametric studies for the 6 ECT Reactor filled with 1.2 kg $La_{0.9}Ce_{0.1}Ni_5$ were performed at different conditions, which is depicted in **Table 5.1**.

Table 5.1 Parameter for parametric study (6 ECT with 1.2 kg $La_{0.9}Ce_{0.1}Ni_5$)

Study	Half Cycle	Operating parameters	Value
Parametric Study	Absorption	Supply pressure (P_s)	2, 5, 10, 15 and 20 bar
		Absorption temperature (T_a)	25 °C
		HTF flow rate	4 lpm
	Desorption	Desorption temperature (T_d)	10, 15, 20, 30, 60, 70, 80 and 90 °C
		HTF flow rate	4 lpm

5.2.1.1 Effect of supply pressure on absorption

As depicted in **Fig. 5.5a**, rate of absorption increased with increase in P_s, wherein 1.13 g, 11.59 g, 13.77 g, 13.8935 g and 14.84 g was absorbed in 40 s, 490 s, 390 s, 305 s and 240 s respectively for P_s of 2 bar, 5 bar, 10 bar, 15 bar and 20 bar at fixed absorption temperature of 25 °C. This also constituted to 0.094 wt.%, 0.97 wt.%, 1.15 wt.%, 1.16 wt.% and 1.24 wt.% of hydrogen storage at P_s of 2 bar, 5 bar, 10 bar, 15 bar and 20 bar, respectively. This improvement is due to the variation in pressure gradient between the bed equilibrium pressure and the supply pressure. The pressure gradient acts as driving force for the faster absorption. Similar effect can also be witnessed in the temperature variation plot, which is depicted in **Fig. 5.5b**. It can be observed that, peak temperature of about 36.7 °C, 47.2 °C, 59.2 °C, 65.4 °C and 80.1 °C was attained for supply pressure of 2 bar, 5 bar, 10 bar, 15 bar and 20 bar respectively. Because of faster rate of absorption at higher pressure, the heat accumulation in the MH reactor is more, which results in attaining higher peak temperature at higher pressure. Similar effect can also be observed on the HTF outlet temperature, which is recorded maximum and minimum of 33.3 °C & 26.1 °C for 20 bar & 2 bar.

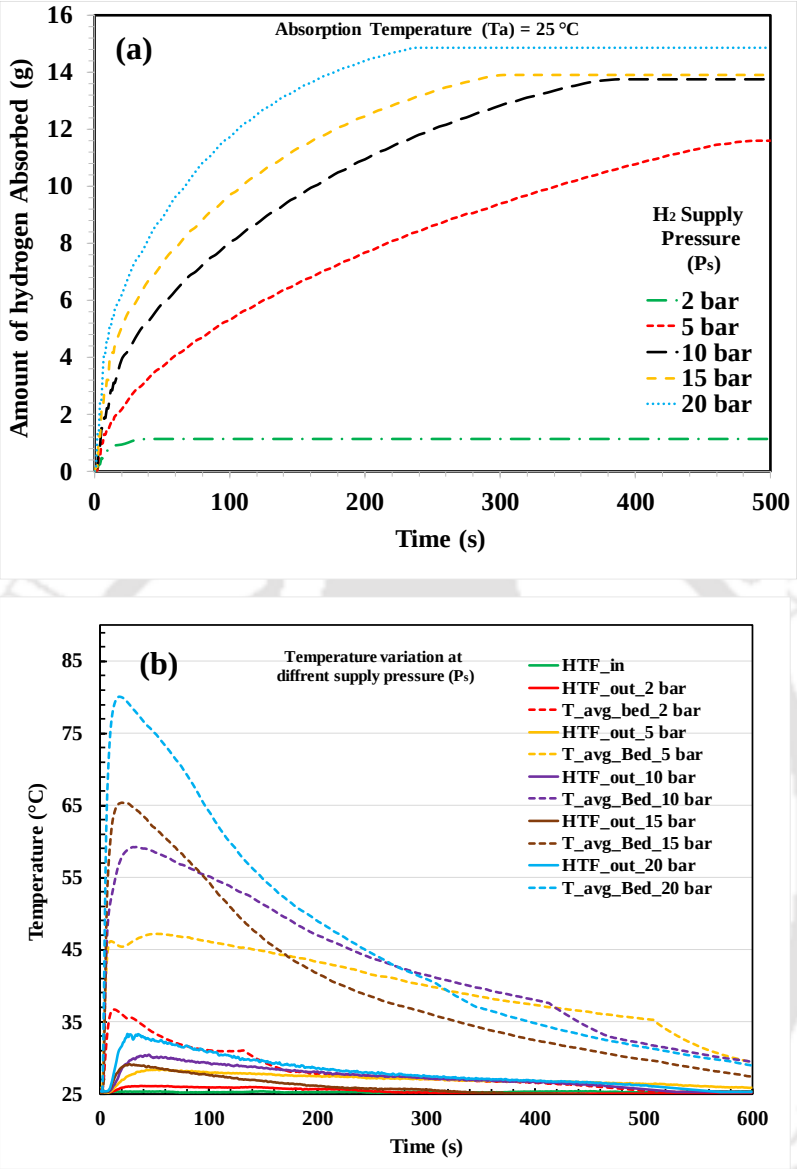

Fig. 5.5 (a) Effect of supply pressure (**P_s**) on amount of hydrogen absorbed and **(b)** temperature variation in MH bed and HTF during absorption at different **P_s**.

5.2.1.2 Effect of desorption temperature on desorption

Similarly, in order to determine the suitable flushing and desorption temperature, desorption study was conducted by varying desorption temperature from 10 °C to 90 °C, as depicted in **Fig. 5.6**. It was observed that with increase in desorption temperature, the rate of desorption increased significantly with simultaneous increase in the reversible characteristics of the MHHPS. As shown

in **Fig. 5.6a**, for a fixed absorption of 15.5 g, the amount of hydrogen desorbed was recorded as 0.79 g, 1.42 g, 1.45 g, 8.69 g, 13.93 g, 14.16 g, 14.48 g and 15.20 g respectively in 30 s, 65 s, 35 s, 560 s, 410 s, 325 s, 265 s and 290 s for respective desorption temperature of 10 °C, 15 °C, 20 °C, 30 °C, 60 °C, 70 °C, 80 °C and 90 °C.

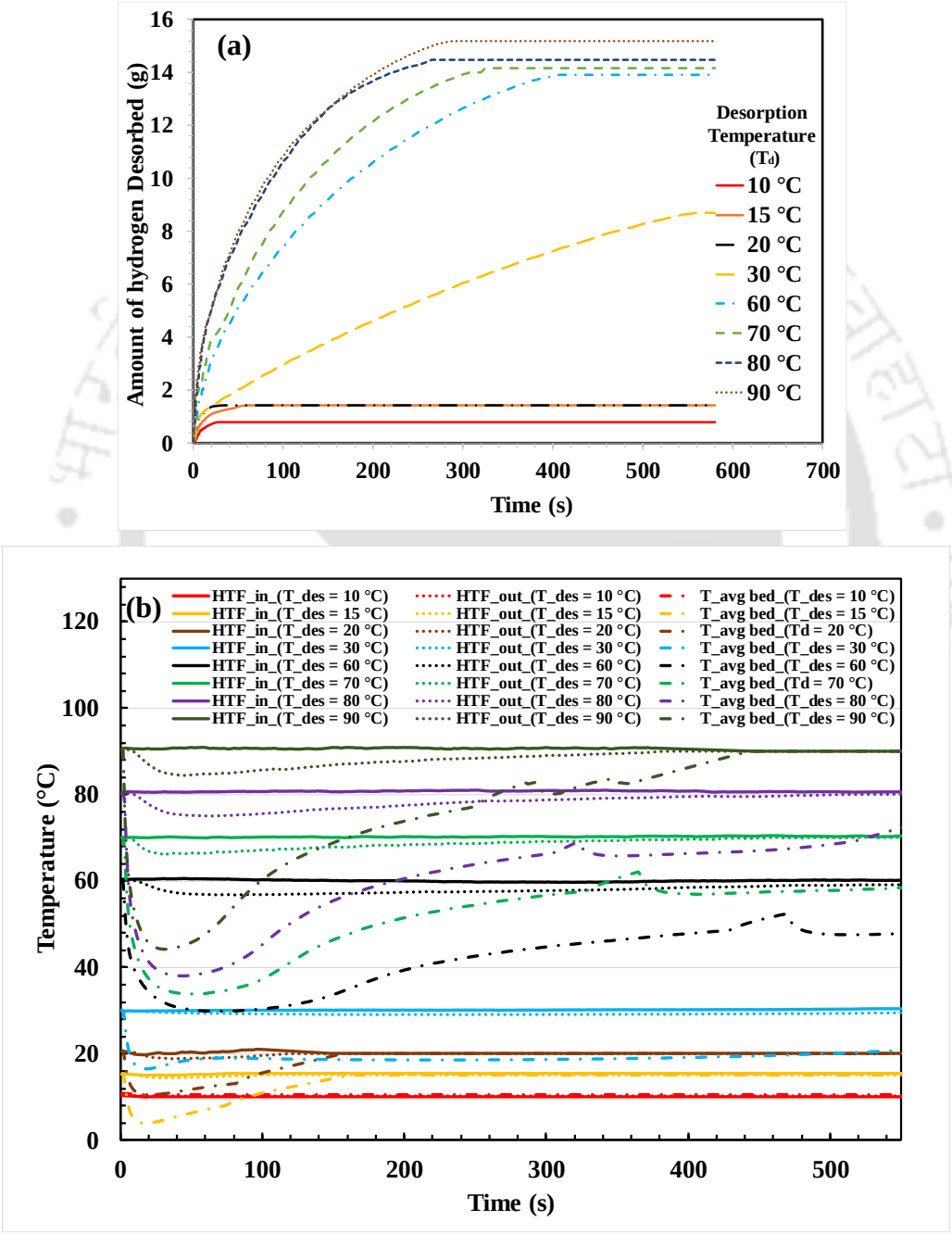

Fig. 5.6 (a) Effect of desorption temperature (**T_d**) on amount of hydrogen desorbed and **(b)** temperature variation in MH bed and HTF during desorption at different **T_d.**

This behaviour was due to significant pressure difference between desorption and bed equilibrium pressure which was influenced by the bed temperature. The variation in the bed and HTF temperature during the desorption process is depicted in **Fig. 5.6b**. For 10 °C desorption temperature, there was hardly any change in the bed and HTF temperature. However, as the temperature was increased, the bed desorbed a little till 20 °C, and with further increase in the temperature there was significant drop in the bed temperature due to increase in the rate of desorption. According to the results obtained, suitable flushing temperature for $La_{0.9}Ce_{0.1}Ni_5$ could be 10-15 °C and the desorption temperature could be 70-90 °C. The drop in the HTF temperature was 0.6 °C to 5.6 °C for desorption temperature of 15 °C to 90 °C. Similarly drop in the bed temperature was in the range of 9.5 °C to 45.8 °C for desorption temperature of 15 °C to 90 °C.

5.2.2 Parametric Study of 6 ECT Reactor filled with 1.2 kg $LaNi_5$

The parametric studies for the 6 ECT Reactor filled with 1.2 kg $LaNi_5$ were performed at different conditions, which is depicted in **Table 5.2**.

Table 5.2 Parameter for parametric study (6 ECT with 1.2 kg $LaNi_5$ & $LaNi_{4.7}Al_{0.3}$)

Study	Half Cycle	Operating parameters	Value
Parametric Study	**Absorption**	Supply pressure (**P_s**)	2, 5, 10, 15 and 20 bar
		Absorption temperature (**T_a**)	25 °C
		HTF flow rate	4 lpm
	Desorption	Desorption temperature (**T_d**)	15, 20, 30, 60, 70, 80 and 90 °C
		HTF flow rate	4 lpm

5.2.2.1 Effect of supply pressure on absorption

In order to obtain the optimum operating condition of supply pressure (**P_s**) and desorption temperature (**T_d**) for efficient absorption, flushing and desorption process in MHHPS, absorption and desorption studies were performed at different conditions with pure hydrogen. For observing absorption behaviour of the MHHPS, parametric study was performed by varying **P_s** from 2 bar to 20 bar, at 25 °C absorption temperature (**T_a**). As depicted in **Fig. 5.7a**, rate of absorption increased with increase in **P_s**, wherein 7.8491 g, 12.8141 g, 14.1873 g, 14.2893 g and 14.8997 g was absorbed in 450 s, 420 s, 280 s, 260 s and 190 s respectively for P_s of 2 bar, 5 bar, 10 bar, 15 bar and 20 bar. This also constituted to 0.66 wt.%, 1.06 wt.%, 1.18 wt.%, 1.19 wt.% and 1.24 wt.% of hydrogen

storage at P_s of 2 bar, 5 bar, 10 bar, 15 bar and 20 bar, respectively. This variation is due to the pressure gradient between bed equilibrium pressure and supply pressure; wherein, for higher pressure gradient rate of absorption is high and vice-versa.

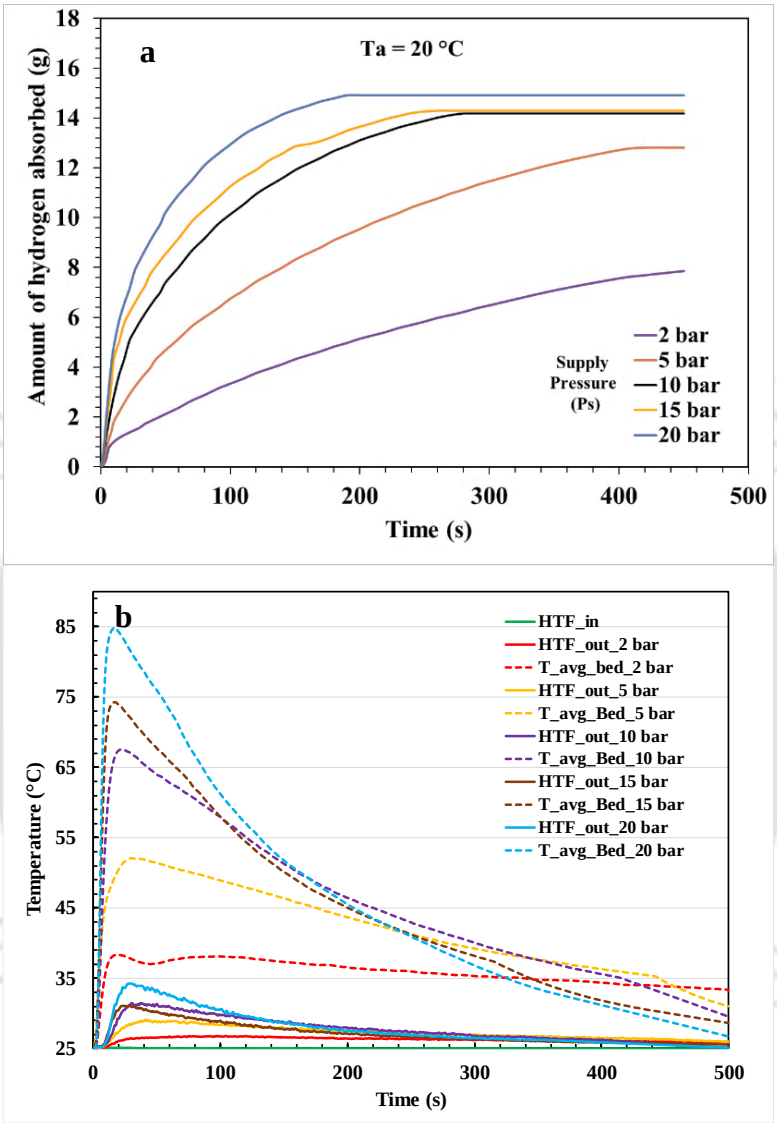

Fig. 5.7 (a) Effect of supply pressure (**P_s**) on amount of hydrogen absorbed and **(b)** variation in the bed and HTF temperature during absorption for $LaNi_5$

Similar effect can also be witnessed in the temperature variation plot, which is depicted in **Fig. 5.7b**. It can be observed that, peak temperature of about 38.3 °C, 52 °C, 67.5 °C, 74.3 °C and 84.8 °C was attained for supply pressure of 2 bar, 5 bar, 10 bar, 15 bar and 20 bar respectively. Because of faster rate of absorption at higher pressure, the heat accumulation in the MH reactor is more, which results in attaining higher peak temperature at higher pressure. Similar effect can also be

observed on the HTF outlet temperature, which is recorded maximum and minimum of 34.4 °C & 26.5 °C for 20 bar & 2 bar. From the results obtained, the suitable absorption pressure at room temperature could be between 10-20 bar.

5.2.2.2 Effect of desorption temperature on desorption

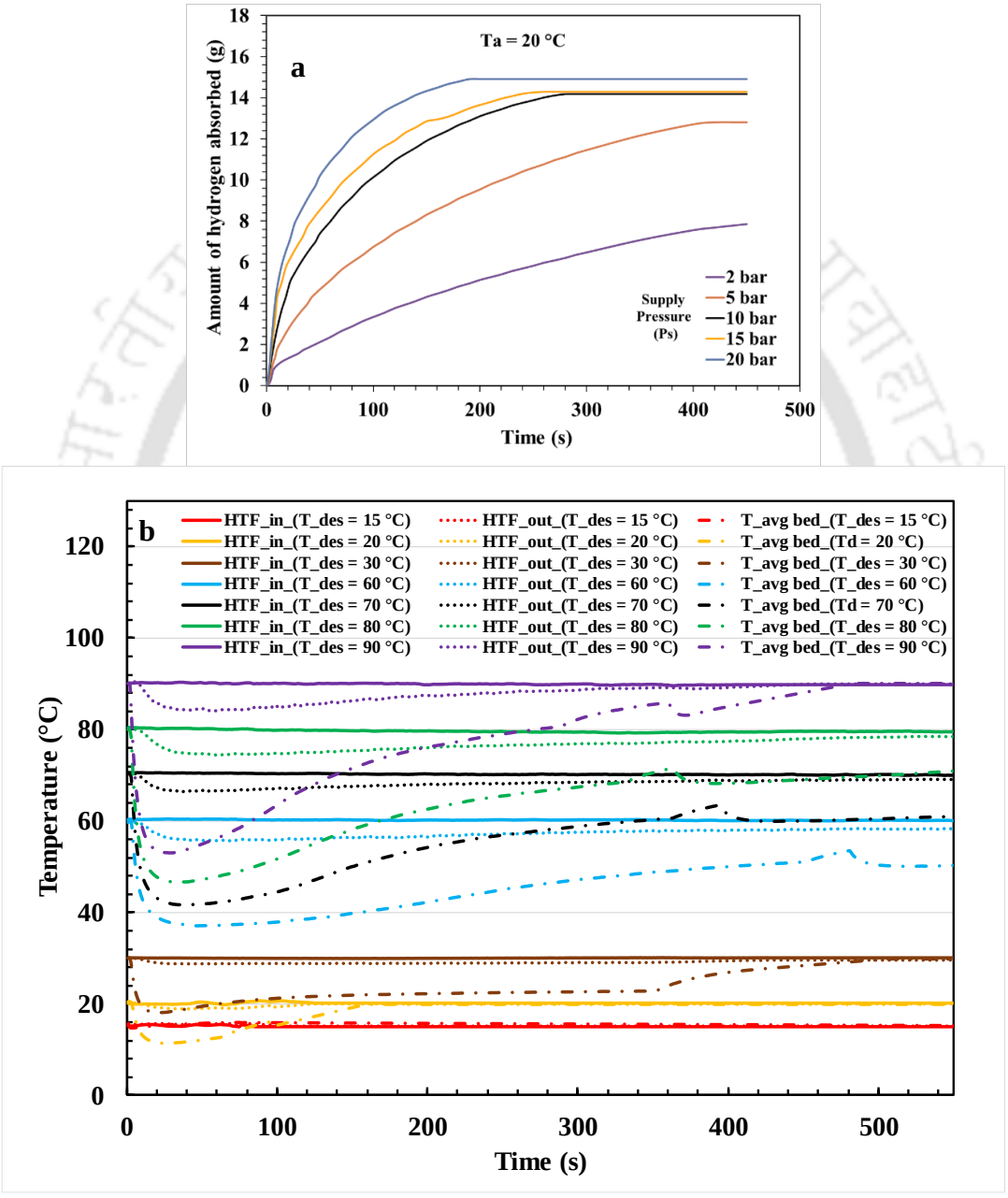

Fig. 5.8 (a) Effect of desorption temperature (T_d) on amount of hydrogen desorbed and **(b)** temperature variation in MH bed and HTF during desorption at different T_d.

Similarly, in order to the determine the optimum flushing and desorption temperature, desorption study was conducted by varying desorption temperature from 15 °C to 90 °C, as depicted in **Fig. 5.8a**. It was observed that with increase in desorption temperature, rate of desorption increased significantly with simultaneous increase in the reversible characteristics of the MHHPS. For a fixed absorption of 15.5 g, the amount of hydrogen desorbed was recorded as 0.1737 g, 1.5243 g, 4.4413 g, 13.4700 g, 14.0465 g, 15.099 g and 15.1812 g respectively in 4 s, 46 s, 350 s, 430 s, 350 s, 330 s and 290 s. The respective desorption temperature was 15 °C, 20 °C, 30 °C, 60 °C, 70 °C, 80 °C and 90 °C. This behaviour was due to significant pressure difference between desorption pressure and bed equilibrium pressure which is influenced by the bed temperature.

The variation in the bed and HTF temperature during the desorption process is depicted in **Fig. 5.8b**. For 15 °C desorption temperature, there was hardly any change in the bed and HTF temperature. However, as the temperature was increased, the bed desorbed a little till 30 °C, and with further increase in the temperature there was significant drop in the bed temperature due to increase in the rate of desorption. The drop in the HTF temperature was in the range of 1.2 °C to 5.8 °C for desorption temperature of 20 °C to 90 °C. Similarly drop in the bed temperature was in the range of 8.7 °C to 37 °C for desorption temperature of 20 °C to 90 °C. According to the results obtained, suitable flushing temperature for $LaNi_5$ could be 15-20 °C and the desorption temperature could be 80-90 °C.

5.2.3 Parametric Study of 6 ECT Reactor filled with 1.2 kg $LaNi_{0.7}Al_{0.3}$

The parametric studies for the 6 ECT Reactor filled with 1.2 kg $LaNi_{0.7}Al_{0.3}$ were performed at different conditions, similar to $LaNi_5$, which is depicted in the table 5.2. In order to obtain the optimum operating condition of supply pressure ($\mathbf{P_s}$) and desorption temperature ($\mathbf{T_d}$) for efficient absorption, flushing and desorption process in MHHPS, absorption and desorption studies were performed at different conditions with pure hydrogen.

5.2.3.1 Effect of supply pressure on absorption

For observing absorption behaviour of the MHHPS, parametric study was performed by varying $\mathbf{P_s}$ from 2 bar to 20 bar, at 25 °C absorption temperature ($\mathbf{T_a}$). As depicted in **Fig. 5.9a**, rate of absorption was increased with increase in $\mathbf{P_s}$, wherein 13.6743 g, 14.6293 g, 15.1140 g, 15.2000 g and 15.2900 g was absorbed in 350 s, 270 s, 190 s, 180 s and 150 s respectively for P_s of 2 bar, 5

bar, 10 bar, 15 bar and 20 bar. This also constituted to 1.14 wt.%, 1.22 wt.%, 1.26 wt.%, 1.27 wt.% and 1.27 wt.% of hydrogen storage at P_s of 2 bar, 5 bar, 10 bar, 15 bar and 20 bar, respectively. This variation is due to the pressure gradient between bed equilibrium pressure and supply pressure; wherein, for higher pressure gradient rate of absorption is high and vice-versa.

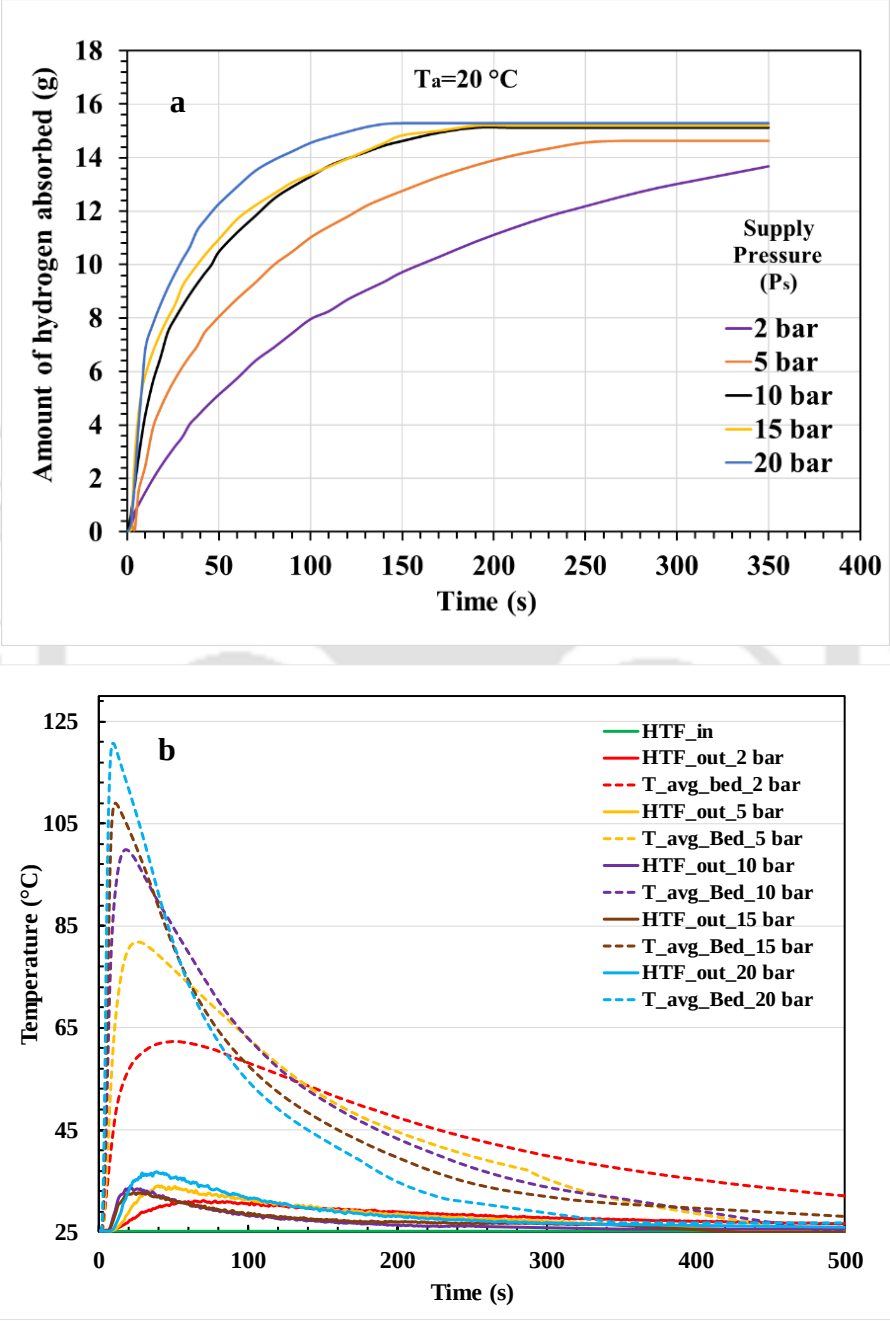

Fig 5.9 (a) Effect of supply pressure (**P_s**) on amount of hydrogen absorbed and **(b)** variation in the bed and HTF temperature during absorption for $LaNi_{4.7}Al_{0.3}$

Similar effect can also be witnessed in the temperature variation plot, which is depicted in **Fig. 5.9b**. It can be observed that, peak temperature of 62.3 °C, 81.8 °C, 99.9 °C, 108.9 °C and 120 °C was attained for supply pressure of 2 bar, 5 bar, 10 bar, 15 bar and 20 bar respectively. Because of faster rate of absorption at higher pressure, the heat accumulation in the MH reactor is more, which results in attaining higher peak temperature at higher pressure. Similar effect can also be observed on the HTF outlet temperature, which is recorded maximum and minimum of 36.6 °C & 30.1 °C for 20 bar & 2 bar. From the results obtained, the suitable absorption pressure at room temperature could be between 5-20 bar.

5.2.3.2 Effect of desorption temperature on desorption rate

Similarly, in order to the determine the optimum flushing and desorption temperature, desorption study was conducted by varying desorption temperature from 15 °C to 80 °C, as depicted in **Fig.5.10a**. It was observed that with increase in desorption temperature, rate of desorption increased significantly with simultaneous increase in the reversible characteristics of the MHHPS. For a fixed absorption of 15.5 g, the amount of hydrogen desorbed was recorded as 0.5593 g, 0.7536 g, 1.5653 g, 8.8650 g, 11.3158 g, and 12.4974 g respectively in 10 s, 14 s, 42 s, 390 s, 510 s, and 490 s. The respective desorption temperature was 15 °C, 20 °C, 30 °C, 60 °C, 70 °C and 80 °C. This behaviour was due to significant pressure difference between desorption pressure and bed equilibrium pressure which is influenced by the bed temperature.

The variation in the bed and HTF temperature during the desorption process is depicted in **Fig. 5.10b**. For 15 °C desorption temperature, there was hardly any change in the bed and HTF temperature. However, as the temperature was increased, the bed desorbed a little till 30 °C, and with further increase in the temperature there was significant drop in the bed temperature due to increase in the rate of desorption. The drop in the HTF temperature was in the range of 0.5 °C to 7 °C for desorption temperature of 20 °C to 90 °C. Similarly, the drop in the bed temperature was in the range of 7.1 °C to 29.5 °C for desorption temperature of 20 °C to 90 °C. According to the results obtained, suitable flushing temperature for $LaNi_5Al_{0.3}$ could be 15-20 °C and the desorption temperature could be 90 °C. Because of the HTF constrain, the experiments above 90 °C was not performed, as water was used as HTF. However, the desorption and reversibility of the MH bed with $LaNi_5Al_{0.3}$ could have been better at 95-105 °C. However, because of poor desorption at low temperature, the alloy is highly suitable for hydrogen purification application.

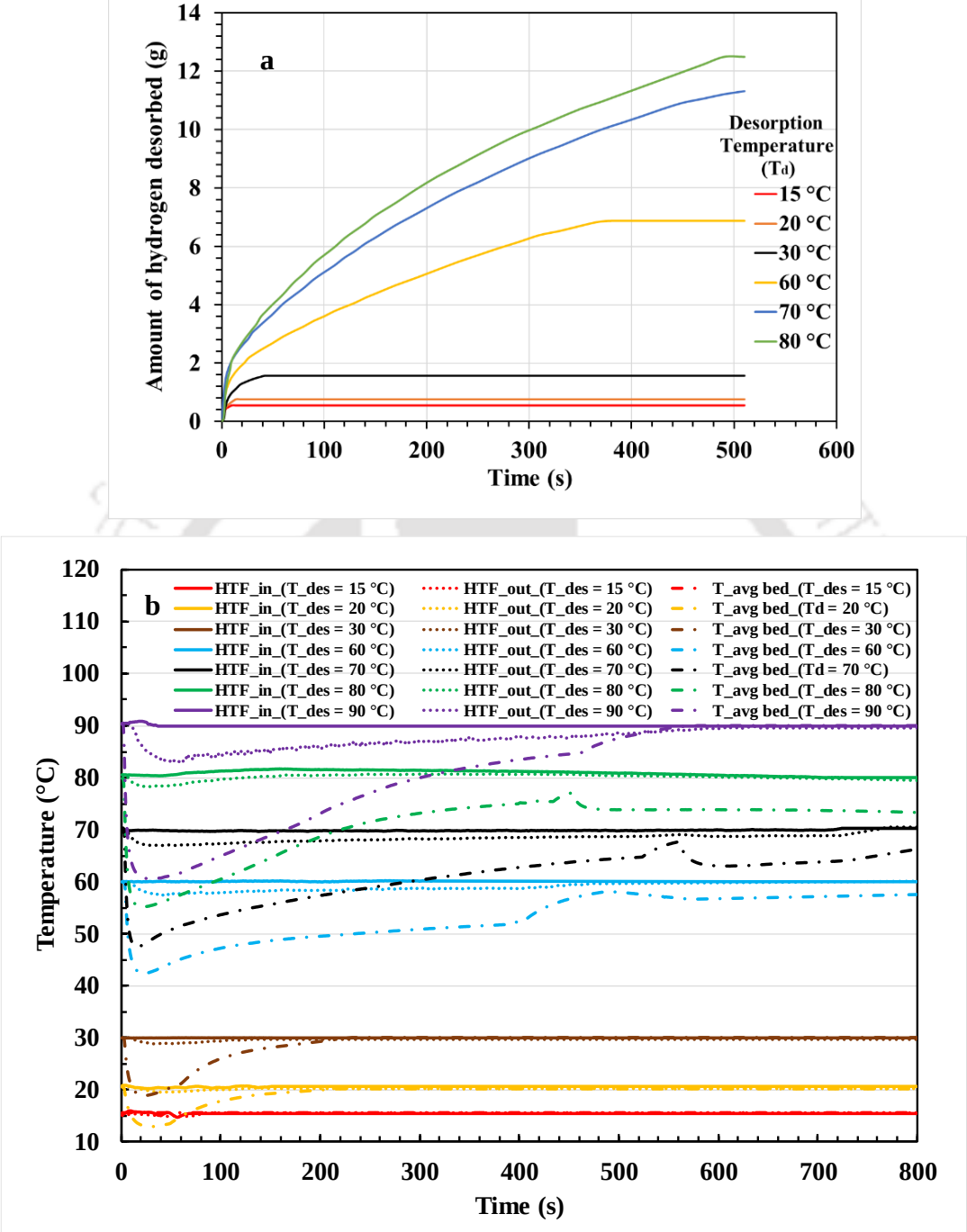

Fig 5.10 (a) Effect of desorption temperature (T_d) on amount of hydrogen desorbed and **(b)** temperature variation in MH bed and HTF during desorption at different T_d.

5.2.4 Parametric Study of 99 ECT Reactor filled with 40 kg $LaNi_{0.7}Al_{0.3}$

To investigate the influence of operating conditions, parametric investigation has been carried out on 99 ECT reactor. The supply pressure (Ps) was varied from 5 bar to 25 bar in steps of 5 bar. To

understand the effect of low supply pressure on hydriding kinetics, absorption was carried out at 2 bar as well. To effectively compare the absorption performance, the total amount of hydrogen gas available for absorption was maintained at about 425 g which is the amount of gas available in a commercial supply cylinder of 47 lit capacity at 150 bar. This amounts to a hydrogen storage capacity of 1.06 wt%, which is nearly 80% of maximum storage capacity of $LaNi_{4.7}Al_{0.3}$. From prior studies (Gopal and Murthy, 1992), it was observed that the effect of absorption temperature ($\mathbf{T_a}$) is not significant for $LaNi_{4.7}Al_{0.3}$ due to minuscule variation in its equilibrium pressure with respect to bed temperature. Hence, an absorption temperature of 30 °C was maintained while the HTF flow rate (HTF_a) was varied from 10 lpm to 30 lpm in steps of 10 lpm. Similarly, during desorption, HTF flow rate (HTF_d) was varied from 8 lpm to 24 lpm in steps of 8 lpm while the desorption temperature (T_d) was varied from 60 °C to 90 °C in steps of 10 °C. The details of the parameter variations is depicted in the **Table 5.3**

Table 5.3 Parameters used in parametric study (99 ECT with 40 kg & $LaNi_{4.7}Al_{0.3}$)

Half cycle	Parameters	Value
Absorption	H_2 supply pressure (P_s)	2, 5, 10, 15, 20 & 25 bar
	Temperature (T_a)	30 °C
	HTF flow rate (HTF_a)	10, 20 & 30 lpm
Desorption	Temperature (T_d)	60, 70, 80 & 90 °C
	HTF flow rate (HTF_d)	8, 16 & 24 lpm

5.2.4.1 Effect of supply pressure on absorption

As observed in **Fig. 5.11**, varying the supply pressure (P_s) had predominant effect on the absorption reaction kinetics. At supply conditions of 2 bar, 30 °C and 30 lpm water flow rate, 402.66 g of hydrogen was absorbed in 1908 s. The average bed temperature was reached a peak of 40.4 °C and the reaction kinetics was slow as evident from Fig. 5.12. Increasing P_s to 5 bar, led to an increase in absorption kinetics wherein 413.586 g of hydrogen was absorbed in 1442 s, which was a reduction of 25% in absorption time. This increase in supply pressure had caused a delayed improvement in absorption reaction kinetics as seen from **Fig. 5.12**. The peak average bed temperature of 46.5 °C was attained in 680 s. When P_s was increased to 10 bar, 424.87 g of hydrogen was absorbed which was nearly the total amount of hydrogen gas available in the supply

cylinder. This absorption took place within 1253 s, leading to a reduction of 13% in absorption time. This improvement in absorption rate can be attributed to a higher rate of heat generation from the bed. Increasing in supply from 10 bar to 15 bar, caused 1017 s reduction in absorption cycle time which was 19%. However, further increase in supply pressure to 20 bar and 25 bar brought only 10% reduction in absorption time at each consecutive case. At P_s of 15 bar, 20 bar and 25 bar, hydrogen absorption of 425.731 g, 425.767 g and 425.883 g were observed respectively, while the peak values of corresponding average bed temperature were 54 °C, 57 °C and 65 °C.

It was observed that when P_s was increased, the rate of generated absorption heat was higher which in turn facilitated better heat removal by HTF resulting in enhanced absorption performance. Increase in supply pressure potentially increased the pressure gradient between the supply condition and the equilibrium bed pressure at a given bed temperature. This in turn acted as a creditable driving force for the absorption kinetics. Considering overall variation, supply pressure in the range of 10-15 bar is appreciable for better absorption performance. However, even at supply pressure as low as 2-5 bar, remarkable performance could be discerned.

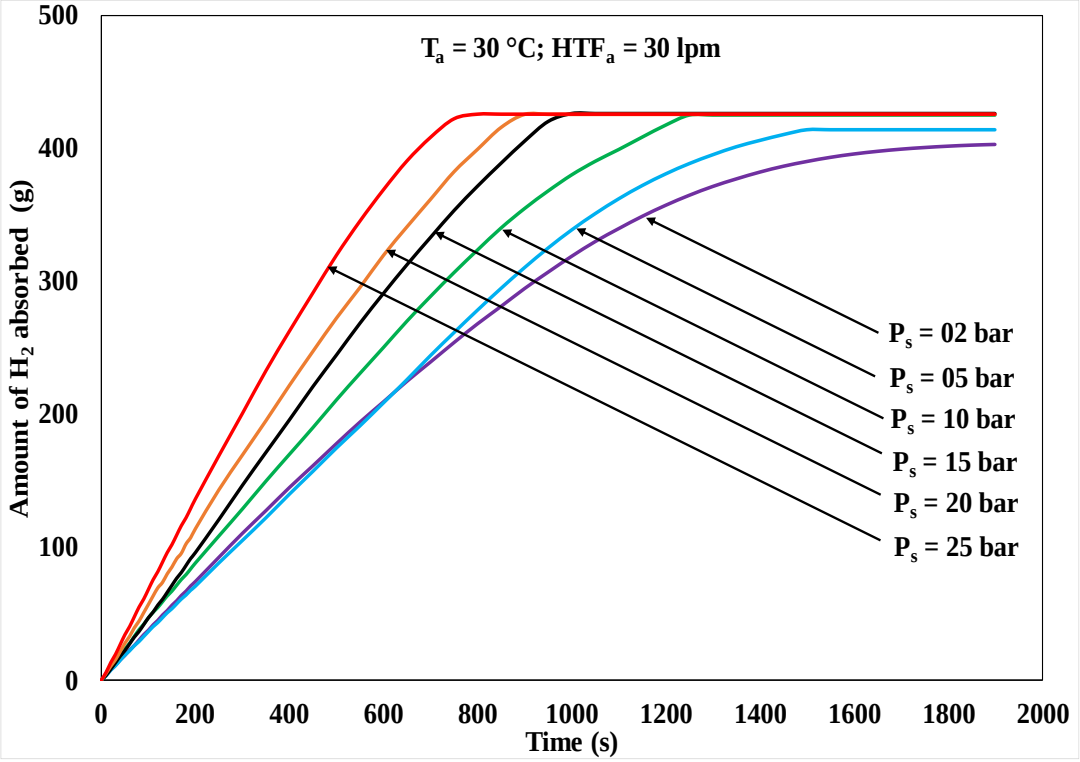

Fig. 5.11 Amount of H_2 absorbed with varying supply pressure (P_s).

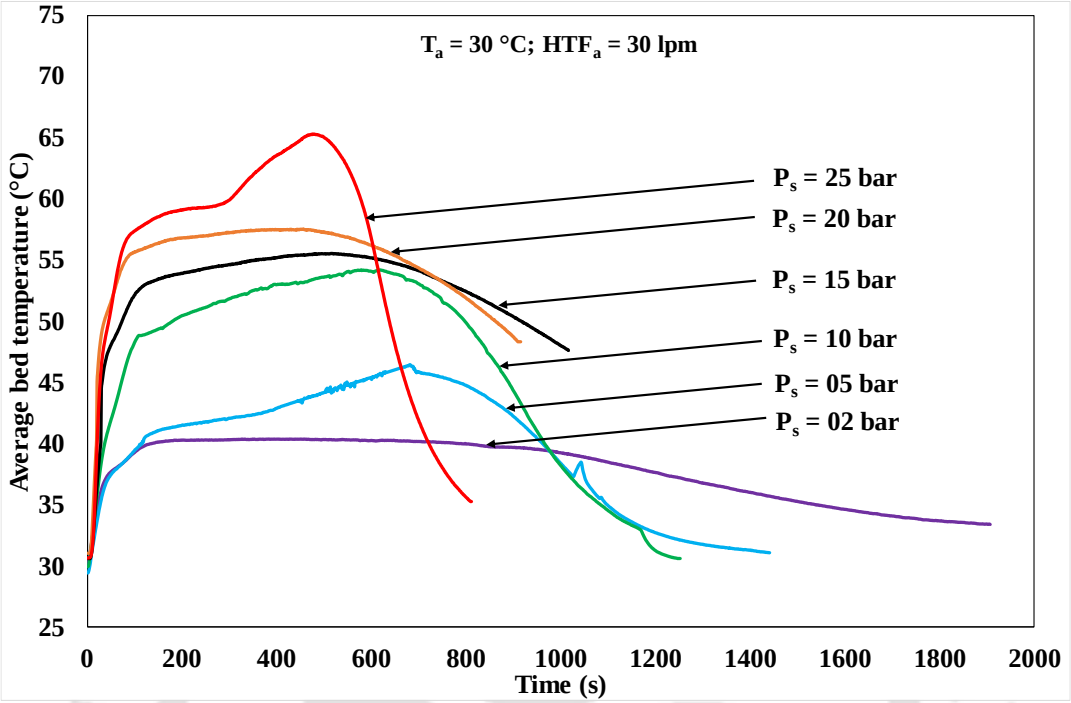

Fig. 5.12 Variation of average bed temperature with varying supply pressure.

5.2.4.2 Effect of HTF flow rate on absorption

Compared to the effect of P_s, varying HTF flow rate (HTF_a) had minor effect on the rate of absorption, which is illustrated in **Figs. 5.13** and **5.14**. When HTF_a was decreased from 30 lpm to 20 lpm while maintaining a supply condition of 10 bar and 30 °C, the absorption cycle time increased to 1366 s, which was a 9% increase in time for 424.926 g of hydrogen absorption. However, decreasing it further to 10 lpm, the amount absorbed was 425.119 g with slower reaction kinetics leading to absorption time of 1454 s. The average bed temperature attained a peak value of 45.7 °C when compared to 51–54 °C in case of 20–30 lpm. When HTF_a was decreased, the heat removal rate lagged as well due to increase in HTF temperature. This is evident from the comparatively lower peak value of average bed temperature attained at 10 lpm.

An interesting behavior that can be observed was the prominent impact of HTF flow rate on average bed temperature variation when compared to its effect on the amount of hydrogen absorbed. The increase in HTF flow rate caused an increase in the rate of heat removal from the bed to HTF resulting in enhanced variation in average bed temperature. However, the subsequent variation in equilibrium bed pressure was minor owing to the PCT characteristics of the alloy. For

a wide range of temperature variation, the change in equilibrium bed pressure is quite minuscule for this alloy. Hence, the amount of hydrogen absorbed did not vary as compared to the variation in average bed temperature.

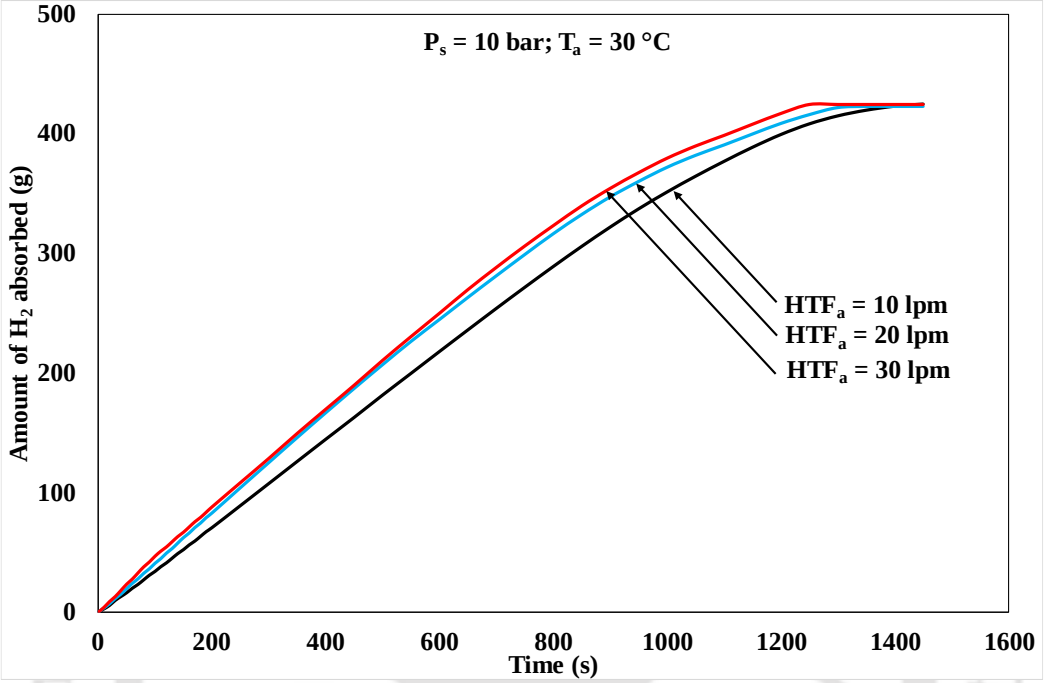

Fig. 5.13. Amount of H_2 absorbed with varying HTF flow rate (HTF_a).

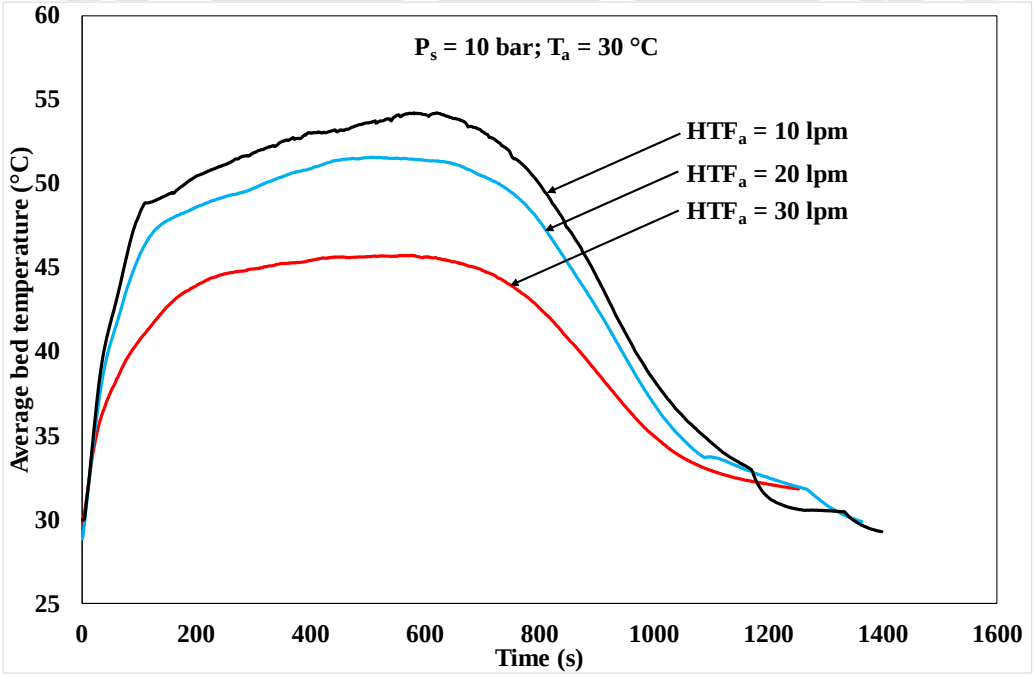

Fig. 5.14. Variation of average bed temperature with varying HTF flow rate.

5.2.4.3 Effect of desorption temperature on desorption

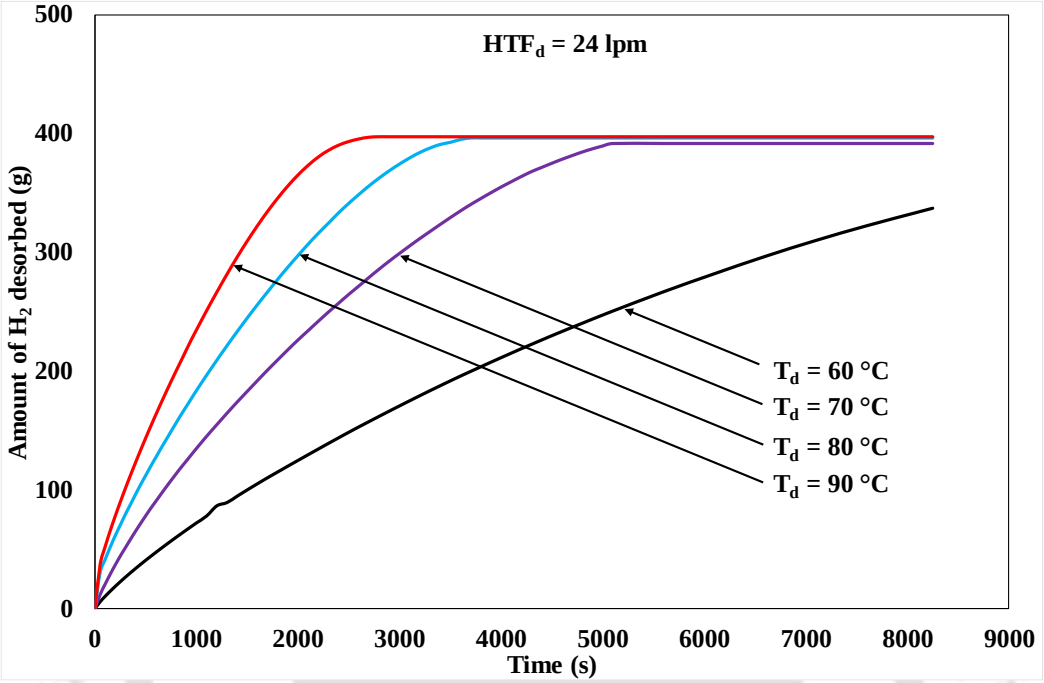

Fig. 5.15. Amount of H_2 desorbed with varying desorption temperature (T_d).

During desorption, the heat input facilitated through high HTF temperature caused an increase in bed temperature of 99 ECT reactor. This effected an increase in equilibrium pressure of MH bed. The resultant pressure gradient arising when the delivery valve was opened to a constant pressure collection tank resulted in effective desorption of bed as the tank was maintained at atmospheric pressure. Essentially, the increase in desorption temperature (T_d) directed a drastic variation in amount of H_2 desorbed as evident from **Figs. 5.15** and **5.16**. For T_d of 60 °C, 336.775 g of H_2 desorption was observed in 8280 s. Desorption kinetics was quite poor as evident from the drop of just 2.5 °C in average bed temperature. When the kinetics was slower, the flow rate of desorbed hydrogen was also minuscule because of which the Coriolis mass flow meter was unable to record such infinitesimal flow. However, the flow meter was capable of recording the totalized flow using inbuilt integration option due to which total amount of hydrogen desorbed could be observed. Increasing in desorption temperature from 60 °C to 70 °C, resulted in hydrogen desorption of 394.970 g while desorption cycle time was reduced by 3150 s, which was a reduction of 38%. The improvement in desorption kinetics was reflected in average bed temperature, which recorded a decrease of 4.3 °C.

When T_d was increased further to 80 °C, 395.812 g of hydrogen was desorbed within 3720 s. Nearly 27% reduction in desorption time was observed compared to T_d of 70 °C while the drop in average bed temperature was 5.5 °C. Further, increasing T_d to 90 °C resulted in a drop of 9 °C in average bed temperature with 890 s reduction in time for a hydrogen desorption of 396.135 g. Though improvement in dehydriding rate was obtained, the magnitude of improvement was reduced with increase in temperature. This pointed to the fact that the bed equilibrium pressure approached a saturation level with increase in desorption temperature.

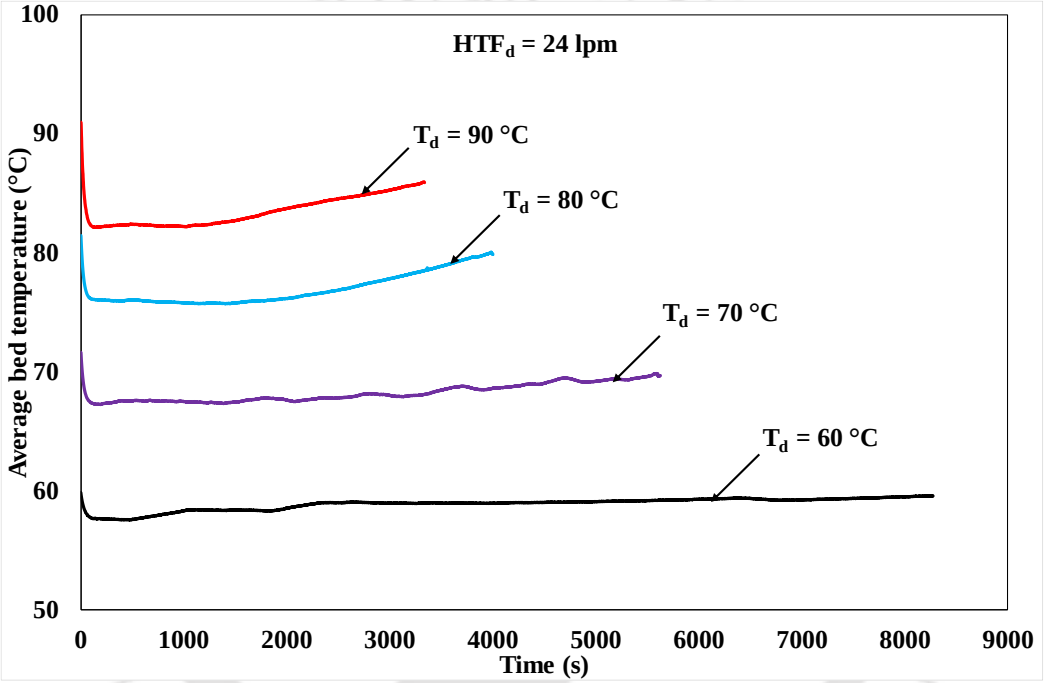

Fig. 5.16. Variation of average bed temperature with varying desorption temperature.

5.2.4.4 Effect of HTF flow rate on desorption

Variation in HTF flow rate (HTF_d) affected the desorption rate only as deduced from **Figs. 5.17** and **5.18**. This effect was observed as the decrease in HTF flow rate reduced the rate of heat addition. At HTF_d of 16 lpm and T_d of 80 °C, hydrogen desorption of 395.456 g was reported within 3750 s. Though desorption cycle time was nearly equal for HTF flow rate of 24 lpm and 16 lpm, it increased to 4510 s when HTF_d was reduced to 8 lpm for similar desorption of 394.833 g. A drop of 7.8 °C was discerned in the average bed temperature at HTF_d of 8 lpm. This produced a reduction in equilibrium bed pressure for same T_d of 80 °C leading to slightly poorer desorption

kinetics. Hence, slower HTF flow rates were adverse for desorption of selected alloy in the designed 99 ECT reactor.

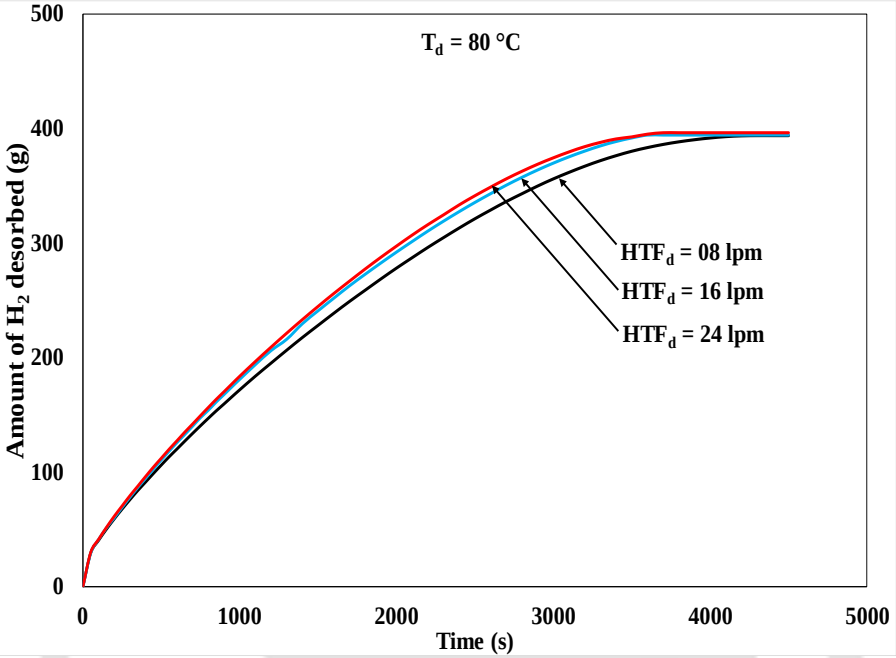

Fig. 5.17. Amount of H_2 desorbed with varying HTF flow rate (HTF_d).

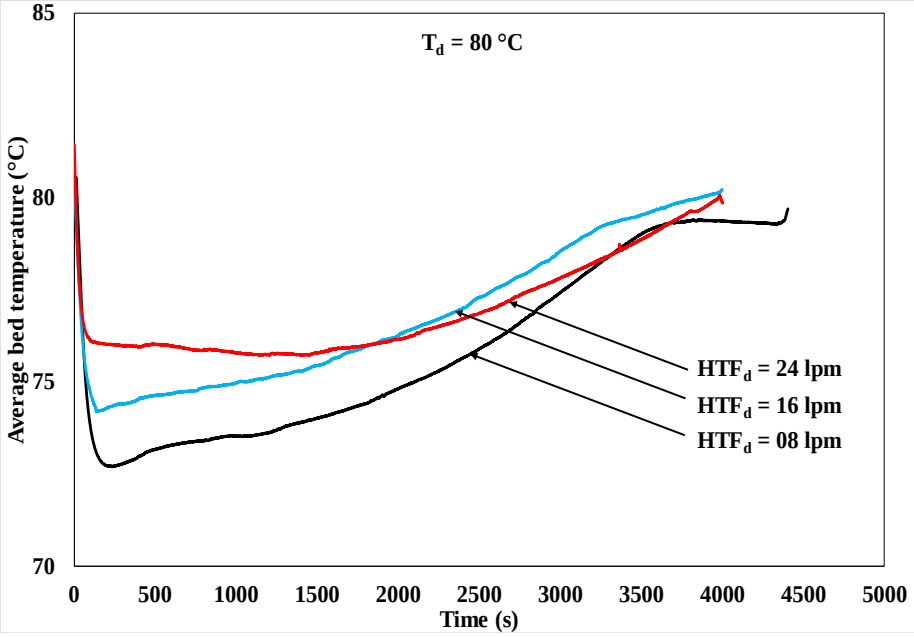

Fig. 5.18. Variation of average bed temperature by varying HTF flow rate during desorption.

5.3 Summary

Upon parametric study of different alloys, the poor reversibility at low desorption temperature (10 °C to 20 °C) was absorbed. Hence, flushing temperature for the purification study was fixed in the range of 10-20 °C. Whereas, due to significant reversibility at high desorption temperature (70 °C to 90 °C), the desorption temperatures can be varied between 70 °C and 90 °C. Similarly, the bed depicted significant absorption at 10-20 bar supply pressure. However, considering low-pressure applications, 10-20 bar and 20-25 °C can be considered as set condition for absorption in MHHPS.

CHAPTER 6 STUDIES ON METAL HYDRIDE BASED HYDROGEN PURIFICATION SYSTEMS

In comparison with different purification techniques, metal hydride (MH) based hydrogen purification technique is the simplest one to purify/separate hydrogen through thermally driven procedure, wherein the purification process is accomplished in three simple steps, i.e. absorption, flushing and desorption (Muthukumar et al., 2018). When the activated intermetallic alloy interacts with impure hydrogen mixture, it absorbs only hydrogen and the other gases remain in the void space. The impurity in the void space is flushed at low temperature. And then, during desorption at an elevated temperature, pure hydrogen is obtained. However, the continuous interaction of the impure gases deteriorates the reaction kinetics within the MH bed and decreases the hydrogen storage capacity of the MH bed, which can be regenerated back to its original capacity (Chen et al., 2014). In the previous chapter, the discussion was focused on obtaining the optimum operational parameters for the hydrogen storage and purification systems of different alloys. In the present chapter, the discussion is concentrated on the poisoning effect of the different gaseous impurities on different AB_5 alloys and the regeneration of MHHPS after bed poisoning.

6.1 Hydrogen Purification Characteristics of $La_{0.9}Ce_{0.1}Ni_5$

$La_{0.9}Ce_{0.1}Ni_5$ alloy has been selected as hydrogen purification alloy on the basis of its PCT characteristics as depicted in the Fig. 3.13. It is observed from the PCT curve that, the alloy is capable of absorbing hydrogen at even low pressure (5-10 bar) and ambient temperature. Further, because of hysteresis, the desorption pressure of alloy is nearly 1-2 bar at 25 °C, which makes it a compatible alloy for hydrogen purification application. The alloy was procured from "Whole Win (Beijing) Materials Sci. & Tech. Co., Ltd" with particle size in the range of 150-200 µm. The purification characteristics of $La_{0.9}Ce_{0.1}Ni_5$ have been obtained by studding the effect of the various gaseous impurities like CH_4, CO, CO_2, N_2, Ar, etc. on the absorption/desorption characteristics and hydrogen separation characteristics of the alloy.

6.1.1 Effect of CH_4 on the purification characteristics of $La_{0.9}Ce_{0.1}Ni_5$

In order to study the poisoning characteristics of MHHPS, an impure sample (CH_4 as impurity in H_2 gas) of different composition varying from 10% to 50% impurity was prepared using commercially available gas cylinders. The bed poisoning test was carried out by two different

methods. Initially cyclic study was carried out with 10% impurity level for 20 cycles and further bed was tested with different impurity level, varying from 10% to 50%.

6.1.1.1 Cyclic performance of $La_{0.9}Ce_{0.1}Ni_5$ with CH_4 as impurity

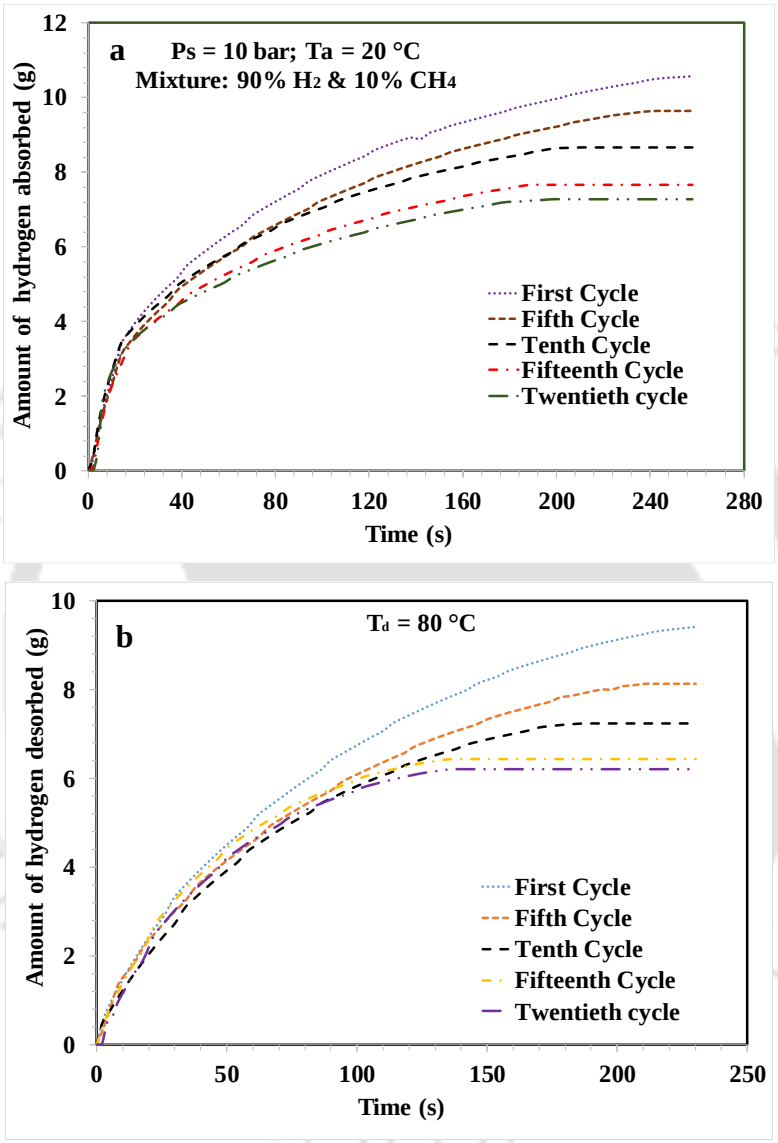

Fig. 6.1. (a) Amount of hydrogen absorbed and **(b)** desorbed during the cyclic study of MHHPS with input mixture with composition of 10% CH_4 & 90% H_2 by weight

Cyclic study was carried out with 10% impurity level for 20 absorption and desorption half cycles. The absorption and flushing temperatures for all the absorption cycle were fixed at 20 °C, while the desorption temperature was maintained at 80 °C. As shown in **Fig. 6.1a**, the amount of hydrogen absorbed was decreased from 10.59 g to 7.29 g from 1st to 20th absorption cycles. This

significant decrease in amount of hydrogen absorbed was due to the continuous interaction of CH_4 with alloy bed, which deteriorated the absorption kinetics of the bed. The presence of CH_4 in the absorption sample also resists the direct interaction of hydrogen with MH bed. Similarly, during desorption cycle (**Fig. 6.1b**), the amount of hydrogen desorbed for respective absorption was recorded as 9.41 g, 8.13 g, 7.25 g, 6.45 g & 6.22 g, respectively for 1st, 5th, 10th, 15th and 20th cycle. Amount of flushed gases in each cycle were about 0.5-0.7 g. Therefore, amount of hydrogen recovered after purification was in order of 95-97 % for all the purification cycles.

6.1.1.2 Effect of varying impurity level of CH_4 on the reaction kinetics of $La_{0.9}Ce_{0.1}Ni_5$

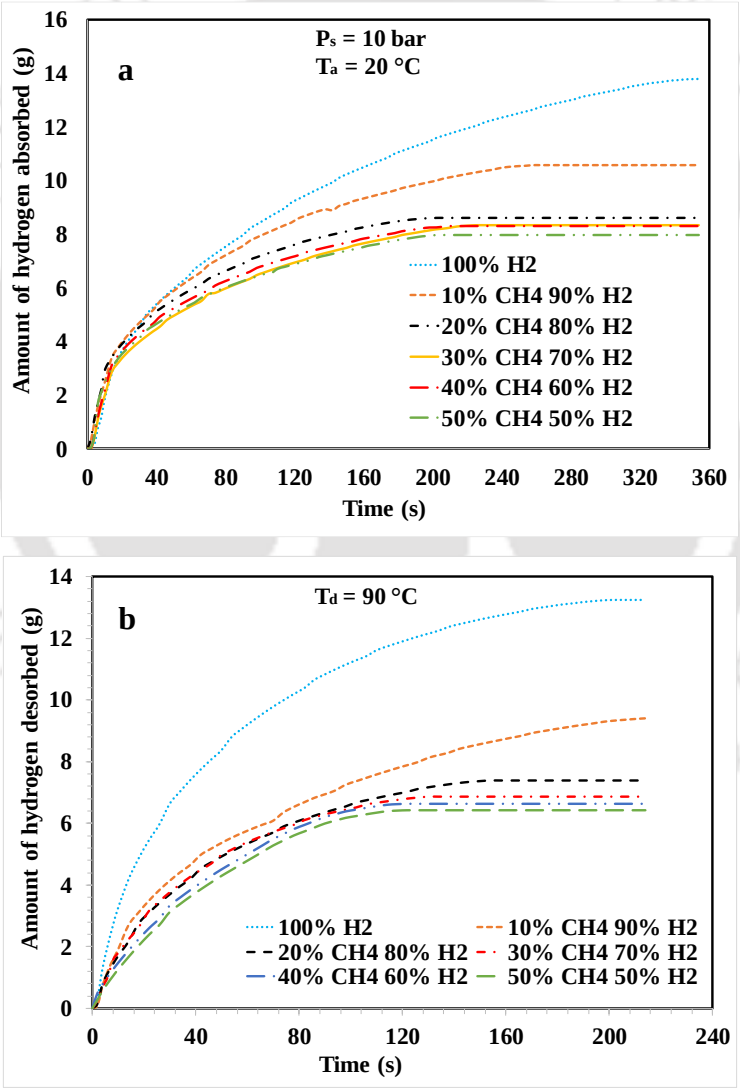

Fig. 6.2 Effect of impurity level of CH_4 on **(a)** amount of hydrogen absorbed and **(b)** desorbed during the purification study of $La_{0.9}Ce_{0.1}Ni_5$ based MHHPS.

Amount of hydrogen absorbed in a MHHPS was significantly affected by impurity level in the hydrogen gas. As depicted in **Fig. 6.2a**, for P_s =10 bar & T_a = 20 °C absorption condition, 13.79 g, 10.58 g, 8.63 g, 8.35 g, 8.31 g and 7.96 g was absorbed, respectively for 0%, 10%, 20%, 30%, 40% & 50% impurity content (CH_4 in H_2 gas) in 354 s, 258 s, 202 s, 226 s, 210 s and 202 s time duration. This significant decrease in the absorbed hydrogen was due to presence of higher impurity, which occupies the void space of the reactor bed and restricts the direct interaction of hydrogen with $La_{0.9}Ce_{0.1}Ni_5$ alloy.

Further, the desorption half cycle was conducted at 90 °C and P_d = 1 bar. As shown in **Fig. 6.2b**, 13.24 g, 9.41 g, 7.40 g, 6.86 g, 6.63 g and 6.42 g of hydrogen was desorbed for their respective absorbed amount, which contributes to 96%, 89%, 86%, 82%, 81% and 80 % for respective absorbed gas amount. If the reactor is flushed to ambient condition, some amount of impurity always remains in the reactor. With each purification cycle, the residual impurity increases in the reactor, that leads to bed poisoning and slows reaction kinetics. Hence, it is suggested to flush the reactor at pressure lesser than ambient, to avoid accumulation of impurity within the reactor.

6.1.2 Effect of CO_2 on the purification characteristics of $La_{0.9}Ce_{0.1}Ni_5$

In order to study the alloy poisoning characteristics of MHHPS, two different kind of test were performed. Initially, cyclic stability of the system was Carried out, wherein the repetitive analysis of absorption/desorption characteristics in MHHPS was performed with fixed impurity level of 10% by weight, for 25 cycles. Further, the reactor was exposed to impurity of different levels, varying from 10% to 50% by weight (CO_2 in H_2).

6.1.2.1 Cyclic performance of $La_{0.9}Ce_{0.1}Ni_5$ with CO_2 as impurity

The cyclic test on MHHPS was conducted using a gas mixture of composition 10% CO_2 and 90% H_2 by weight, for 25 absorptions/desorption half cycle. The experiment was performed at 20 °C and 10 bar supply pressure for all the absorption half cycle. As depicted in **Fig. 6.3a**., the amount of hydrogen absorbed was 11.1174 g, 10.4576 g, 10.1294 g, 10.0255 g, 9.9557 g and 9.2255 g respectively for 1^{st}, 5^{th}, 10^{th}, 15^{th}, 20^{th} and 25^{th} absorption cycle. This constituted to the hydrogen storage capacity of 0.92 wt%, 0.87 wt%, 0.84 wt%, 0.83 wt%, 0.82 wt% and 0.78 wt% respectively in 260 s, 256 s, 242 s, 272 s, 254 s and 240 s, from 1^{st} to 25^{th} absorption cycle. This drop in the amount of hydrogen absorbed from 1^{st} to 25^{th} absorption cycle was due to continuous interaction with CO_2 impurity on $La_{0.9}Ce_{0.1}Ni_5$. The presence of CO_2 in the void space of the reactor also

restricts the direct interaction of total surface area of the alloy to the hydrogen gas, which finally decreases the rate of absorption. This effect can also be observed from the temperature variation curve depicted in **Fig. 6.3b**. The peak temperature achieved during the absorption process was decreased from 1st to 25th absorption cycle, for the same absorption condition of 10 bar and 20 °C.

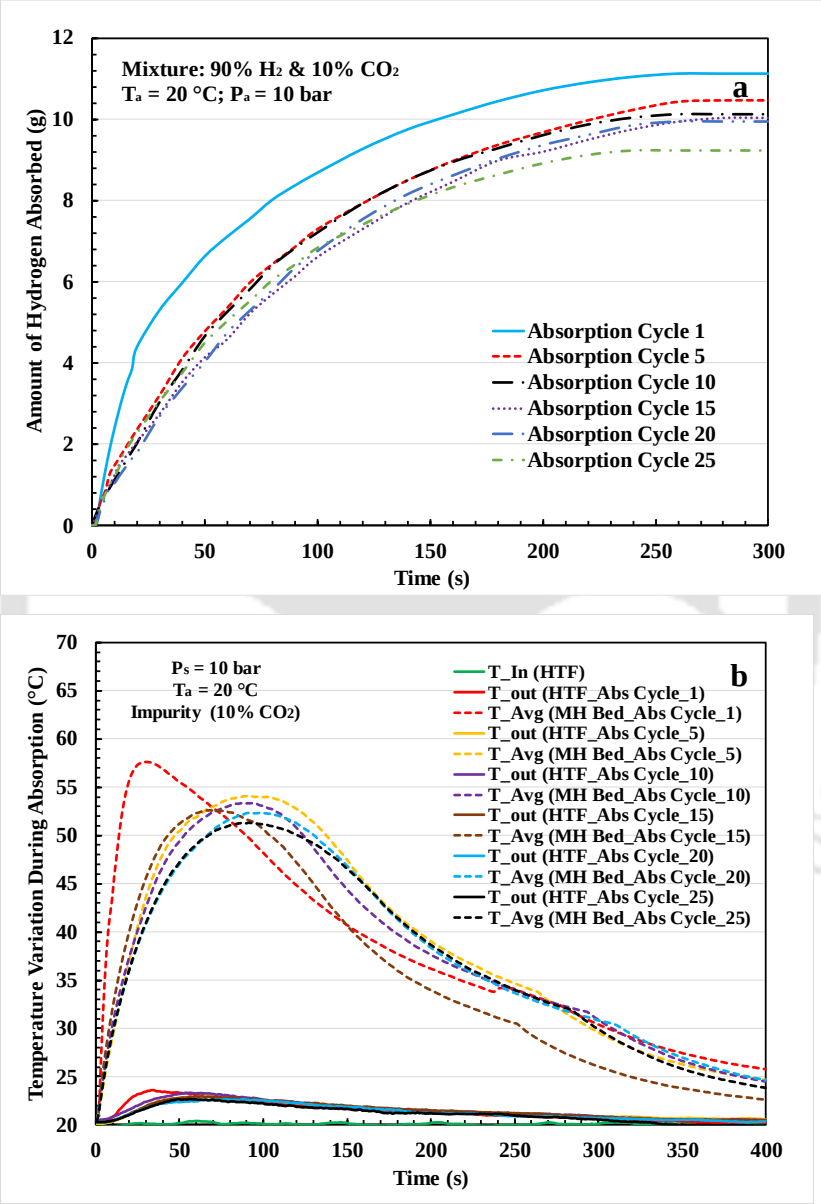

Fig. 6.3 (a) Rate of hydrogen absorbed and **(b)**Variation in temperature of MH bed and HTF during absorption process of the cyclic study in MHHPS

On completion of absorption half cycle, the reactor was flushed at 15 °C, wherein 0.5 to 1 g of gas (mainly impurity) were removed from the reactor, which was trapped in the void space. The reason of maintaining low flushing temperature was to restrict the desorption of hydrogen during flushing, as the equilibrium bed pressure at 15 °C is below ambient for the $La_{0.9}Ce_{0.1}Ni_5$.

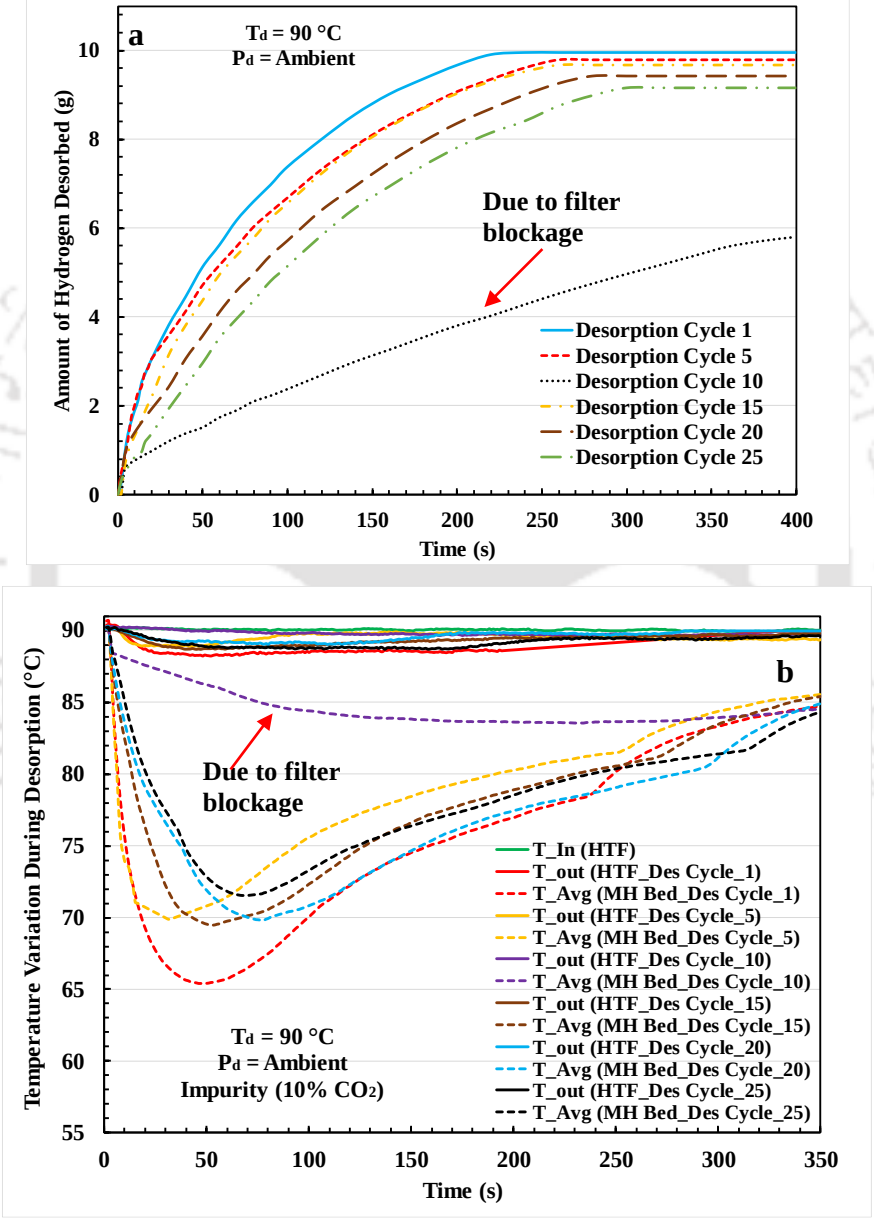

Fig. 6.4 (a) Rate of hydrogen desorbed and (b) Variation in temperature of MH bed and HTF during desorption cycle of the cyclic study in MHHPS

Further, the desorption was performed at 90 °C and atmospheric pressure. As depicted in **Fig. 6.4a**, the amount of hydrogen desorbed was 9.9559 g, 9.7907 g, 9.6701 g, 9.4291 g and 9.1609 g respectively for 1st, 5th, 15th, 20th and 25th cycle, which corresponded to reversibility of 89.6%, 93.6%, 94.3%, 94.6% and 98% for respective desorption cycle. However, the flushing losses are not considered in the reversibility calculation, which varied from 0.5 to 1 g in each cycle. If the flushing losses are considered, the reversibility will be in order of 95-99%.

However, for the 10th desorption cycle, because of the reactor filter chocking, the rate of desorption was significantly slow, which can be also observed in the temperature curves as depicted in **Fig. 6.4b**. The filter chocking occurred due to accumulation of MH alloy at the filter pores, during the desorption. However, during absorption cycle self-cleaning of the filter occurred as the pressurised gases went back to the reactor. Because of alloy poisoning, the rate of desorption also got affected, which can be observed in Fig. 6.4b, wherein, the drop in the bed temperature decreases for each desorption cycle. The desorption was completed in 240 s, 255 s, 260 s, 275 s and 290 s respectively for 1st, 5th, 15th, 20th and 25th desorption cycle.

6.1.2.2 Effect of varying impurity level of CO_2 on reaction kinetics of $La_{0.9}Ce_{0.1}Ni_5$

For obtaining the effect of different impurity level of CO_2 on the MHHPS, the impurity level of CO_2 in H_2 was varied from 10% to 50% by weight. As depicted in **Fig. 6.5**, during the absorption half cycle, significant drop in the absorption capacity of MHHPS was observed for 10% to 50% of CO_2 impurity. The amount of hydrogen absorbed was 11.1174 g, 10.2123 g, 9.3214g, 8.30 g and 8.01 g respectively for 10%, 20%, 30%, 40% and 50% impurity content, with absorption time of 260 s, 270 s, 240 S, 218 s and 255 s respectively. This significant drop in the absorption capacity of the MHHPS, was due to the increase in the amount of CO_2 in the void space of the reactor, which restricted the direct interaction of H_2 with the MH alloy, resulting in the lowering of the absorption capacity of the reactor.

For the respective absorption half cycle, the desorption was carried out at 90 °C and atmospheric pressure. As depicted in **Fig. 6.6**, the amount of hydrogen desorbed for each desorption cycle corresponding to 10%, 20%, 30%, 40% and 50% impurities were 9.559 g, 9.1012 g, 8.3272 g, 7.8715 g and 7.4946 g respectively in 240 s, 280 s, 235 s, 216 s and 220 s, which corresponds to the reversible desorption capacity of 86%, 89.2%, 89%, 99.8% and 93.5% respectively.

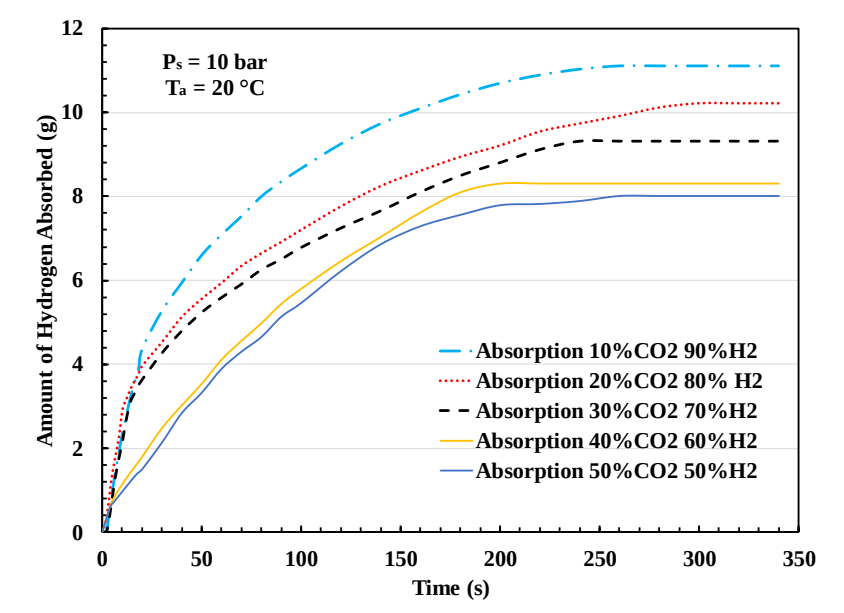

Fig. 6.5 Rate of hydrogen absorbed during absorption cyclic for hydrogen sample of different impurity level

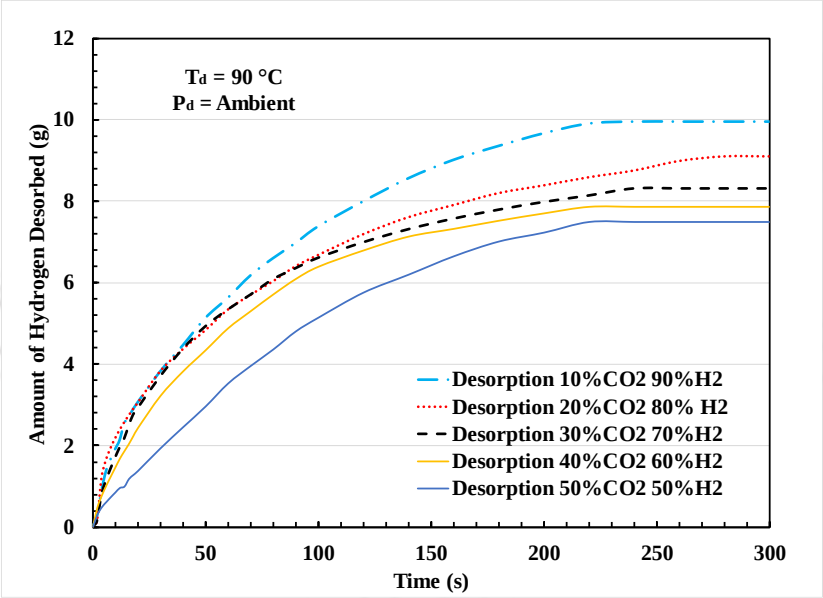

Fig. 6.6 Rate of hydrogen desorbed during absorption cyclic for hydrogen sample of different impurity level

All the flushing cycle were carried out at atmospheric pressure, considering the actual fussing condition during the operation of MHHPS. This resulted in the accumulation of some CO_2, within the reactor during each flushing cycle, which finally added up to bed poisoning and resulted in the slower absorption kinetics. It was also observed that the alloy poisoning was directly proportional

to the impurity content in the gas mixture. Hence, with increase in the impurity content of the mixture, the purification characteristics of the alloy decreases.

6.1.3 Effect of CO on the purification characteristics of $La_{0.9}Ce_{0.1}Ni_5$

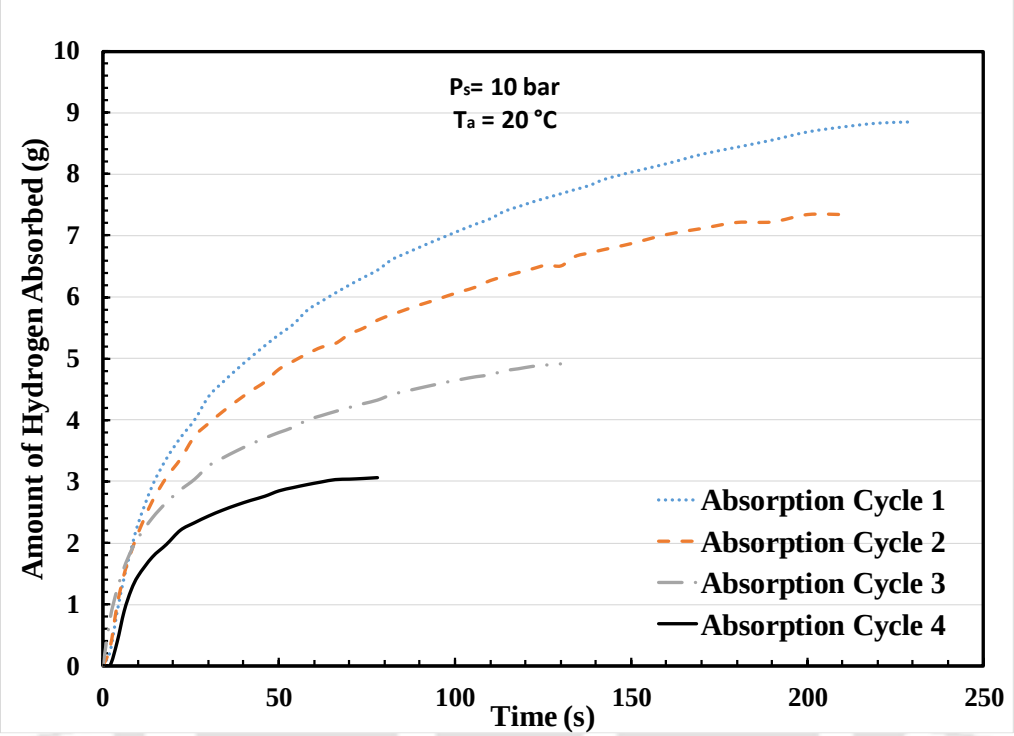

Fig. 6.7 Effect of CO as impurity on the amount of hydrogen absorbed

In order to study the alloy poisoning characteristics of CO as impurity in the hydrogen gas, cyclic study of the system was carried out, wherein the repetitive analysis of absorption/desorption characteristics in MHHPS was performed with fixed impurity level of 10% by weight. Initially, like other gaseous impurities, it was decided to carry out experiments for 25 cycles, but as the experimental outcomes were unexpected, the cyclic study was restricted to 4 cycles.

The cyclic test on $La_{0.9}Ce_{0.1}Ni_5$ was conducted using a gas mixture of composition 10% CO and 90% H_2 by weight. The absorption was performed at 20 °C and 10 bar supply pressure for all the absorption half cycles. As depicted in **Fig. 6.7**, the amount of hydrogen absorbed was 8.8551 g, 7.3362 g, 4.9107 g and 3.0689 g respectively for 1st, 2nd, 3rd and 4th absorption half cycle. This constituted to the hydrogen storage capacity of 0.73 wt%, 0.61 wt%, 0.41 wt% and 0.25 wt% respectively in 230 s, 210 s, 130 s, and 78 s, from 1st to 4th absorption half cycle. This significant

drop in the absorption capacity of $La_{0.9}Ce_{0.1}Ni_5$ was due chemical reaction within the bed in presence of CO. It was observed that, in presence of AB_5 alloy, CO was reacting with hydrogen and forming methane and moisture end product. The possible reaction happening within the MH bed is depicted in equation 6.1.

$$CO + 3H_2 \rightarrow CH_4 + H_2O \text{ (Moisture)} + \text{Heat} \quad (6.1)$$

Because of moisture, the bed poisoning is very rigorous. Therefore, MHHPS is least capable of separating H_2 with CO as impurity. The proof of methanation is discussed in the later section (section 6.5.4) of this chapter, wherein sample TCD results are reported.

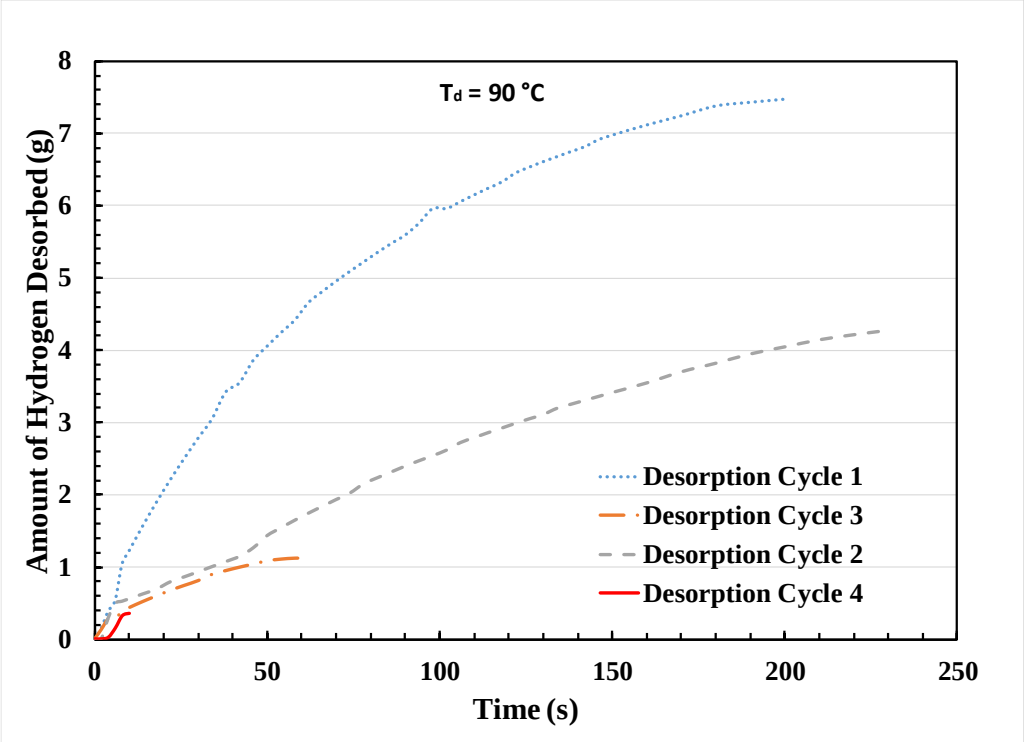

Fig. 6.8 Effect of CO as impurity on the amount of hydrogen desorbed

For the respective absorption half cycle, the desorption was carried out at 90 °C and atmospheric pressure. As depicted in **Fig. 6.8**, the amount of hydrogen desorbed for each desorption cycle were 7.4695 g, 4.2791 g, 1.1221 g, and 0.3568 g respectively in 200 s, 230 s, 62 s, 216 s and 10 s, which corresponds to the reversible desorption capacity of 85%, 60%, 21%, and 8% respectively for 1st to 4th desorption cycle.

6.2 Hydrogen Purification Characteristics of $LaNi_5$

Similar to $La_{0.9}Ce_{0.1}Ni_5$, $LaNi_5$ has been selected as hydrogen purification alloy on the basis of its thermodynamic screening based on PCT characteristics as depicted in **Fig. 3.14**. It can be observed from its PCT curve that, the alloy is capable of absorbing hydrogen at even low pressure (2-10 bar) and ambient temperature. Further, because of hysteresis, the desorption pressure of alloy is nearly 1 bar at 25 °C, which makes it a compatible alloy for hydrogen purification application. The alloy was procured from "Whole Win (Beijing) Materials Sci. & Tech. Co., Ltd" with particle size in the range of 150-200 µm. The purification characteristics of $LaNi_5$ have been obtained by studding the effect of the various gaseous impurities like CH_4, CO, CO_2, etc. on the absorption/desorption characteristics and hydrogen separation characteristics of the alloy

6.2.1 Effect of CH_4 on the purification characteristics of $LaNi_5$

In order to study the poisoning characteristics of CH_4 on $LaNi_5$, an impure sample (CH_4 as impurity in H_2 gas) of different composition varying from 10% to 50% impurity was prepared using commercially available gas cylinders. The bed poisoning test was carried out by two different methods. Firstly, cyclic study was performed with 10% impurity level for 25 cycles and secondly, bed was tested with varying impurity level, between 10% to 50%.

6.2.1.1 Cyclic performance of $LaNi_5$ with CH_4 as impurity

Cyclic study was performed with 10% impurity for 25 absorption and desorption half cycles. The absorption and flushing temperatures for all the absorption cycle were fixed at 20 °C, while the desorption temperature was maintained at 90 °C. As shown in **Fig. 6.9**, the amount of hydrogen absorbed decreased from 10.8270 g to 7.3887 g from 1st to 25th absorption cycles. This significant decrease in amount of hydrogen absorbed was due to the continuous interaction of CH_4 with $LaNi_5$, which deteriorated the absorption kinetics of the bed. The presence of CH_4 in the absorption sample also resists the direct interaction of hydrogen with MH bed. Similarly, during desorption cycle (**Fig. 6.10**), the amount of hydrogen desorbed for respective absorption was recorded as 9.1763 g, 8.8140 g, 8.3395 g, 6.523 g 6.4109 g & 6.3511 g, respectively for 1st, 5th, 10th, 15th, 20th and 25th cycle. Amount of flushed gases in each cycle were about 0.5-1.2 g. Therefore, amount of hydrogen recovered after purification was in order of 70-85 % for all the purification cycles.

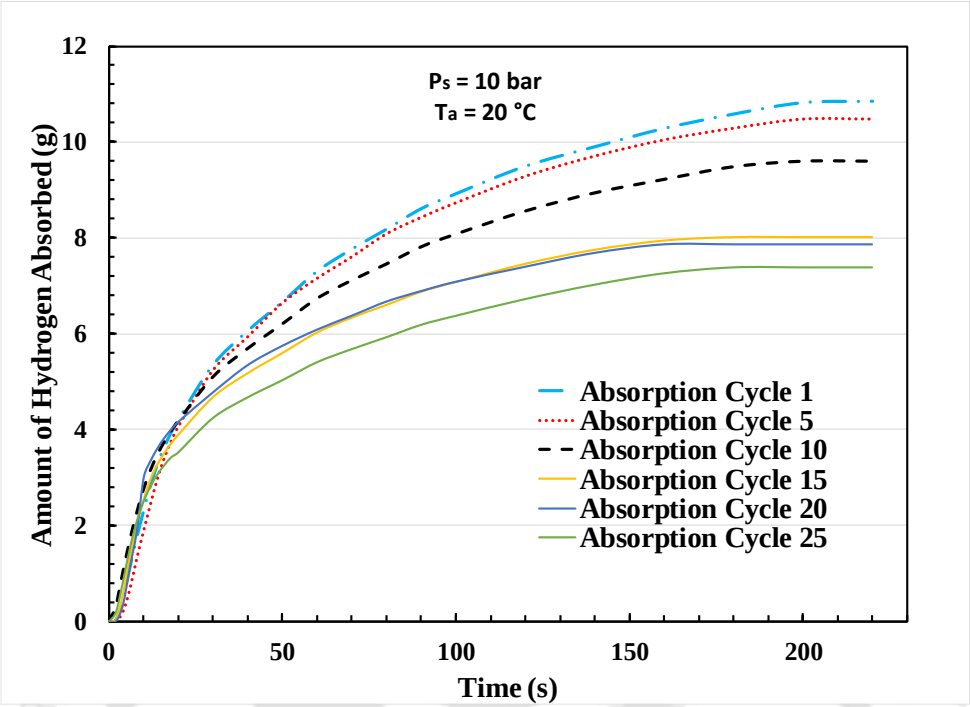

Fig. 6.9. Effect of CH_4 as impurity on amount of hydrogen absorbed in $LaNi_5$ based MHHPS

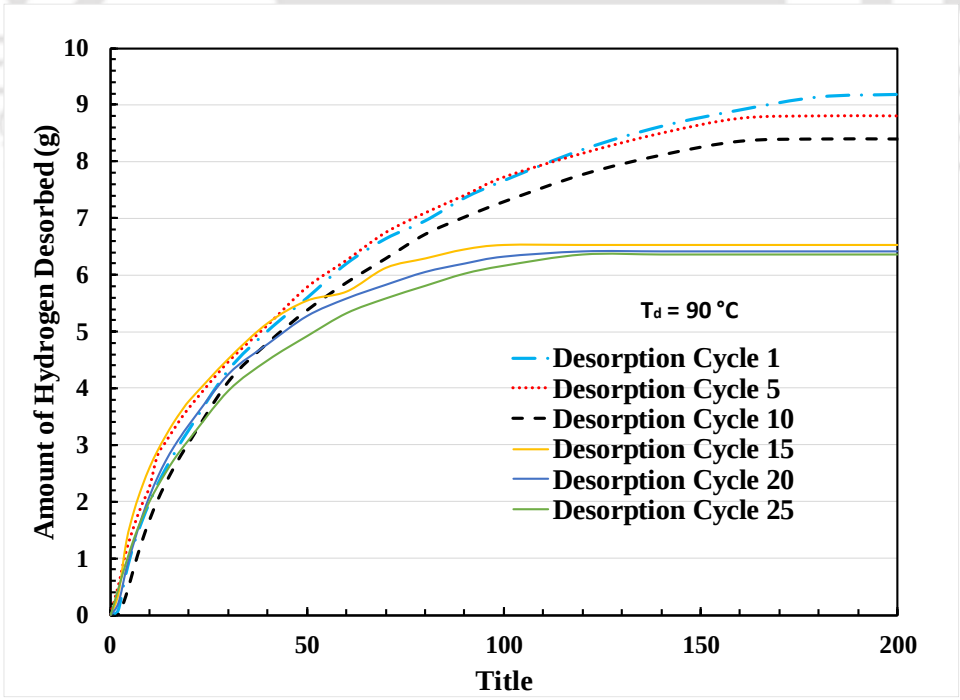

Fig. 6.10. Effect of CH_4 as impurity on amount of hydrogen desorbed in $LaNi_5$ based MHHPS.

6.2.1.2 Effect of varying impurity level of CH_4 on the reaction kinetics of $LaNi_5$

Amount of hydrogen absorbed in $LaNi_5$ based MHHPS was significantly affected by impurity level of CH_4 in the hydrogen gas. As depicted in **Fig. 6.11**, for P_s =10 bar & T_a = 20 °C absorption condition, 10.8271 g, 9.6195 g, 8.7475 g, 8.0255 g, 8.31 g and 7.0347 g was absorbed, respectively for 10%, 20%, 30%, 40% & 50% impurity content (CH_4 in H_2 gas) in 198 s, 200 s, 170 s, 178 s, and 160 s. This significant decrease in the absorbed hydrogen was due to presence of higher impurity, which occupies the void space of the reactor bed and restricts the direct interaction of hydrogen with MH alloy.

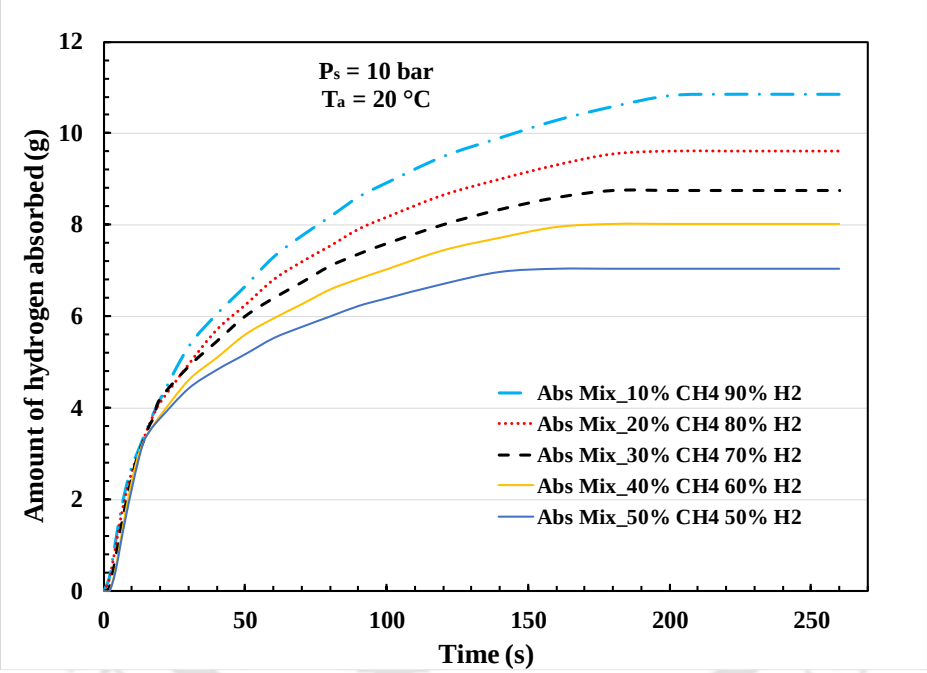

Fig. 6.11 Effect of impurity level of CH_4 on amount of hydrogen absorbed in $LaNi_5$ based MHHPS.

Further, the desorption half cycle was conducted at 90 °C and P_d = 1 bar. As shown in **Fig. 6.12**, 9.5012 g, 8.2462 g, 7.9231 g, 7.3226 g and 6.4521 g of hydrogen was desorbed for their respective absorbed amount, which contributes to 85%, 84%, 70%, 81%, 81% and 86 % for respective absorbed gas amount. If the reactor is flushed to ambient condition, some amount of impurity always remains in the reactor. With each purification cycle, the residual impurity increases in the reactor, that leads to bed poisoning and slows reaction kinetics. Hence, it is suggested to flush the reactor at pressure lesser than ambient, to avoid accumulation of impurity within the reactor.

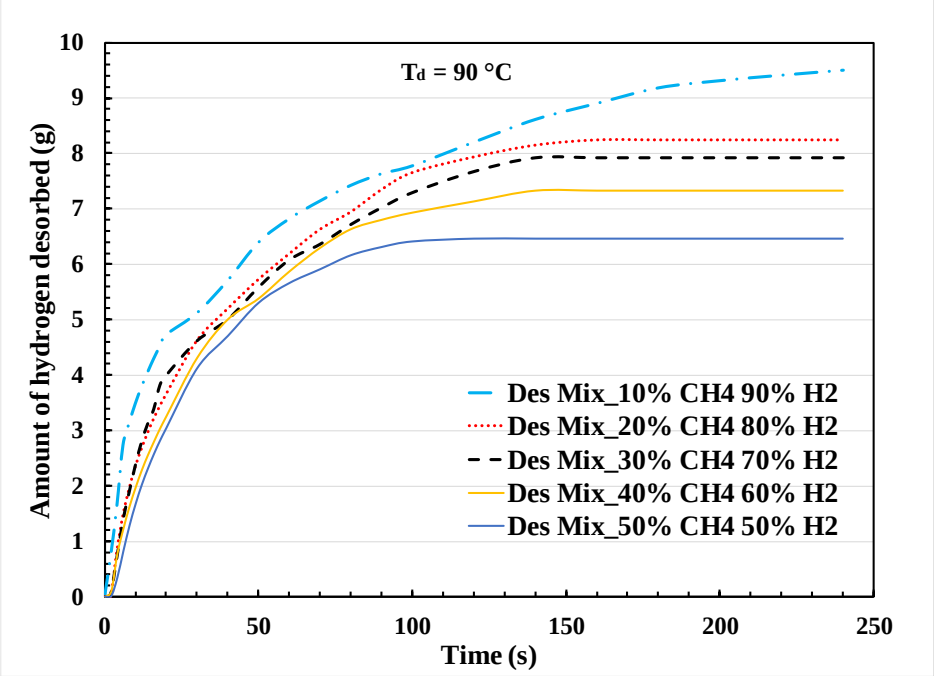

Fig. 6.12 Effect of impurity level of CH4 on amount of hydrogen desorbed in $LaNi_5$ based MHHPS.

6.2.2 Effect of CO_2 on the purification characteristics of $LaNi_5$

In order to study the alloy poisoning characteristics of $LaNi_5$ based MHHPS, two different kind of test were performed. Initially, cyclic stability of the system was carried out, wherein the repetitive analysis of absorption/desorption characteristics in MHHPS was performed with fixed impurity level of 10% by weight, for 25 cycles. Further, the reactor was exposed to impurity of different levels, varying from 10% to 50% by weight (CO_2 in H_2).

6.2.2.1 Cyclic performance of $LaNi_5$ with CO_2 as impurity

The cyclic test on $LaNi_5$ based MHHPS was conducted using a gas mixture of composition 10% CO_2 and 90% H_2 by weight, for 25 absorptions/desorption half cycle. The experiment was performed at 20 °C and 10 bar for all the absorption half cycle. As depicted in **Fig. 6.13**, the amount of hydrogen absorbed was 13.0360 g, 10.4576 g, 10.8912 g, 10.5886 g, 10.4132 g 10.1010 g and 9.8058 g respectively for 1st, 5th, 10th, 15th, 20th and 25th absorption cycle. This constituted to the hydrogen storage capacity of 1.08 wt%, 0.91 wt%, 0.88 wt%, 0.87 wt%, 0.84 wt% and 0.82 wt% respectively in 260 s, 218 s, 220 s, 236 s, 220 s and 220 s, from 1st to 25th absorption cycle.

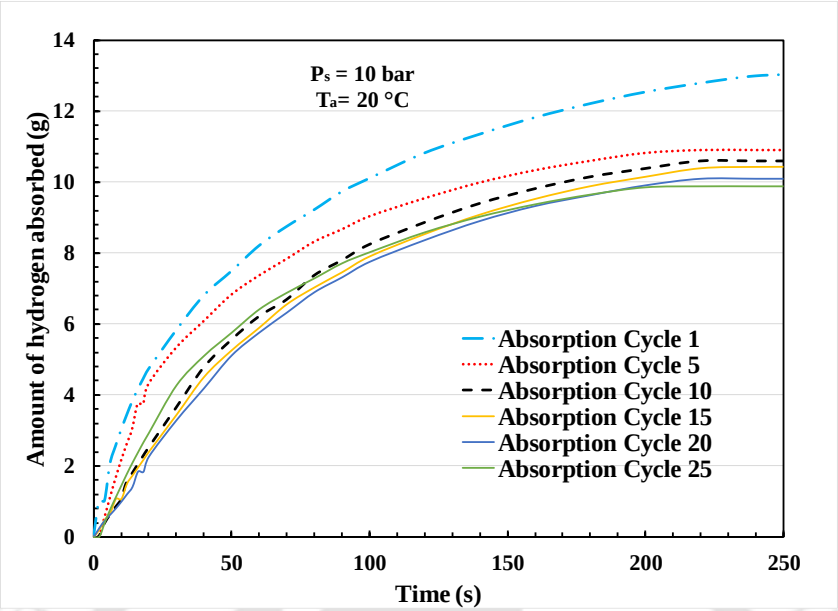

Fig. 6.13 Effect of CO_2 as impurity on amount of hydrogen desorbed in $LaNi_5$ based MHHPS

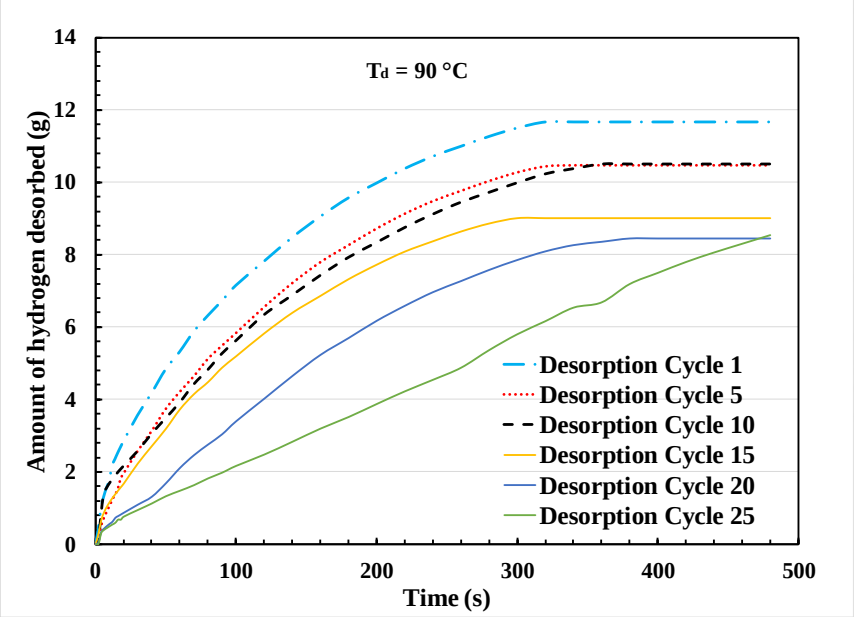

Fig. 6.14 Effect of CO_2 as impurity on amount of hydrogen desorbed in $LaNi_5$ based MHHPS

This drop in the amount of hydrogen absorbed from the 1st to 25th absorption cycle was due to the bed poisoning of $LaNi_5$, due to continuous interaction with CO_2 impurity. The presence of CO_2 in the void space of the reactor also restricts the direct interaction of total surface area of the alloy to the hydrogen gas, which finally decreases the rate of absorption.

Further, the desorption was performed at 90 °C and atmospheric pressure. As depicted in **Fig. 6.14**, the amount of hydrogen desorbed was 11.6542 g, 10.4562 g, 10.5040 g, 9.0067 g, 8.4553 g and 8.5407 g respectively for 1st, 5th, 10th, 15th, 20th and 25th cycle, which corresponded to reversibility of 89.6%, 96%, 97%, 86%, 84% and 87% for respective desorption cycle. However, the flushing losses are not considered in the reversibility calculation, which varied from 0.5 to 1 g in each cycle. If the flushing losses are considered, the reversibility will be in order of 95-99%.

6.2.2.2 Effect of varying impurity level of CO_2 on reaction kinetics of $LaNi_5$

For obtaining the effect of different impurity level of CO_2 on the $LaNi_5$ based MHHPS, the impurity level of CO_2 in H_2 was varied from 10% to 50% by weight. As depicted in **Fig. 6.15**, during the absorption half cycle, significant drop in the absorption capacity of $LaNi_5$ was observed for 10% to 50% of CO_2 impurity. The amount of hydrogen absorbed was 13.0361 g, 10.1223 g, 9.8715 g, 9.2581 g and 8.0255 g respectively for 10%, 20%, 30%, 40% and 50% impurity content, with absorption time of 244 s, 218 s, 250 s, 262 s and 200 s respectively.

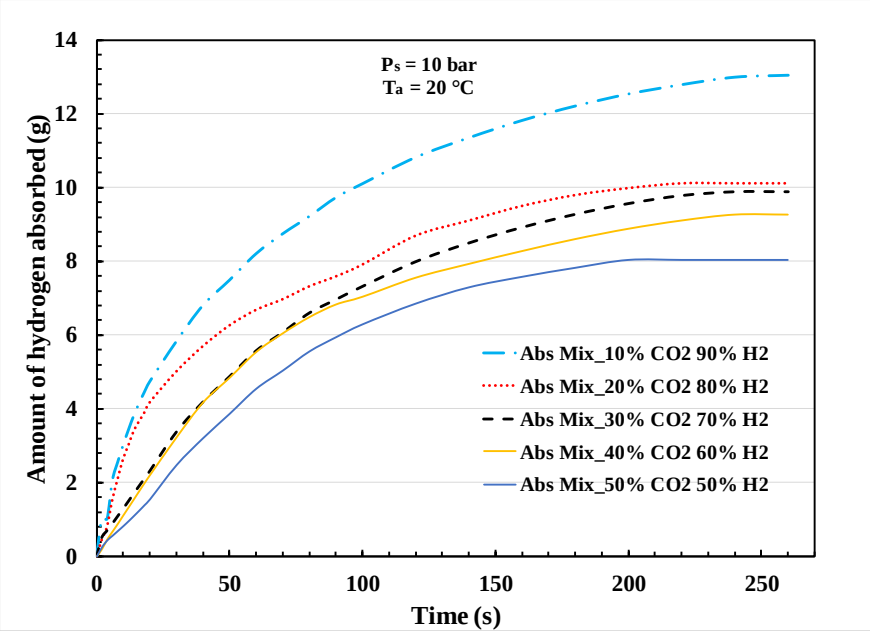

Fig. 6.15 Effect of impurity level of CO_2 on amount of hydrogen absorbed in $LaNi_5$ based MHHPS.

This significant drop in the absorption capacity of the MHHPS, was due to the increase in the amount of CO_2 in the void space of the reactor, which restricted the direct interaction of H_2 with the MH alloy, resulting in the lowering of the absorption capacity of the reactor.

For the respective absorption half cycle, the desorption was carried out at 90 °C and atmospheric pressure. As depicted in **Fig. 6.16**, the amount of hydrogen desorbed for each desorption cycle corresponding to 10%, 20%, 30%, 40% and 50% impurities were 11.6540 g, 8.9159 g, 85092 g, 8.3014 g and 7.2589 g respectively in 320 s, 400 s, 380 s, 460 s and 560 s, which corresponds to the reversible desorption capacity of 89.4%, 88.2%, 86.2%, 89.6% and 88% respectively.

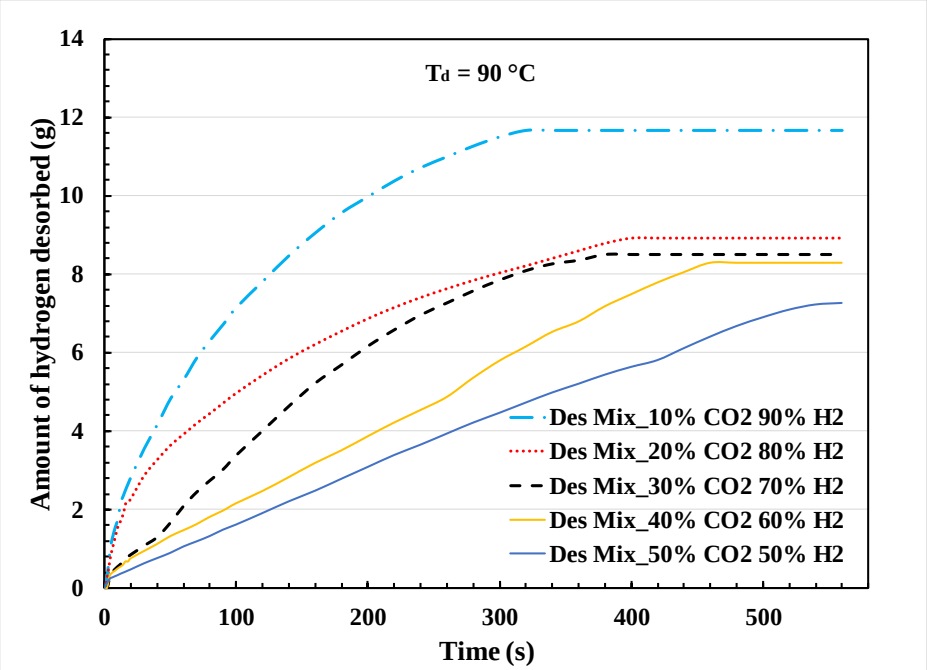

Fig. 6.16 Effect of impurity level of CH_4 on amount of hydrogen desorbed in $LaNi_5$ based MHHPS.

All the flushing cycle were carried out at atmospheric pressure, considering the actual fussing condition during the operation of MHHPS. This resulted in the accumulation of some CO_2, within the reactor during each flushing cycle, which finally added up to bed poisoning and resulted in the slower absorption kinetics. It was also observed that the alloy poisoning was directly proportional to the impurity content in the gas mixture. Hence, with increase in the impurity content of the mixture, the purification characteristics of the alloy decreases.

6.2.3 Effect of CO on the purification characteristics of $LaNi_5$

In order to study the alloy poisoning characteristics of CO as impurity in the hydrogen gas, cyclic study of the system was carried out, wherein the repetitive analysis of absorption/desorption characteristics in MHHPS was performed with fixed impurity level of 10% by weight. Similar to

$La_{0.9}Ce_{0.1}Ni_5$ based MHHPS, the experimental outcomes were unexpected, the cyclic study was restricted to 4 cycles.

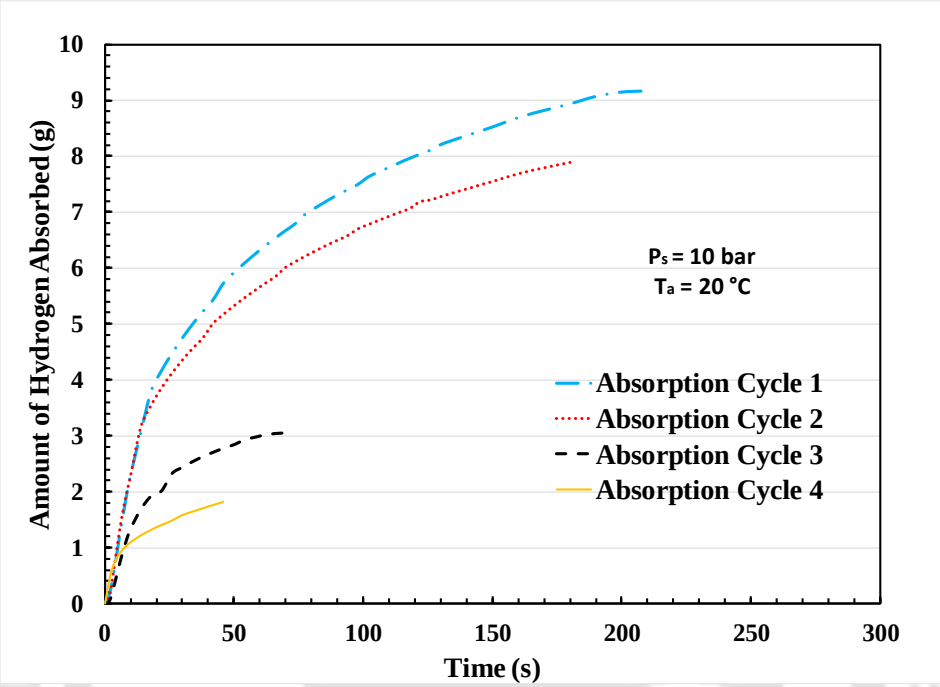

Fig. 6.17 Effect of CO as impurity on amount of hydrogen absorbed in $LaNi_5$ based MHHPS

The cyclic test on $LaNi_5$ was conducted using a gas mixture of composition 10% CO and 90% H_2 by weight. The absorption was performed at 20 °C and 10 bar for all the absorption half cycles. As depicted in **Fig. 6.17**, the amount of hydrogen absorbed was 9.1628 g, 7.8809 g, 3.0409 g and 1.8178 g respectively for 1st, 2nd, 3rd and 4th absorption half cycle. This constituted to the hydrogen storage capacity of 0.76 wt%, 0.65 wt%, 0.25 wt% and 0.15 wt% respectively in 210 s, 180 s, 70 s, and 46 s, from 1st to 4th absorption half cycle. This significant drop in the absorption capacity of $La_{0.9}Ce_{0.1}Ni_5$ was due chemical reaction within the bed in presence of CO. It was observed that, in presence of AB_5 alloy, CO was reacting with hydrogen and forming methane and moisture end product. The possible reaction happening within the MH bed is depicted in Eq. 6.1. Because of moisture, the bed poisoning is very rigorous. Therefore, it is MHHPS is least capable of separating H_2 with CO as impurity.

For the respective absorption half cycle, the desorption was carried out at 90 °C and atmospheric pressure. As depicted in **Fig. 6.18**, the amount of hydrogen desorbed for each desorption cycle were 7.6199 g, 3.6647 g, 0.3497 g, and 0.3568 g respectively in 130 s, 78 s, 10 s, and 10 s, which corresponds to the reversible desorption capacity of 82.8%, 47%, 8%, and 13% respectively for 1st to 4th desorption cycle.

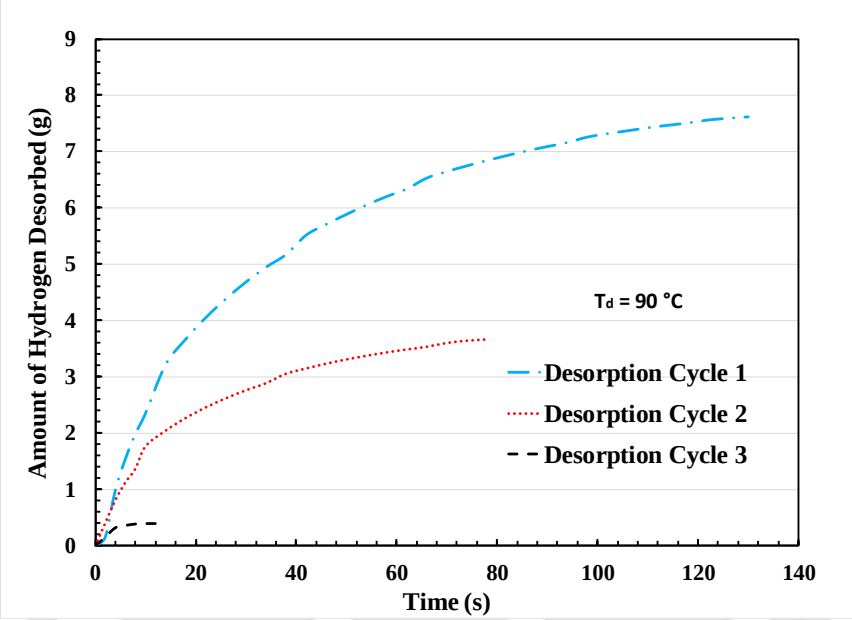

Fig. 6.18 Effect of CO as impurity on amount of hydrogen desorbed in $LaNi_5$ based MHHPS

6.3 Hydrogen Purification Characteristics of $LaNi_{0.7}Al_{0.3}$

Similar to $La_{0.9}Ce_{0.1}Ni_5$ and $LaNi_5$, the alloy for the third reactor was finalised as $LaNi_{0.7}Al_{0.3}$. The alloy selection was based on the thermodynamic screening based on its PCT characteristics as depicted in **Fig. 3.12**. It can be observed from its PCT curve that, the alloy is capable of absorbing hydrogen at even low pressure (1-5 bar) and ambient temperature. Further, because of hysteresis, the desorption pressure of alloy is < 1 bar at 25 °C, which makes it a most suited alloy for hydrogen purification application. The purification characteristics of $LaNi_{0.7}Al_{0.3}$ have been obtained by studding the effect of the various gaseous impurities like CH_4, CO, CO_2, etc. on the absorption/desorption characteristics and hydrogen separation characteristics of the alloy.

6.3.1 Effect of CH_4 on the purification characteristics of $LaNi_{0.7}Al_{0.3}$

6.3.1.1 Cyclic performance of $LaNi_{0.7}Al_{0.3}$ with CH_4 as impurity

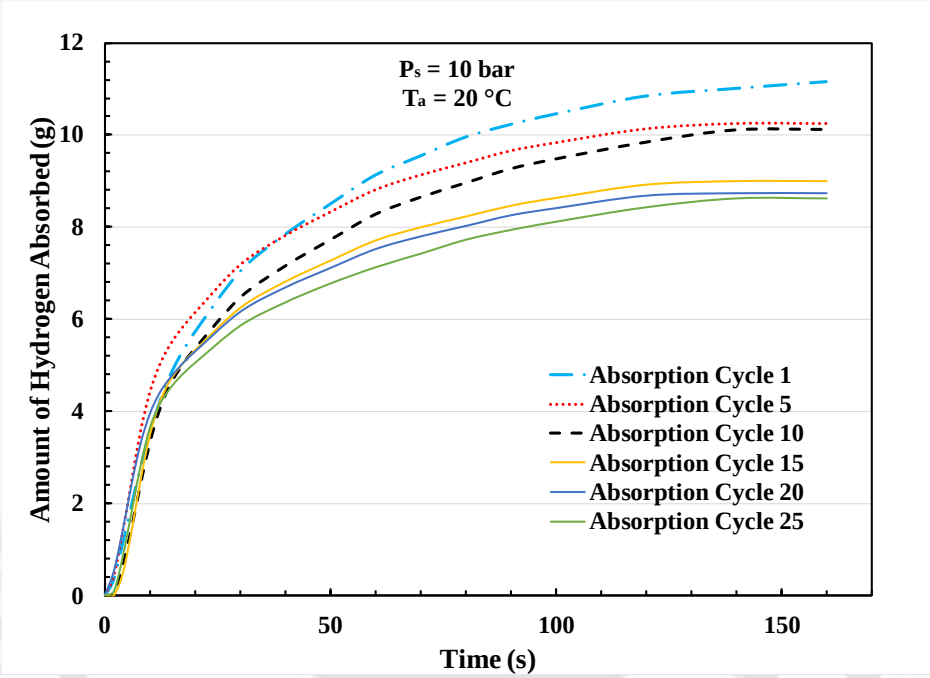

Fig. 6.19 Effect of CH_4 as impurity on amount of hydrogen absorbed in $LaNi_{4.7}Al_{0.3}$ based MHHPS

Cyclic study was carried out with 10% impurity level for 20 absorption and desorption half cycles. The absorption and flushing temperatures for all the absorption cycle were fixed at 20 °C, while the desorption temperature was maintained at 90 °C. As shown in **Fig. 6.19**, the amount of hydrogen absorbed decreased from 11.1526 g to 8.6307 g from 1st to 25th absorption cycles. This significant decrease in amount of hydrogen absorbed was due to the continuous interaction of CH_4 with alloy bed, which deteriorated the absorption kinetics of the bed. The presence of CH_4 in the absorption sample also resists the direct interaction of hydrogen with MH bed. Similarly, during desorption cycle (**Fig. 6.20**), the amount of hydrogen desorbed for respective absorption was recorded as 8.1041 g, 7.0887 g, 7.0907 g, 6.7207 g & 5.9664 g, respectively for 1st, 5th, 10th, 15th, 20th and 25th cycle. Amount of flushed gases in each cycle were about 0.5-1.2 g. Therefore, amount of hydrogen recovered after purification was in order of 90-95 % for all the purification cycles.

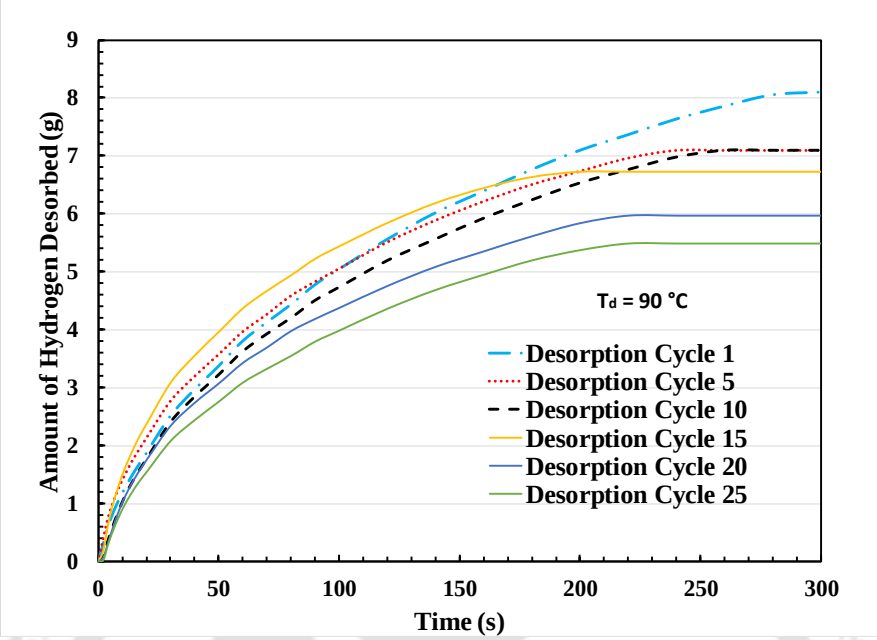

Fig. 6.20 Effect of CH_4 as impurity on amount of hydrogen desorbed in $LaNi_{4.7}Al_{0.3}$ based MHHPS

6.3.1.2 Effect of varying impurity level of CH_4 on the reaction kinetics of $LaNi_{4.7}Al_{0.3}$

Amount of hydrogen absorbed in a $LaNi_{4.7}Al_{0.3}$ based MHHPS was significantly affected by impurity level in the hydrogen gas. As depicted in **Fig. 6.21**, for P_s =10 bar & T_a = 20 °C absorption condition, 11.5012 g, 11.101 g, 9.3356 g, 8.0123 g and 7.0319 g was absorbed, respectively for 10%, 20%, 30%, 40% & 50% impurity content (CH_4 in H_2 gas) in 160 s, 150 s, 160 s, 152 s and 144 s time duration. This significant decrease in the absorbed hydrogen was due to presence of higher impurity, which occupies the void space of the reactor bed and restricts the direct interaction of hydrogen with MH alloy.

Further, the desorption half cycle was conducted at 90 °C and P_d = 1 bar. As shown in **Fig. 6.22**, 9.1631 g, 8.2122 g, 7.0987 g, 6.5012 g and 5.6035 g of hydrogen was desorbed for their respective absorbed amount, which contributes to 79.8%, 74.9%, 76.03%, 81.4% and 79.68 % for respective absorption. With each purification cycle, the residual impurity increases in the reactor, that leads to bed poisoning and slows reaction kinetics. Hence, it is suggested to flush the reactor at pressure lesser than ambient, to avoid accumulation of impurity within the reactor.

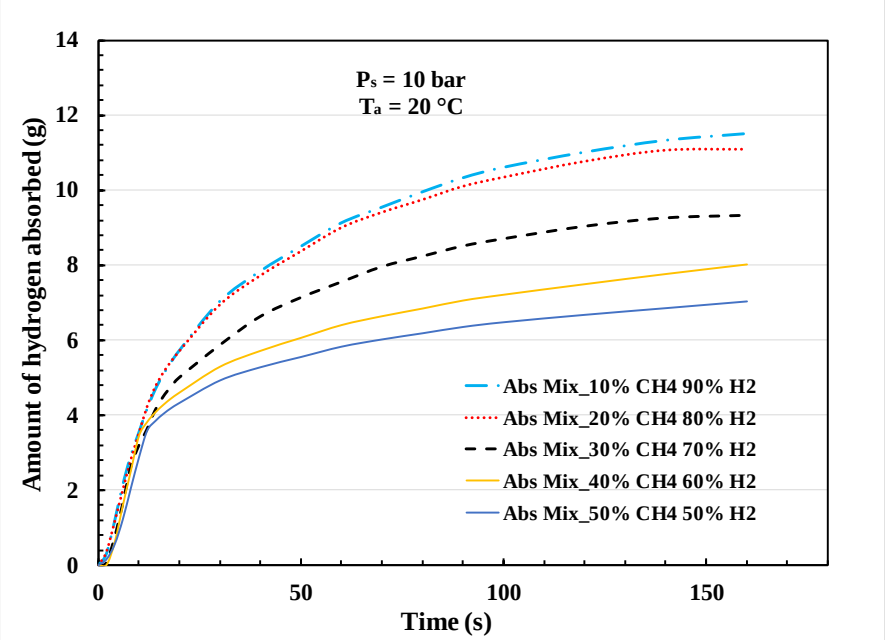

Fig. 6.21 Effect of impurity level of CH_4 on amount of hydrogen absorbed in $LaNi_5$ based MHHPS.

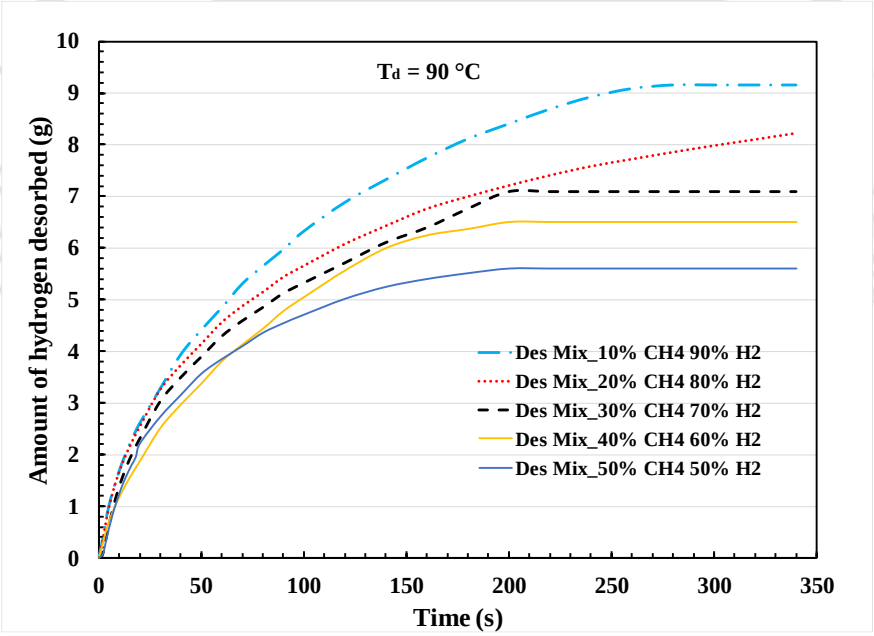

Fig. 6.22 Effect of impurity level of CH_4 on amount of hydrogen desorbed in $LaNi_5$ based MHHPS

6.3.2 Effect of CO_2 on the purification characteristics of $LaNi_{0.7}Al_{0.3}$

In order to study the alloy poisoning characteristics of $LaNi_{0.7}Al_{0.3}$ based MHHPS, two different kind of test were performed. Initially, cyclic stability of the system was carried out, wherein the

repetitive analysis of absorption/desorption characteristics in MHHPS was performed with fixed impurity level of 10% by weight, for 25 cycles. Further, the reactor was exposed to impurity of different levels, varying from 10% to 50% by weight (CO_2 in H_2).

6.3.2.1 Cyclic performance of $LaNi_{0.7}Al_{0.3}$ with CO_2 as impurity

The cyclic test on the MHHPS was conducted using a gas mixture of composition 10% CO_2 and 90% H_2 by weight, for 25 absorptions/desorption half cycle. The experiment was performed at 20 °C and 10 bar for all the absorption half cycle. As depicted in **Fig. 6.23**, the amount of hydrogen absorbed was 14.0672 g, 12.2030 g, 11.8782 g, 11.673 g, 11.4552 g and 11.0682 g respectively for 1st, 5th, 10th, 15th, 20th and 25th absorption cycle. This constituted to the hydrogen storage capacity of 1.17 wt%, 1.02 wt%, 0.99 wt%, 0.97 wt%, 0.95 wt% and 0.92 wt% respectively in 164 s, 168 s, 170 s, 180 s, 178 s and 300 s, from 1st to 25th absorption cycle.

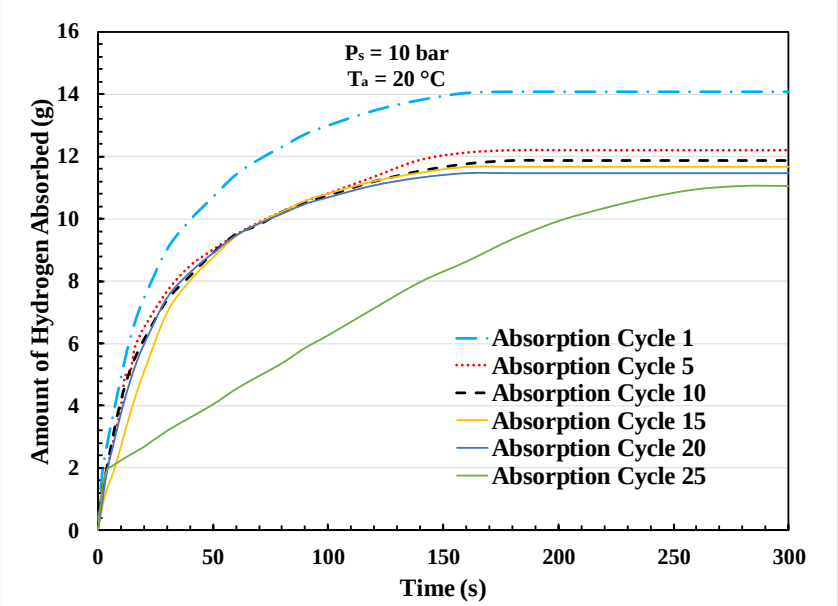

Fig. 6.23 Effect of CO_2 as impurity on amount of hydrogen absorbed in $LaNi_{0.7}Al_{0.3}$ based MHHPS

This drop in the amount of hydrogen absorbed from the 1st to 25th absorption cycle was due to the bed poisoning of $LaNi_{0.7}Al_{0.3}$, due to continuous interaction with CO_2 impurity. The presence of CO_2 in the void space of the reactor also restricts the direct interaction of total surface area of the alloy to the hydrogen gas, which finally decreases the rate of absorption. Further, the desorption was performed at 90 °C and atmospheric pressure. As depicted in **Fig. 6.24**, the amount of

hydrogen desorbed was 11.7283 g, 10.8912 g, 10.6321 g, 10.5440 g 10.5131 g and 10.3123 g respectively for 1st, 5th, 10th, 15th, 20th and 25th cycle, which corresponded to reversibility of 83.6%, 89%, 89%, 90.2%, 92% and 93% for respective desorption cycle. However, the flushing losses are not considered in the reversibility calculation, which varied from 0.5 to 1 g in each cycle. If the flushing losses are considered, the reversibility will be in order of 95-99%. The desorption was completed in 320 s, 340 s, 360 s, 300 s 380 s and 480 s respectively for 1st, 5th, 15th, 20th and 25th desorption cycle.

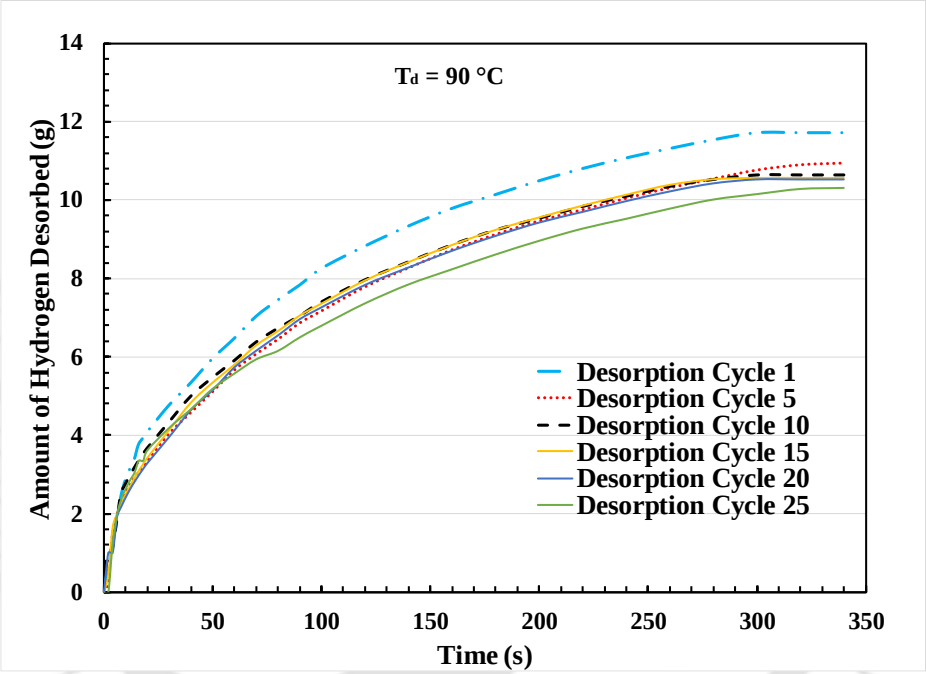

Fig. 6.24 Effect of CO_2 as impurity on amount of hydrogen desorbed in $LaNi_{0.7}Al_{0.3}$ based MHHPS

6.3.2.2 Effect of varying impurity level of CO_2 on reaction kinetics of $LaNi_{0.7}Al_{0.3}$

For obtaining the effect of different impurity level of CO_2 on $LaNi_{0.7}Al_{0.3}$ based MHHPS, the impurity level of CO_2 in H_2 was varied from 10% to 50% by weight. As depicted in **Fig. 6.25**, during the absorption half cycle, significant drop in the absorption capacity of MHHPS was observed for 10% to 50% of CO_2 impurity. The amount of hydrogen absorbed was 14.0671 g, 11.8780 g, 10.0501 g, 9.8092 g and 9.5123 g respectively for 10%, 20%, 30%, 40% and 50% impurity content, with absorption time of 168 s, 178 s, 170 S, 160 s and 180 s respectively. This significant drop in the absorption capacity of the MHHPS, was due to the increase in the amount

of CO_2 in the void space of the reactor, which restricted the direct interaction of H_2 with the MH alloy, resulting in the lowering of the absorption capacity of the reactor.

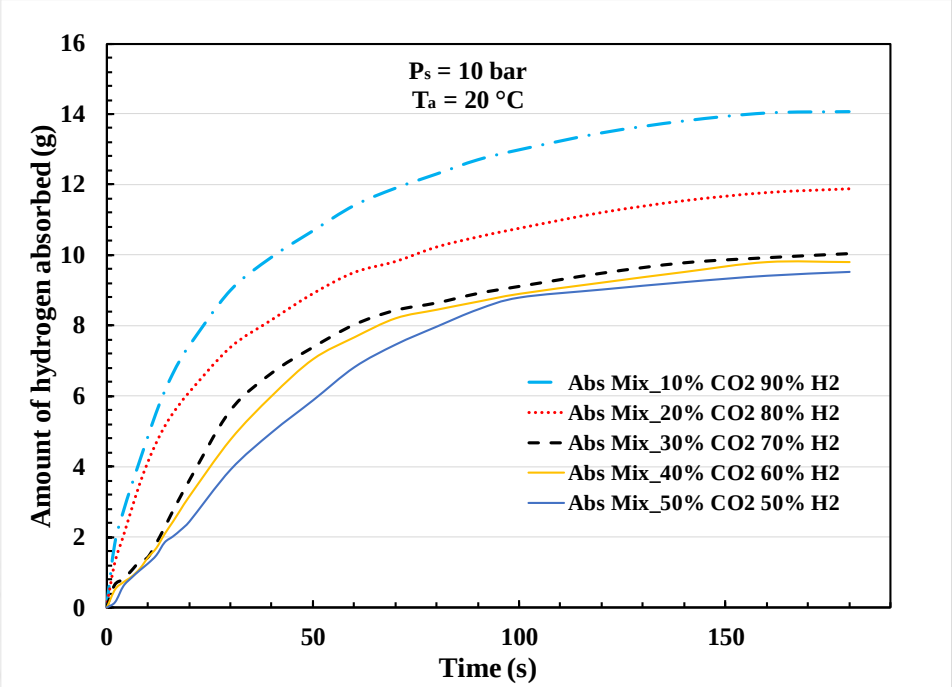

Fig. 6.25 Effect of impurity level of CO_2 on amount of hydrogen desorbed in $LaNi_{0.7}Al_{0.3}$ based MHHPS.

For the respective absorption half cycle, the desorption was carried out at 90 °C and atmospheric pressure. As depicted in **Fig. 6.26**, the amount of hydrogen desorbed for each desorption cycle corresponding to 10%, 20%, 30%, 40% and 50% impurities were 11.7280 g, 10.8852 g, 9.0575 g, 8.9637 g and 8.7512 g respectively in 300 s, 298 s, 180 s, 190 s and 200 s, which corresponds to the reversible desorption capacity of 83.35%, 91.6%, 90.14%, 91.4% and 92.01% respectively.

All the flushing cycle were carried out at atmospheric pressure, considering the actual fussing condition during the operation of MHHPS. This resulted in the accumulation of some CO_2, within the reactor during each flushing cycle, which finally added up to bed poisoning and resulted in the slower absorption kinetics. It was also observed that the alloy poisoning was directly proportional to the impurity content in the gas mixture. Hence, with increase in the impurity content of the mixture, the purification characteristics of the alloy decreases.

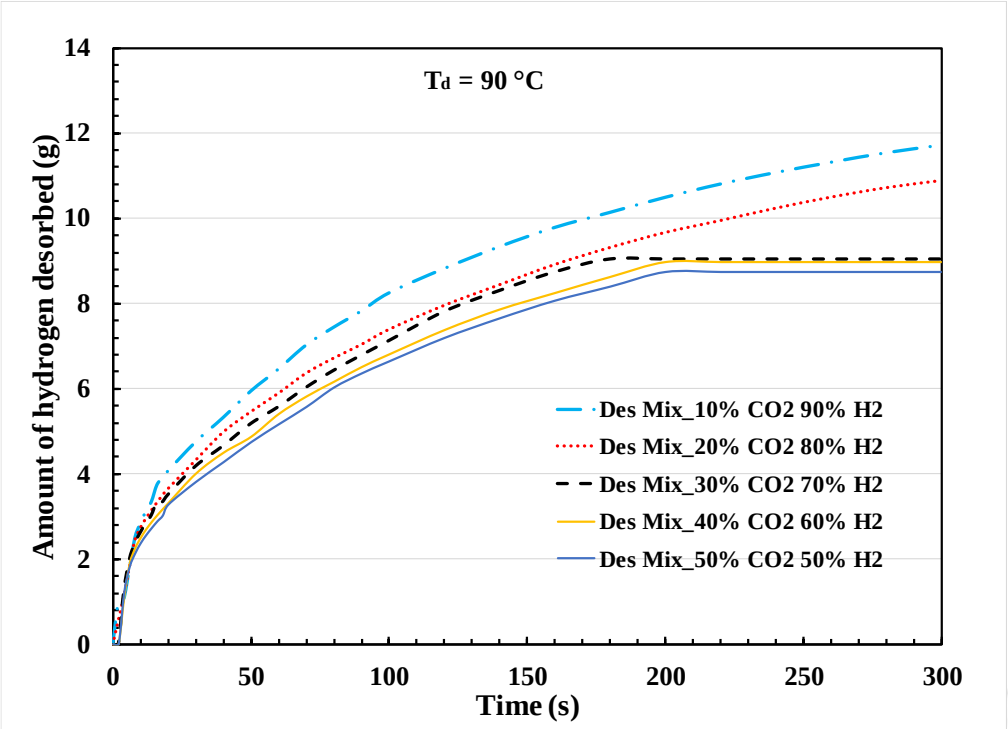

Fig. 6.26. Effect of impurity level of CO_2 on amount of hydrogen desorbed in $LaNi_{0.7}Al_{0.3}$ based MHHPS.

6.3.3 Effect of CO on the purification characteristics of $LaNi_{0.7}Al_{0.3}$

The cyclic tests on $LaNi_{0.7}Al_{0.3}$ was conducted using a gas mixture of composition 10% CO and 90% H_2 by weight. The absorption was performed at 20 °C and 10 bar for all the absorption half cycles. As depicted in **Fig. 6.27**, the amount of hydrogen absorbed was 7.2320 g, 6.6356 g, 21642 g and 0.6336 g respectively for 1st, 2nd, 3rd and 4th absorption half cycle. This constituted to the hydrogen storage capacity of 0.6 wt%, 0.55 wt%, 0.18 wt% and 0.05 wt% respectively in 250 s, 142 s, 62 s, and 6 s, from 1st to 4th absorption half cycle. This significant drop in the absorption capacity of $LaNi_{0.7}Al_{0.3}$ was due chemical reaction within the bed in presence of CO. It was observed that, in presence of AB_5 alloy, CO was reacting with hydrogen and forming methane and moisture end product. The possible reaction happening within the MH bed is depicted in Eq. 6.1. Because of moisture, the bed poisoning is very rigorous. Therefore, it is MHHPS is least capable of separating H_2 with CO as impurity.

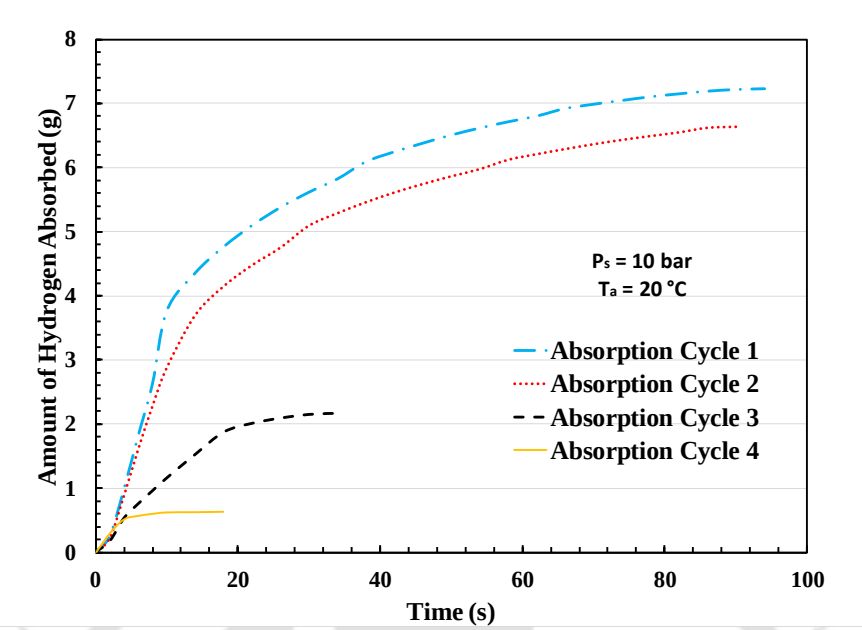

Fig. 6.27 Effect of CO as impurity on amount of hydrogen absorbed in $LaNi_{0.7}Al_{0.3}$ based MHHPS

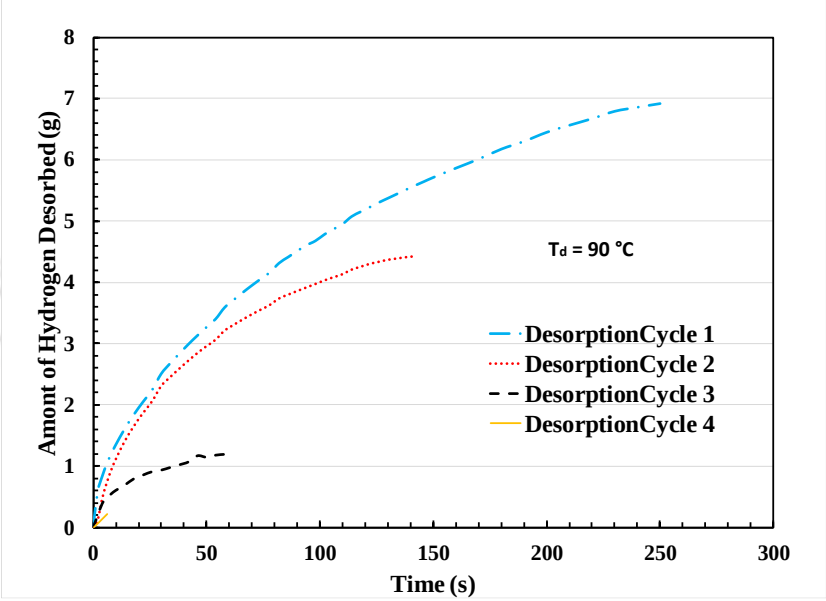

Fig. 6.28 Effect of CO as impurity on amount of hydrogen desorbed in $LaNi_{0.7}Al_{0.3}$ based MHHPS

For the respective absorption half cycle, the desorption was carried out at 90 °C and atmospheric pressure. As depicted in **Fig. 6.28**, the amount of hydrogen desorbed for each desorption cycle were 6.9238 g, 4.4240 g, 1.2071 g, and 0.2142 g respectively in 250 s, 142 s, 62 s, and 6 s, which

corresponds to the reversible desorption capacity of 96%, 67%, 55%, and 40% respectively for 1st to 4th desorption cycle.

6.4 Metal Hydride Bed Regeneration

Poisoning of MH bed is a very common phenomenon, when it is exposed to gases other than hydrogen. Sometimes, even a little entrapment of moisture or air in the MH bed can cause bed poisoning. However, poisoning is not a permanent problem in the MH-hydrogen systems, as it can be removed/eliminated by bed/alloy regeneration. The level of bed poisoning totally depends on the amount of impurity present in the impure absorption mixture. For higher level of impurities, the bed poisoning is more frequent as compared to lower impurity level. Poisoning also depends upon the type of impurity present in the gas samples. In this section, the regeneration of MH bed after poisoning is discussed.

6.4.1 Regeneration of $La_{0.9}Ce_{0.1}Ni_5$ after poisoning effect of CH_4

During bed regeneration, initially the MH bed was completely desorbed and evacuated till 0.02 mbar at 90 °C, to ensure the removal of impurities from the void space of the MH reactor. Further, first absorption cycle (with pure hydrogen) was performed at 20 bar hydrogen supply pressure (P_s) and 20 °C absorption temperature (T_a). As depicted in **Fig 6.29a**, due to significant bed poisoning, amount of hydrogen absorbed in the first bed regeneration cycle was 13.44 g in about 280 s. Considering the slower reaction kinetics and 1.12 wt.% of hydrogen storage in the first regeneration cycle, the MH bed was prepared for second regeneration cycle, wherein it was completely desorbed and evacuated till 0.02 mbar at 90 °C. Further, in the second regeneration cycle, the bed got fully reactivated by absorbing 15.24 g in 192 s. Because of enhanced reaction kinetic (rate of absorption), the peak bed temperature achieved in second regeneration cycle was 80 °C, which was 18 °C more than first regeneration activation (**Fig. 6.29b**). Due to evacuation at high temperature followed by pure hydrogen absorption cycle at elevated supply pressure, the impurities from the MH bed are removed and the bed gets regenerated.

However, the poisoning of MH bed, during the purification process can be delayed, by keeping desorption temperature of each purification cycle on the higher side (>90 °C for $La_{0.9}Ce_{0.1}Ni_5$). The elevated desorption temperature acts as self-regeneration temperature for the alloy bed and delays the

bed poisoning. The bed poisoning can be further delayed by practicing bed evacuation (up to 10^{-1} mbar) every 10^{th} -15^{th} cycle (depending upon impurity level) during the desorption.

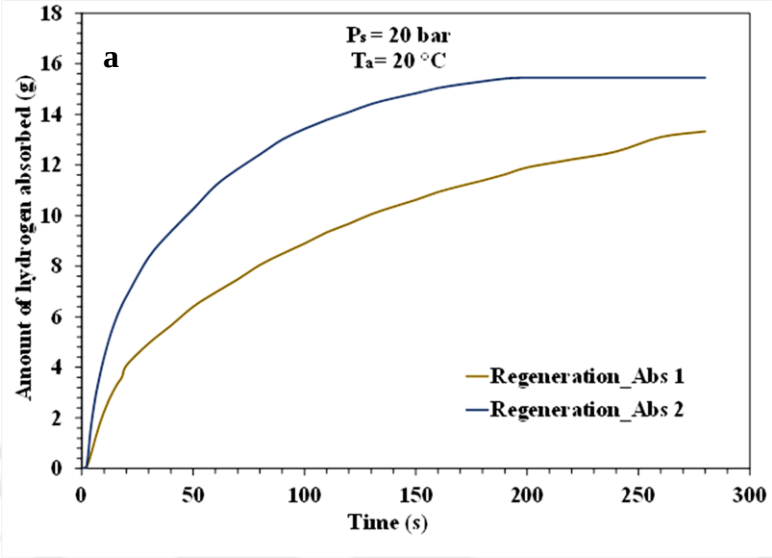

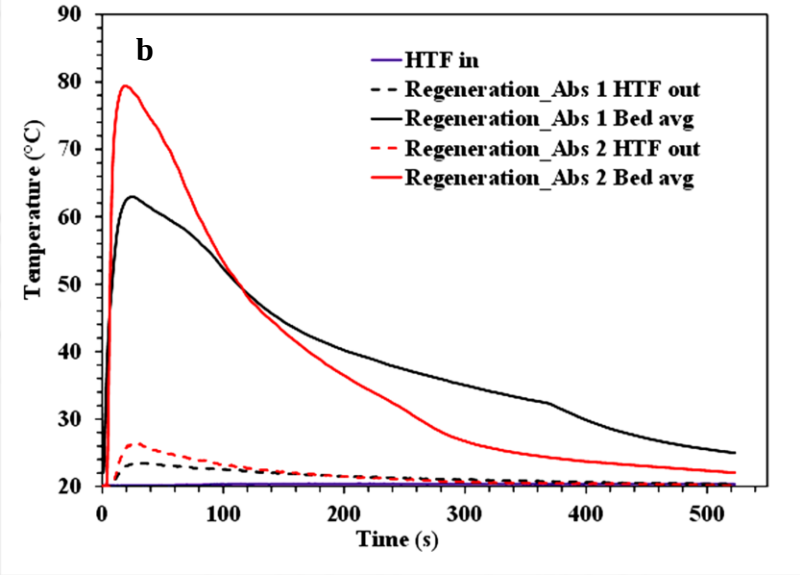

Fig 6.29 (a) Amount of hydrogen absorbed during the bed regeneration, and **(b)** temperature variation of the MH bed and HTF during respective regeneration cycle for $La_{0.9}Ce_{0.1}Ni_5$.

6.4.2 Regeneration of $LaNi_5$ after poisoning effect of CH_4

The alloy regeneration was conducted by evacuating the MH bed at elevated temperature of 90 °C followed by bed evacuation at 10^{-1}-10^{-2} mbar. After successful evacuation, the bed was prepared for absorption by cooling it down to 20 °C through continuous circulation of HTF at low temperature. The first regeneration absorption was conducted at 20 bar and 20 °C. As depicted in

Fig 6.30a, the first bed regeneration cycle was 14.1213 g in about 300 s. Considering the slower reaction kinetics, the MH bed was prepared for second regeneration cycle, wherein it was completely desorbed and evacuated till 10^{-1} mbar at 90 °C. Further, in the second regeneration cycle, the bed got fully reactivated by absorbing 15.36 g in 220 s. The variation in bed and HTF temperature during respective regeneration cycle is depicted in **Fig. 6.30b**. The $LaNi_5$ based MH bed attained maximum peak temperature of 81.1 °C in 22 s in the second regeneration cycle, predicting faster kinetics.

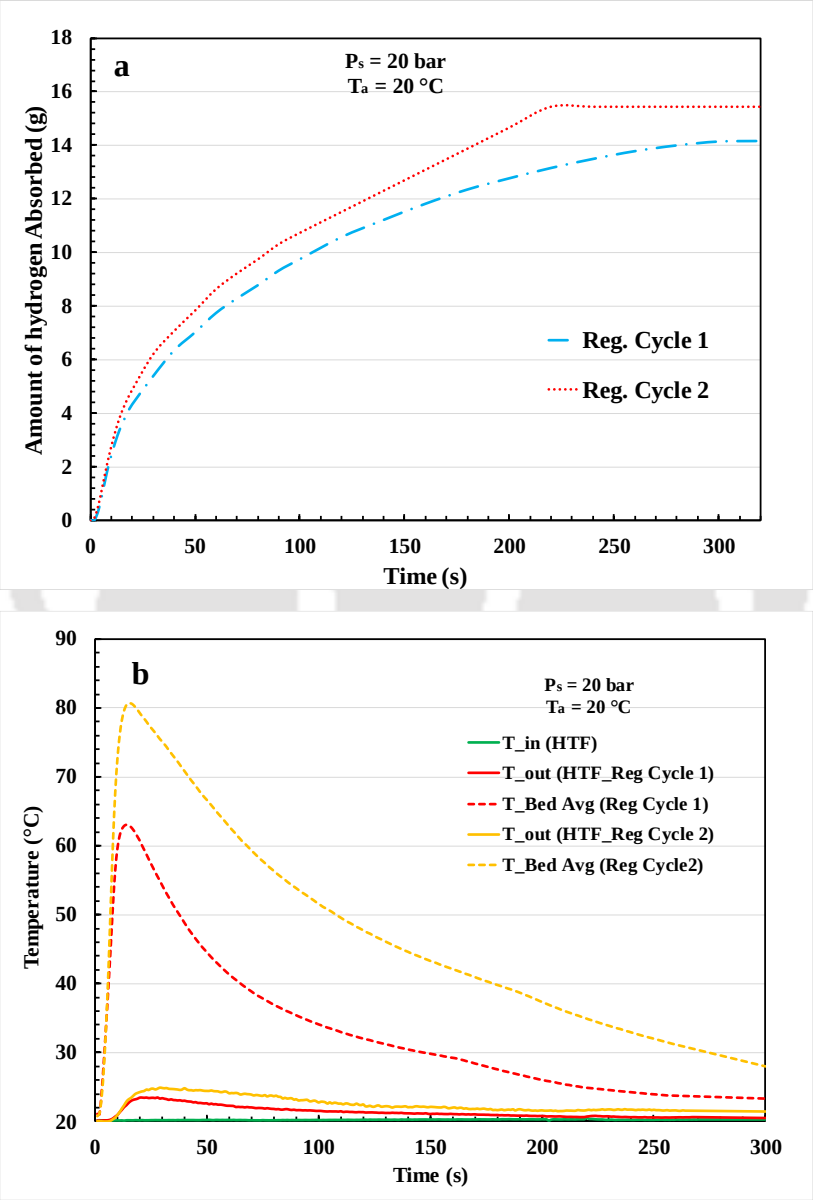

Fig 6.30 (a) Amount of hydrogen absorbed during the bed regeneration, and **(b)** temperature variation of the MH bed and HTF during respective regeneration cycle in $LaNi_5$.

6.4.3 Regeneration of $LaNi_{4.7}Al_{0.3}$ after poisoning effect of CH_4

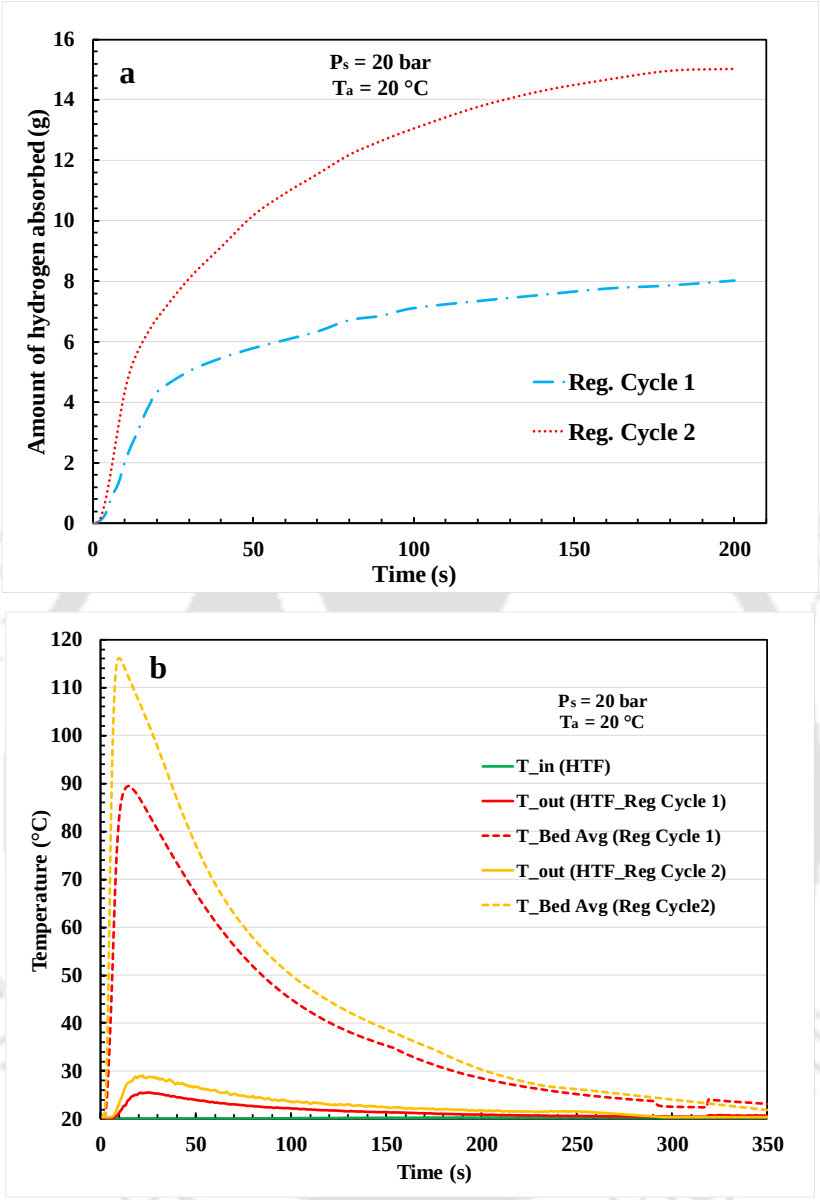

Fig 6.31 (a) Amount of hydrogen absorbed during the bed regeneration, and **(b)** temperature variation of the MH bed and HTF during respective regeneration cycle in $LaNi_{4.7}Al_{0.3}$.

The alloy regeneration was conducted by evacuating the MH bed at elevated temperature of 90 °C followed by bed evacuation at 10^{-2} mbar. After successful evacuation, the bed was prepared for absorption by cooling it down to 20 °C through continuous circulation of HTF at low temperature. The first regeneration absorption was conducted at 20 bar and 20 °C. As depicted in **Fig 6.31a**, the first bed regeneration cycle was 8.0231 g in about 200 s. Considering the slower reaction kinetics, the

MH bed was prepared for second regeneration cycle, wherein it was completely desorbed and evacuated till 10^{-2} mbar at 90 °C. Further, in the second regeneration cycle, the bed got fully reactivated by absorbing 15.25 g hydrogen in 170 s. The variation in bed and HTF temperature during respective regeneration cycle is depicted in **Fig. 6.31b**. The $LaNi_{4.7}Al_{0.3}$ based MH bed attained peak temperature of 118 °C in 14 s in the second regeneration cycle, predicting faster kinetics.

6.4.4 Regeneration of $La_{0.9}Ce_{0.1}Ni_5$ after poisoning effect of CO_2

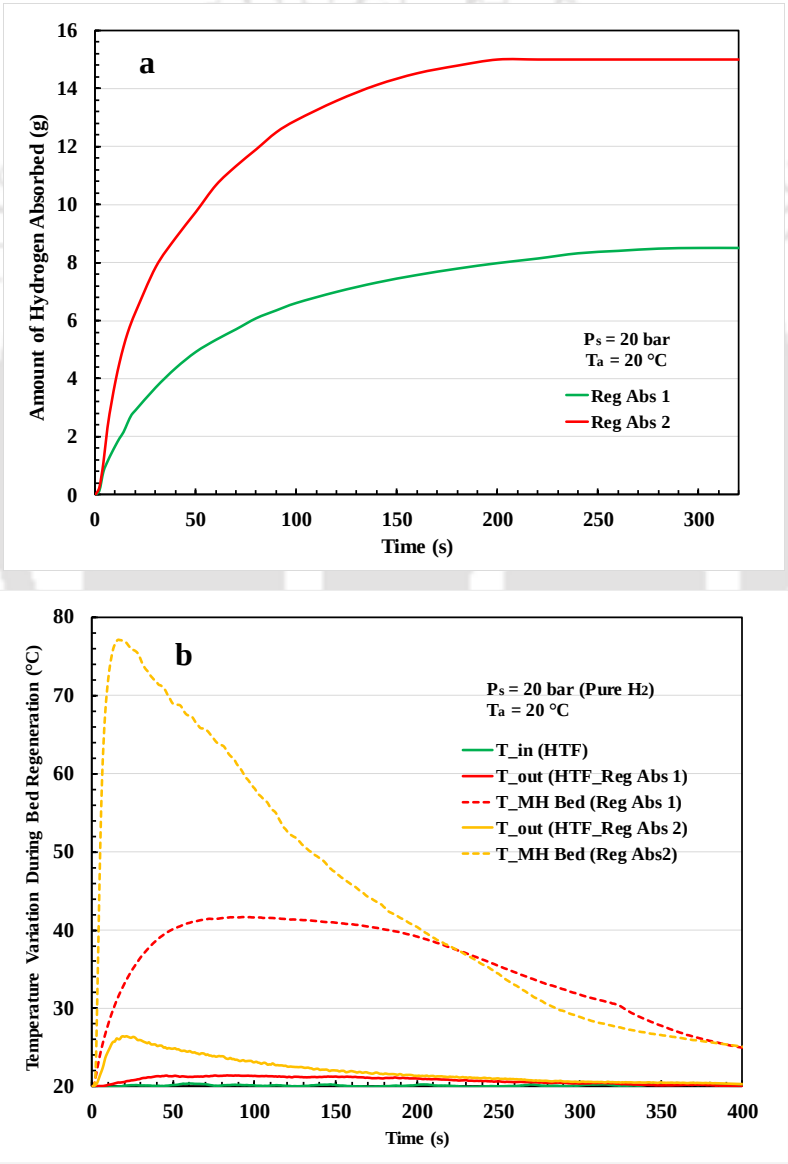

Fig. 6.32 (a) Rate of hydrogen absorbed during alloy regeneration, and **(b)** temperature variation of the alloy bed and HTF during regeneration cycle in $La_{0.9}Ce_{0.1}Ni_5$.

The alloy regeneration in the present case was caused due to continuous interaction of CO_2 impurity with the MHHPS. Once the effect of poisoning was significant, the alloy regeneration cycle was performed, wherein, initially the MHHPs was heated to 90-95 °C and evacuated using vacuum pump till 10^{-2} mbar. After evacuation, the bed was cooled down to 20 °C and pure hydrogen was supplied at 20 bar. As depicted in **Fig. 6.32a**, in the first regeneration cycle, the bed absorbed 8.58 g hydrogen, which constitutes to 0.72 wt% of the storage capacity. The absorption time was around 342 s wherein the peak bed temperature reached was around 41.8 °C (Fig. 6.32b). The same process was repeated for 2nd regeneration cycle, wherein the MH bed was again evacuated at 90-95 °C and 10^{-2} mbar, followed by absorption at 20 bar and 20 °C. In the second regeneration cycle, the bed showed rapid absorption, wherein it absorbed 15.2315 g of hydrogen in just around 200 s, with peak bed temperature of 77.6 °C. This rapid absorption and peak temperature confirmed the alloy regeneration in the second absorption cycle.

6.4.5 Regeneration of $LaNi_5$ after poisoning effect of CO_2

Similar to $La_{0.9}Ce_{0.1}Ni_5$ based reactor, $LaNi_5$, also got regenerated in two reactivation cycle. As depicted in **Fig. 6.33a**, in the first regeneration cycle, the bed absorbed 9.8546 g hydrogen, which constitutes to 0.82 wt% of the storage capacity. The absorption time was around 200 s wherein the peak bed temperature reached was around 50 °C (**Fig. 6.33b**). In the second regeneration cycle, the bed showed rapid absorption, wherein it absorbed 15.1426 g of hydrogen in just around 180 s, with peak bed temperature of 80 °C.

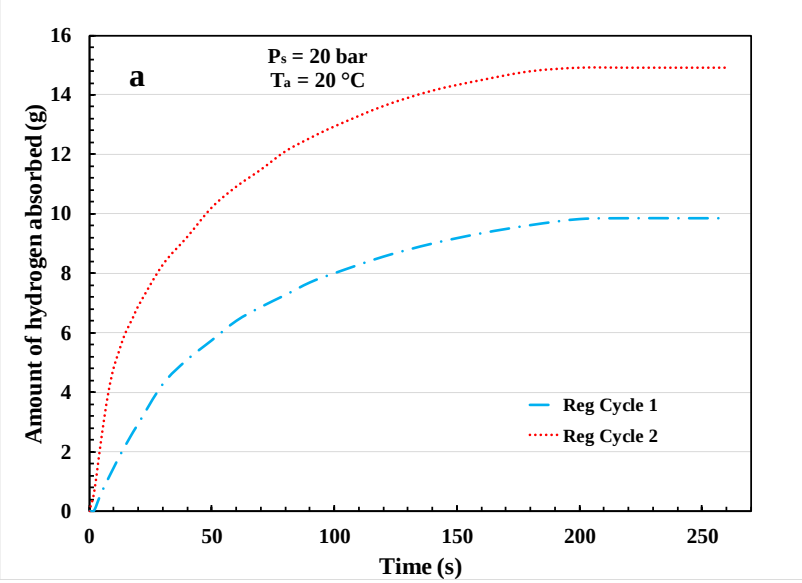

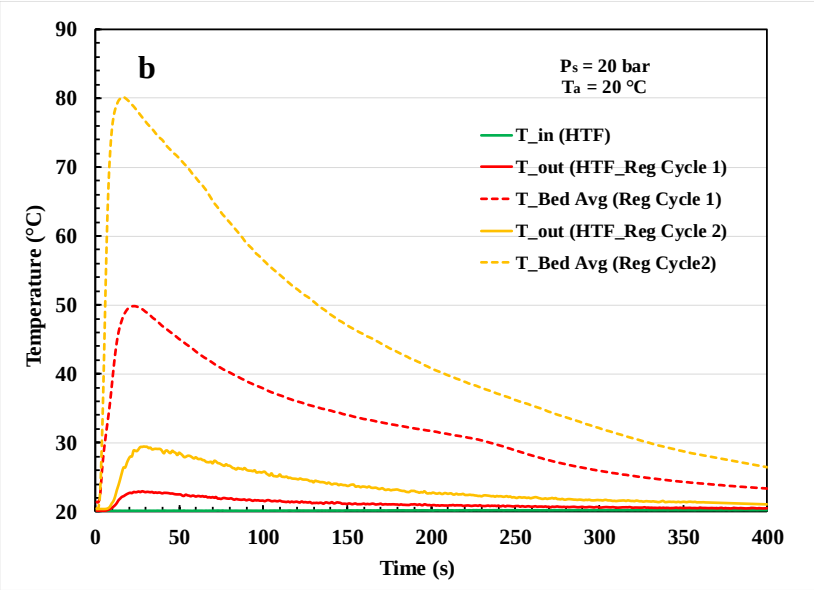

Fig. 6.33 (a) Rate of hydrogen absorbed during alloy regeneration, and **(b)** temperature variation of the alloy bed and HTF during regeneration cycle in $LaNi_5$.

6.4.6 Regeneration of $LaNi_{4.7}Al_{0.3}$ after poisoning effect of CO_2

The alloy regeneration was carried out adopting the same procedure as discussed in the previous sections. As depicted in **Fig. 6.34a**, in the first regeneration cycle, the bed absorbed 11.5328 g hydrogen, which constitutes to 0.96 wt% of the storage capacity. The absorption time was around 200 s wherein the peak bed temperature reached was around 83 °C (**Fig. 6.34b**). In the second regeneration cycle, the bed absorbed 15.2013 g of hydrogen in just around 160 s, with peak bed temperature of 116 °C.

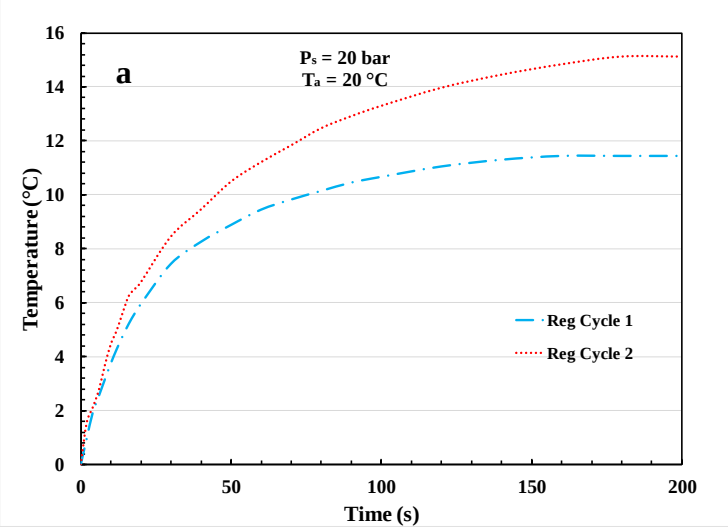

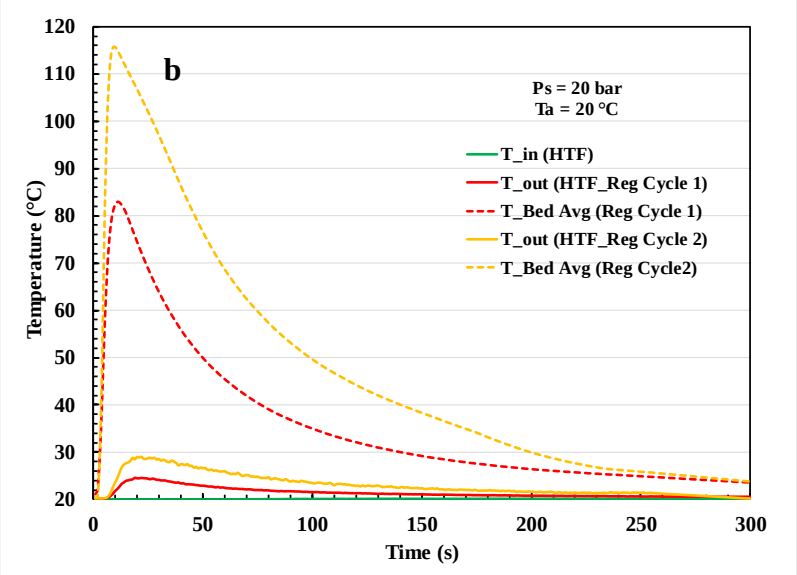

Fig. 6.34 (a) Rate of hydrogen absorbed during alloy regeneration, and **(b)** temperature variation of the alloy bed and HTF during regeneration cycle in $LaNi_{4.7}Al_{0.3}$.

6.4.7 Regeneration of $La_{0.9}Ce_{0.1}Ni_5$ after poisoning effect of CO

Amongst different gaseous impurities, poisoning effect of CO on the AB_5 type of MH alloys were very significant. Because of methane and moisture formation within the MH bed, the MH alloy gets poisoned very severely. As discussed in section 6.3, the absorption capacity of the MH bed deteriorates such that, it can hardly absorb any hydrogen after 4-5 purification cycles. Considering the rigorous deterioration of the MH bed and presence of moisture within the bed, the regeneration of alloys took an extra absorption cycle as compared to the regeneration after gases like CO_2, CH_4, N_2 etc. The alloy regeneration was conducted by evacuating the MH bed at elevated temperature of 95 °C followed by bed evacuation at 10^{-2} mbar. After successful evacuation, the bed was prepared for absorption by cooling it down to 20 °C through continuous circulation of HTF at low temperature. The regeneration absorption was conducted at 20 bar and 20 °C. As depicted in Fig 6.35a, the amount of hydrogen absorbed in the 1st, 2nd and 3rd bed regeneration cycle was 8.1030 g, 14.0013 g and 14.8722 g respectively in about 300 s, 220 s and 216 s. The variation in bed and HTF temperature during respective regeneration cycle is depicted in **Fig. 6.35b**. The peak temperature reached during 1st, 2nd and 3rd bed regeneration cycle was 66 °C, 74 °C and 80 °C respectively in 115 s, 66 s and 22 s. The faster rate of absorption towards the third regeneration cycle confirms the bed regeneration after 3rd activation/regeneration cycle.

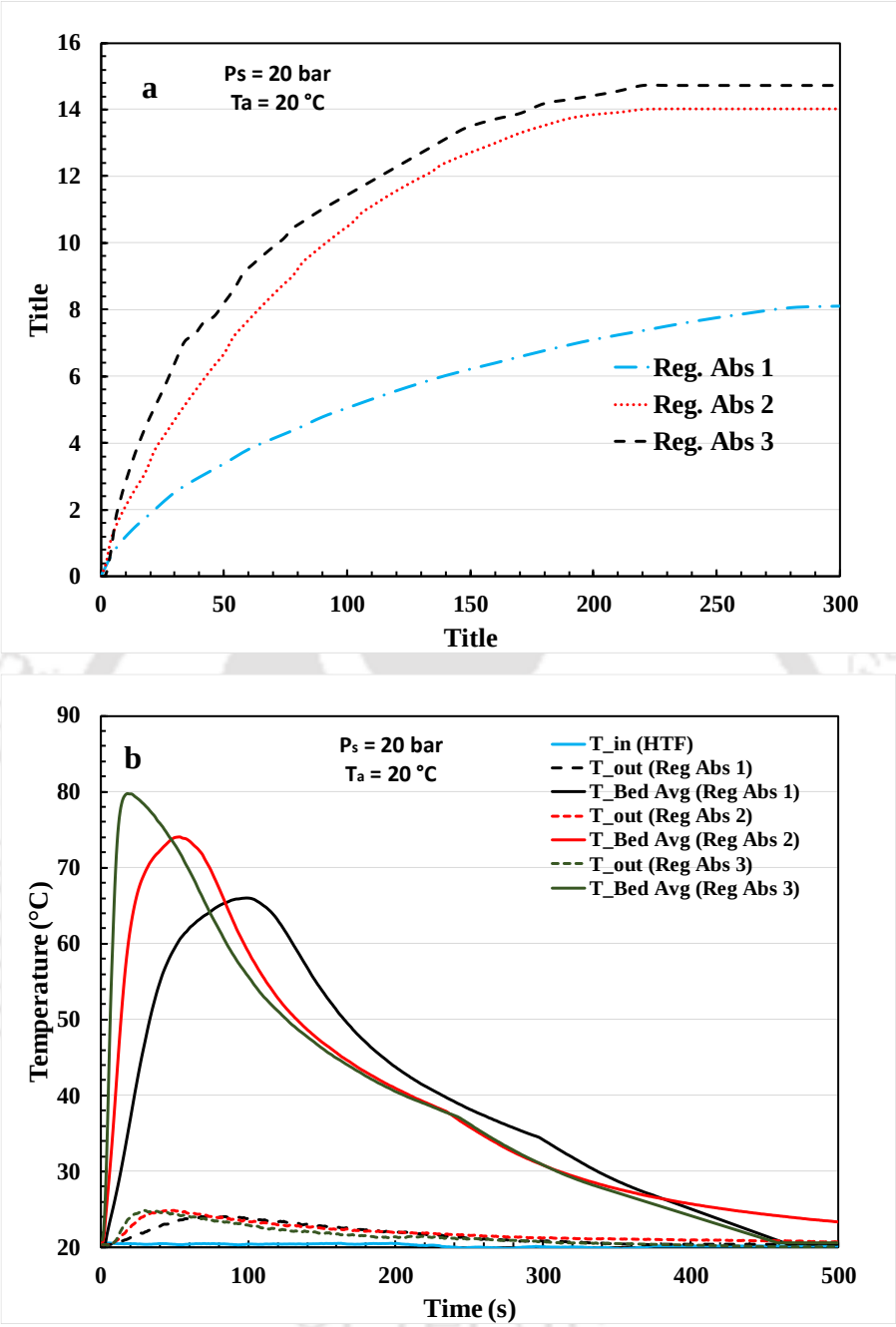

Fig. 6.35 (a) Rate of hydrogen absorbed during alloy regeneration, and **(b)** temperature variation of the alloy bed and HTF during regeneration cycle in $La_{0.9}Ce_{0.1}Ni_5$.

6.4.8 Regeneration of $LaNi_5$ after poisoning effect of CO

Similar to $La_{0.9}Ce_{0.1}Ni_5$, the bed regeneration for $LaNi_5$ after poisoning from CO was performed in three regeneration cycle. As depicted in **Fig 6.36a**, the amount of hydrogen absorbed in the 1st, 2nd and 3rd bed regeneration cycle was 13.0607 g, 13.9210 g and 14.9997 g respectively in about 240 s,

200 s and 190 s. The variation in bed and HTF temperature during respective regeneration cycle is depicted in **Fig. 6.36b**. The peak temperature reached during 1st, 2nd and 3rd bed regeneration cycle was 58.6 °C, 76.2 °C and 80.9 °C respectively in 127 s, 37 s and 21 s. The faster rate of absorption confirms the bed regeneration after 3rd activation/regeneration cycle.

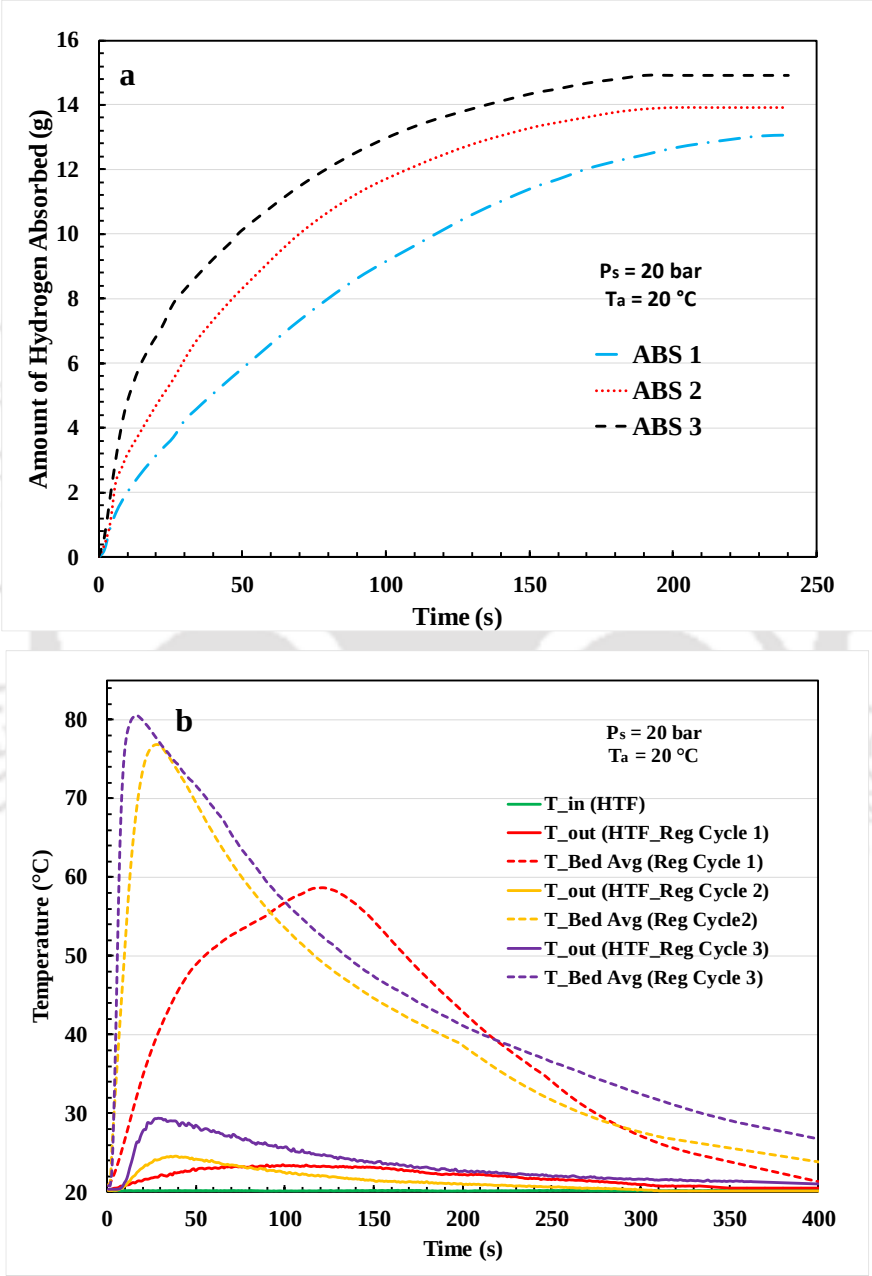

Fig. 6.36 (a) Rate of hydrogen absorbed during alloy regeneration, and **(b)** temperature variation of the alloy bed and HTF during regeneration cycle in $LaNi_5$.

6.4.9 Regeneration of $LaNi_{4.7}Al_{0.3}$ after poisoning effect of CO

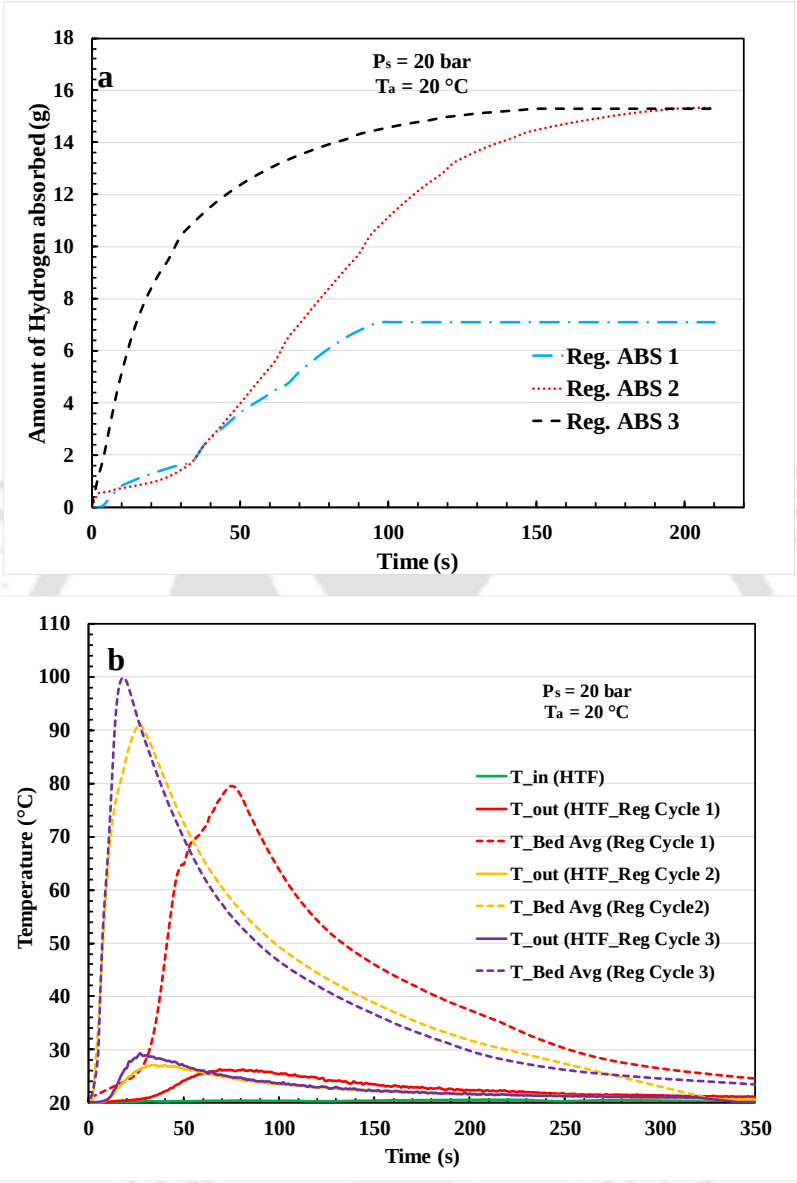

Fig. 6.37 (a) Rate of hydrogen absorbed during alloy regeneration, and **(b)** temperature variation of the alloy bed and HTF during regeneration cycle in $LaNi_{4.7}Al_{0.3}$.

Similar to $La_{0.9}Ce_{0.1}Ni_5$ and $LaNi_5$, the bed regeneration for $LaNi_{4.7}Al_{0.3}$ after poisoning from CO was performed in three regeneration cycle. As depicted in **Fig 6.37a**., the amount of hydrogen absorbed in the 1st, 2nd and 3rd bed regeneration cycle was 7.0907 g, 15.3012 g and 15.3090 g respectively in about 98 s, 210 s and 150 s. The variation in bed and HTF temperature during respective regeneration cycle is depicted in Fig. 6.37b. The peak temperature reached during 1st, 2nd

and 3rd bed regeneration cycle was 58.6 °C, 76.2 °C and 80.9 °C respectively in 127 s, 37 s and 21 s. The faster rate of absorption confirms the bed regeneration after 3rd activation/regeneration cycle. Though the bed regeneration is possible after poisoning through CO as impurities in MH-hydrogen systems, it is suggested to avoid such impurities to enter the system. However, if CO content is minimal (100-200 ppm) there will be no such significant alloy poisoning. The summary of alloy poisoning and regeneration is depicted in **Table 6.1**

Table 6.1 Summary of alloy poisoning and regeneration

MH Alloy	Impurity Type	Expected Bed Poisoning after Number of Purification Cycle (Impurity level)	No. of Cycle for Regeneration
$La_{0.9}Ce_{0.1}Ni_5$	CH_4	100-125 cycle (<15%); 25-35 cycle (>30%)	1 to 2
	CO_2	150-200 cycle (<15%); 50-60 cycle (>30%)	1 to 2
	N_2	1500-2000 cycle (<15%); 800-1000 cycle (>30%)	1
	Ar	No Poisoning Observed	1
	CO	20-30 cycle (<1%); 3-5 cycle (>5%)	3 to 4
$LaNi_5$	CH_4	150-175 cycle (<15%); 35-40 cycle (>30%)	1 to 2
	CO_2	175-200 cycle (<15%); 70-75 cycle (>30%)	1 to 2
	N_2	1500-2000 cycle (<15%); 800-1000 cycle (>30%)	1
	Ar	No Poisoning Observed	1
	CO	20-30 cycle (<1%); 3-5 cycle (>5%)	3 to 4
$LaNi_{4.7}Al_{0.3}$	CH_4	175-200 cycle (<15%); 40-50 cycle (>30%)	1 to 2
	CO_2	200-225 cycle (<15%); 80-100 cycle (>30%)	1 to 2

	N_2	1500-2000 cycle (<15%); 800-1000 cycle (>30%)	1
	Ar	No Poisoning Observed	1
	CO	25-35 cycle (<1%); 3-5 cycle (>5%)	3 to 4

6.5 Results of TCD Analysis for Different Impurities

6.5.1 TCD analysis for CH4 as impurity in MHHPS

The samples collected for each stage of purification cycle were further analysed using TCD in GC. Upon TCD analysis, it was observed that, for 10% and 20% impurity level, the purity of recovered hydrogen was 99.9999%, whereas it was reduced to 99.6%, 97.8% and 95.9% respectively for 30%, 40% and 50% impurity level. The reduction in the purity level for higher level of impurities was due to the temporary deposition of CH_4 on the alloy surface, which comes out in traces during the desorption cycle. The result obtained from absorption, desorption and flushing gas samples, for purification cycle with 30% impurity is depicted in **Fig. 6.38**. Further, the TCD results for samples with 30% impurity level is presented in **Fig. 6.39**.

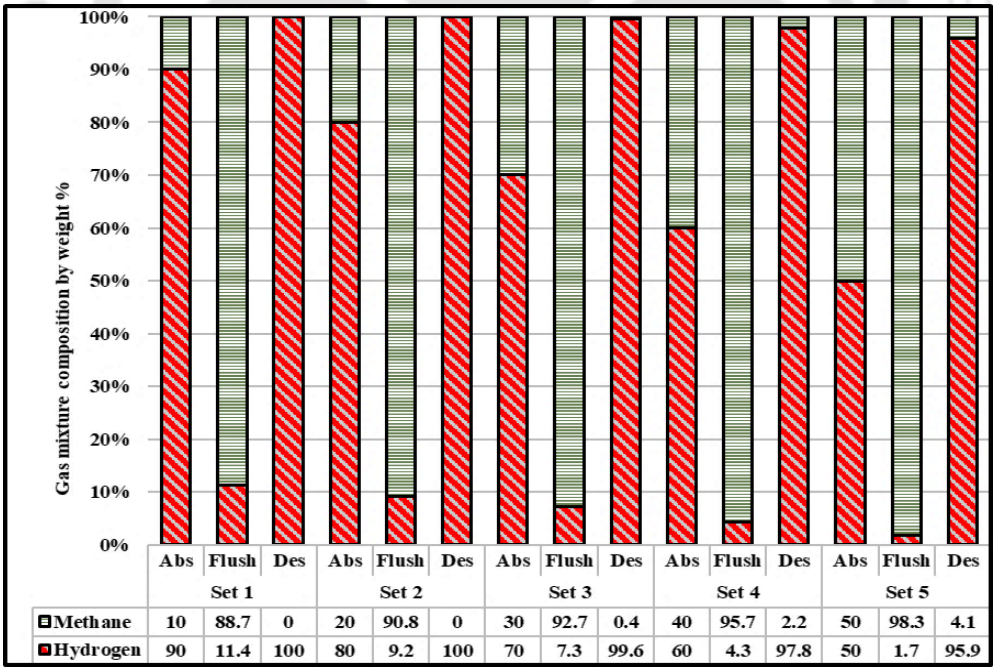

Fig. 6.38 Gas composition by weight % during absorption, desorption and flushing based on gas chromatography (TCD analysis) data for CH_4.

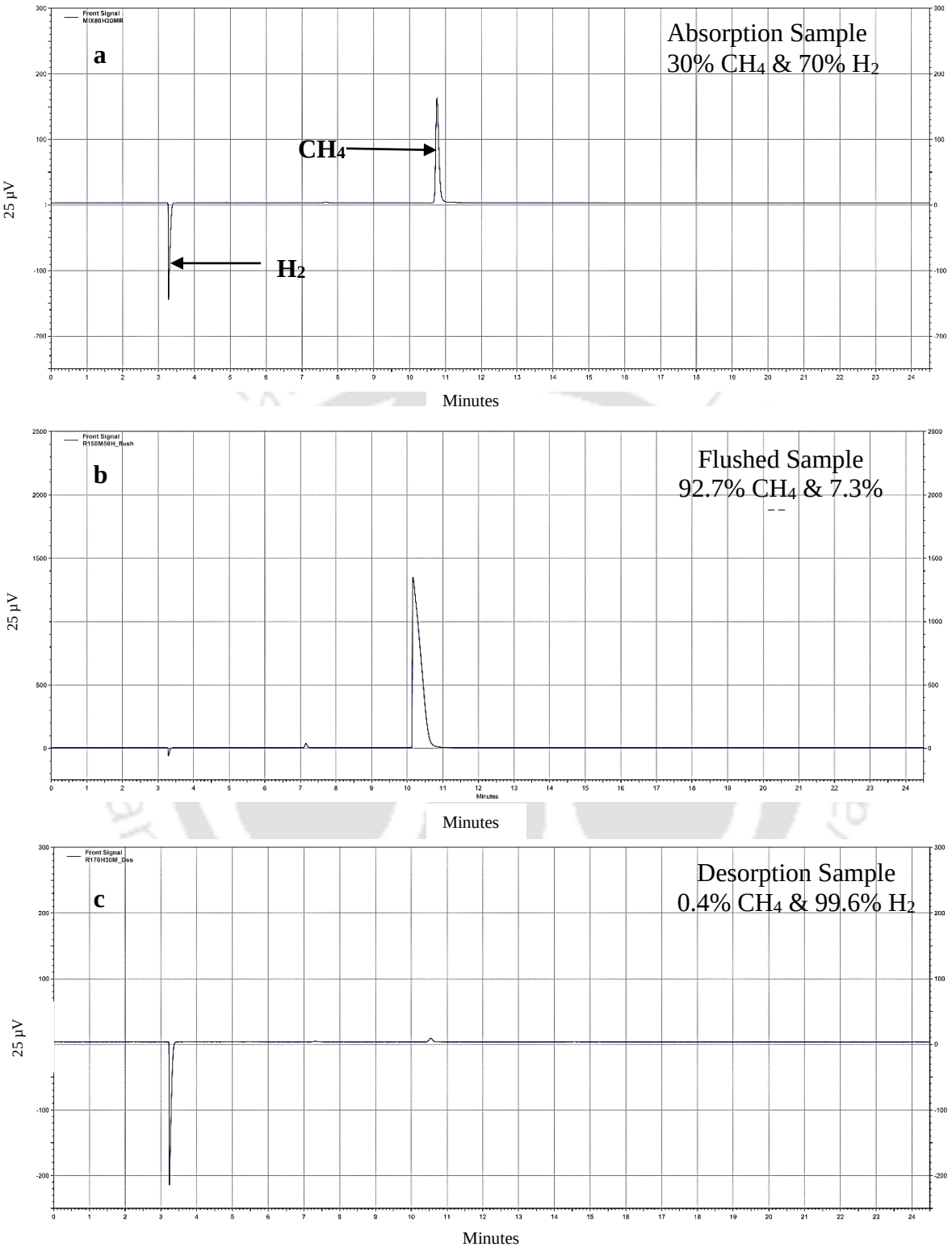

Fig. 6.39 TCD results for (a) absorption, (b) flushing and (c) desorption samples, for 30% CH_4 as impurity in the absorption sample.

6.5.2 TCD analysis for CO_2 as impurity in MHHPS

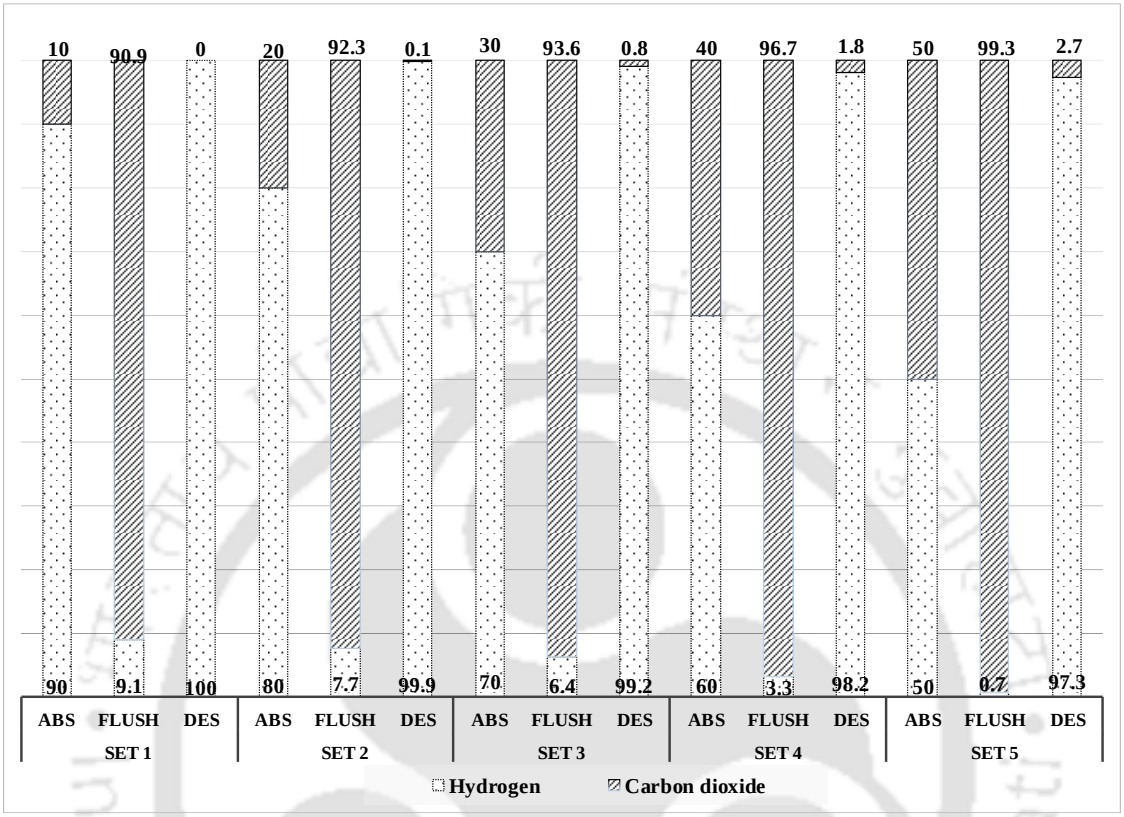

Fig. 6.40 TCD results of the gas compositions for absorption, desorption and flushing gas samples for different impurities levels of CO_2.

Gas samples were collected during each absorption, desorption and flushing process of the MHHPS, for TCD analysis using the gas chromatography. The result obtained from the TCD analysis is summarised in **Fig. 6.40**, wherein the average of 3 experimental study for each impurity level is presented. According to the experimental outcome of single stage purification system, it suggested to use MHHPS below impurity level of 20%. However, if the impurity level increases further, multiple purification cycle can be performed to obtain high grade pure hydrogen (99.9999%). In the present case for 10 % impurity, the purity level obtained was nearly 100%. However, it decreases to 99.9%, 99.2%, 98.2% and 97.3% respectively for 20%, 20%, 40% and 50%. A sample TCD result for absorption mixture of 20% CO_2 and 80% H_2 is depicted in **Fig. 6.41**. The result shows the gas composition of absorption, flush and desorption gas samples analysed during the experiments. During the TCD analysis, hydrogen gas was detected in the 1st minute of the runtime wherein carbon dioxide was detected in the 2nd minute.

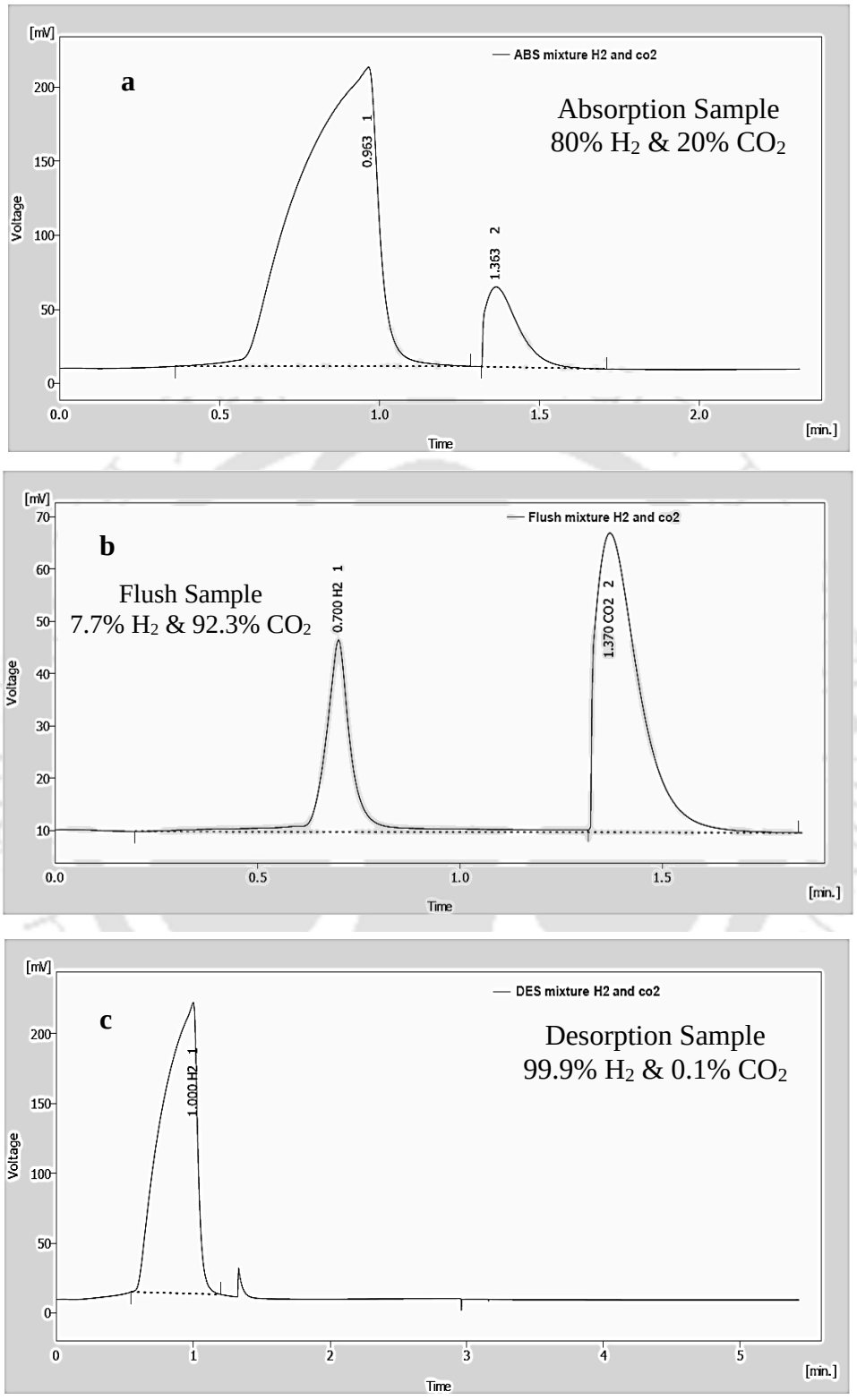

Fig. 6.41 TCD results for **(a)** absorption, **(b)** flushing and **(c)** desorption samples, for 20% CO_2 as impurity in the absorption sample

6.5.3 TCD analysis for N_2 as impurity in MHHPS

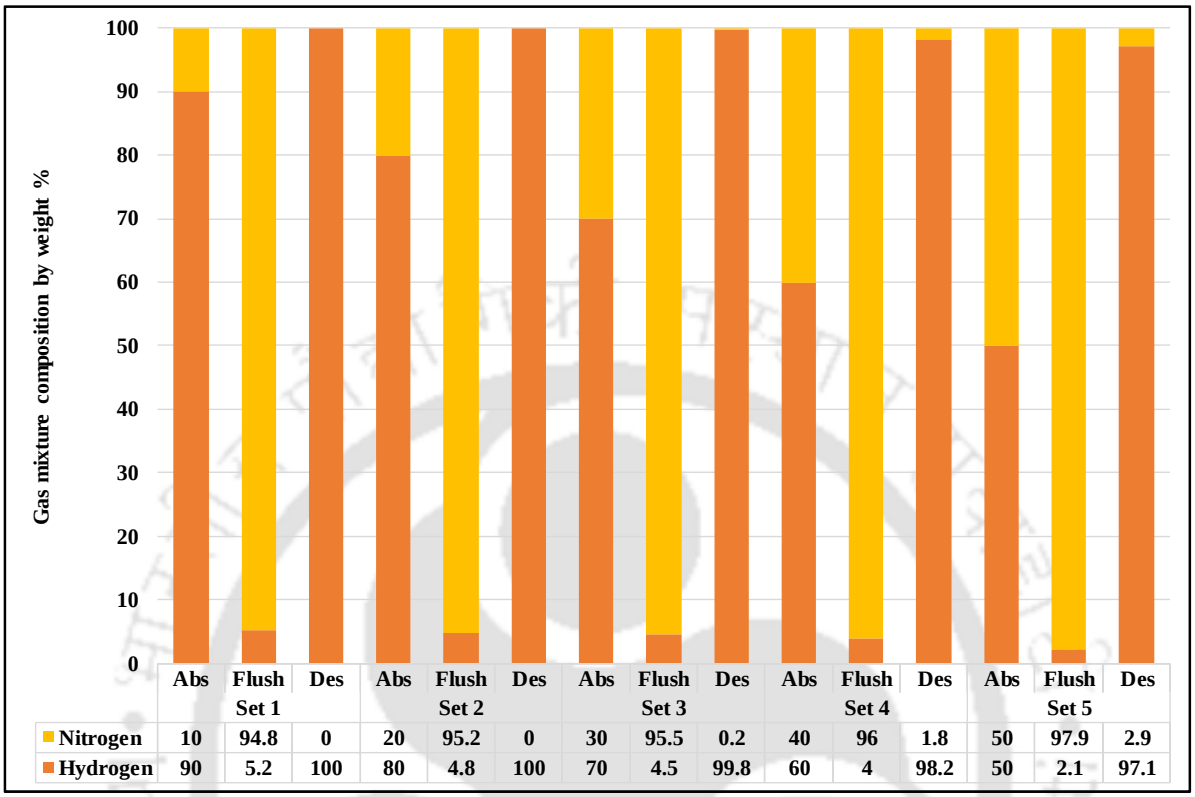

	Abs	Flush Set 1	Des	Abs	Flush Set 2	Des	Abs	Flush Set 3	Des	Abs	Flush Set 4	Des	Abs	Flush Set 5	Des
Nitrogen	10	94.8	0	20	95.2	0	30	95.5	0.2	40	96	1.8	50	97.9	2.9
Hydrogen	90	5.2	100	80	4.8	100	70	4.5	99.8	60	4	98.2	50	2.1	97.1

Fig. 6.42 TCD results of the gas compositions for absorption, desorption and flushing gas samples for different impurities levels of N_2.

The result obtained from the TCD analysis for absorption, flush and desorption mixtures for purification study on N_2 and H_2 gas mixture is summarised in **Fig. 6.42**. According to the experimental outcome it can be observed that, N_2 has least impact on the alloy poisoning. Even for 30% impure mixture the purity level of hydrogen obtained was around 100% in a single stage. However, if the impurity level increases further, multiple purification cycle can be performed to obtain high grade pure hydrogen (99.9999%). In the present case for up to 30% impurity the purity level obtained was nearly 100%. However, it decreases to 98.2% and 97.1%, respectively for 40% and 50%. A sample TCD result for absorption mixture of 20% N_2 and 80% H_2 is depicted in **Fig. 6.43**. The result shows the gas composition of absorption, flush and desorption gas samples analysed during the experiments. During the TCD analysis, hydrogen gas was detected after 3 minute of the runtime wherein nitrogen was detected in the 8th minute.

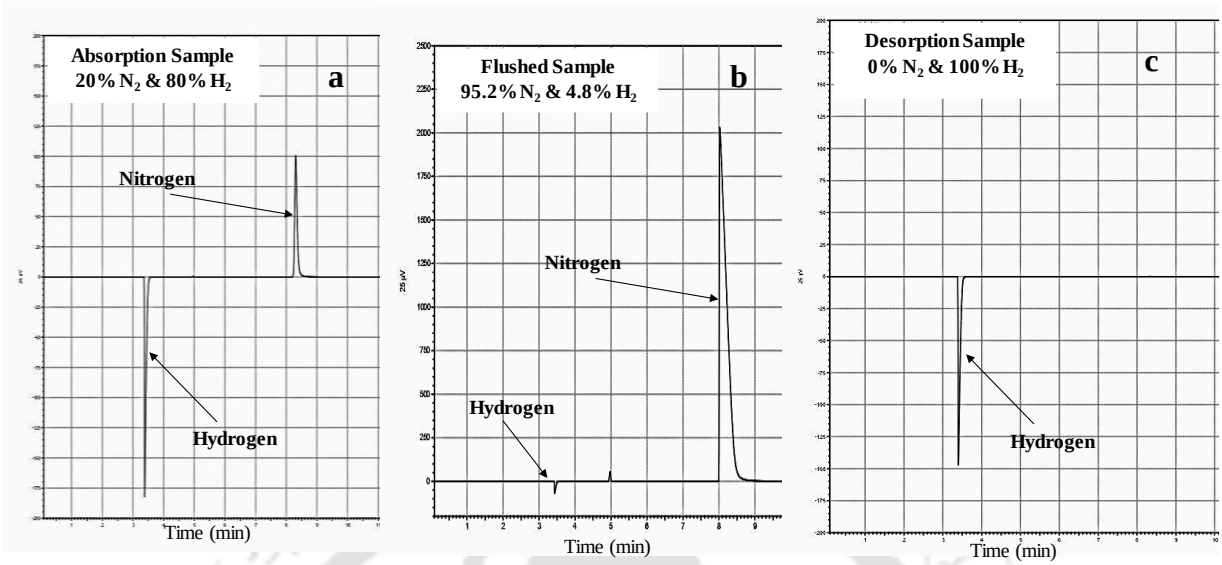

Fig. 6.43 TCD results for (a) absorption, (b) flushing and (c) desorption samples, for 20% N_2 as impurity in the absorption sample

6.5.4 TCD analysis for CO as impurity in MHHPS

It was absorbed that methanation was dominant once CO and H_2 mixture interacts with La-Ni alloy, which caused faster bed poisoning. The result obtained from the TCD analysis is summarised in **Fig. 6.44**, wherein it can be observed that, in the absorption sample the detection of CO was after 15 minute of the sample run and hydrogen get detected after the third run (Fig. 6.44a). However, as it can be observed in **Fig. 6.44b**, the TCD result of the flushed gas sample do not have any trace of CO, rather CH_4 peak can be seen after 10^{th} minute of the run time. Moreover, due to the presence of moisture in the flush sample, the baseline of the TCD cure shifts after 12^{th} minute of run time (**Fig. 6.44b**). This causes GC column poisoning due to moisture entrapment in the column wall. As depicted in Fig. 6.44c, the desorption sample also contains CH_4 traces along with hydrogen.

Therefore, it is advised to use CO free impure gas sample, wherever MH based hydrogen purification technologies are used. However, presence of less CO content (100-200 ppm) may not affect the working of such system. Maintaining desorption temperature above 100 °C could also be possible solution for such impurities, wherein the moisture generated can be removed in each desorption cycle. Apart from CO and O_2 as impurity, MHHPS can handle almost all gaseous impurities and separate hydrogen from it.

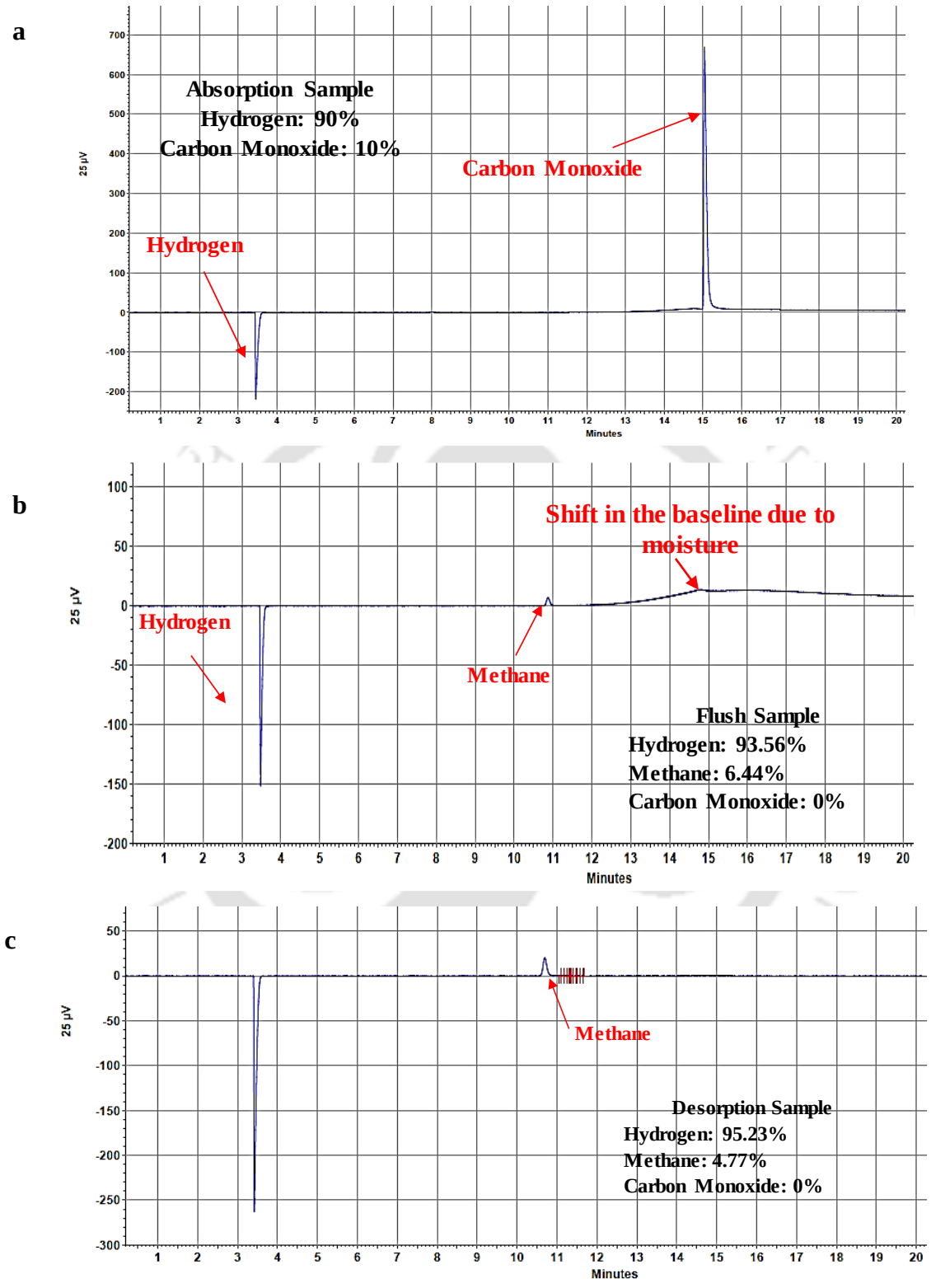

Fig. 6.44 TCD results for **(a)** absorption, **(b)** flushing and **(c)** desorption samples, for 10% CO as impurity in the absorption sample

6.6 Studies in Multistage Hydrogen Purification System

From the previous sections of this chapter, it is observed that, as impurity level increases above 10-20%, the purity level of hydrogen obtained after purification through MHHPS degrades slowly. Therefore, it is suggested to go for multiple purification stages for obtaining ultra-pure hydrogen. This section presents the reaction kinetics and rate of hydrogen transfer in the coupled reactor system. The multistage system constitutes of 3-reactor system, wherein stage 1, stage 2 and stage 3 reactors are represented by R1, R2 and R3 respectively. Here, R1 represents reactor with $La_{0.9}Ce_{0.1}Ni_5$, R2 represents reactor with $LaNi_5$ and R3 represents reactor with $LaNi_{4.7}Al_{0.3}$. As discussed in the previous chapter's, all the reactors are identical in design and filled with 1.2 kg of each alloy.

6.6.1 Experimental investigation on hydrogen transfer from R1 to R2

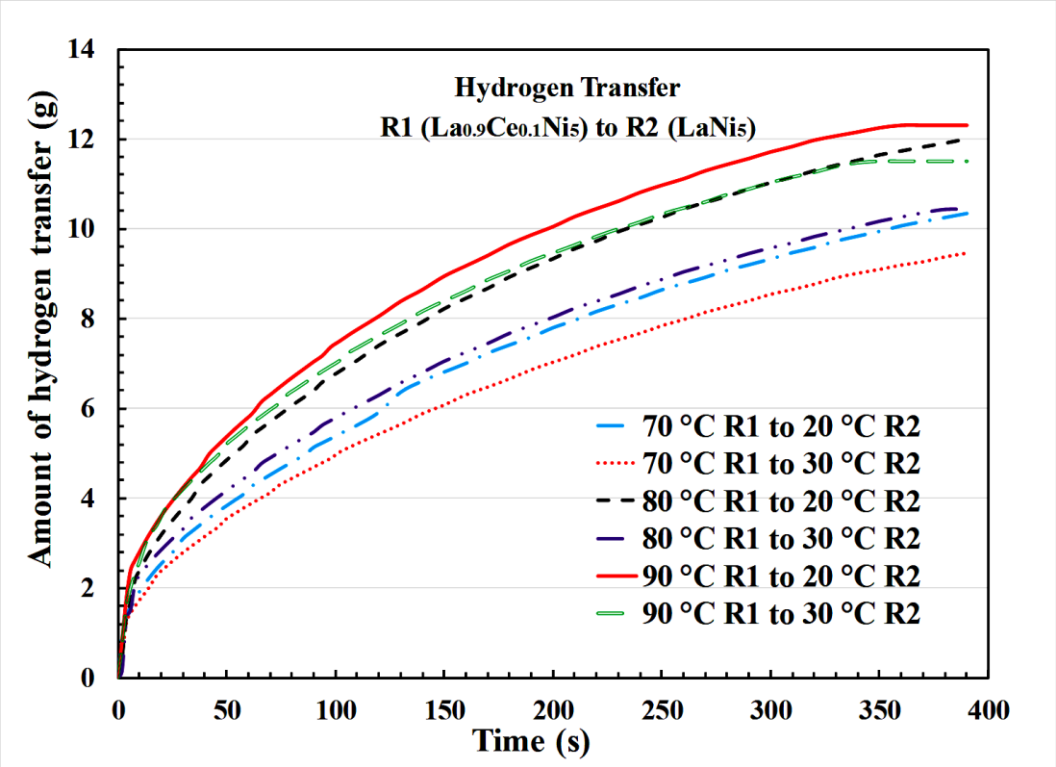

Fig. 6.45 Hydrogen transfer from R1 to R2 at different absorption/desorption temperatures

In order to depict the amount of hydrogen transfer from R1 (filled) to R2 (empty), parametric study on the coupled reactor system was performed by varying temperature of absorbing and desorbing

reactor. In this study, the desorbing reactor was filled with a fixed amount of 14.5 g hydrogen while the absorbing reactor was kept empty. As depicted in **Fig. 6.45**, the rate of hydrogen transfer was largely affected by the temperatures of absorption and desorbing reactors. For 70 °C desorption temperature (R1) and 30 °C absorption temperature (R2), the amount of hydrogen transfer was 9.4587 g, which was 65.25% of the total hydrogen available for transfer in R1. With increase in the temperature of desorbing reactor and decrease in the temperature of absorbing reactor, hydrogen transfer from R1 to R2 increased significantly. For 90 °C desorption temperature (R1) and 20 °C absorption temperature (R2), the amount of hydrogen transfer was 12.3132 g, which constitutes of nearly 85% of the total hydrogen available for transfer.

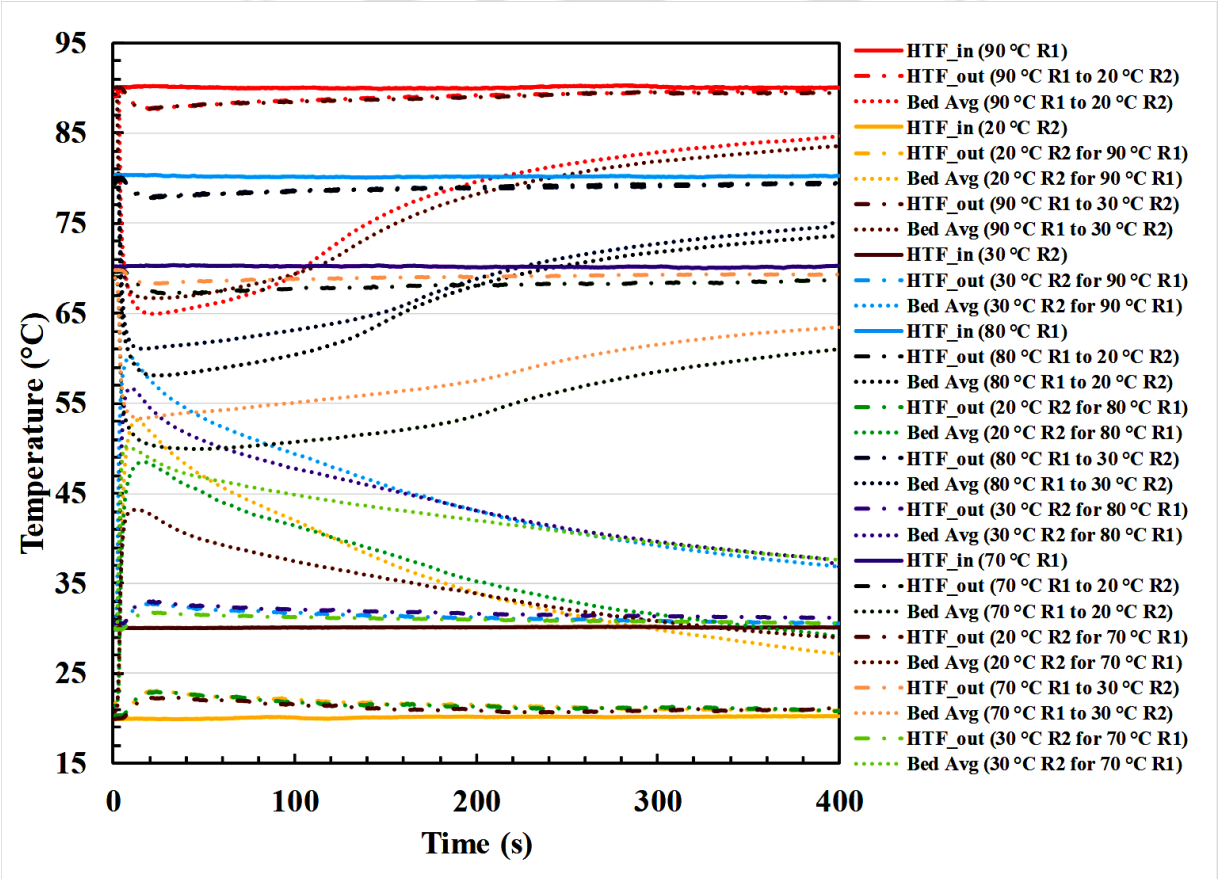

Fig. 6.46 Temperature variation curve during hydrogen transfer from R1 to R2

With increase in temperature difference between the absorbing and desorbing reactors, the pressure gradient between the reactors also increases. This leads to faster rate of hydrogen transfer between the reactors. Moreover, for lower absorption temperature, the equilibrium bed pressure of the alloy

is lower, this increases the rate of absorption for the absorbing reactor. The details of the hydrogen transfer between the coupled reactor R1 & R2 is depicted in **Table 6.2**. The temperature variation of the MHHPS and HTF during coupled reactor study is depicted in **Fig. 6.46**. The endothermic nature of the desorbing bed and the exothermic reaction in the absorbing bed can be clearly observed.

Table 6.2 Details of hydrogen transfer in the coupled reactor (R1 to R2)

R1 Desorption Temp (T_d)	R2 Absorption Temp (T_a)	H_2 Transfer from R1 to R2	Time
70 °C	20 °C	10.3349 g	390 s
70 °C	30 °C	9.4587 g	385 s
80 °C	20 °C	12.0145 g	390 s
80 °C	30 °C	10.4451 g	380 s
90 °C	20 °C	12.3132 g	350 s
90 °C	30 °C	11.4919 g	350 s

6.6.2 Experimental investigation on hydrogen transfer from R1 to R3

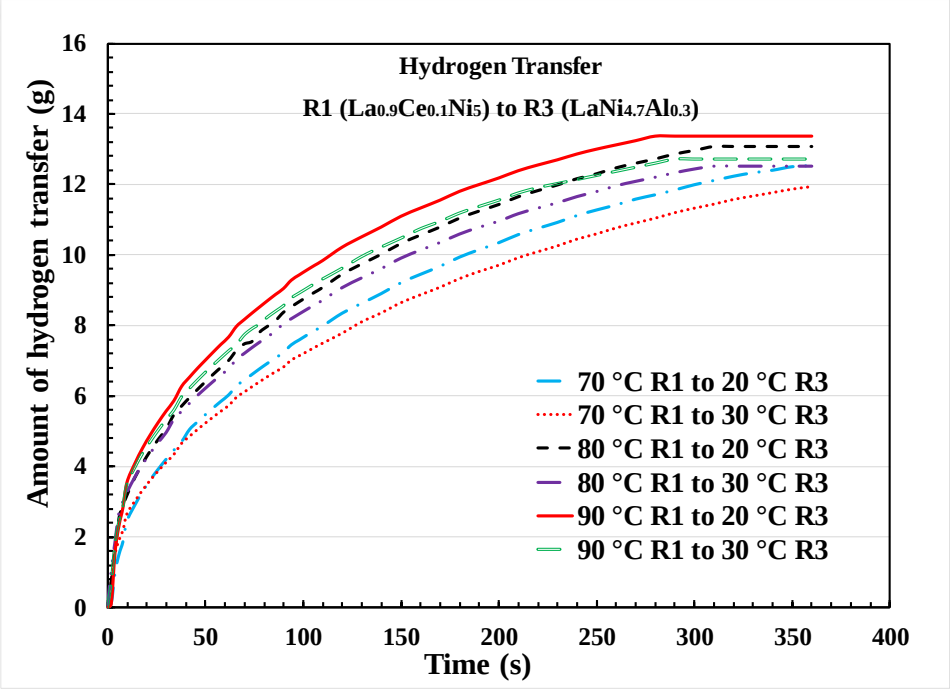

Fig. 6.47 Hydrogen transfer from R1 to R3 at different absorption/desorption temperatures

In order to depict the reaction kinetics and amount of hydrogen transfer from R1 (filled) to R3 (empty), the experiments were conducted similar to the study reported for R1 and R2 reactors. As depicted in **Fig. 6.47**, for 70 °C desorption temperature (R1) and 30 °C absorption temperature (R3), the amount of hydrogen transfer was 11.9482 g, which was 82.4% of the total hydrogen available for transfer. Hydrogen transfer from R1 to R3 increased significantly with increase in the temperature of desorbing reactor and decrease in the temperature of absorbing reactor. For 90 °C desorption temperature (R1) and 20 °C absorption temperature (R3), the amount of hydrogen transfer was 13.3733 g, which constitutes of nearly 92.2% of the total hydrogen available for transfer. With increase in temperature difference between the absorbing and desorbing reactors, the pressure gradient between the reactors also increases. This leads to faster rate of hydrogen transfer between the reactors. Moreover, for lower absorption temperature, the equilibrium bed pressure of the alloy is lower, this increases the rate of absorption for the absorbing reactor.

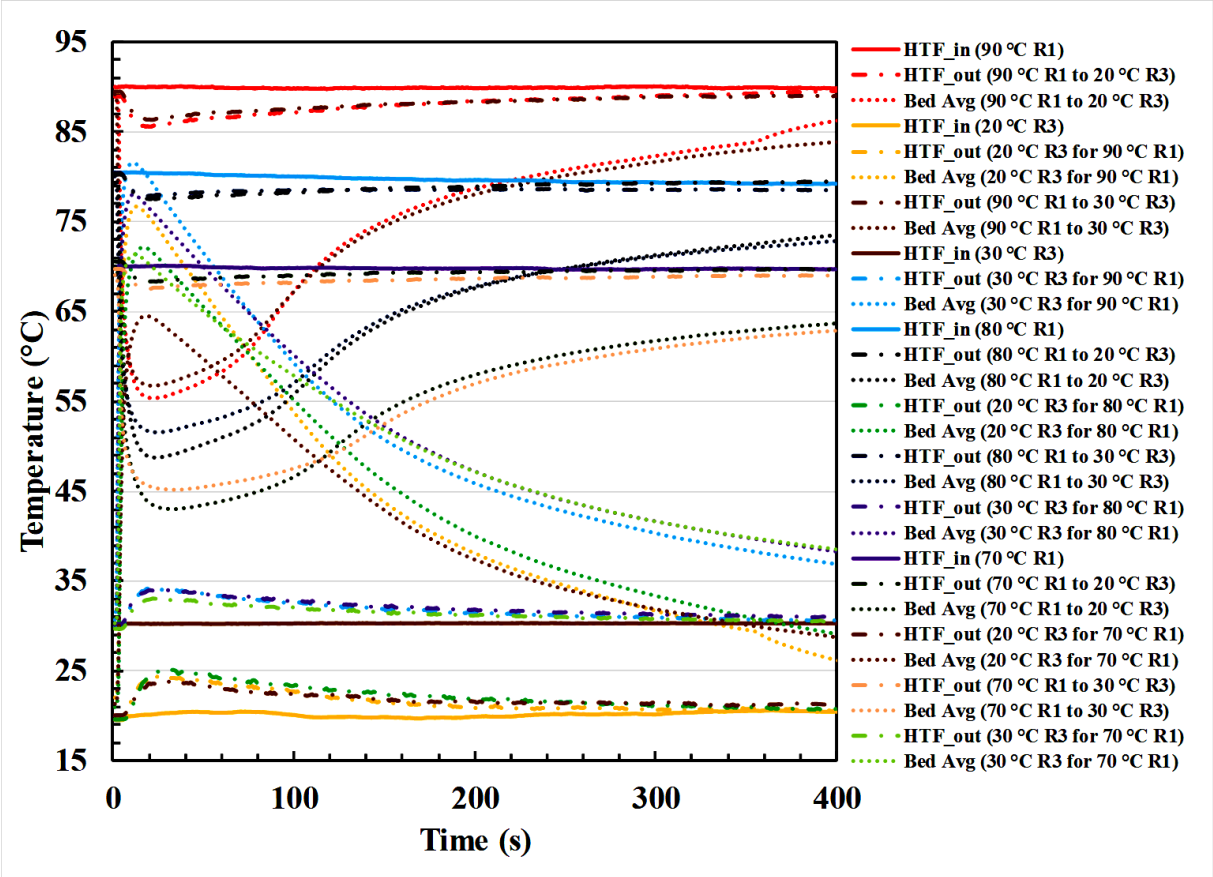

Fig. 6.48 Temperature variation curve during hydrogen transfer from R1 to R3

The details of the hydrogen transfer between the coupled reactor R1 & R3 is depicted in **Table 6.3**. The temperature variation of the MHHPS and HTF during coupled reactor study is depicted in **Fig. 6.48**. The endothermic nature of the desorbing bed and the exothermic reaction in the absorbing bed can be clearly observed.

Table 6.3 Details of hydrogen transfer in the coupled reactor (R1 to R3)

R1 Desorption Temp (T_d)	R3 Absorption Temp (T_a)	H_2 Transfer from R1 to R3	Time
70 °C	20 °C	12.5276 g	360 s
70 °C	30 °C	11.9482 g	360 s
80 °C	20 °C	13.0691 g	310 s
80 °C	30 °C	12.5107 g	305 s
90 °C	20 °C	13.3733 g	280 s
90 °C	30 °C	12.7090 g	290 s

6.6.3 Experimental investigation on hydrogen transfer from R2 to R3

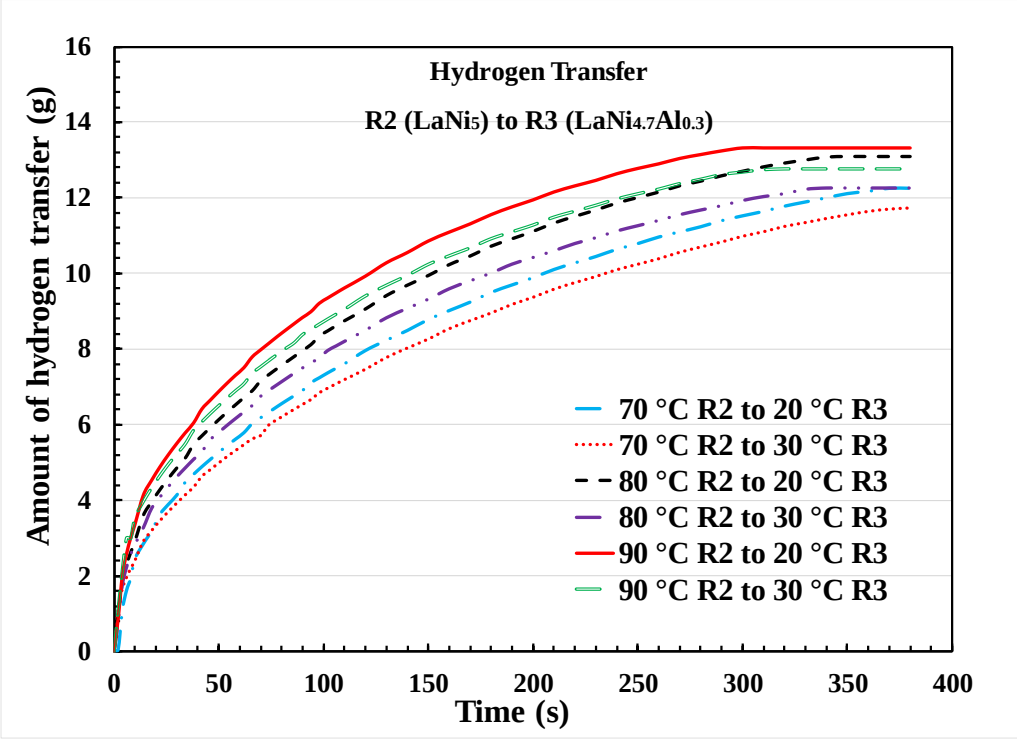

Fig. 6.49 Hydrogen transfer from R2 to R3 at different absorption/desorption temperatures

Similarly, hydrogen transfer between R2 and R3 was also studied. As depicted in **Fig. 6.49**, for 70 °C desorption temperature (R2) and 30 °C absorption temperature (R2), the amount of hydrogen transfer was 11.7240 g, which was 80.8% of the total hydrogen available for transfer. Hydrogen transfer from R2 to R3 increased significantly with increase in the temperature of desorbing reactor and decrease in the temperature of absorbing reactor. For 90 °C desorption temperature (R2) and 20 °C absorption temperature (R3), the amount of hydrogen transfer was 13.3333 g, which constitutes of nearly 92% of the total hydrogen available for transfer. With increase in temperature difference between the absorbing and desorbing reactors, the pressure gradient between the reactors also increases. This leads to faster rate of hydrogen transfer between the reactors. Moreover, for lower absorption temperature, the equilibrium bed pressure of the alloy is lower, this increases the rate of absorption for the absorbing reactor.

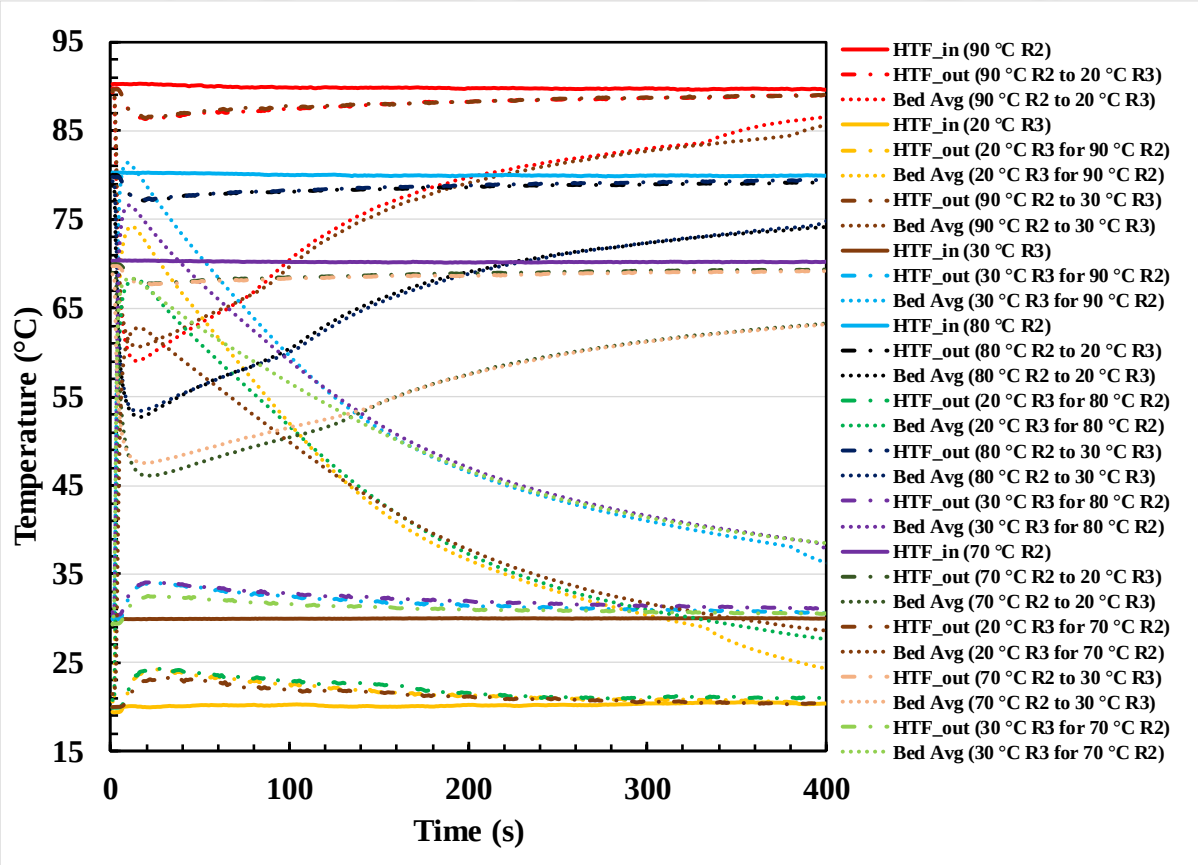

Fig. 6.50 Temperature variation curve during hydrogen transfer from R2 to R3

The details of the hydrogen transfer between the coupled reactor R1 & R3 is depicted in **Table 6.4**. The temperature variation of the MHHPS and HTF during coupled reactor study is depicted

in **Fig. 6.50**. The endothermic nature of the desorbing bed and the exothermic reaction in the absorbing bed can be clearly observed. For all the three cases, it was observed that for 90 °C desorption temperature and 20 °C absorption temperature, the amount of hydrogen absorbed was maximum. This is because of higher pressure difference between the equilibrium pressure of desorbing reactor at 90 °C and absorbing reactor at 20 °C. Therefore, it is suggested to maintain maximum temperature difference between the absorbing and the desorbing reactor.

Table 6.4 Details of hydrogen transfer in the coupled reactor (R2 to R3)

R2 Desorption Temp (T_d)	R3 Absorption Temp (T_a)	H_2 Transfer from R2 to R3	Time
70 °C	20 °C	12.2373 g	370 s
70 °C	30 °C	11.7240 g	380 s
80 °C	20 °C	13.0828 g	350 s
80 °C	30 °C	12.2614 g	340 s
90 °C	20 °C	13.3333 g	300 s
90 °C	30 °C	12.7725 g	320 s

6.6.4 Purification results for sample having 80% impurity and 20% hydrogen

To test the developed multistage hydrogen purification system with higher level of impurities, experiments were conducted with the multiple gas mixtures containing CH_4, N_2, Ar, CO_2, CO and H_2. The gas composition constitutes of 20% H_2, 18% Ar, 20% N_2, 20% CH_4, 20% CO_2 and 2% CO by weight. According to previous discussion in this chapter, CO causes severe bed poisoning, hence the quantity of CO is kept very less in the mixture. TCD analysis on the absorption sample was performed using Agilent make CP Molsieve 5A GC column, wherein Helium was used as carrier gas. As depicted in **Fig. 6.51**, hydrogen being higher thermal conductive as compared to helium, shows negative peak after 3 minute of the sample run. For other gases, the peak is in the positive side, as their thermal conductivities are lower than helium. According to the result obtained, Ar, N_2, CH_4 and CO got detected in 5^{th}, 8^{th}, 11^{th} and 15^{th} minute of the sample run time respectively. However, no peak was detected for CO_2, as CP Molsieve 5A column absorbs CO_2 in its surface and does not allows to elutes through the column even at higher temperatures. The magnitude of peaks depends on the relative thermal conductivity of gases with helium.

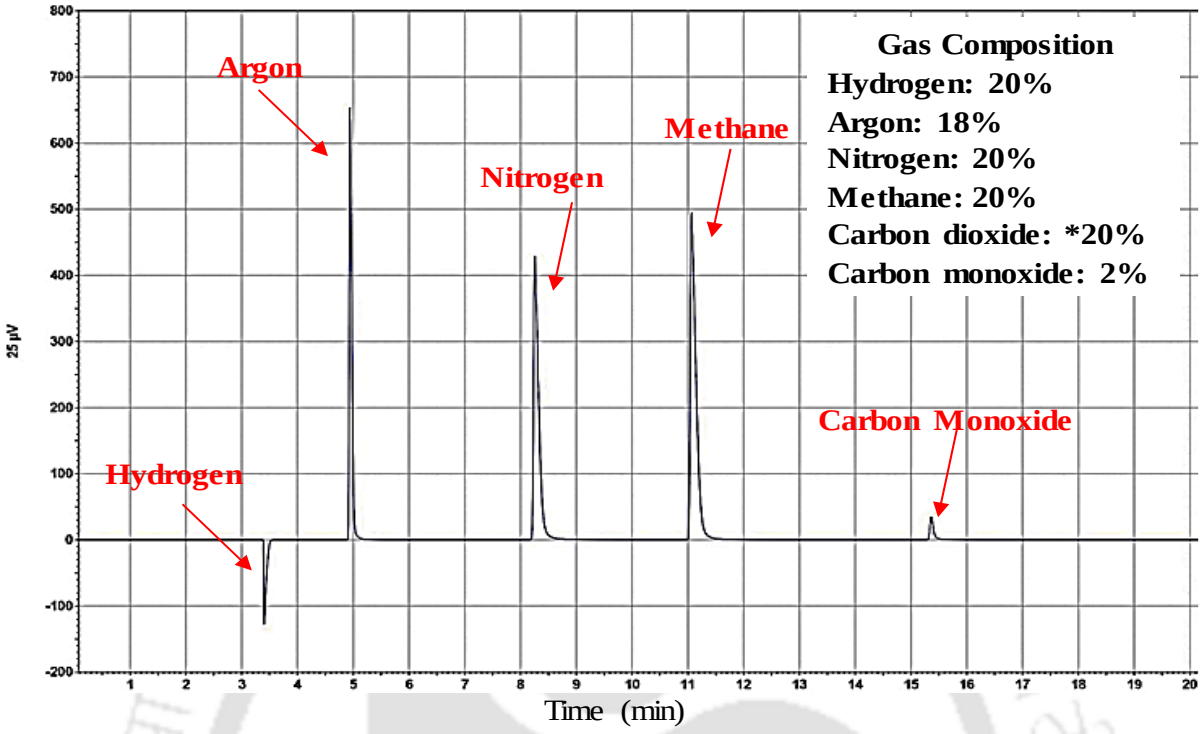

Fig. 6.51 TCD result of the absorption sample using Agilent CP Molsieve 5A column (Part no: CP7539PT; *Unable to detect CO_2 as it gets absorbed in the column wall)

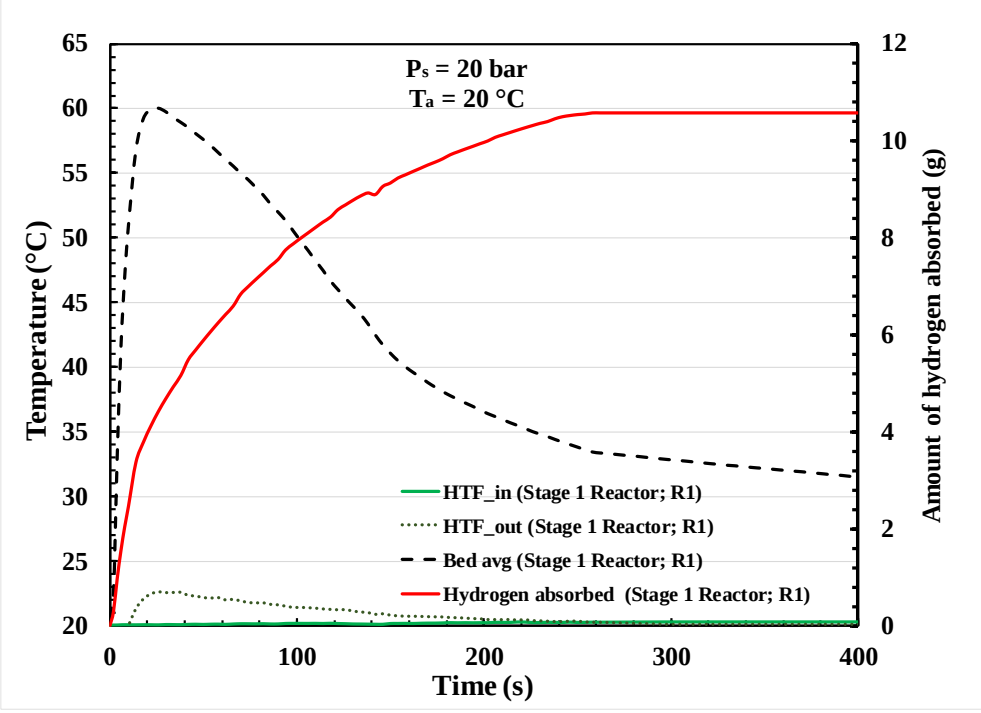

Fig. 6.52 Temperature variation and amount of H2 absorbed in stage 1 reactor (R1)

Further, the prepared sample with 20% hydrogen and 80% impurity (Ar, CO_2, N_2, CO & CH_4) was sent for absorption in stage 1 reactor i.e. R1 ($La_{0.9}Ce_{0.1}Ni_5$). The absorption was performed at 20 bar and 20 °C absorption condition. As the impurity content in the absorption gas sample was very high, the absorption was conducted at higher pressure and lower temperature. As depicted in **Fig. 6.52**, the amount of hydrogen absorbed in stage 1 reactor was 10.5786 g. The absorption got completed in 262 s, attaining the peak bed temperature of 60 °C in 23 s and peak HTF temperature of nearly 22.5 °C. Despite of high supply pressure (20 bar) the rate of absorption was on the slower side, because of the high impurity content in the absorption gas sample.

Once the absorption was completed, the reactor R1 was cooled down to 15 °C, and prepared for flushing. During flushing, the reactor was maintained at 15 °C, and the discharge valve was opened to flush the reactor. The flushed sample was further analysed using TCD, which is depicted in **Fig. 6.53**. Because of methanation Co was not detected in the flushed sample, however the other gases from the void space came out and was detected in the TCD. Flushed gas constitutes of 4.65% H_2, 30.19% Ar, 31.88% N_2 and 33.28% CH_4. Apart from these gases, CO_2, must have been present in the desorption sample, but it was not detected in TCD due to column specifications.

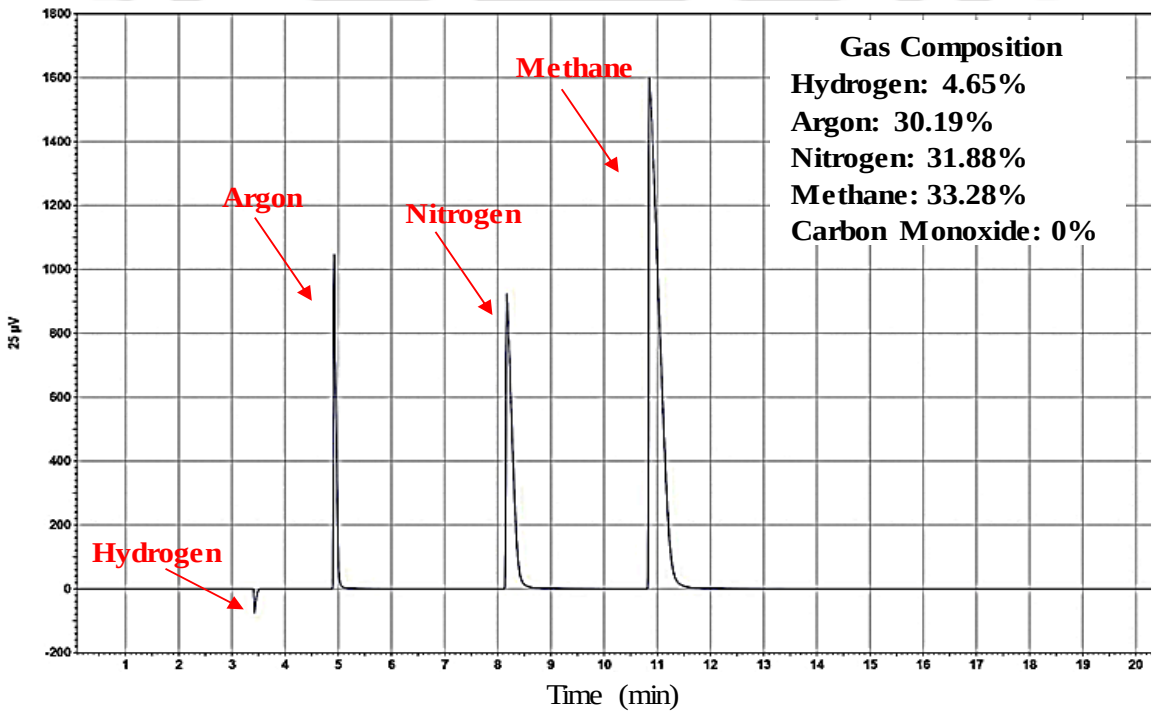

Fig. 6.53 TCD result of the flush sample using Agilent CP Molsieve 5A column

After successful flushing of the impurities from R1, the reactor was prepared for desorption. Simultaneously, the stage 2 reactor (R2 filled with $LaNi_5$) was prepared for absorption. Before hydrogen transfer in the coupled reactor system, R1 was maintained at 90 °C and R2 was maintained at 20 °C. Once the respective bed and HTF temperatures stabilizes, the rector valves are opened for facilitating hydrogen transfer from R1 to R2. The experimental outcome of the coupled reactor hydrogen transfer is depicted in **Fig. 6.54**. The amount of hydrogen transferred from R1 to R2 was 8.9106 g in 330 s. During this process, the peak bed temperature of 49.5 °C in 14 s and peak HTF temperature of nearly 22.2 °C was attained in the absorbing reactor R2. However, because of endothermic desorption the bed and HTF temperature of R1 dropped to 70.8 °C and 87.6 °C respectively.

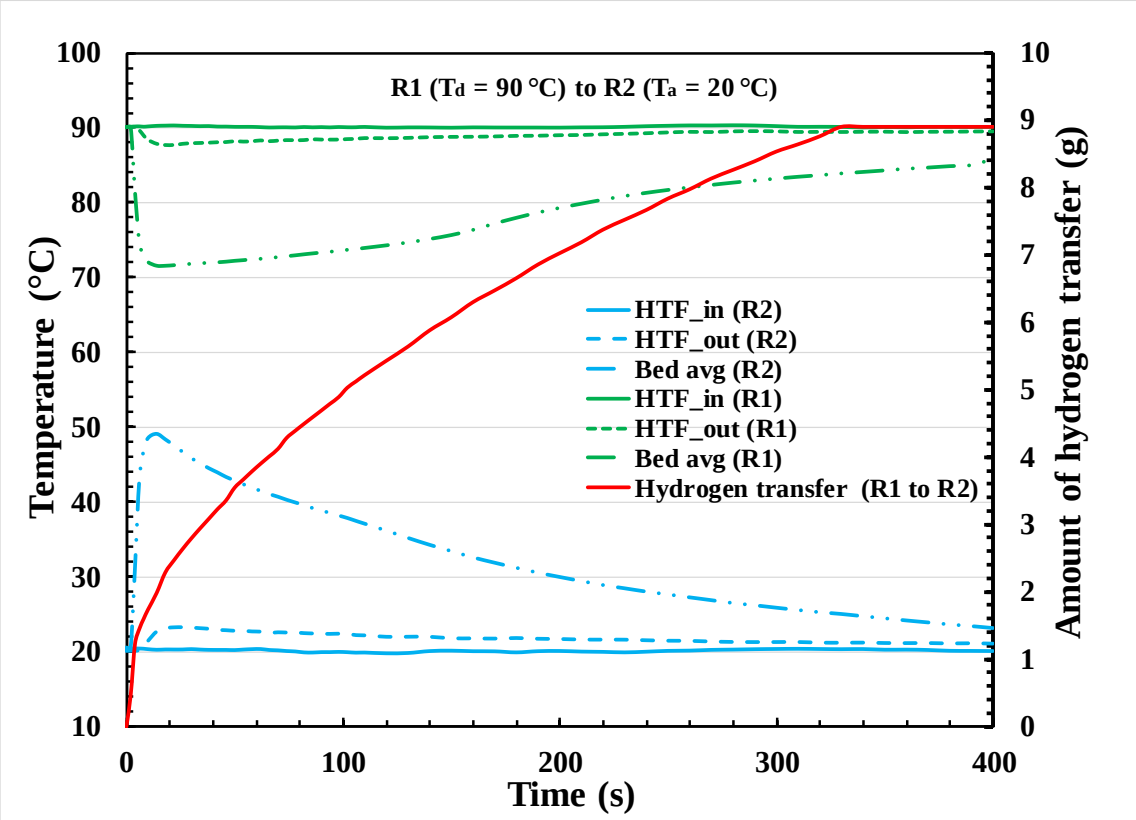

Fig. 6.54 Temperature variation and amount of H2 absorbed in stage 1 reactor (R1)

The desorption sample of stage 1 purification (R1 to R2) was collected and analysed. The TCD result of the gas sample analysis is depicted in **Fig. 6.55**. it was observed that, after stage 1

purification, 91.54% pure hydrogen was obtained with impurity of 8.46%. The impurities comprise of 2.54% Ar, 2.14% N_2, 3.79% CH_4 and trace of 0.01% CO.

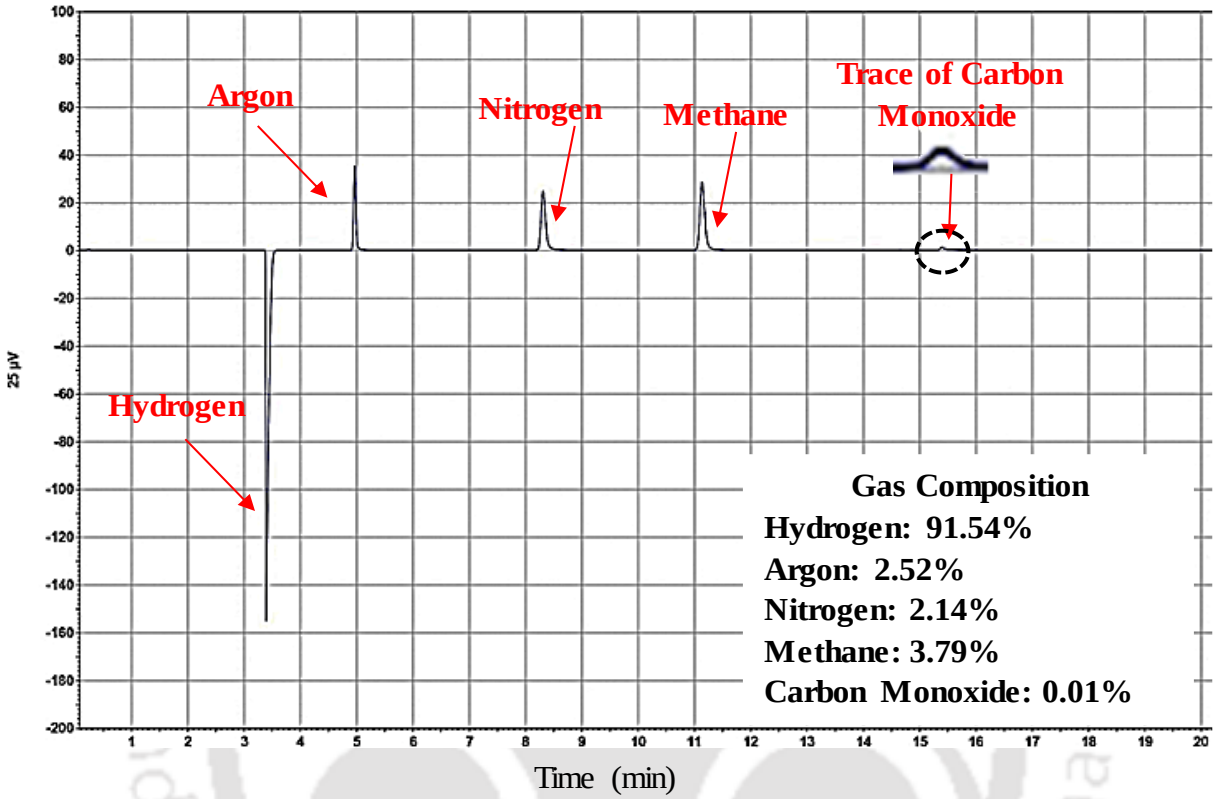

Fig. 6.55 TCD result of desorption sample after stage-1 purification (R1 to R3)

After successful flushing of the impurities from R2, the reactor was prepared for desorption. Simultaneously the stage 3 reactor (R3 filled with $LaNi_{47}Al_{0.3}$) was prepared for absorption. Before hydrogen transfer in the coupled reactor system, R2 was maintained at 90 °C and R3 was maintained at 20 °C. Once the respective bed and HTF temperatures stabilizes, the rector valves were opened to facilitate hydrogen transfer from R2 to R3. The experimental outcome of the coupled reactor hydrogen transfer is depicted in **Fig. 6.56**. the amount of hydrogen transferred from R2 to R3 was 8.1231 g in 150 s. During this process the peak bed temperature of 74.8 °C in 18 s and peak HTF temperature of nearly 24.5 °C was attained in the absorbing reactor R3. However, because of endothermic desorption the bed and HTF temperature of R2 dropped to 59.6 °C and 86.2 °C respectively. Because of lower equilibrium pressure of R3 at 20 °C, the rate of absorption was faster as compared to R1 to R2.

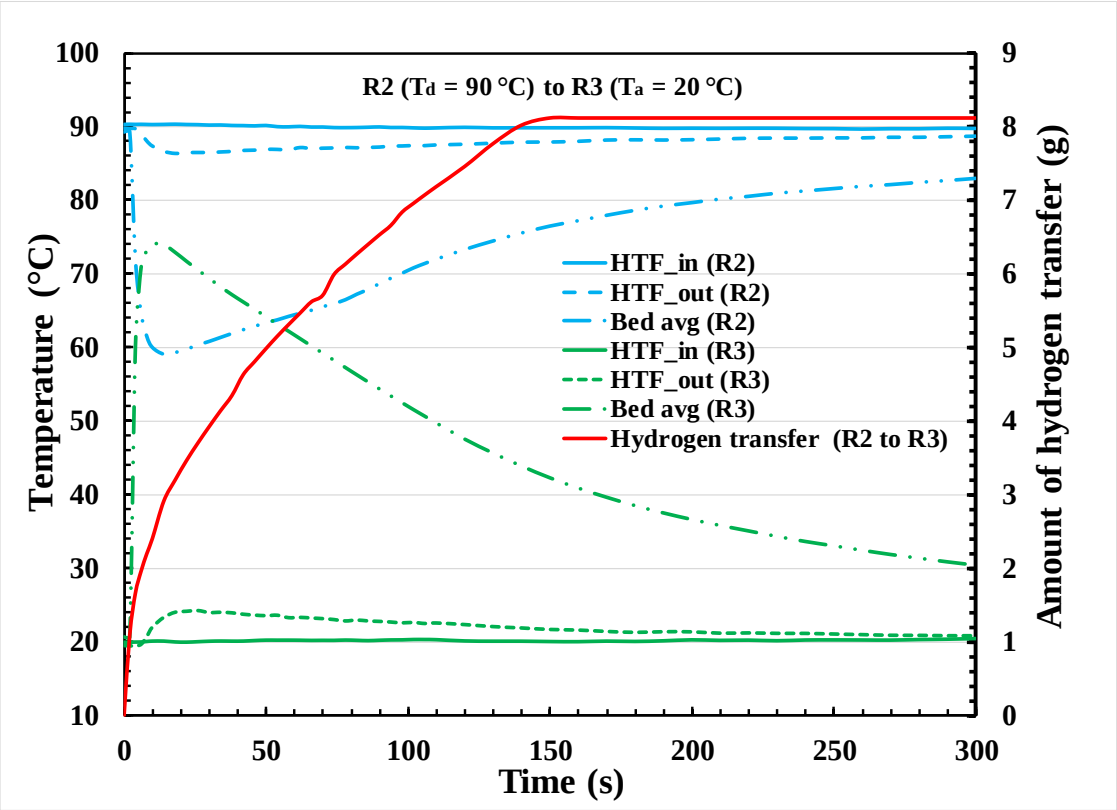

Fig. 6.56 Temperature variation and amount of H2 absorbed in stage 3 reactor (R2 to R3)

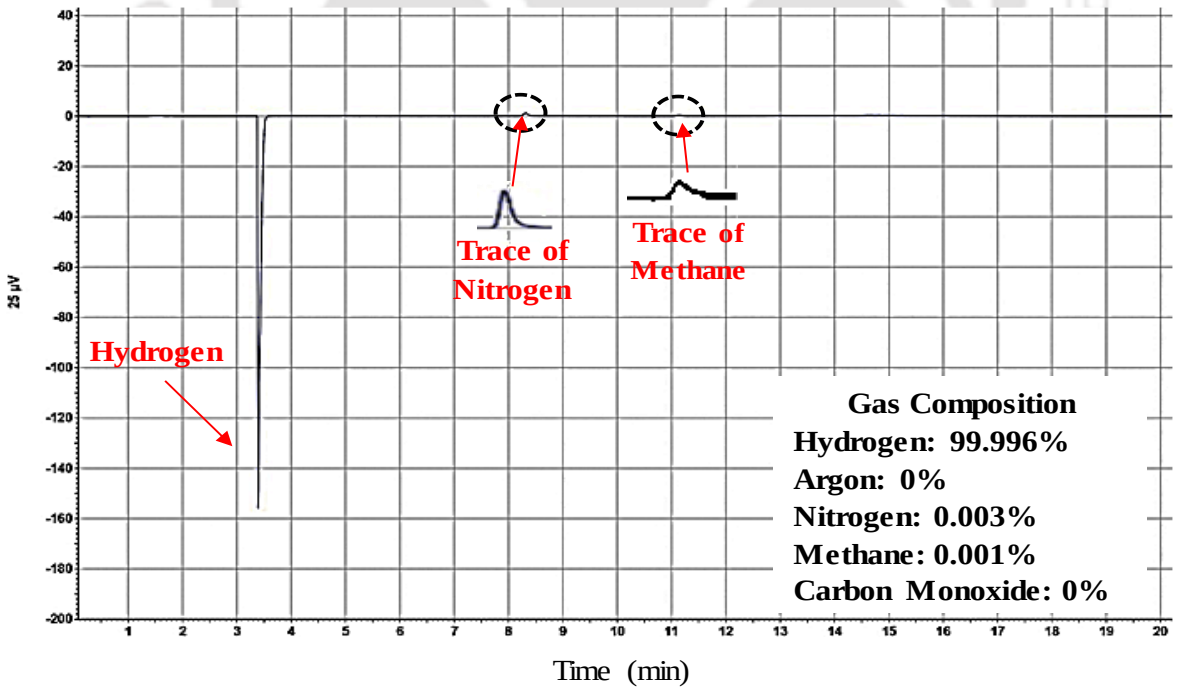

Fig. 6.57 TCD result of desorption sample after stage-2 purification (R2 to R3)

The desorption sample of stage 2 purification (R2 to R3) was collected and analysed in GC. The TCD result of the gas sample analysis is depicted in **Fig. 6.57**. it was observed that, after stage 2 purification, 99.996% pure hydrogen was obtained with impurity of 0.004%. The impurities comprise of trace of 0.003% N_2 and 0.001% CH_4.

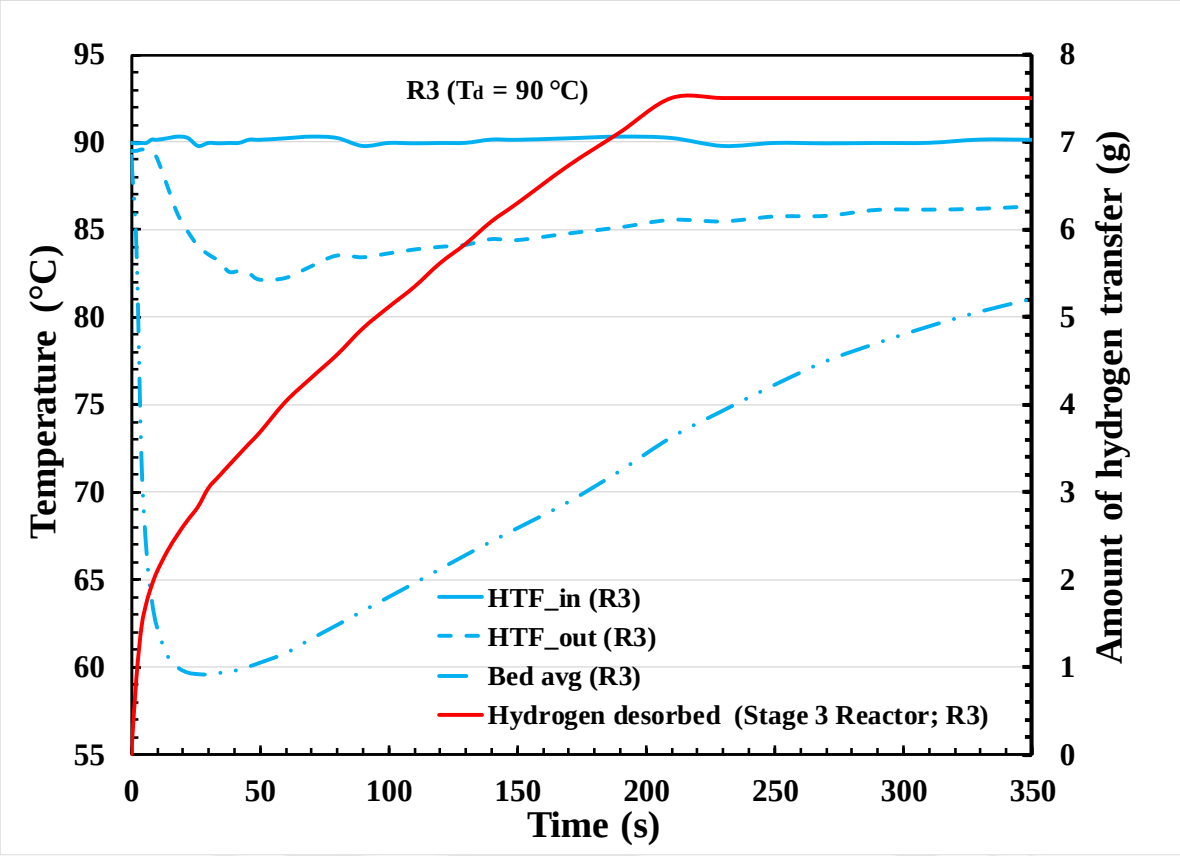

Fig. 6.58 Temperature variation & amount of H_2 desorbed from stage 3 reactor (R3)

Finally, stage 3 purification was carried out by desorbing R3 ($LaNi_{4.7}Al_{03}$). The reactor was prepared for desorption by circulating HTF at 90 °C from the HTF circuit. Once the bed and HTF temperatures stabilizes, the rector valves were opened to facilitate hydrogen collection from R3. The experimental outcome of R3 reactor hydrogen is depicted in **Fig. 6.58**. The amount of hydrogen desorbed from R3 was 7.5057 g in 210 s. During this process because of endothermic desorption the bed and HTF temperature of R2 dropped to 59.3 °C and 82.1 °C respectively. Because of significant equilibrium pressure of R3 at 90 °C, the reversibility of the R3 reactor was 92.4%. This high reversibility was due to negligible loss of gas during the flushing process, as the 99.996% pure hydrogen was transferred from R2 to R3. The desorption sample of stage 3

purification (R3) was collected and analysed in GC. The TCD result of the gas sample analysis is depicted in **Fig. 6.59**. It was observed that, after stage 3 purification, ultra-pure hydrogen was obtained with purity level of 99.9999% and negligible or no impurity. So, it can be concluded that, the MHHPS are capable of separating hydrogen from even from highly impure gas sample.

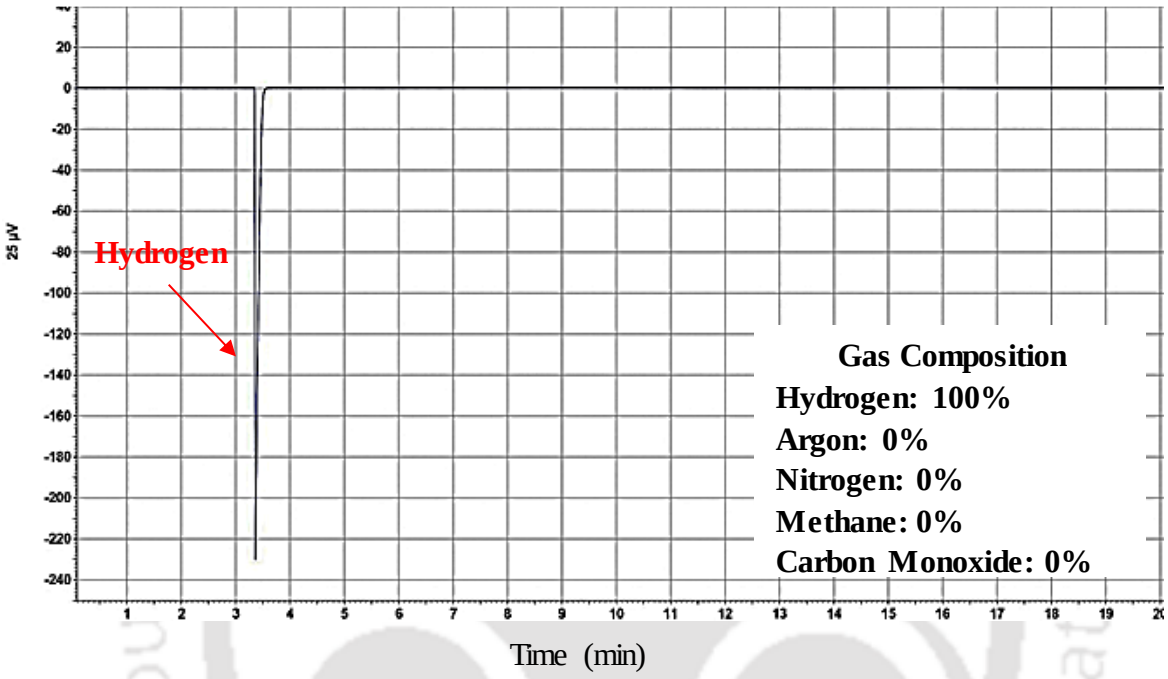

Fig. 6.59 TCD result of desorption sample after stage-3 purification (R3)

6.7 Summary

In this chapter, the experimental outcome for the single and multistage metal hydride based hydrogen purification system have been reported. The purification capacity of the various alloy bed (mainly $LaNi_{4.7}Al_{0.3}$, $LaNi_5$ and $La_{0.9}Ce_{0.1}Ni_5$) under different impurity range and type have been discussed in detail. The cyclic stability and reversibility of the MH beds have been reported under various absorption/desorption conditions. Results related to TCD (thermal conductivity detector) analysis for absorption, desorption and flushed gas sample has been discussed in details. This chapter also reports the bed poisoning characteristics of 6 ECT reactor filled with $LaNi_{4.7}Al_{0.3}$, $LaNi_5$ and $La_{0.9}Ce_{0.1}Ni_5$ under different impurities like CO, CO_2, N_2, CH_4 and Ar, along with the bed regeneration conditions for different impurities has been also covered in this chapter.

CHAPTER 7 CONCLUSIONS AND FUTURE ENDEAVOUR

7.1 Conclusions

With primary focus on hydrogen economy, MH-hydrogen systems are suitable alternatives for wide range of engineering applications. Hydrogen purification using metal hydride is one of the most significant application of such systems. In the present study, single and multistage MH based hydrogen purification systems were designed, developed and tested under various absorption/desorption conditions. From the literature, it was observed that there is a need of developing MHHPS for low temperature and low pressure application. Hydrogen obtained from the biological and chemical means are available at low pressure, and are purified using expensive and complex purification techniques like pressure swing adsorption, membrane separation, hydrogen separation using liquefaction, etc. Hence, it is required to explore MH based hydrogen purification technology as an alternative. From thermodynamic screening of MH alloys, $La_{0.9}Ce_{0.1}Ni_5$, $LaNi_5$ and $LaNi_{4.7}Al_{0.3}$ were selected as suitable alloys for the present study. These alloys can be operated in temperature range of 20 °C to 90 °C, and can be coupled with solar-thermal or waste heat recovery system. The reactors were designed using simulation performed based on coupled heat and mass transfer relations using COMSOL Multiphysics as simulation tool. From the comparative analysis among the 5 ECT, 6 ECT and 9 ECT reactors, 6 ECT reactor was fabricated using SS316 alloy and TIG welding. The reactors were designed for small alloy capacity (1.5 kg) for performing rigorous purification test. Similarly, for large scale study 99 ECT reactor with 50 kg alloy capacity was fabricated. The fabricated reactors were tested under 140 bar pressure conditions using argon gas, and were successful in leak test. The conclusions drawn from the studies are summarised below:

- For 99 ECT reactor, H_2 supply pressure showed a significant effect on absorption time. At low supply pressure of 2 bar with HTF at 30 °C and 30 lpm flow rate, 402.66 g of hydrogen was absorbed in 1908 s. When the supply pressure was increased to 5 bar and 10 bar, 413.586 g and 424.867 g of hydrogen was absorbed respectively with decrease in absorption time by 466 s (~25%) and 655 s (37%) respectively as compared to 2 bar pressure. When the supply pressure was further increased, the similar absorption performance was observed with nearly 10% reduction in half cycle time. Considering the overall observation, the recommended supply

pressure is in the range of 5 - 15 bar. However, even at pressures as low as 2 bar, remarkable absorption rate can be observed.

- Varying HTF flow rate had minor effect on absorption time. When the flow rate was decreased to 10 lpm, it caused a slight reduction in absorption kinetics. Hence, it is advisable to utilize water at flow rate above 20 lpm. This conclusion is based on the experimental outcomes of 99 ECT reactor.
- For small scale 6 ECT reactors, the suitable absorption temperature and pressure for efficient working of $La_{0.9}Ce_{0.1}Ni_5$ based MHHPS was in the range of 15-25 °C & 10-20 bar. While, the flushing temperature should be less than 15 °C to minimise hydrogen losses during flushing. The desorption temperature can be maintained above 70 °C. For efficient working of $LaNi_5$ based MHHPS, absorption condition need to be maintained in the range of 20-25 °C & 5-20 bar. While, the flushing temperature should be less than 20 °C to minimise hydrogen losses during flushing. The desorption temperature can be maintained above 80 °C. Similarly, for efficient working of $LaNi_{4.7}Al_{0.3}$ based MHHPS, absorption condition need to be maintained in the range of 25-30 °C & 2-15 bar. While, the flushing temperature should be less than 25 °C to minimise hydrogen losses during flushing. The desorption temperature can be maintained above 90 °C.
- Methane as an impurity showed significant bed poisoning characteristics, as after 20-25 cycles the absorption capacity of the MH bed was decreased significantly. Hence, it is advised to evacuate MH bed at high temperature (90 °C) after every 15^{th} purification cycle. The effect of CO_2 on alloy poisoning was lesser than CH_4. With CO_2 as impurities, the bed regeneration can be performed even after $25\text{-}30^{th}$ purification cycle. N_2 and Ar showed least effect on the alloy poisoning. Though there was a slight poisoning effect in case of N_2, but Ar hardly showed any poisoning effect.
- CO showed significant poisoning effect in the La-Ni based AB_5 alloys. Methanation was dominant when CO interacted with hydrogen and alloy simultaneously. Therefore, it is advised to use CO free impure gas sample, wherever MH based hydrogen purification technologies are used. However, presence of less CO content (1-2%) may not affect the working of such system. Maintaining desorption temperature above 100 °C could also be possible solution for such impurities, wherein the moisture generated during methanation can be removed in each desorption cycle. Apart from CO and O_2 as impurity should not be used in such systems, as it oxidises the

MH reactor. Apart from these two gases, MHHPS can handle almost all gaseous impurities and separate hydrogen from it.

- All the three selected alloys are capable of purifying hydrogen up to impurity range of 20% in a single stage, however further increase in the impurity content requires two/multi stage purification. The poisoning effect of gases are in the order $Ar<N_2<CO_2<CH_4<CO$. Moreover, it is not suggested to use CO above 0.5-1%.
- Bed regeneration is possible for poisoning caused from any of the impurities. It was observed that within one regeneration cycle (evacuation followed by absorption of pure hydrogen), the MH bed was completely regenerated for N_2 and Ar and Impurity. However, it took two regeneration cycle to reactivate alloy bed, which got poisoned from CH_4 and CO_2. For poisoning from CO, the regeneration time was maximum, as it took 3 regeneration cycle to reactivate the alloy bed.
- The purification ability of the alloys was in order $LaNi_{7.4}Al_{0.3}$ > $LaNi_5$ > $La_{0.9}Ce_{0.1}Ni_5$, However, the reversible storage capacity was in the reverse order.
- The system has its own operational and economic advantages, as it can be operated using minimal power input and can be coupled with solar/waste heat recovery system for its operation. The system is very simple in operation and cost effective. It can be coupled with the waste heat recovery system in the industry or solar-thermal heat input, to facilitate thermal input to the system, in the range of 80 °C to 90 °C for its efficient working.

7.2 Limitations and Challenges

The present system has following limitations:

- The system suffers immediate poisoning, when CO as impurity is present in the absorption gas line. It is advisable to separate CO with some primary separation techniques for CO, before sending the impure gases to the MH reactor.
- Gas sample with oxygen should never be allowed to enter the reactor. It will cause bed oxidation. Moreover, can cause explosion after reacting with alloy in presence of hydrogen (O2 > 3%, in hydrogen forms explosive mixture)
- The reactor should not be exposed to moisture. If the gas line contains moisture, it should be condensed/superheated and removed.

7.3 Future Endeavors

Following points can be considered in the future developments:

- Alloy composition (other than La-Ni composition) can be explored for CO as impurity.
- Ti-Mn-V composition (AB_2 Type MH) can be explored for purification application.
- Numerical model on MH based hydrogen purification can be developed.

7.4 Summary

This chapter presents the outline of key conclusions drawn from the present study and the limitations offered by the single and multistage metal hydride based hydrogen purifications system, while its operations. The chapter also reports the future prospective of the system and a brief summary on challenges to be taken for future improvement of the system performance.

REFERENCES

Abdalla, A.M., Hossain, S., Nisfindy, O.B., Azad, A.T., Dawood, M., Azad, A.K., 2018. Hydrogen production, storage, transportation and key challenges with applications: A review. Energy Convers. Manag. 165, 602–627. https://doi.org/10.1016/j.enconman.2018.03.088

Abdul Majid, N.A., Maeda, N., Notomi, M., 2019. Improved hydrogen desorption properties of magnesium hydride with TiFe 0.8 Mn 0.2 , graphite and iron addition. Int. J. Hydrogen Energy. https://doi.org/10.1016/j.ijhydene.2019.02.190

Abe, J.O., Popoola, A.P.I., Ajenifuja, E., Popoola, O.M., 2019. Hydrogen energy, economy and storage: Review and recommendation. Int. J. Hydrogen Energy 44, 15072–15086. https://doi.org/10.1016/j.ijhydene.2019.04.068

Acar, C., Dincer, I., 2019. Review and evaluation of hydrogen production options for better environment. J. Clean. Prod. 218, 835–849. https://doi.org/10.1016/j.jclepro.2019.02.046

Afzal, M., Gupta, N., Mallik, A., Vishnulal, K.S., Sharma, P., 2021. Experimental analysis of a metal hydride hydrogen storage system with hexagonal honeycomb-based heat transfer enhancements-part B. Int. J. Hydrogen Energy 46, 13131–13141. https://doi.org/10.1016/j.ijhydene.2020.11.275

Afzal, M., Mane, R., Sharma, P., 2017. Heat transfer techniques in metal hydride hydrogen storage: A review. Int. J. Hydrogen Energy 42, 30661–30682. https://doi.org/10.1016/j.ijhydene.2017.10.166

Akhlaghi, N., Najafpour-Darzi, G., 2020. A comprehensive review on biological hydrogen production. Int. J. Hydrogen Energy 45, 22492–22512. https://doi.org/10.1016/j.ijhydene.2020.06.182

Akiba, E., Iba, H., 1998. Hydrogen absorption by Laves phase related BCC solid solution. Intermetallics. https://doi.org/10.1016/S0966-9795(97)00088-5

Aldas, K., Mat, M.D., Kaplan, Y., 2002. A three-dimensional mathematical model for absorption in a metal hydride bed. Int. J. Hydrogen Energy 27, 1049–1056. https://doi.org/10.1016/S0360-3199(02)00010-1

Allen B. Wright, Tucson, AZ (US); Eddy J. Peters, Tucson, A. (US), 2002. (12) United States Patent (16) Patent No .: (45) Date of Patent : Syst. Method Sel. Transm. Images Interes. To a User 1, 1–4.

Anbarasu, S., Muthukumar, P., Mishra, S.C., 2014a. Thermal modeling of LmNi4.91Sn0.15 based solid state hydrogen storage device with embedded cooling tubes. Int. J. Hydrogen Energy 39, 15549–15562. https://doi.org/10.1016/j.ijhydene.2014.07.088

Anbarasu, S, Muthukumar, P., Mishra, S.C., 2014. ScienceDirect state hydrogen storage device with embedded cooling tubes. Int. J. Hydrogen Energy 39, 15549–15562. https://doi.org/10.1016/j.ijhydene.2014.07.088

Anbarasu, S., Muthukumar, P., Mishra, S.C., 2014b. Tests on $LmNi_{4.91}Sn_{0.15}$ based solid state hydrogen storage device with embedded cooling tubes - Part B: Desorption process. Int. J. Hydrogen Energy 39, 4966–4972. https://doi.org/10.1016/j.ijhydene.2014.01.039

Ao, B., Zhang, Z., He, Y., Zhao, Y., 2013. Semiconducting ground-state of three polymorphs of Mg2NiH 4 from first-principles calculations. Int. J. Hydrogen Energy 38, 16471–16476. https://doi.org/10.1016/j.ijhydene.2013.09.120

Arto, I., Capellán-Pérez, I., Lago, R., Bueno, G., Bermejo, R., 2016. The energy requirements of a developed world. Energy Sustain. Dev. 33, 1–13. https://doi.org/10.1016/j.esd.2016.04.001

Askri, F., Ben Salah, M., Jemni, A., Ben Nasrallah, S., 2009. Optimization of hydrogen storage in metal-hydride tanks. Int. J. Hydrogen Energy 34, 897–905. https://doi.org/10.1016/J.IJHYDENE.2008.11.021

Au, M., Chen, C., Ye, Z., Fang, T., Wu, J., Wang, O., 1996. The recovery, purification, storage and transport of hydrogen separated from industrial purge gas by means of mobile hydride containers. Int. J. Hydrogen Energy 21, 33–37. https://doi.org/10.1016/0360-3199(95)00044-E

Balcerzak, M., 2019. Hydrogenation properties of nanocrystalline Ti[sbnd]V[sbnd]Mn body-centered-cubic alloys. Int. J. Hydrogen Energy. https://doi.org/10.1016/j.ijhydene.2019.02.092

Belz, S., 2016. A synergetic use of hydrogen and fuel cells in human spaceflight power systems. Acta Astronaut. 121, 323–331. https://doi.org/10.1016/j.actaastro.2015.05.031

Bhuiya, M.M.H., Kumar, A., Kim, K.J., 2015. Metal hydrides in engineering systems, processes, and devices: A review of non-storage applications. Int. J. Hydrogen Energy 40, 2231–2247. https://doi.org/10.1016/j.ijhydene.2014.12.009

Bogdanović, B., Spliethoff, B., 1987. Active MgH_2Mg-systems for hydrogen storage. Int. J. Hydrogen Energy. https://doi.org/10.1016/0360-3199(87)90108-X

Bossel, U., Eliasson, B., 2002. Energy and Hydrogen Economy. Eur. Fuel Cell Forum, Lucerne 36.

Broom, D., 2011. Hydrogen Storage Materials and the Characterisation of their Hydrogen Sorption Properties. Spectroscopy.

Cao, Z., Ouyang, L., Wang, H., Liu, J., Sun, L., Felderhoff, M., Zhu, M., 2016. Development of Zr-Fe-V alloys for hybrid hydrogen storage system. Int. J. Hydrogen Energy 41, 11242–11253. https://doi.org/10.1016/j.ijhydene.2016.04.083

Carrea;, G., Warrick, B.D., 2001. Hydrogen purifiction using metal hydride getter material. United States Pat.

Carrea;, G., Warrick, B.D., 2000. Hydrogen purifiction using metal hydride getter material. United States Pat.

Casini, J.C.S., Silva, F.M., Guo, Z. ping, Liu, H.K., Faria, R.N., Takiishi, H., 2016. Effects of substituting Cu for Sn on the microstructure and hydrogen absorption properties of Co-free AB 5 alloys. Int. J. Hydrogen Energy 41, 17022–17028. https://doi.org/10.1016/j.ijhydene.2016.07.107

Chen, J., Takeshita, H.T., Tanaka, H., Kuriyama, N., Sakai, T., Uehara, I., Haruta, M., 2000. Hydriding properties of $LaNi_3$ and $CaNi_3$ and their substitutes with $PuNi_3$ -type structure. J. Alloys Compd. 302, 304–313. https://doi.org/10.1016/S0925-8388(00)00694-0

Chen, P., Zhu, M., 2008. Recent progress in hydrogen storage. Mater. Today 11, 36–43. https://doi.org/10.1016/S1369-7021(08)70251-7

Chen, R.R., Chen, X.Y., Ding, X., Li, X.Z., Guo, J.J., Ding, H.S., Su, Y.Q., Fu, H.Z., 2018. Effects of Ti/Mn ratio on microstructure and hydrogen storage properties of Ti-V-Mn alloys. J. Alloys Compd. 748, 171–178. https://doi.org/10.1016/j.jallcom.2018.03.154

Chen, X.Y., Chen, R.R., Ding, X., Li, X.Z., Ding, H.S., Su, Y.Q., Guo, J.J., Fu, H.Z., 2018. Substitution effect of Hf on hydrogen storage capacity and cycling durability of Ti 23 V 40 Mn 37 metal hydride alloys. Int. J. Hydrogen Energy 43, 19567–19574. https://doi.org/10.1016/j.ijhydene.2018.08.203

Chen, X.Y., Chen, R.R., Yu, K., Ding, X., Li, X.Z., Ding, H.S., Su, Y.Q., Guo, J.J., 2019. Effect of Ce substitution on hydrogen absorption/ desorption of Laves phase-related BCC solid solution Ti 33 V 37 Mn 30 alloy. J. Alloys Compd. 783, 617–624. https://doi.org/10.1016/j.jallcom.2018.12.302

Chen, X.Y., Wei, L.X., Deng, L., Yang, F.S., Zhang, Z.X., 2014. A review on the metal hydride based hydrogen purification and separation technology. Appl. Mech. Mater. 448–453, 3027–3036. https://doi.org/10.4028/www.scientific.net/AMM.448-453.3027

Ćirić, K.D., Kocjan, A., Gradišek, A., Koteski, V.J., Kalijadis, A.M., Ivanovski, V.N., Laušević, Z. V., Stojić, D.L., 2012. A study on crystal structure, bonding and hydriding properties of Ti-Fe-Ni intermetallics - Behind substitution of iron by nickel. Int. J. Hydrogen Energy 37, 8408–8417. https://doi.org/10.1016/j.ijhydene.2012.02.047

Crivello, J.C., Denys, R. V., Dornheim, M., Felderhoff, M., Grant, D.M., Huot, J., Jensen, T.R., de Jongh, P., Latroche, M., Walker, G.S., Webb, C.J., Yartys, V.A., 2016. Mg-based compounds for hydrogen and energy storage. Appl. Phys. A Mater. Sci. Process. 122, 1–17. https://doi.org/10.1007/s00339-016-9601-1

Davids, M.W., Lototskyy, M., Malinowski, M., van Schalkwyk, D., Parsons, A., Pasupathi, S., Swanepoel, D., van Niekerk, T., 2019. Metal hydride hydrogen storage tank for light fuel cell vehicle. Int. J. Hydrogen Energy 1–10. https://doi.org/10.1016/j.ijhydene.2019.01.227

Dehouche, Z., Grimard, N., Laurencelle, F., Goyette, J., Bose, T.K., 2005. Hydride alloys properties investigations for hydrogen sorption compressor. J. Alloys Compd. 399, 224–236. https://doi.org/10.1016/ J. Alloys Compd. 2005.01.029

Dincer, I., Acar, C., 2014. Review and evaluation of hydrogen production methods for better sustainability. Int. J. Hydrogen Energy 40, 11094–11111. https://doi.org/10.1016/j.ijhydene.2014.12.035

Dixit, V., Huot, J., 2019. Structural, microstructural and hydrogenation characteristics of Ti-V-Cr alloy with Zr-Ni addition. J. Alloys Compd. 776, 614–619. https://doi.org/10.1016/j.jallcom.2018.10.283

Dunikov, D., Blinov, D., 2020. Extraction of hydrogen from a lean mixture with methane by metal hydride. Int. J. Hydrogen Energy 45, 9914–9926. https://doi.org/10.1016/j.ijhydene.2020.01.201

Dunikov, D., Borzenko, V., Blinov, D., Kazakov, A., Lin, C.Y., Wu, S.Y., Chu, C.Y., 2016. Biohydrogen purification using metal hydride technologies. Int. J. Hydrogen Energy 41, 21787–21794. https://doi.org/10.1016/j.ijhydene.2016.08.190

Dunikov, D., Borzenko, V., Malyshenko, S., 2012. Influence of impurities on hydrogen absorption in a metal hydride reactor. Int. J. Hydrogen Energy 37, 13843–13848.

https://doi.org/10.1016/j.ijhydene.2012.04.078

Dunikov, D.O., Blinov, D. V., 2019a. Use of methane-hydrogen mixtures for energy accumulation. J. Phys. Conf. Ser. 1370. https://doi.org/10.1088/1742-6596/1370/1/012033

Dunikov, D.O., Blinov, D. V., 2019b. On efficiency of metal hydride extraction of hydrogen from a mixture with methane. J. Phys. Conf. Ser. 1359. https://doi.org/10.1088/1742-6596/1359/1/012132

El-Eskandarany, M.S., Al-Salem, S.M., Ali, N., Banyan, M., Al-Ajmi, F., Al-Duweesh, A., 2020. From gangue to the fuel-cells application. Sci. Rep. 10, 1–18. https://doi.org/10.1038/s41598-020-76503-6

Fleming, W.H., Khan, J.A., Rhodes, C.A., 2001. Effective heat transfer in a metal-hydride-based hydrogen separation process. Int. J. Hydrogen Energy 26, 711–724. https://doi.org/10.1016/S0360-3199(00)00129-4

Floriano, R., Leiva, D.R., Dessi, J.G., Asselli, A.A.C., Junior, A.M.J., Botta, W.J., 2016. Mg-based nanocomposites for hydrogen storage containing Ti-Cr-V alloys as additives, in: Materials Research. https://doi.org/10.1590/1980-5373-MR-2016-0179

Flueckiger, S., Voskuilen, T., Pourpoint, T., Fisher, T.S., Zheng, Y., 2010. In situ characterization of metal hydride thermal transport properties. Int. J. Hydrogen Energy 35, 614–621. https://doi.org/10.1016/J.IJHYDENE.2009.11.001

Fukai, Y., 2005. The Metal-Hydrogen System, The Metal-Hydrogen System. https://doi.org/10.1007/3-540-28883-x

Gao, Y., Jiang, J., Meng, Y., Yan, F., Aihemaiti, A., 2018. A review of recent developments in hydrogen production via biogas dry reforming. Energy Convers. Manag. 171, 133–155. https://doi.org/10.1016/j.enconman.2018.05.083

Golben, P.M., 2010. Hydrogen purification System. United States Pat.

Golben, P.M., 2003. Passive purification in metal hydride storage apparatus. United States Pat.

Gopal, M.R.A.M., Murthy, S.S., 1992. Cylindrical Metal Hydride Beds 17, 795–805.

Grashoff, G.J., Pilkington, C.E., Corti, C.W., 1983. Purification of Hydrogen. Platin. Met. Rev. 27, 157–169.

Gregory, K., Rogner, H.-H., 1998. Energy resources and conversion technologies for the 21st century by Gregory and Rogner.pdf. Mitig. Adapt. Strateg. Glob. Chang.

Han, S.S., Goo, N.H., Jeong, W.T., Lee, K.S., 2001. Synthesis of composite metal hydride alloy

of A_2B and AB type by mechanical alloying. J. Power Sources 92, 157–162. https://doi.org/10.1016/S0378-7753(00)00516-4

Hanada, N., Asada, H., Nakagawa, T., Higa, H., Ishida, M., Heshiki, D., Toki, T., Saita, I., Asano, K., Nakamura, Y., Fujisawa, A., Miura, S., 2017. Effect of CO_2 on hydrogen absorption in Ti-Zr-Mn-Cr based AB_2 type alloys. J. Alloys Compd. 705, 507–516. https://doi.org/10.1016/j.jallcom.2017.02.067

Hanada, N., Nakagawa, T., Asada, H., Ishida, M., Takahashi, K., Isobe, S., Saita, I., Asano, K., Nakamura, Y., Fujisawa, A., Miura, S., 2015. Dependence of constituent elements of AB_5 type metal hydrides on hydrogenation degradation by CO2 poisoning. J. Alloys Compd. 647, 198–203. https://doi.org/10.1016/j.jallcom.2015.05.253

Huston, E.L., Sandrock, G.D., 1980. Engineering properties of metal hydrides. J. Less Common Met. 74, 435–443. https://doi.org/10.1016/0022-5088(80)90182-4

Iba, H., Akiba, E., 1997. Hydrogen absorption and modulated structure in Ti-V-Mn alloys. J. Alloys Compd. https://doi.org/10.1016/S0925-8388(96)03072-1

Jacobson, M.Z., 2009. Review of solutions to global warming, air pollution, and energy security. Energy Environ. Sci. 2, 148–173. https://doi.org/10.1039/b809990c

Jain, I.P., 2009. Hydrogen the fuel for 21st century. Int. J. Hydrogen Energy 34, 7368–7378. https://doi.org/10.1016/j.ijhydene.2009.05.093

Jana, S., Raju, N.N., Muthukumar, P., 2022. Performance tests on embedded cooling tube type metal hydride reactor for heating and cooling applications. Therm. Sci. Eng. Prog. 33, 101349. https://doi.org/10.1016/J.TSEP.2022.101349

Jemni, A., Nasrallah, S. Ben, 1995a. Study of two-dimensional heat and mass transfer during absorption in a metal-hydrogen reactor. Int. J. Hydrogen Energy 20, 43–52. https://doi.org/10.1016/0360-3199(93)E0007-8

Jemni, A., Nasrallah, S. Ben, 1995b. Study of two-dimensional heat and mass transfer during desorption in a metal-hydrogen reactor. Int. J. Hydrogen Energy 20, 881–891. https://doi.org/10.1016/0360-3199(94)00115-G

Jenne, S.P., Jana, S., Palanisamy, M., 2020. Experimental investigation on absorption and desorption characteristics of $La_{0.9}Ce_{0.1}Ni_5$ for hydrogen storage application. Int. J. Energy Res. 1–12. https://doi.org/10.1002/er.5983

Kabutomori, T., Ohnishi, K., n.d. Kinds and characteristics of hydrogen storage alloy. Energy Carr.

Convers. Syst. II.

Kadier, A., Kalil, M.S., Abdeshahian, P., Chandrasekhar, K., Mohamed, A., Azman, N.F., Logroño, W., Simayi, Y., Hamid, A.A., 2016. Recent advances and emerging challenges in microbial electrolysis cells (MECs) for microbial production of hydrogen and value-added chemicals. Renew. Sustain. Energy Rev. 61, 501–525. https://doi.org/10.1016/j.rser.2016.04.017

Kallweit, J., Hahne, E., 2019. Effective Thermal Conductivity of Metal Hydride Powders: Measurement and Theoretical Modelling 373–378. https://doi.org/10.1615/ihtc10.790

Kamble, A., Sharma, P., Huot, J., 2018. Effect of addition of Zr, Ni, and Zr-Ni alloy on the hydrogen absorption of Body Centred Cubic 52Ti-12V-36Cr alloy. Int. J. Hydrogen Energy 43, 7424–7429. https://doi.org/10.1016/j.ijhydene.2018.02.106

Karmakar, A., Mallik, A., Gupta, N., Sharma, P., 2020. Studies on 10 kg alloy mass metal hydride based reactor for hydrogen storage. Int. J. Hydrogen Energy. https://doi.org/10.1016/j.ijhydene.2020.11.091

Kazakov, A.N., Dunikov, D.O., Mitrokhin, S. V., 2016. AB_5-type intermetallic compounds for biohydrogen purification and storage. Int. J. Hydrogen Energy 41, 21774–21779. https://doi.org/10.1016/j.ijhydene.2016.07.243

Kazakov, A.N., Romanov, I.A., Mitrokhin, S. V., Kiseleva, E.A., 2020. Experimental investigations of AB_5-type alloys for hydrogen separation from biological gas streams. Int. J. Hydrogen Energy 45, 4685–4692. https://doi.org/10.1016/j.ijhydene.2019.11.207

Klein, H.P., Groll, M., 2002. Development of a two-stage metal hydride system as topping cycle in cascading sorption systems for cold generation. Appl. Therm. Eng. 22, 631–639. https://doi.org/10.1016/S1359-4311(01)00115-6

Köhler, J., Wietschel, M., Whitmarsh, L., Keles, D., Schade, W., 2010. Infrastructure investment for a transition to hydrogen automobiles. Technol. Forecast. Soc. Change 77, 1237–1248. https://doi.org/10.1016/j.techfore.2010.03.010

Leng, H., Yu, Z., Yin, J., Li, Q., Wu, Z., Chou, K.C., 2017. Effects of Ce on the hydrogen storage properties of TiFe0.9Mn0.1 alloy. Int. J. Hydrogen Energy 42, 23731–23736. https://doi.org/10.1016/j.ijhydene.2017.01.194

Li, J., Li, B., Shao, H., Li, W., Lin, H., 2018. Catalysis and downsizing in Mg-based hydrogen storage materials. Catalysts. https://doi.org/10.3390/catal8020089

Li, Y., Hu, F., Luo, L., Xu, J., Zhao, Z., Zhang, Y., Zhao, D., 2018. Hydrogen storage of casting MgTiNi alloys. Catal. Today 318, 103–106. https://doi.org/10.1016/j.cattod.2017.10.046

Lin, H.C., Lin, K.M., Sung, C.W., Wu, K.C., 2007. Characteristics of activation and anti-poisoning in an LmNi4.8 Al0.2 hydrogen storage alloy. Int. J. Hydrogen Energy 32, 2494–2500. https://doi.org/10.1016/j.ijhydene.2006.10.064

Linder, M., Mertz, R., Laurien, E., 2010. Experimental analysis of fast metal hydride reaction bed dynamics. Int. J. Hydrogen Energy 35, 8755–8761. https://doi.org/10.1016/J.IJHYDENE.2010.05.023

Liu, P., Xie, X., Xu, L., Li, X., Liu, T., 2017. Hydrogen storage properties of $(Ti_{0.85}Zr_{0.15})_{1.05}Mn_{1.2}Cr_{0.6}V_{0.1}M_{0.1}$ (M=Ni, Fe, Cu) alloys easily activated at room temperature. Prog. Nat. Sci. Mater. Int. 27, 652–657. https://doi.org/10.1016/j.pnsc.2017.09.007

Liu, W., Webb, C.J., Gray, E.M.A., 2016. Review of hydrogen storage in AB_3 alloys targeting stationary fuel cell applications. Int. J. Hydrogen Energy 41, 3485–3507. https://doi.org/10.1016/j.ijhydene.2015.12.054

Łodziana, Z., Dębski, A., Cios, G., Budziak, A., 2019. Ternary $LaNi_{4.75}M_{0.25}$ hydrogen storage alloys: Surface segregation, hydrogen sorption and thermodynamic stability. Int. J. Hydrogen Energy 44, 1760–1773. https://doi.org/10.1016/j.ijhydene.2018.11.104

López Ortiz, A., Meléndez Zaragoza, M.J., Collins-Martínez, V., 2016. Hydrogen production research in Mexico: A review. Int. J. Hydrogen Energy 41, 23363–23379. https://doi.org/10.1016/j.ijhydene.2016.07.004

Lototsky, M. V., Williams, M., Yartys, V.A., Klochko, Y. V., Linkov, V.M., 2011. Surface-modified advanced hydrogen storage alloys for hydrogen separation and purification. J. Alloys Compd. 509, S555–S561. https://doi.org/10.1016/J.JALLCOM.2010.09.206

Lototskyy, M., Satya Sekhar, B., Muthukumar, P., Linkov, V., Pollet, B.G., 2015. Niche applications of metal hydrides and related thermal management issues. J. Alloys Compd. 645, S117–S122. https://doi.org/10.1016/j.jallcom.2014.12.271

Lototskyy, M. V., Davids, M.W., Tolj, I., Klochko, Y. V., Sekhar, B.S., Chidziva, S., Smith, F., Swanepoel, D., Pollet, B.G., 2015a. Metal hydride systems for hydrogen storage and supply for stationary and automotive low temperature PEM fuel cell power modules. Int. J. Hydrogen Energy 40, 11491–11497. https://doi.org/10.1016/j.ijhydene.2015.01.095

Lototskyy, M. V., Davids, M.W., Tolj, I., Klochko, Y. V., Sekhar, B.S., Chidziva, S., Smith, F.,

Swanepoel, D., Pollet, B.G., 2015b. Metal hydride systems for hydrogen storage and supply for stationary and automotive low temperature PEM fuel cell power modules. Int. J. Hydrogen Energy 40, 11491–11497. https://doi.org/10.1016/J.IJHYDENE.2015.01.095

Lototskyy, M. V., Tolj, I., Davids, M.W., Klochko, Y. V., Parsons, A., Swanepoel, D., Ehlers, R., Louw, G., van der Westhuizen, B., Smith, F., Pollet, B.G., Sita, C., Linkov, V., 2016. Metal hydride hydrogen storage and supply systems for electric forklift with low-temperature proton exchange membrane fuel cell power module. Int. J. Hydrogen Energy 41, 13831–13842. https://doi.org/10.1016/J.I J Hyd Ene.2016.01.148

Lu, L., H, L., Orgaz, E., 2001. Journal of Alloys and Compounds 322 (2001) 45–54. J. Alloys Compd. 322, 45–54.

Lynch, F.E., 1991. Metal hydride practical applications. J. Less-Common Met. 172–174, 943–958. https://doi.org/10.1016/S0022-5088(06)80001-9

Magnetto, D., Mola, S., Dacosta, D.H., Golben, M., Rosso, M., 2006. A metal hydride mobile air conditioning system. SAE Tech. Pap. 115, 1150–1159. https://doi.org/10.4271/2006-01-1235

Martin, M., Gommel, C., Borkhart, C., Fromm, E., 1996. Absorption and desorption kinetics of hydrogen storage alloys. J. Alloys Compd. 238, 193–201. https://doi.org/10.1016/0925-8388(96)02217-7

Matsushita, M., Monde, M., Mitsutake, Y., 2014. Predictive calculation of the effective thermal conductivity in a metal hydride packed bed. Int. J. Hydrogen Energy 39, 9718–9725. https://doi.org/10.1016/J.IJHYDENE.2014.04.072

Mayer, U., Groll, M., Supper, W., 1987. Heat and mass transfer in metal hydride reaction beds: Experimental and theoretical results. J. Less Common Met. 131, 235–244. https://doi.org/10.1016/0022-5088(87)90523-6

Mesarić, P., Krajcar, S., 2015. Home demand side management integrated with electric vehicles and renewable energy sources. Energy Build. 108, 1–9. https://doi.org/10.1016/j.enbuild.2015.09.001

Mi, W. liang, Liu, Z. sen, Kimura, T., Kamegawa, A., Wang, H. liang, 2019. Crystal structure and hydrogen storage properties of (La,Ce)Ni_{5-x} M_x (M = Al, Fe, or Co) alloys. Int. J. Miner. Metall. Mater. 26, 108–113. https://doi.org/10.1007/s12613-019-1714-z

Miura, S., Fujisawa, A., Ishida, M., 2012. A hydrogen purification and storage system using metal hydride. Int. J. Hydrogen Energy 37, 2794–2799.

https://doi.org/10.1016/J.IJHYDENE.2011.03.150

Miura, S., Fujisawa, A., Tomekawa, S., Taniguchi, Y., Hanada, N., Ishida, M., 2013. A hydrogen purification and storage system using CO adsorbent and metal hydride. J. Alloys Compd. 580, S414–S417. https://doi.org/10.1016/J.JALLCOM.2013.03.154

Modibane, K.D., Williams, M., Lototskyy, M., Davids, M.W., Klochko, Y., Pollet, B.G., 2013. Poisoning-tolerant metal hydride materials and their application for hydrogen separation from CO_2/CO containing gas mixtures. Int. J. Hydrogen Energy 38, 9800–9810. https://doi.org/10.1016/J.IJHYDENE.2013.05.102

Mohammedi, L., Daoudi, B., Boukraa, A., 2015. Ab-initio structural and electronic properties of the intermetallic compound TiFeH2. Comput. Condens. Matter 2, 11–15. https://doi.org/10.1016/j.cocom.2014.12.001

Mohtadi, R., Orimo, S.I., 2016. The renaissance of hydrides as energy materials. Nat. Rev. Mater. https://doi.org/10.1038/natrevmats.2016.91

Moradi, R., Groth, K.M., 2019. Hydrogen storage and delivery: Review of the state of the art technologies and risk and reliability analysis. Int. J. Hydrogen Energy 44, 12254–12269. https://doi.org/10.1016/j.ijhydene.2019.03.041

Muthukumar, P., Kumar, A., Raju, N.N., Malleswararao, K., Rahman, M.M., 2018. A critical review on design aspects and developmental status of metal hydride based thermal machines. Int. J. Hydrogen Energy 43, 17753–17779. https://doi.org/10.1016/j.ijhydene.2018.07.157

Muthukumar, P., Maiya, M.P., Murthy, S.S., 2005. Experiments on a metal hydride based hydrogen compressor. Int. J. Hydrogen Energy 30, 879–892. https://doi.org/10.1016/j.ijhydene.2004.09.003

Muthukumar, P., Patil, M.S., Raju, N.N., Imran, M., 2016. Parametric investigations on compressor-driven metal hydride based cooling system. Appl. Therm. Eng. 97, 87–99. https://doi.org/10.1016/j.applthermaleng.2015.10.155

Muthukumar, P., Satheesh, A., 2013. Analysis of crossed van't Hoff metal hydride based heat pump. Int. J. Hydrogen Energy 38, 11415–11420. https://doi.org/10.1016/j.ijhydene.2013.06.070

Muthukumar, P., Singh Patel, K., Sachan, P., Singhal, N., 2012a. Computational study on metal hydride based three-stage hydrogen compressor. Int. J. Hydrogen Energy 37, 3797–3806. https://doi.org/10.1016/j.ijhydene.2011.05.104

Muthukumar, P., Singhal, A., Bansal, G.K., 2012b. Thermal modeling and performance analysis of industrial-scale metal hydride based hydrogen storage container. Int. J. Hydrogen Energy 37, 14351–14364. https://doi.org/10.1016/J.IJHYDENE.2012.07.010

Nahar, G., Mote, D., Dupont, V., 2017. Hydrogen production from reforming of biogas : Review of technological advances and an Indian perspective. Renew. Sustain. Energy Rev. 76, 1032–1052. https://doi.org/10.1016/j.rser.2017.02.031

Ngene, P., Longo, A., Mooij, L., Bras, W., Dam, B., 2017. Metal-hydrogen systems with an exceptionally large and tunable thermodynamic destabilization. Nat. Commun. 8. https://doi.org/10.1038/s41467-017-02043-9

Nishizaki, T., Miyamoto, K., Yoshida, K., 1983a. Coefficients of performance of hydride heat pumps. J. Less-Common Met. 89, 559–566. https://doi.org/10.1016/0022-5088(83)90372-7

Nishizaki, T., Miyamoto, K., Yoshida, K., 1983b. Coefficients of performance of hydride heat pumps. J. Less Common Met. 89, 559–566. https://doi.org/10.1016/0022-5088(83)90372-7

Odysseos, M., De Rango, P., Christodoulou, C.N., Hlil, E.K., Steriotis, T., Karagiorgis, G., Charalambopoulou, G., Papapanagiotou, T., Ampoumogli, A., Psycharis, V., Koultoukis, E., Fruchart, D., Stubos, A., 2013. The effect of compositional changes on the structural and hydrogen storage properties of (La-Ce)Ni_5 type intermetallics towards compounds suitable for metal hydride hydrogen compression. J. Alloys Compd. 580, S268–S270. https://doi.org/10.1016/j.jallcom.2013.01.057

Ogden, J.M., 1999. Prospects for building ahydrogen energy infrastructure. Annu. Rev. Energy Environ. 24, 227–279.

Oztek, M.T., 2005. Recovery of hydrogen and helium from their mixtures using metal hydrides. Thesis, Master Sci. Univ. Cent. Florida Orlando, Florida.

Pan, H., Liu, Y., Gao, M., Zhu, Y., Lei, Y., 2003. The structural and electrochemical properties of $La_{0.7}Mg_{0.3}(Ni_{0.85}Co_{0.15})x$ (x = 3.0-5.0) hydrogen storage alloys. Int. J. Hydrogen Energy 28, 1219–1228. https://doi.org/10.1016/S0360-3199(02)00285-9

Patel, A.K., Sharma, P., Huot, J., 2018. Effect of annealing on microstructure and hydrogenation properties of TiFe + X wt% Zr (X = 4, 8). Int. J. Hydrogen Energy 43, 6238–6243. https://doi.org/10.1016/j.ijhydene.2018.02.029

Payá, J., Linder, M., Laurien, E., Corberán, J.M., 2009. Mathematical models for the P-C-T characterization of hydrogen absorbing alloys. J. Alloys Compd. 484, 190–195.

https://doi.org/10.1016/j.jallcom.2009.05.069

Peterson, janice C., Dimartino, S.P., 1987. Metal hydride adsorption process for hydrogen purification. United States Pat.

Petrecca, G., Decarli, M., 2008. A review of hydrogen applications: Technical and economic aspects. Proc. Mediterr. Electrotech. Conf. - MELECON 658–662. https://doi.org/10.1109/MELCON.2008.4618510

Principi, G., Agresti, F., Maddalena, A., Lo Russo, S., 2009. The problem of solid state hydrogen storage. Energy 34, 2087–2091. https://doi.org/10.1016/j.energy.2008.08.027

Raju, Nithin Narmada, Kumar, A., Malleswararao, K., Muthukumar, P., 2019. Parametric studies on $LaNi_{4.7}Al_{0.3}$ based hydrogen storage reactor with embedded cooling tubes. Energy Procedia 158, 2384–2390. https://doi.org/10.1016/j.egypro.2019.01.288

Raju, Nithin N., Muthukumar, P., Selvan, P.V., Malleswararao, K., 2019. Design methodology and thermal modelling of industrial scale reactor for solid state hydrogen storage. Int. J. Hydrogen Energy 44, 20278–20292. https://doi.org/10.1016/j.ijhydene.2019.05.193

Ram Gopal, M., Srinivasa Murthy, S., 1993. Parametric studies on heat and mass transfer in metal hydride beds. Chem. Eng. Process. Process Intensif. 32, 217–223. https://doi.org/10.1016/0255-2701(93)80003-Y

Sandrock, G., 1999. Panoramic overview of hydrogen storage alloys from a gas reaction point of view. J. Alloys Compd. 293, 877–888. https://doi.org/10.1016/S0925-8388(99)00384-9

Sastri, M., Viswanathan, B., Murthy, S., 1998. Metal Hydrides : Fundamentals and Applications. Narosa Publishing House, Springer.

Satheesh, A., Muthukumar, P., 2010. Performance investigation of double-stage metal hydride based heat pump. Appl. Therm. Eng. 30, 2698–2707. https://doi.org/10.1016/j.applthermaleng.2010.07.021

Satheesh, A., Muthukumar, P., Dewan, A., 2009. Computational study of metal hydride cooling system. Int. J. Hydrogen Energy 34, 3164–3172. https://doi.org/10.1016/j.ijhydene.2009.01.083

Satya Sekhar, B., Muthukumar, P., 2013. Performance tests on a double-stage metal hydride based heat transformer. Int. J. Hydrogen Energy 38, 15428–15437. https://doi.org/10.1016/j.ijhydene.2013.09.103

Satya Sekhar, B., Suresh, P., Muthukumar, P., 2013. Performance tests on metal hydride based

hydrogen storage devices. Int. J. Hydrogen Energy 38, 9570–9577. https://doi.org/10.1016/j.ijhydene.2012.09.095

Schlapbach, L., Züttel, A., 2001. Hydrogen-storage materials for Mobile Applications. Nature 414, 353–358. https://doi.org/10.1038/35104634

Schweppe, F., Martin, M., Fromm, E., 1997. Hydrogen absorption of LaNi5 powders precovered with O_2, CO, H_2S, CO_2 or N_2. J. Alloys Compd. 253–254, 511–514. https://doi.org/10.1016/S0925-8388(96)03002-2

Sengodan, S., Lan, R., Humphreys, J., Du, D., Xu, W., Wang, H., 2018. Advances in reforming and partial oxidation of hydrocarbons for hydrogen production and fuel cell applications. Renew. Sustain. Energy Rev. 82, 761–780. https://doi.org/10.1016/j.rser.2017.09.071

Shafiee, S., McCay, M.H., 2016. Different reactor and heat exchanger configurations for metal hydride hydrogen storage systems - A review. Int. J. Hydrogen Energy 41, 9462–9470. https://doi.org/10.1016/j.ijhydene.2016.03.133

Shaijumon, M.M., Rajalakshmi, N., Ryu, H., Ramaprabhu, S., 2005. Synthesis of multi-walled carbon nanotubes in high yield using Mm based AB_2 alloy hydride catalysts and the effect of purification on their hydrogen adsorption properties. Nanotechnology 16, 518–524. https://doi.org/10.1088/0957-4484/16/4/031

Shaltiel, D., Jacob, I., Davidov, D., 1977. Hydrogen absorption and desorption properties of AB_2 laves-phase pseudobinary compounds. J. Less-Common Met. 53, 117–131. https://doi.org/10.1016/0022-5088 (77) 90162-X

Shang, H., Zhang, Y., Li, Y., Qi, Y., Guo, S., Zhao, D., 2019. Effects of adding over-stoichiometrical Ti and substituting Fe with Mn partly on structure and hydrogen storage performances of TiFe alloy. Renew. Energy 135, 1481–1498. https://doi.org/10.1016/j.renene.2018.09.072

Shao, H., Xin, G., Zheng, J., Li, X., Akiba, E., 2012. Nanotechnology in Mg-based materials for hydrogen storage. Nano Energy. https://doi.org/10.1016/j.nanoen.2012.05.005

Sheppard, D.A., Paskevicius, M., Humphries, T.D., Felderhoff, M., Capurso, G., Bellosta von Colbe, J., Dornheim, M., Klassen, T., Ward, P.A., Teprovich, J.A., Corgnale, C., Zidan, R., Grant, D.M., Buckley, C.E., 2016. Metal hydrides for concentrating solar thermal power energy storage. Appl. Phys. A 122, 395. https://doi.org/10.1007/s00339-016-9825-0

Singh, L., Wahid, Z.A., 2015. Methods for enhancing bio-hydrogen production from biological

process: A review. J. Ind. Eng. Chem. 21, 70–80. https://doi.org/10.1016/j.jiec.2014.05.035

Smil, V., 2017. Energy Transitions Global and National Perspectives. Praeger.

Smith, K.C., Fisher, T.S., 2012. Models for metal hydride particle shape, packing, and heat transfer. Int. J. Hydrogen Energy 37, 13417–13428. https://doi.org/10.1016/J.IJHYDENE.2012.06.087

Sohn, H.Y., Emami, S., 2011. Kinetics of dehydrogenation of the Mg–Ti–H hydrogen storage system. Int. J. Hydrogen Energy 36, 8344–8350. https://doi.org/10.1016/J.IJHYDENE.2011.03.167

Souza, E.C., Ticianelli, E.A., 2003. on the Properties of $LaNi_5$ -Type Metal Hydride Alloys. J. Brazalian Chem. Soc. 14, 544–550.

Sun, D.W., Groll, M., Werner, R., 1992. Selection of alloys and their influence on the operational characteristics of a two-stage metal hydride heat transformer. Heat Recover. Syst. CHP 12, 49–55. https://doi.org/10.1016/0890-4332(92)90006-4

Sunku prasad, J., Muthukumar, P., 2022. Performance and Energy Efficiency of a Solid-state Hydrogen Storage System: An Experimental Study on $La_{0.7}Ce_{0.1}Ca_{0.3}Ni_5$. Appl. Therm. Eng. 119030. https://doi.org/10.1016/J.Appl Thermal Eng.2022.119030

Sunku prasad, J., Muthukumar, P., 2021. Experimental investigation on annular metal hydride reactor for medium to large-scale hydrogen storage applications. J. Energy Storage 44, 103473. https://doi.org/10.1016/j.est.2021.103473

Sunku Prasad, J., Muthukumar, P., Desai, F., Basu, D.N., Rahman, M.M., 2019. A critical review of high-temperature reversible thermochemical energy storage systems. Appl. Energy 254, 113733. https://doi.org/10.1016/j.apenergy.2019.113733

Tarasov, B.P., Bocharnikov, M.S., Yanenko, Y.B., Fursikov, P. V., Lototskyy, M. V., 2020. A comprehensive review on hydrogen absorption behaviour of metal alloys prepared through mechanical alloying. Metals (Basel). 10, 1–26. https://doi.org/10.3390/met10050562

Tessier, P., Coignet, P., Jurcik, B., Adleman, R., 2018. Method of purifying hydrogen from a metal hydride storage system. United States Pat.

Van Mal, H.H., Buschow, K.H.J., Miedema, A.R., 1974. Hydrogen absorption in $LaNi_5$ and related compounds: Experimental observations and their explanation. J. Less-Common Met. 35, 65–76. https://doi.org/10.1016/0022-5088(74)90146-5

Voskuilen, T.G., Waters, E.L., Pourpoint, T.L., 2014. A comprehensive approach for alloy

selection in metal hydride thermal systems. Int. J. Hydrogen Energy 39, 13240–13254. https://doi.org/10.1016/j.ijhydene.2014.06.119

Wan, Q.I., Li, P., Li, Y., Zhai, F., Zhang, W., Cui, L., 2014. Hydrogenation / Dehydrogenation Properties 37, 837–842.

Wang, X.L., Iwata, K., Suda, S., 1995. Hydrogen purification using fluorinated $LaNi_{4.7}Al_{0.3}$ alloy. J. Alloys Compd. 231, 860–864. https://doi.org/10.1016/0925-8388(95)01773-9

Wiedenhofer, D., Lenzen, M., Steinberger, J.K., 2013. Energy requirements of consumption: Urban form, climatic and socio-economic factors, rebounds and their policy implications. Energy Policy 63, 696–707. https://doi.org/10.1016/j.enpol.2013.07.035

Xie, X.B., Ni, C., Wang, Baolei, Zhang, Y., Zhao, X., Liu, L., Wang, Bing, Du, W., 2020. Recent advances in hydrogen generation process via hydrolysis of Mg-based materials: A short review. J. Alloys Compd. 816, 152634. https://doi.org/10.1016/j.jallcom.2019.152634

Yan, H., Xiong, W., Wang, L., Li, B., Li, J., Zhao, X., 2017. Investigations on AB_3-, A_2B_7- and A_5B_{19}-type La[sbnd]Y[sbnd]Ni system hydrogen storage alloys. Int. J. Hydrogen Energy 42, 2257–2264. https://doi.org/10.1016/j.ijhydene.2016.09.049

Yang, F.S., Wang, G.X., Zhang, Z.X., Meng, X.Y., Rudolph, V., 2010. Design of the metal hydride reactors - A review on the key technical issues. Int. J. Hydrogen Energy 35, 3832–3840. https://doi.org/10.1016/j.ijhydene.2010.01.053

Yao, Z., Liu, L., Xiao, X., Wang, C., Jiang, L., Chen, L., 2018. Effect of rare earth doping on the hydrogen storage performance of $Ti_{1.02}Cr_{1.1}Mn_{0.3}Fe_{0.6}$ alloy for hybrid hydrogen storage application. J. Alloys Compd. 731, 524–530. https://doi.org/10.1016/j.jallcom.2017.10.075

Young, K. hsiung, Nei, J., 2013. The current status of hydrogen storage alloy development for electrochemical applications. Materials (Basel). 6, 4574–4608. https://doi.org/10.3390/ma6104574

Zhang, H., Fu, L., Qi, J., Ji, Z., 2019. Effects of doping with yttrium on the hydrogen storage performances of the La 2 Mg 17 alloy surface. J. Power Sources 417, 76–82. https://doi.org/10.1016/j.jpowsour.2019.02.023

Zhang, T.B., Yang, X.W., Li, J.S., Hu, R., Xue, X.Y., Fu, H.Z., 2012. On the poisoning effect of O 2 and N 2 for the Zr 0.9Ti 0.1V 2 hydrogen storage alloy. J. Power Sources 202, 217–224. https://doi.org/10.1016/j.jpowsour.2011.12.002

Zhao, W., Yang, Y., Bao, Z., Yan, D., Zhu, Z., 2020. Methods for measuring the effective thermal

conductivity of metal hydride beds: A review. Int. J. Hydrogen Energy 45, 6680–6700. https://doi.org/10.1016/j.ijhydene.2019.12.185

Zhou, C., Wang, H., Ouyang, L., Zhu, M., 2019. The state of the art of hydrogen storage materials for high vessel. Mater. Rep. 33. https://doi.org/10.11896/db.201901013.

Zhu, M., Lu, Y., Ouyang, L., Wang, H., 2013. Thermodynamic tuning of mg-based hydrogen storage alloys: A review. Materials (Basel). https://doi.org/10.3390/ma6104654

Zhu, Y., Yang, C., Zhu, J., Li, L., 2011. Structural and electrochemical hydrogen storage properties of Mg 2Ni-based alloys. J. Alloys Compd. 509, 5309–5314. https://doi.org/10.1016/j.jallcom.2011.02.017

Zuttel, A., 2003. Materials for hydrogen storage. Mater. Today 24–33.

Züttel, A., 2004. Hydrogen storage methods. Naturwissenschaften 91, 157–172. https://doi.org/10.1007/s00114-004-0516-x

APPENDIX A UNCERTAINTY ANALYSIS

Experimental uncertainties are integral part of experiments, as several electrical, mechanical and human errors are involved in performing experiment. The uncertainty in measurement of different measurements in the present work have been estimated using the method proposed by Kline and McClintock (1953). The basic principle of estimating uncertainty are following:

Consider a variable N dependent on various indepedndent measeured variables such as X_1, X_2, … X_n, then,

$$N = f(x_1, x_2, ..., x_n) \tag{A.1}$$

If the uncertainty in measured quantity N be ΔN and that for independent variables be ΔX_1, ΔX_2,… ΔX_n, then the uncertainty ΔN is given by,

$$\Delta N = \frac{\partial N}{N} = \sqrt{\left[\left(\frac{\partial f}{\partial x_1}\right)\Delta x_1\right]^2 + \left[\left(\frac{\partial f}{\partial x_2}\right)\Delta x_2\right]^2 + ... + \left[\left(\frac{\partial f}{\partial x_n}\right)\Delta x_n\right]^2} \tag{A.2}$$

where, $\pm\partial N$ is the error in N. The primary measured parameters in the experimental investigations are temperature, amount of hydrogen transferred and the flow rate of HTF during the reactions. Hence, the error in their individual measurements are estimated.

A.1 Temperature measurement

The temperature at different locations of MH bed and HTF was measured using K-type thermocouples. The minimum bed temperature measured is 15.2 °C and the accuracy is ± 0.5 °C for K-type thermocouple. Hence, the maximum uncertainty in temperature measurement is:

$$\frac{\partial T}{T} = \pm\frac{0.5}{15.2} = \pm 0.032 = \pm 3.2\% \tag{A.3}$$

A.2 Supply pressure measurement

The supply pressure is set through pressure regulator by monitoring pressure gauge. The

minimum set pressure was 10 bar and the accuracy of pressure transmitter is ± 0.5 bar. Hence, the maximum uncertainty in supply pressure measurement is:

$$\frac{\partial P}{P} = \pm\frac{0.5}{10} = \pm 0.05 = \pm 5\% \quad \text{(A.4)}$$

A.3 Measurement of hydrogen transferred

The amount of hydrogen transferred is obtained from Coriolis mass flow meter. The minimum value of hydrogen transferred was 1.2 g in 60 s. Hence, the maximum uncertainty in measurement of hydrogen transfer is:

$$\frac{\partial m_{H_2}}{m_{H_2}} = \pm\sqrt{\left(\frac{0.001}{1.2}\right)^2 + \left(\frac{0.1}{60}\right)^2} = \pm 0.0084 = \pm\ 0.84\% \quad \text{(A.5)}$$

A.4 Measurement of flow rate

Similarly, the flow rate of HTF is measured from flow meter for duration of 60 s. Hence, the maximum uncertainty in measurement of HTF flow rate calculated from volume and time is:

$$\frac{\partial m_{HTF}}{m_{HTF}} = \pm\sqrt{\left(\frac{10}{1000}\right)^2 + \left(\frac{0.1}{60}\right)^2} = \pm 0.0101 = \pm\ 1.01\% \quad \text{(A.6)}$$

A.5 Estimation of hydrogen storage capacity

The hydrogen storage capacity of MH is estimated as the amount of hydrogen absorbed/desorbed per kg of MH alloy (wt%). Minimum alloy considered in the system is of 1.2 kg which was filled using weighing balance with accuracy of ± 0.5 g. Hence, the maximum uncertainty in estimation of hydrogen storage capacity is:

$$\frac{\partial HSC}{HSC} = \pm\sqrt{\left(\frac{0.001}{1.2}\right)^2 + \left(\frac{0.0005}{12}\right)^2 + \left(\frac{0.1}{60}\right)^2} = \pm 0.0243 = \pm\ 2.4\% \quad \text{(A.7)}$$

APPENDIX B EQUIPMENT SPECIFICATIONS

The measurement during the experimental investigation were conducted using various instruments and equipment's. The technical specifications and manufacturing details of the equipment are listed below:

B.1 Mass flow meter

Make	:	Emerson
Model	:	1700R12ABFEZZZ
Type	:	Coriolis mass flow meter
Fluid	:	Hydrogen and any other gas
Flow band	:	0-50 g/s
Accuracy	:	± 0.35%
Precision	:	4 digits after decimal
Sensitivity	:	0.01 g/s
Operating pressure range	:	up to 413 bar at 37 °C
Operating temperature range	:	-10 °C - 80 °C
Output signal	:	4-20 mA

B.2 Data acquisition system (DAQ)

Make	:	Keysight
Model	:	34972A
Scan intervals	:	0-99 hour; 1 ms record time step
Accuracy	:	± 0.004%
Precision	:	6 digits after decimal
Record signals	:	DC (100 mA – 1A; 100 mV – 300 V)
		AC (100 mA – 2A; 100 mV – 100 V)
Scan temperature	:	-100 – 1820 °C

B.3 Pressure gauge

Make	:	Swagelok
Model	:	PGI-63A-NG150-L-AQ-X - BH
Type	:	Analog
Sensitivity	:	0.25 bar
Operating pressure range	:	0 – 60 bar (in circuit); 0 – 150 bar (cylinder)

B.4 Thermocouple

Make	:	Industrial
Model	:	Specifically configured for application
Type	:	K type
Sensitivity	:	± 0.5 °C
Operating temperature range	:	-200 – 1250 °C

B.5 High temperature recirculating bath

Make	:	Siskin Instruments Co. Pvt. Ltd.
Model	:	HCB200S
Type	:	Recirculating
Fluid	:	Water/Silicon oil
Flow band	:	up to 50 lpm
Bath stability	:	± 0.1 °C
Precision	:	2 digits after decimal
Operating temperature range	:	30 – 180 °C
Bath volume	:	50 l
Heating capacity	:	9 kW
Power input	:	3 Phase AC; 240 V; 32 A (max)
Volts-frequency	:	400 V; 50 Hz

B.6 Low temperature recirculating bath

Make	:	Siskin Instruments Co. Pvt. Ltd.
Model	:	Profichil RCC 7000 ST400
Type	:	Recirculating
Fluid	:	Water/Silicon oil
Flow band	:	up to 50 lpm
Bath stability	:	± 0.1 °C
Precision	:	2 digits after decimal
Operating temperature range	:	-40 – 40 °C
Bath volume	:	50 l
Heating capacity	:	7 kW at 0 °C
Power input	:	3 Phase AC; 240 V; 32 A (max)
Volts-frequency	:	400 V; 50 Hz

B.7 Vacuum Pump

Make	:	Ran-Vac Technologies Pvt. Ltd.
Model	:	Vacpro -2063
Type	:	Rotary vane pump
System cooling	:	Air cooled
Operating fluid	:	Vacpro ultra 3 (6 l)
Pumping speed	:	63 m^3/h (at 50 Hz)
Vacuum pressure range	:	1 – 10^{-3} mbar
Operating temperature range	:	30 – 180 °C
Bath volume	:	50 l
Heating capacity	:	9 kW
Power input	:	2.24 kW
Rotation speed	:	1440 rpm
Frequency	:	50 Hz

B.8 Weighing balance

Make	:	Saffron
Model	:	SES 20TH
Capacity	:	up to 20 kg
Accuracy	:	± 0.1 g

B.9 Valves

Make	:	Swagelok
Model	:	SS-43GS4, SS 1RS4 and SS 4BG
Pressure range	:	206 bar, 344 bar and 70 bar at 37 °C
Type	:	Ball valve, Needle valve and Bellow sealed

B.10 Filter

Make	:	Swagelok
Model	:	SS-4F-05
Type	:	Inline
Pressure range	:	60 bar differential pressure
End fittings	:	¼ inch NTP
Pore size	:	0.5 µm

B.11 Other tube fittings

Make	:	Swagelok
Model (2-way connector)	:	SS-400-6
Model (3-way connector)	:	SS-400-3
Model (4-way connecter)	:	SS-400-2
Model (Braided hose)	:	SS-XT4TA4TA4-78; SS-XT4TA4TA4-24
Model (Tube)	:	THT-3R60-6.35-0.89

LIST OF PUBLICATIONS AND PATENTS

Patents

[1] P. Muthukumar, **A Kumar**, System and Process for Hydrogen Separation Through Metal Hydride Reactors (**Granted**; Patent Number – 403389; Application No. – 202131059468).

[2] P. Muthukumar, **A Kumar**, N.N Raju, R Nagarajan, S. Prakash, System and Process for Hydrogen Purification (Communicated; Patent Application No. – 202111001818).

Journal Publications

[1] **Alok Kumar,** P. Muthukumar, Parametric Investigation on the Purification Characteristics of $La_{0.9}Ce_{0.1}Ni_5$ under various Absorption/Desorption conditions (Selected for publication in ***Int J Hydrogen Energy***, from World Hydrogen Energy Conference 2022)

[2] **Alok Kumar**, P. Muthukumar, Bed Poisoning Characteristics of CO_2 impurity on the $La_{0.9}Ce_{0.1}Ni_5$ based Hydrogen Purification System (Communicated ***Int J Hydrogen Energy***, **Manuscript No: HE-D-22-04810**.)

[3] **Alok Kumar**, P. Muthukumar, Experimental Investigation on the Poisoning Characteristics of Methane as Impurity in $La_{0.9}Ce_{0.1}Ni_5$ based Hydrogen Storage and Purification System, ***Energy,*** 259 (2022) 124888.

[4] **Alok Kumar**, P. Muthukumar, Pratibha Sharma, E. Anil Kumar, Absorption Based Solid State Hydrogen Storage System: A Review, ***Sustainable Energy Technologies and Assessments*** 52 (2022) 102204

[5] **Alok Kumar**, N.N. Raju, P. Muthukumar, Parametric studies on $MmNi_{4.7}Fe_{0.3}$ based reactor with embedded cooling tubes for hydrogen storage and cooling application, ***J. Energy Storage***. 35 (2021) 102317

[6] **Alok Kumar**, N.N. Raju, P. Muthukumar, P.V. Selvan, Experimental studies on industrial scale metal hydride based hydrogen storage system with embedded cooling tubes, ***Int J Hydrogen Energy*** 44 (2019) 13549-13560.

[7] N.N. Raju, **Alok Kumar**, K. Malleswararao, P. Muthukumar, Parametric Studies on $LaNi_{4.7}Al_{0.3}$ based Hydrogen Storage Reactor with Embedded Cooling Tubes, ***Energy Procedia*** 158 (2019) 2384–2390.

[8] P. Muthukumar, **Alok Kumar**, N.N. Raju, K. Malleswararao, M.M. Rahman, A critical review on design aspects and developmental status of metal hydride based thermal machines, ***Int J Hydrogen Energy*** 43 (2018) 17753-17779.

Conference Publications

[1] **Alok Kumar,** P. Muthukumar, Parametric Investigation on the Purification Characteristics of $La_{0.9}Ce_{0.1}Ni_5$ under various Absorption/Desorption conditions. *23rd World Hydrogen Energy Conference*, Istanbul, Turkey, 26th–30th June 2022.

[2] **Alok Kumar,** P. Muthukumar, Bed Poisoning Characteristics of CO_2 impurity on the $La_{0.9}Ce_{0.1}Ni_5$ based Hydrogen Purification System, *International Conference on Renewable Energy*, 25th-27th Feb. 2022

[3] **Alok Kumar,** N. N. Raju, P. Muthukumar, Experimental Investigation on the Poisoning Characteristics of Gaseous as Impurity in $La_{0.9}Ce_{0.1}Ni_5$ based Hydrogen Storage and Purification System, *International Conference on Polygeneration* (ICP) 4th–6th October 2021.

[4] **Alok Kumar**, N.N. Raju, P. Muthukumar, Experimental Studies on $MmNi_{4.7}Fe_{0.3}$ based Hydrogen Storage Device for Cooling Application, *6th National Conference on Refrigeration and Air Conditioning*, NCRAC 32, 20th – 22nd Feb 2020.

[5] **Alok Kumar**, N.N. Raju, P. Muthukumar, Parametric Studies on $MmNi_{4.7}Fe_{0.3}$ based Reactor with Embedded Cooling Tubes for Hydrogen Storage and Cooling Application, *International conference on innovations in thermo-fluid engineering and sciences*, ICITFES 2020 - 13702, 10th – 12th Feb 2020.

[6] N.N. Raju, **Alok Kumar**, P. Muthukumar, Experimental Studies on Metal Hydride Based Hydrogen Storage and Cooling Applications, *REFCOLD India*, 2019.

Book Chapters

[1] **Alok Kumar**, S. Jana, P. Muthukumar, Thermodynamic analysis on Hydrogen Storage system, *Encyclopedia of Energy Storage, Elsevier, 1 (2022)* 253-263.

[2] **Alok Kumar**, N.N. Raju, J.S. Prasad, P. Muthukumar, Engineering Applications of Metal Hydride – Hydrogen System, *PATH OF PROGRESS A Voyage of Mechanical Engineering in Sixth IIT*, (2021) 161-190.

Awards and achievements

- Received Science and Engineering Research Board-International Travel Support (SERB-ITS; File No: ITS/2022/000768), DST, Govt. of India, for attending world hydrogen energy conference 2022.
- Paper ID 13702, "Parametric Studies on $MmNi_{4.7}Fe_{0.3}$ based Reactor with Embedded Cooling Tubes for Hydrogen Storage and Cooling Application" selected as best paper at International conference on innovations in thermo-fluid engineering and sciences 2020, NIT Rourkela.
- Second runner up at "Global Poster Competition" REFCOLD India 2019.